UNIVERSITY OF SOUTHAMPTON

FACULTY OF ENGINEERING AND THE ENVIRONMENT

Silver Nanoprisms Embedded in a Polymeric Matrix for Energy Saving Glazing

by

Michele Carboni

Thesis for the degree of Doctor of Philosophy

September 2014

To my father, a mentor, an example, a friend.

ABSTRACT

According to the data from government institutions (Energy Information Administration, 2012), the consumption of energy will show an average growth of 42.5% by 2035 from the heating, ventilation and air conditioning devices solely (Perez-Lombard et al., 2008). For this reason the interest in technologies that can reduce the consumption of energy for heating or cooling houses is growing. In particular, the glazing of houses could offer great potential for energy saving as these elements of the building envelopment still have a margin for improvement. Currently, the research is focusing on stopping the heat exchange through radiative transfer. The problems of the current technologies are associated with the high costs and the colour they give to windows. Technologies using nanoparticles have started to emerge and have shown promise as methods for absorbing the radiation which passes through the glazing. Thanks to the unique control over their size and shape dependent properties, their absorbance can be moved to lower energy and this can satisfy both the requirements of stopping the heat carrying radiation and still providing a good illumination. Through the wide range of nanoparticle materials, sizes and shapes, silver triangular nanoprisms are a promising candidate for further research due to their strong absorption in the near infrared region.

As their synthesis and the control over their geometrical properties are challenging using conventional batch-based macro reactor systems, a novel microreactor system was developed in this study in order to continuously produce silver triangular nanoprisms and monitoring their optical properties by mean of integrated spectroscopy techniques. By using sol-gel chemistry, the particles were coated with a shell of SiO_2 which can further be functionalised with various chemical functional groups such as thiol and allyl.

Coated particles were then embedded in polymeric matrix (i.e. poly(methylmethacrylate), or PMMA) with covalent interactions between the polymer and the functional groups attached to the silica shell surface. Finally, the composite solutions were casted onto a glass-slide and the optical performance was evaluated using spectroscopic methodologies.

Compared to similar composite materials, the systems herein reported offers several advantages, such as the low coloration in the visible spectrum and no risk of aggregation of the metal nuclei once they are dispersed in the polymer matrix. The use of a microreactor can also grant good control over high volumes of such colloids, opening to the possibility for a large scale production of such materials.

Contents

3 Experimental 41

List of Figures

List of Tables

Declaration of Authorship

I, Michele Carboni, declare that the thesis entitled *Silver Nanoprisms Embedded in a Polymeric Matrix for Energy Saving Glazing* and the work presented in the thesis are both my own, and have been generated by me as the result of my own original research. I confirm that:

- this work was done wholly or mainly while in candidature for a research degree at this University;
- where any part of this thesis has previously been submitted for a degree or any other qualification at this University or any other institution, this has been clearly stated;
- where I have consulted the published work of others, this is always clearly attributed;
- where I have quoted from the work of others, the source is always given. With the exception of such quotations, this thesis is entirely my own work;
- I have acknowledged all main sources of help;
- where the thesis is based on work done by myself jointly with others, I have made clear exactly what was done by others and what I have contributed myself;
- Part of this work has been published before submission, and a list of these publications is included in Appendix E.1.

Signed:...

Date:..

Acknowledgements

At the end of this long journey, there are several people I would like to aknowledge, starting from my supervisors, Dr. Xunli Zhang and Dr. Eugen Stulz, who always trusted my research skills and helped me during the hard times of this project. A big thanks to all my family, my father, my sister and Mariagrazia, my lovely granmothers, aunts and uncles. They always supported me, pushing me to achieve the best for me and my future. Also, I want to acknowledge the Faculty of Engineering & the environment and ERDF (IS:CE-Chem & InterReg IVa program 4061) for funding my studentship. All the people from Lab 5003, James, Gabi, Andy and Jo were amazing journey mates during these three and a half years along with Rute and Amelie, the two lovely girls who shared with me the little (very little) joys of nanotechnology. A special mention to Warren and Dan to which I own a lot of laughs and boozes: you were great friends and I'm going to miss our productive procrastinations hours. A big thanks to all the University staff, in particular to Carl and Clive from the store, the guys from the mechanical workshop in the Chemistry Building and to Patricia from the Bioimaging Unit at the Hospital of Southampton, who were always helpful and contribute to the successes of my work. A great thanks to all my friend from engineering, Jonathan, Orestis&Orestis Jr., Maria, Amir, Giorgos, Marina, Mohamed, Dyan and Natalia and to all my Italians friends, Stefano, Lorenzo, Dario, Edu, Luca, Giorgio, Alessandra, the little Emma, Marco L., Mr. Zuppone, Stefania F., Marco P., Eleonora, Andrea, Paolino, Stefania M. and my amazing housemate Federico to make my hours inside and outside the university much funnier. Thanks to all the Covo's friends and Goliardia's brothers, it is always nice to have a place and people that makes me feel at home back in Parma. In particular I want to thank Silvio and Simon Le Blonde for winning their big battle and being back with us. A thank to Djope (the D is mute), for being one of my best friends in all these years. A thank to Alessio and Cecilia, who taste a bit of the English lifestyle and who always be such great friends. A thank to all my friend from the Universitá degli Studi di Parma, Irene, Daniela, Antonio and all the other people who spend five long years of hard study, and to Alessio and Michele who had with me the (amazing?) idea of starting a PhD. To the little and cruel Tenia, the most sweet and annoying pet in the world. Walking on my face every morning at 7:00 am crying for food was the best alarm clock I could have asked for to finish my PhD. Chiara, you walked beside me for more than 5 years, always supporting me and making me happy with your beautiful smile and for this I will be always thankful to you. I hope we will continue our journey and that we will share a great future together.

List of Symbols and Abbreviations

A	Area of Heat Exchange
A.M.	Air Mass
$A_b(\lambda)$	Blackbody Absorbance
AFM	Atomic Force Microscopy
AIBN	Azobisisobutyronitrile
$A(\lambda)$	Absorbance
ASHRAE	American Society of Heating, Refrigerating, and Air Conditioning Engineers
$\mathrm{A}_s ol$	Absorbance of Total Solar Radiation
ASTM	American Society for Testing and Materials
ATES	Allyltriethoxysilane
Au NRs	Gold Nanorods
AZO	Aluminium Doped Zinc Oxide
$\mathbf{B}$	Magnetic Field
BRE	Building Research Establishment
c	Speed of Light (300000[km/h])
C_{ext}	Cross-section Extinction
CFD	Computational Fluid Dynamic
CIE	Commision International de l'Éclairage
C_{Rn}	Concentration associated with the Nucleation Rate
CTAB	Cetyl Trimethylammonium Bromide
CVS	Chemical Vapour Synthesis
D	Dielectric Material
$\mathbf{D}$	Electric Displacement
DDA	Discrete Dipole Approximation
DEA	Diethylamine
ΔE	Band Gap
D_i	Mass Diffusion Coefficient Species i
DMA	Dimethylamine
dTGA	First Derivate of TGA Curve

$\mathbf{E}$	Electric Field
e	Electron Charge
E_b	Blackbody Emissive Power
$E_b(\lambda)$	Spectral Blackbody Emissive Power
EC	Electrochromic
EDAX	Energy Dispersive X-ray Spectroscopy
EDTA	Ethylenediaminetetraacetic Acid
EIA	Energy Information Administration
ε_0	Permittivity in the Free Space
ε_1	Real Part of $\varepsilon(\omega)$
ε_2	Imaginary Part of $\varepsilon(\omega)$
ε_m	Dielectric Constant of the Medium Surrounding the Particles
$\varepsilon(\omega)$	Frequency-dependent Dielectric Constant
ε_∞	Dielectric Constant of the Medium
ET	Equilateral Triangularity
E$therm$	Thermal Radiation Emission
FIR	Far Infrared Radiation
FMR	Feret Major Axis Ratio
FOM	Figure of Merit
FWHM	Full Width Half Maximum
Γ	Crystal Damping Constant
GC	Gasochromic
GHGs	Green House Gases
GZO	Gallium Doped Zinc Oxide
$\mathbf{H}$	Magnetic Field Strength
h	Planck Constant $(6.62 \times 10^{-34}[m^2Kgs^-1])$
h_{con}	Convection Coefficient
HVAC	Heating Ventilation Air Conditioning
IR	Infrared Radiation
ITO	Tin Doped Indium Oxide
$\mathbf{j}$	Electric Current of the Free Electron
$\mathbf{J}$	Diffusion Flux
K	Restoring Force
k	Thermal Conductivity
k_B	Boltzmann Constant $(1.38 \times 10^{-23}[m^2Kgs^{-2}K^{-1}])$
L	Edge Length
LaB$_6$ NPs	LaB$_6$ Nanoparticles
λ	Wavelength
λ_a	Absorbed Wavelength

λ_{max}	Maximum Absorbance Wavelength
LC	Liquid Crystal
LOD	Limit of Detection
M	Metal
$\mathbf{M}$	Magnetisation
MA	Methylamine
m_e	Effective Electron Mass
MEHQ	Monomethyl Ether of Hydroquinone
$\mathrm{M}_{f,i}$	Mass Fraction of Species i
MHA	16-mercaptohexadecanoic Acid
MMA	Methyl Methacrylate
MNPs	Metal Nanoparticles
MPTES	(3-Mercaptopropyl)triethoxysilane
MPTMS	(3-Mercaptopropyl)trimethoxysilane
μ	Fluid Dynamic Viscosity
μ_0	Permeability in the Free Space
N	Free Carrier Concentration
n	Electron Density
n_e	Extraordinary Refractive Index
NIR	Near Infrared Radiation
NMR	Nuclear Magnetic Resonance
n_o	Ordinary Refractive Index
n_p	Polymer Refractive Index
ν	Electrons Speed
OECD	Organisation for Economic Co-operation and Development
ω	Frequency
ω_R	Eigen Frequency of the Electrons Cloud
PAA	Polyacrylic Acid
PDLC	Polymer Dispersed Liquid Crystal
PDMS	Polydimethylsiloxane
PEDOT	Poly(3,4-ethylene-dioxithiophene)
PIPS	Polymerisation Induced Phase Separation
PMMA	Poly(methylmethacrylate)
PSSS	Poly(sodium styrenesulphonate)
PVA	Poly(vinylalchol)
PVB	Poly(vinylbutyral)
PVP	Poly(vinylpyrrolidone)
$\dot{Q}$	Heat Transfer Rate [W]
$\dot{q}$	Heat Flux

R	Flow Rate Ratio
R	Sphere Radius
R	Thermal Resistance $[(K \cdot m^2)/W]$
RAR	Reciprocal Aspect Ratio
RD	Roundness
ρ	Current Density of the Free Electron
ρ_f	Fluid Density
$R(\lambda)$	Reflectance
RMS	Root Mean Square
Rn	Nucleation Rate
rpm	Revolutions Per Minute
R$_sol$	Reflectance of Total Solar Radiation
RT	Residence Time
RTY	Rectangularity
$S_b(\lambda)$	Blackbody Spectra (calculated at 300K)
SERS	Surface Enanched Raman Scattering
SERS	Surface Enhanced Raman Scattering
SHE	Standard Hydrogen Electrode
SHGC	Solar Heat Gain Coefficient
σ	Stefan-Boltzmann Constant (5.7×10^{-8} $[W/(m^2 \cdot K^4)]$)
$\sigma(\omega)$	Frequency-dependent Conductivity of the Medium
$S(\lambda)$	Solar Irradiance
SMA	Self Multi Assembly
SNPs	Silver Nanoprisms
SPR	Surface Plasmon Resonance
T	Temperature
t	Time
TC	Thermochromic
T_c	Critical Temperature
TEM	Transmission Electron Microscopy
TEOS	Tetraethyl Orthosilicate
TGA	Thermogravimetric Analysis
T$_g$	Glass Transition Temperature
Tk	Prisms Thickness
t_k	Film Thickness
$T(\lambda)$	Transmittance
T$_lum$	Transmittance of Visibile Light
TOAB	Tetraoctylammonium Bromide
TSCD	Trisodium Citrate Dihydrate

$\mathrm{T}_{s}ol$	Transmittance of Total Solar Radiation
$\mathrm{T}_{t}herm$	Transmittance of Thermal Radiation
U	U-value, Thermal Conductance, $[W/(K \cdot m^2)]$
u	Electron Mobility
$\mathbf{v}$	Fluid Velocity
vis	Visible Radiation
VP	Vapour Phase
V_{tot}	Total Flow Rate
x	Position of the Electrons Cloud
$Y(\lambda)$	Eye Response

Chapter 1

Introduction

Contents

1.1 Aim and Objectives

The aim of this research is to investigate metal nanoparticles as novel materials for applications in energy saving glazing. The research focuses on anisotropic nanoparticles, i.e. silver nanoprisms (SNPs), including their synthesis, their embedding in a polymeric matrix (i.e. PMMA) and testing their quality as an NIR absorber. Those materials should be able to provide a cheap and ready-to-be-commercialised solution to the increasing energy demand from non-commercial buildings due to heating, ventilation and air condition (HVAC) devices, particularly in developing countries. The objectives of the project are:

- To synthesise SNPs with a silica shell in order to add further chemical functional groups on the shell surface;
- To covalently link the nanoparticles to a polymer network, and deposit them on glass surface;
- To evaluate the properties of SNPs/PMMA composite materials as energy saving glazing.

This research focus on investigating the optical properties of these novel materials (i.e NIR absorbance, spectral position of nanoparticles' surface plasmon resonance) and on improving the dispersion of the particles in the polymeric matrix by meaning of grafting. As the optical properties of these coating are related to silver nanoprisms' size and shape distribution, studies for improving them are included in this research project. In particular, the hydrodinamics of the process is studied, using a microreactor as platform both for the production and the monitoring of the metallic nanoparticles,

1.2 Economical and Environmental Aspects

In the recent years the demand for energy has showed an overall increasing trend worldwide. This has been particularly relevant in the fast developing non-OECD (Organisation for Economic Co-operation and Development) Asian and South American countries, due to the rapid and constant emerging economy. According to the previsions reported in the Energy Information Administration (EIA) Outlook 2012, the energy demand of these countries will face an increase of ∼72% in the next 30 years, while the OECD members demand will increase by ∼18%. This growth is so significant that in the next few years, India and China will contribute to half of the entire world energy consumption alone. Increasing demand for electricity is strictly related to environmental risk, such as Greenhouse Gases (GHGs) production. CO_2 emission, an indication of GHGs amount in the atmosphere, rose 43% in the last two decades as reported by Perez-Lombard et al. (2008). Energy consumption from non-commercial buildings (i.e. houses) starts to emerge as a third independent sector, following transports and industries.

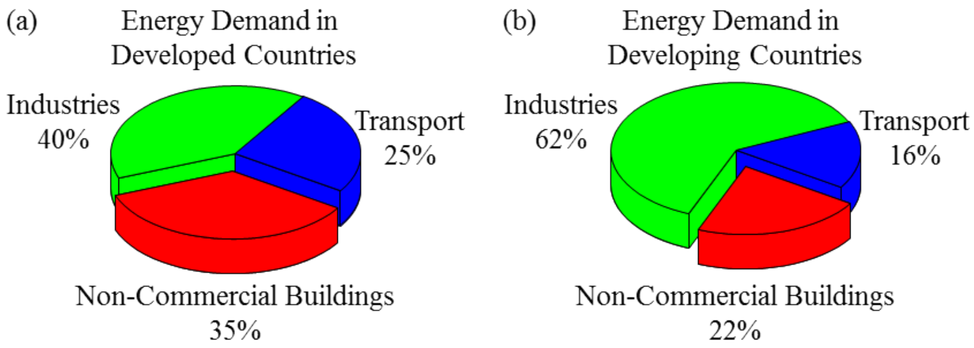

Figure 1.1: Energy demand per end-use sector in developed countries (Figure 1.1a) and developing countries (Figure 1.1b) as reported from Energy Information Administration (2011)

A report from Energy Information Administration (2011) shows that non-commercial buildings become the second end-use sector after industrial production in non-OECD countries (as shown in Figure 1.1) and the first in terms of growth. Reasons for this change in energy demand distribution may be found in the increasing world population, an overall improved well-being and the rapid urbanisation of previous rural area in the developing countries (Li and Yao, 2009). As the problem is getting more consistent, identifying and limiting the source of the problem becomes a priority. According to EIA (Energy Information Administration, 2006) and BRE (Building Research Establishment) (Carbon Trust, 2000) energy used for HVAC devices, both for heating and cooling, is the most demanding source in residential buildings (see Table 1.1).

Consequently, several countries and confederations (such as the EU) have undertaken actions aiming to limit the use of HVAC devices. In particular, improving the thermal insulation of buildings and reducing the heat exchange with the external environment appears to be the most appealing solution for cutting energy demand and CO_2 emission at the most accessible cost (Verbeeck and Hens, 2005). Among all the elements of the building envelope, glazing received particular interest due to the increasing number and size of windows in residential houses and the extensive use of glass in skyscraper façades.

Compared to other elements of the building envelope (walls, roof, floors and doors), insulation of windows is a tougher challenge due to their dual function as both insulation

Energy demand source	**EU**	**USA**	**UK**
Space Conditioning	68%	53%	62%
Domestic Hot Water	14%	17%	22%
Lighting and Appliances	18%	30%	16%

Table 1.1: Energy demand per source (%) in building for EU, USA, and UK as reported from Energy Information Administration (2006) and Carbon Trust (2000)

element and source of light income. Furthermore, in addition to conductive and convective heat transfer, they can exchange heat also through radiation. Much attention has been focused on the design of glazing capable of providing good lighting during day time and granting reasonable thermal comfort. In this respect, development of coating and devices able to cut off or reflect the solar radiation just in a particular range of wavelength has been largely studied in recent years, particularly in the field of the so called smart-windows. In general, these devices have the characteristics of changing their optical properties in response to an external stimulus such as electricity (Mortimer, 1997) (such as electrochromic, suspended particles or liquid crystals devices) or temperature (such as thermocromic devices). However, manufacturing issues (O'Brien et al., 1999) and high costs (Lampert, 2003) are limiting the application of such technology.

Recently, other technologies are emerging aside to these switchable materials. In particular, recent advances in nanotechnology led to the development of materials with optical properties that can largely meet the spectral requirements for reducing the heat radiative transfer to and from the building. Compared to the traditional materials employed for energy saving windows, nanomaterials could offer easier and cheaper ways to prepare and deposit functional layers over glass sheets. A recent example of such application was the use of gold nanorods dispersed in a polymeric matrix of poly(vinyl alcohol) (PVA). These colloidal materials show a great absorption in the near infrared (NIR) part of the spectrum, which can be easily tuned by changing the morphology and the concentration of the dispersed particle inside the polymeric matrix (Stokes et al., 2010).

1.3 Organization of the Thesis

In Chapter 2 the basic equations and phenomena involved in the radiation heat transfer through building fenestration are illustrated. Furthermore, an overview of the current available technologies is shown with focus on their strong and weak points. The promising qualities of nanoparticles as energy saving materials and the way of preparing them (particularly triangular silver nanoprisms) are shown, with particular attention on their optical properties.

In Chapter 3, general experimental conditions, reactions, and setups are reported along with a complete list of the chemicals and the equipments employed.

In Chapter 4 the synthesis of silver nanoprisms by batch reaction and its employability in large scale production have been evaluated by means of UV-vis spectroscopy and TEM microscopy. The modification of silver nanoprisms size via Cl^- induced growth and the formation of triangular hollow alloys of silver and gold have been studied in order to move their optical absorbance further in the near infrared region. Different concentrations of both Cl^- and Au^{3+} have been employed and the formed particles have been characterised with both UV-vis spectroscopy and transmission electron microscopy.

Chapter 5 focuses on the development of a microfluidic-based process for the direct synthesis of silver nanoprisms in a continuous flow format using a flow focusing microreactor, along with an experimental setup for the modification of SNPs with halide ions (namely Cl^- and Br^-). Both methods are confronted with traditional batch syntheses. The development of an absorbance detection systems coupled with an optical microscope for UV-vis-NIR spatially resolved micro-spectroscopy measurement along a microfluidic channel is reported.

In Chapter 6 the coating of triangular silver nanoprisms by sol-gel chemistry is presented. The effect of different catalysts on the final thickness and quality of the silica shell and on the final shape of the metallic core are reported. Furthermore, the functionalisation with organosilane bearing different moieties (i.e. -SH and -C=C groups) is shown along with their characterisation with IR and spectroscopical (Ellman test and fluorescence) methods.

In Chapter 7 the synthesis of SNPs@SiO_2/PMMA composite material is reported. In order to properly distribute the inorganic filler in the organic matrix, a grafting through approach was adopted to attach polymeric chain to the surface of the particles and improve the miscibility of the two components. The material was characterise with several techniques (TGA, GPC, NMR, IR) and the presence of polymeric chain covalenty attach to SNPs@SiO_2/PMMA proved by observing characteristic NMR peaks of PMMA after removal of the physisorbed chains from the composite solution. Both thin and thick films of these materials were deposited on glass and tested as potential materials for energy saving glazing.

Chapter 2

Literature Review

Contents

2.1 Heat Transfer in Buildings

Buildings exchange heat (both loss and gain) mainly through the building envelope. A building envelope is what separates the interior space from the outdoor environment. This includes exterior walls, floor, ceiling, roof and fenestration (windows and doors).

By carefully design the construction materials the thermal conductance, U or U-value, can be significantly improved, resulting in a decrease of both energy consumption and GHGs production. Table 2.1 show the improvement of U-values for some building envelope elements. U is defined in Equation 2.1 where k $[W/(m \cdot K)]$ is the thermal conductivity and Δx is the thickness, [m]:

$$U = \frac{k}{\Delta x}\ [W/(K \cdot m^2)] \tag{2.1}$$

The heat can be exchanged through conduction, convection and radiation heat transfer. As not only the greatest radiative heat exchange but also light gain is through glass windows, it becomes challenging to reduce the former without significantly affecting the latter. Although research focused mainly on the design of absorbing materials, improvements are still needed to achieve the requirements of both good insulation and light gain.

Element	**1995 standard U-values** $[W/K]$	**2000 standard U-values** $[W/K]$	**Percentage reduction in U-values(%)**	**Thermal Resistance (1/U)** $[K/W]$
Walls	0.45	0.35	22	2.86
Roofs	0.25	0.16	36	6.25
Floors	0.45	0.25	44	4
Windows	3.3	2.2	33	0.45

Table 2.1: U-value improvement over a five years period as reported from John et al. (2005).

2.1.1 Conduction Heat Transfer

Heat conduction is the phenomenon involving the passage of heat through a body. It is typically observed in solids, where vibrating molecules are unable to move away from each other, but can be also present in liquids and gasses.

Heat conduction can take place in different ways depending on its source. It can take place radially outwards in the case of a hot pipe or in two directions, in the case of a floor that is in contact with the ground and with the air. Fourier's Law describes the rate of heat transfer by conduction, $\dot{Q}$, as proportional to the temperature difference, ΔT, and the heat flow area, A, as shown in Equation 2.2, where $\frac{dT}{dx}$ is the temperature gradient along the body and k is the thermal conductivity.

$$\dot{Q} = -kA\frac{dT}{dx}\ [W] \tag{2.2}$$

Equation 2.2 can be expressed also in Cartesian coordinate through a path where $\dot{Q}$ is constant, T is function of x solely and along which no heating sources are present, as shown in Equation 2.3:

$$\dot{Q} = kA\frac{T_1 - T_2}{\Delta x} = A\frac{T_1 - T_2}{R}\ [W] \tag{2.3}$$

R is called heat transfer resistance, $[(K \cdot m^2)/W]$, and it is the inverse of the the thermal conductance U, shown in Equation 2.1.

2.1.2 Convection Heat Transfer

When a fluid, either a gas or liquid, moves over a warmer or cooler surface, it exchanges heat through a process that is known as convection; the faster the motion of the fluid, the higher the rate of the convection heat transfer. Generally, convection is divided in two categories:

1. Free: the motion results from the difference in density present in the fluid as heat is exchanged;
2. Forced: This exchange is caused when the fluid is moved by an external force (a fan, for example). As the velocity of the fluid is generally higher, usually the heat exchange is faster as well.

Describing convection heat transfer in a building is often complicated as both forced and free convection are present simultaneously; Newton's Law of cooling, however, can be employed to give a simple explanation of convection, where ΔT being the difference between the surface and the fluid and h_{con}, $[W/(m^2 \cdot K)]$, the convection coefficient:

$$\dot{Q} = h_{con}A\Delta T\ [W] \tag{2.4}$$

As for heat conduction (see Equation 2.3), $\dot{Q}$ can be expressed as function of R, with $R = \frac{1}{h_{con}}$.

$$\dot{Q} = A\frac{\Delta T}{R}\ [W] \tag{2.5}$$

2.1.3 Radiation Heat Transfer

Radiation heat transfer is really important for describing the insulation of a building. It has some features that set it apart from conduction and convection heat transfer:

1. Radiation heat transfer does not require an exchange medium;
2. Heat "travels" the same way as light does;

3. As it occurs by electromagnetic waves it is strongly dependent on the portion of the electromagnetic spectrum interacting with the surface;
4. Microscale details of the surfaces involved, i.e. the colour, have a strong effect on the heat radiation transfer rate;
5. Radiation heat transfer is a non-linear function of temperature.

To understand the importance of radiation heat transfer it must be highlighted that all surfaces with a temperature above 0 K can emit radiant heat or, alternatively, absorb, transmit or reflect it.

2.1.3.1 Electromagnetic Spectrum Overview

The electromagnetic spectrum includes all the frequency states in which it is possible to find the electromagnetic radiation, from the low energy radio wave (wavelength$> 10^{-2}$ m) to the high energy X and γ rays, below 10^{-10} m (see Figure 2.1).
Particular interest is given to the portion of the spectrum comprised between 4×10^{-7} and 10^{-5} m, known as thermal radiation. This includes Visible (vis, form 390 nm up to 750 nm) and Infrared Radiation (IR, from 750 nm to 2500 nm) and is usually perceived as both light and heat.

The Visible part of the spectrum is divided in different parts, corresponding to the complementary colour perceived by the human eyes (inset, Figure 2.1):

1. Violet: 390-455 nm;
2. Blue: 455-492 nm;
3. Green: 492-577 nm;
4. Yellow: 577-597 nm;
5. Orange: 597-622 nm;

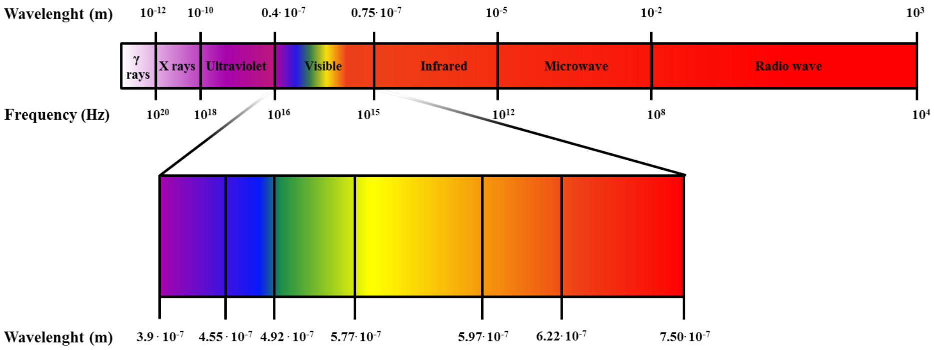

Figure 2.1: Electromagnetic radiation spectrum. The inset shows in detail the visible part of the spectrum.

6. Red: 622-750 nm.

Infrared radiation is divided into Near Infrared (NIR, from 750 to 2500 nm) and Far Infrared (FIR, from 2500 to 10^6 nm) and is commonly perceived as heat. Indeed, more than 50% of the heat is carried by radiation in the infrared range of the electromagnetic spectrum (Granqvist et al., 2009), therefore, it is clear how important it is to block the incoming radiation at those frequencies for reducing the cooling demand or to preserve it to reduce the heating costs. Thus, understanding how the solar radiation interacts with the atmosphere is important during the design of energy saving windows, in order to understand how the radiation reaches the glazing surface. Indeed some parts of the thermal radiation are absorbed by water and CO_2 and do not reach the Earth surface. The graphs shown in Figure 2.2 are calculated for a solar beam irradiating the surface at approximately 48° from the zenith (a standard measurement also known as Air Mass 1.5 (A.M. 1.5), employed in glazing and photovoltaic technologies). It is also important to notice that the human eye is sensitive in a very small portion of the whole solar spectrum.

2.1.3.2 The Blackbody Theory

A blackbody is an ideal body that emits the maximum amount of energy at each wavelength and in all directions and that absorbs all the radiations (Kirchhoff, 1860). The performance of real surfaces are compared to the one of the blackbody. For example, the Sun's surface temperature has been studied by comparing its radiation with the one of the ideal blackbodies.

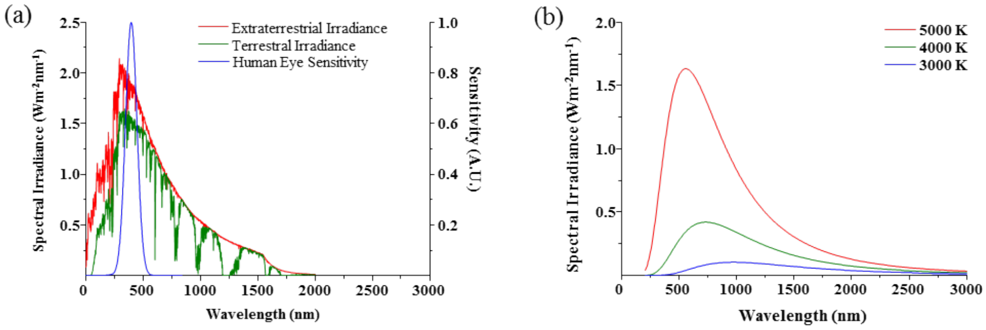

Figure 2.2: Spectral irradiance of the Sun (left y-axis) and human eye sensitivity (right y-axis) are reported in Figure 2.2a. On Figure 2.2b the spectral irradiance of the blackbody at different temperatures. The curves are calculated using Planck's Law, $B_\lambda(T) = (2hc^2)/(\lambda^5 e^{\frac{hc}{\lambda k_B T}} - 1)$, where B_λ is the spectral irradiance, k_B is the Boltzmann constant, h is the Plank constant and c is the speed of light

The law that governs the thermal radiation emission from a blackbody is the Stefan-Boltzmann Law (Boltzmann, 1884) which states that the heat flux, $\dot{q}$ emitted from a blackbody is proportional to the fourth power of the temperature, T, as shown in Equation 2.6, where $\sigma = 5.7 \times 10^{-8}\ [W/(m^2 \cdot K^4)]$, is the Stefan-Boltzmann constant, and E_b is the blackbody emissive power.

$$\dot{q} = \sigma T^4 = E_b\ [W/m^2] \tag{2.6}$$

By applying Wien's Displacement Law (a universal form of the Planck Law for the emission of radiation by a body, which otherwise would be valid only when the emitter is in the vacuum) it is possible to understand how the thermal radiation wavelength is related to the temperature of the emitting body as reported in Equation 2.7, where λ_{max} is the wavelength at which the spectral blackbody emissive power, $E_b(\lambda)$ (i.e. the wavelength dependent expression of E_b), it is at his maximun, and T is the temperature, in K.

$$\lambda_{max} T = 2897.8\ [nm \cdot K] \tag{2.7}$$

As the light hits a surface, it can interact in three different ways: i) Absorption ($A(\lambda)$, the phenomenon for which the electromagnetic radiation is transformed into another form of energy, such as heating), ii) Transmission ($T(\lambda)$, when the radiation passes through the surface without being absorbed) and iii) Reflection ($R(\lambda)$, when the wavefront of the electromagnetic radiation changes direction after hitting the surface) as shown in Figure 2.3.

For each different wavelength the sum of these three different contributions must be

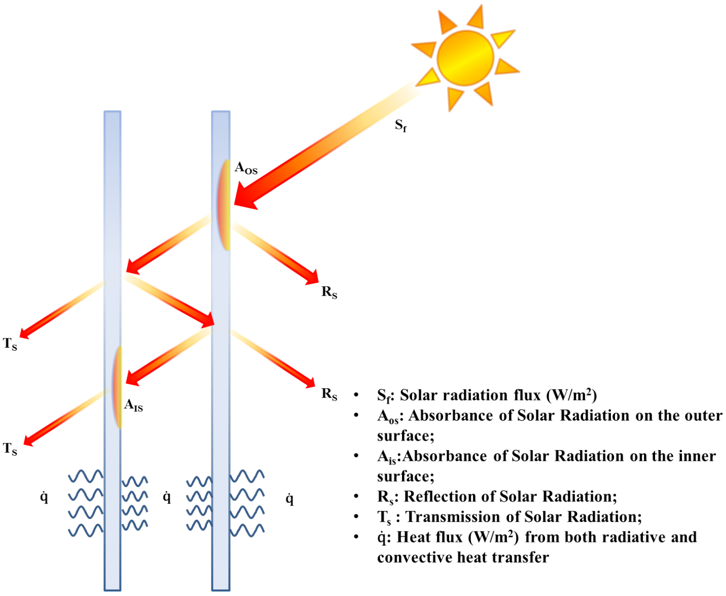

Figure 2.3: Interaction of the solar radiation with double glazed window elements.

equal to 1 due to the conservation of energy. The Kirchhoff's law of thermal radiation (Kirchhoff, 1860) is also important and explains the behaviour of a perfect blackbody in thermodynamic equilibrium, as stated in Equation 2.8, where $E_b(\lambda)$ and $A_b(\lambda)$ are the spectral blackbody emissive power and the blackbody absorbance, respectively, for a given wavelength λ.

$$A_b(\lambda) = E_b(\lambda) \tag{2.8}$$

2.2 Energy Efficient Windows

Energy efficient windows are devices which can provide both good daylight illumination and thermal comfort during the entire day. These requirements must be achieved by using the minimum amount of energy for granting a good cost/benefit ratio. Thermal comfort is defined by the American Society of Heating, Refrigerating and Air-Conditioning Engineers (ASHRAE, 2001) as the satisfaction of people with the surrounding environment (i.e. the perception of a sensation of hot or cold) and it is affected by the heat transfer of the building (by convection, conduction, and radiation) but also by personal factors, such as perspiration. Even if there is no direct connection between temperature and thermal comfort it is necessary to mark which different requirements are imposed by different climates (warm, cold, temperate) for designing the ideal energy-efficient windows.

In a warm climate, the solar radiation that enters through the windows causes the room temperature to rise and air conditioning devices to be employed. Energy saving fenestration employed in such climates have to exclude the incoming IR part of the solar radiation, cutting in this way more than half of the solar energy, without affecting the luminous transmittance (Ebisawa and Ando, 1998). The overall spectral performance of such devices can be summarised in Equations (2.9) and (2.10):

$$T(\lambda) = 1 \; between \; 400 \; nm < \lambda < 700 \; nm \tag{2.9}$$

$$R(\lambda) = 1 \; between \; 700 \; nm < \lambda < 50000 \; nm \tag{2.10}$$

In cold climates the role of an energy-efficient window becomes harder as windows must reflect the building outgoing radiation generated by emitting elements from the house interior (such as radiator) but let the NIR infrared radiation in for heating the building. The optical properties of these glazing are commonly summarised in Equations (2.11) and (2.12):

$$T(\lambda) = 1 \; between \; 400 \; nm < \lambda < 3000 \; nm \tag{2.11}$$

$$R(\lambda) = 1 \; between \; 3000 \; nm < \lambda < 50000 \; nm \tag{2.12}$$

These materials are usually referred to as low-emittance (low-e) as the high reflectance limits the absorption of radiation. This limits the emissive power according to Kirchhoff's Law (Equation 2.8). Limiting the emissive power equals to reducing the U-value of the building envelope in correspondence of the windows, limiting the heat loss from the inside.

In temperate climates it is impossible to define precisely strict optical requirements to achieve the thermal comfort, as the absence of a dominant weather condition requires a dynamic response from the building envelope to maximise the efficiency of the reduction of heating and cooling demand. For this reason, mechanical regulation of the solar income, by rollers, curtains or blinds is usually adopted. These devices have the drawback of significantly reducing the daylight income and therefore, in recent years great effort has been invested in the development of the so called smart-windows (Svensson and Granqvist, 1984). Such devices selectively regulate the amount of light or heating entering inside the building by altering the optical properties of the windows, usually by applying an external stimuli (such as electricity in the electrochromic material).

2.3 Parameters for Evaluating the Performance of Energy Saving Glazing

For evaluating and comparing the influence that different energy-efficient glazing can have on the heat transfer performance of a building several parameters must be taken into account in order to appropriately define their optical performances. In this respect, different standards were introduced as guidelines such as Air Mass 1.5 (which provides the spectra for the solar radiation used in calculating the thermal performance of building) or the data provided by ASHRAE in their handbooks. CIE (Commission Internationale de l'Éclairage), on the other hand, provides guidelines for determining the colour perception of transmitted light through windows, by specifying the colour of the transmitted radiation in terms of three different values which correspond to three different stimuli received by the human eyes (Smith and Guild, 1931).

Parameters used for evaluating the energy saving performance of a glazing include the transmittance of the visible light (T_{lum}), the transmittance of the total solar radiation (T_{sol}, this value takes into account all the solar radiation spectra) and the transmittance of the thermal radiation (T_{therm}). T_{sol} is defined as the transmittance of the light through a window, calculated in the range from 300 nm to 2500 nm, weighted by the solar spectrum. The equation for calculating T_{sol} is described in Equation 2.13, where $T(\lambda)$ is the transmittance for a determinate wavelength and $S(\lambda)$ is the solar spectrum for a wavelength (λ) as reported from the standard A.M. 1.5. This equation can be used also for calculating both total solar absorbance A_{sol} and total solar reflectance R_{sol} by replacing $T(\lambda)$ with $A(\lambda)$ and $R(\lambda)$, respectively.

$$T_{sol} = \frac{\int T(\lambda)S(\lambda)d\lambda}{\int S(\lambda)d\lambda} \tag{2.13}$$

The visible transmittance T_{lum} is, instead, the solar transmittance as it is received by the human eyes, which photonic response is shown in Figure 2.2a and has its maximum peak at 555 nm. Equation 2.14 describes the T_{lum}, where Y(λ) is the eye response for wavelength λ.

$$T_{lum} = \frac{\int T(\lambda)S(\lambda)Y(\lambda)d\lambda}{\int S(\lambda)T(\lambda)d\lambda} \tag{2.14}$$

As for T_{sol}, Equation 2.14 can be used for calculating also A_{lum} and E_{lum}. T_{therm}, as well as A_{therm} and E_{therm}, can be calculated with the same equation used for T_{sol}, where the A.M. 1.5 spectral value for a discrete wavelength is replaced with that of a blackbody calculated at a temperature of 300 K, $S_b(\lambda)$, as shown in Equation 2.15.

$$T_{therm} = \frac{\int T(\lambda)S_b(\lambda)d\lambda}{\int S_b(\lambda)d\lambda} \tag{2.15}$$

To compare the heat transferred, usually the U-value (see Section 2.1) and the Solar Heat Gain Coefficient (SHGC) are employed as a standard reference, where SHGC is defined as the fraction of external solar radiation that is admitted through a window (its value, therefore, varies between 0 and 1). SHGC takes into account not just the incident radiation but also the radiation re-emitted by the object itself as a consequence of the heat change. For this reason SHGC is expressed as the sum of T_{sol} plus the secondary heat transfer factor, q_i, which is an expression of the radiative and convective heat transfers of the window. These parameters can be affected by the outdoor (wind, air temperature, solar radiation) and internal conditions (such as ventilation), the glass geometry, and optical and thermal properties (Manz, 2004).

2.4 State-of-the-art of Coating for Energy-efficient Glazing

2.4.1 Metal-based Thin Films

Thin films of noble metals have been employed for the production of selectively transparent coatings, both in warm climates (where the desired proprieties can be reached with thin film embedded in layers of anti-reflecting dielectric materials) and in cold climates (by metal based multilayers). These are the simplest devices for obtaining high reflectance in the IR region of the solar spectrum and granting good T_{lum}. The best results were achieved by employing different noble materials, such as Cu (Bollero et al., 2009; Correa and Almanza, 2004; Nair and Nair, 1991), Au (Mohelníková, 2009) and Ag (Leftheriotis and Yianoulis, 1999; Schaefer et al., 1997), non-noble metals such as Al (Kunz et al., 1988), but also other metal based materials were employed, such as TiN (Karlsson et al., 1983; Yuste et al., 2011). The reflective properties in metallic materials arise from the interaction between the incoming electromagnetic radiation and the free electrons in the metal structures, which start to oscillate under the action of the incident electromagnetic field and became new radiators.

As a phase difference of π is present between the incoming light and that emitted from electron, the light is not trasmitted. As the reflectance is a function of the electronic density, noble metals show the best result and are the most largely employed in energy efficient windows. Ag coatings proved to be particularly good due to their low absorption of the solar radiation and of the luminous radiation (i.e. good transmission in the vis spectrum) (Fan and Bachner, 1976) compared to Au and Cu (but also TiN) which, in contrast, show an intense peak at ~500 nm and ~600 nm, respectively (Valkonen et al., 1984). Noble metal coatings have very low chemical resistance, for instance silver and copper can easily undergo oxidation and for this reason usually an additional layer of SiO_2, SiC or Al_2O_3 is added to prevent degradation of the underlying metal layer (Lampert, 1981). Those coatings also have a very low mechanical resistance; they are considered “soft coating” and for this reason it is preferable to deposit these material on the internal side of a insulated windows.

The metal film deposition is a critical stage for the formation of these devices and usually consists of a continuous process where different phases can be identified, as shown in Figure 2.4a. Film deposition starts with the formation of metal nuclei on the surface, followed by their growth as other metal atoms adsorb on the glass surface. This leads to the formation of so called “metal islands” which are usually characterised by irregular shapes. This growth process continues until islands completely coalesce and a homogeneus layer is formed (Chopra, 1969).

The relationship between thickness and optical properties is the main issue of metal-based thin films. For example, a uniformly deposited metal film tends to be relatively thick (from 10 to 20 nm, approximately) and this thickness affects the optical properties (Figure 2.4b). As shown in Figure 2.4b, the trends of T_{lum} and R_{sol} are strongly related to the thickness for a plane-parallel slab of metal. As the R_{sol} increases when T_{lum} decreases, it is clear how it is necessary to mediate between reducing the heat income and keeping a reasonable amount of light gain.

For example, to keep a reasonably high R_{sol}, metal layers prepared by evaporation have T_{lum} and T_{sol} <50% (Bruggeman, 1935), while layers prepared with other techniques such as ion assisted deposition (Smith et al., 1986) or dc magnetron sputtering (Valkonen and Ribbing, 1984) show $T_{lum}=T_{sol} < 60\%$. As this limitation in transmittance is due to the reflection of the radiation it is possible to increase it by adding one (D/M) or two (D/M/D) layers to the metal coating. Dielectric materials such as ZnS, Bi_2O_3, In_2O and Sn_2O are commonly employed. Different combinations of these materials and of the metal layer can allow the optical properties to be tuned, and therefore make the range of possible application for these devices wider.

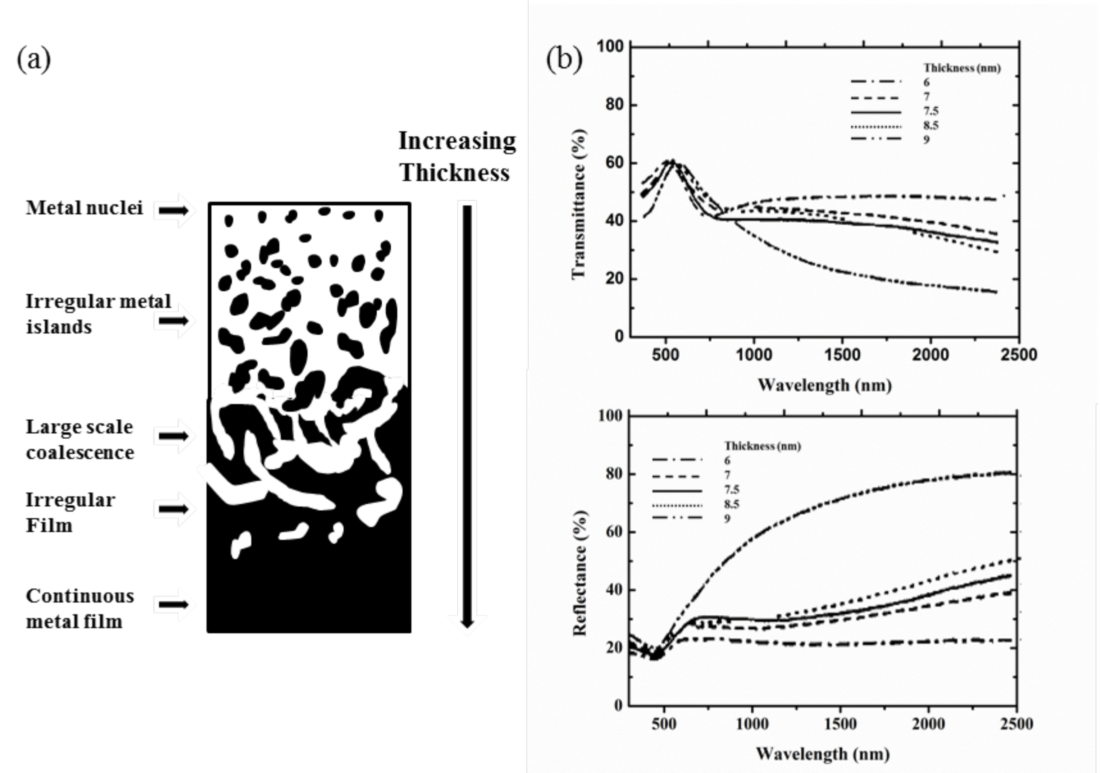

Figure 2.4: Figure 2.4a shows the phases of thin metal formation. Figure 2.4b shows Au thin films Transmittance and Reflectance for different film thickness. Figures are adapted from Valkonen et al. (1984) with permission.

2.4.2 Doped Oxide Semiconductor Coatings

Compared to thin metal films, doped oxide semiconductor coatings offer several advantages. Along with higher transparency in the visible range and high reflectance in the IR region of the spectra, they show an improved adherence to the glass substrate, greater chemical inertness and bigger hardness compared to thin films of noble metal ("hard coating").

The optical properties (T_{sol}, T_{lum}, A_{sol} and R_{sol}) of thin semiconductor films depend on both the free carrier concentration, N, (where carriers are the electrons in the conducting band and holes in the valence band) and thickness, t_k. As for thin metal films, high electron conductivity can grant a more efficient infrared reflectance, but at the same time reduce transmission in the visible range as shown in Equation 2.16, where λ_a is the absorbed wavelenght, h is Plank's constant, c is the speed of light and ΔE is the band gap between the valence and conductive bands.

$$\lambda_a = \frac{\Delta E}{hc} \; [nm] \tag{2.16}$$

Some parameters to take into account when evaluating the optical properties of semiconductor oxides are the electron mobility, u, the effective mass, m_e (used to correctly define the correct mass for free carrier moving in a solid) and the crystal lattice damping constant (Γ). Those parameters can help define some important figures of merit for such materials. For example, the higher the product um_e is, the lower absorption will be in the visible region of the spectra due to the higher reflection thanks to maximised electron conductivity. Crystal lattice damping, on the other hand, is related to how fast the transition is from low to high reflectance in the infrared region. Refractory metals, for example, have high crystal lattice damping and therefore show a gradual transition in their reflective properties. The optimal characteristics of a reflecting glazing are reached when $\Gamma/\omega_P << 1$, where ω_P is the plasma frequency.

Among doped oxide semiconductors, n-type semiconductors such as SnO_2, ITO (Tin doped Indium Oxide), AZO (Aluminium doped Zinc Oxide) (Agura et al., 2003; Tang and Cameron, 1994) and GZO (Gallium doped Zinc Oxide) (Shirakata et al., 2006) are among the most widely employed not just as reflective materials themselves but also as conductive layers for switchable glazing. The doping is usually performed by adding higher valent metal, by replacing oxygen with fluorine or by creating oxygen vacancies. Among these materials indium and tin oxide are examples that have been practically used in commercial applications. SnO_2 has been widely employed due to its good optical and mechanical properties, but mostly due to the inexpensiveness of the raw starting materials (Haacke, 1977). The electrical properties are modified by creating oxygen vacancies or by including Sb or Cl as electron donors. Compared to SnO_2, In_2O_3:Sn (ITO) shows an higher electronic conductivity and therefore a higher reflectance in the IR region and due to a wider energy gap between the conduction and valence band a higher optical transmittance can be reached (Molzen, 1975).

Sintering (Kim et al., 2002a; Yamamura et al., 2001) and post-deposition annealing processes (Lai et al., 2003) are fundamental for the optical properties of such materials; particularly the former has been proven to be essential for the indium oxide based film while the latter is of great importance for tin oxide films. Film deposition procedure (Betz et al., 2006) is also a fundamental step and usually requires high temperature deposition techniques such as spray pyrolysis and chemical vapour deposition. High temperature deposition limits the deposition of this films on plastic materials, even if some success has been achieved for ITO (Itoyama, 1979). For these reasons different approaches to the deposition of nanoparticle of both ITO (Al-Dahoudi and Aegerter, 2006; Kim et al., 2006) and SnO_2:F (Fukano et al., 2005) by wet chemical techniques have been explored. With such materials T_{lum} of about 90% and E_{therm} of approximately 70% have been achieved with ITO and these results are similar to that obtained by the most commonly employed thin films (Ederth et al., 2003).

2.4.3 Angular Selective Coatings

Angular selective methods are the most extensively employed tools used for blocking the incoming radiation. External shading elements such as blinds, eaves or sun-shields in cars are examples of commonly employed angular selective technologies. These elements, however, never satisfy the requirement of granting both a good T_{lum} and a control over the incoming thermal radiation. Blinds, for instance, are very good in controlling solar radiation but they completely block the incoming daylight. Eaves are good in blocking the thermal radiation but they are efficient just in summer as Sun lowers its position during winter. Different approaches have been investigated to incorporate angular selective technologies directly into windows and at the same time improving the daylight income. A method for achieving the requirements of the ideal energy efficient angular selective glazing is to use specific internal structures to selectively bypass the light in function of the incoming direction. These technologies have been particularly efficient in polymer based glazing as they can be easily produced directly by extrusion. Edmonds and co-workers (Edmonds, 1995; Reppel and Edmonds, 1998) studied the performances of different laser cut blocks placed among the two panes of a double glazing. These blocks, placed one over the other, selectively deflect the light inside the building within a range of incident angle thanks to internal reflection; outside this range, light is blocked. Other technologies, on the other hand, use scattering instead of reflection to block the incoming radiation from specific directions. For example, Maeda et al. (1991) developed a polymeric coating made of a copolymer with different refractive indexes. The angular selectivity was created by directing the polymerisation with UV radiation used for inducing the polymerisation. The problem of such devices is the haze they show, which precludes the view and makes the possible applications of these technologies very limited.

A more efficient method for achieving angular selectivity in coating is to employ structured thin films deposited on glazing. These films discriminate the incoming radiation not just by the incidence angle but also by selectively filtering the radiation wavelengths.

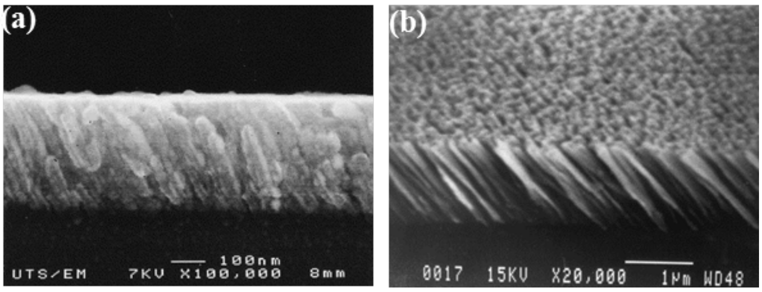

Figure 2.5: Ag/Al_2O_2 (Smith et al., 1998) (Figure 2.5a) and Cr (Granqvist, 2007) ((Figure 2.5b) oblique pillar structure picture, collected by SEM. Pictures reprinted with permission.

Most of these angular selective coatings show a columnar cermet structure made by metal oxide deposited by oblique sputtering techniques (see Figure 2.5a). Pillar arrays made of metal (alternating with void space) are also available. In contrast to what happens in a traditional noble metal or doped oxide semiconductor thin film, the very small distance between columns compared to the wavelength of the incoming radiation makes these materials acting not as reflector but as an absorber. The most widely employed studied material is chromium (Mbise et al., 1989; Smith et al., 1985); its films usually show reduced transmittance for radiation hitting the windows with an incident angle of 60°. Among films made of metal and metal oxide composite, Al/Al_2O_3 (Le Bellac et al., 1995a) and Ti/TiO_2 (Le Bellac et al., 1995b) have shown good potential in energy saving glazing. The former, compared to chromium films, shows a better transmittance in the visible part of the solar spectrum, while the latter show a unique angular selective in the infrared region.

2.4.4 Smart Windows

Coatings discussed in Section 2.4.1, Section 2.4.2 and Section 2.4.3 have the disadvantage of working only under fixed operative conditions. These materials offer potential advantages mainly in a rigid climate, while temperate climate regions, on the other hand, require flexible systems to satisfy the different weather conditions over the course of the year. Efforts were made to use materials that were able to change their optical properties in response to external stimuli and therefore adapt to different climatic conditions. Particularly progress have been made in this field owing to the development of devices based on chromic materials, liquid crystals and suspended particle devices. Among those, only the last two have already found commercial applications, including large surface windows, while applications of chromic material is still limited to small surfaces.

2.4.4.1 Chromic Materials

Chromic materials act as energy-saving materials by changing their colour in response to stimuli, which can be introduced by the user (such as in electrochromic materials (EC)) or an environmental external agent (such as temperature in thermochromic materials (TC)). TC and EC are the most suitable for energy-efficient glazing, while materials such as gasochromic (GC), whose colour changes in the presence of a reducing or oxidising gas such as oxygen or hydrogen, show less potential in switchable glazing as their number of life cycles ("OFF" and "ON" state) is quite limited compared to EC and TC (Baetens et al., 2010; Bao et al., 2007).

Electrochromic Materials Electrochromic materials exhibit different colourations on the application of an electric voltage. These external stimuli change the electronic state of the EC materials by insertion or subtraction of ions. The electric voltage does not need to be applied continuously, but just for the time necessary for the colouration to change. To allow ions to be exchanged, layers of different materials must be deposited (see Figure 2.6), as listed below, between two glass slides:

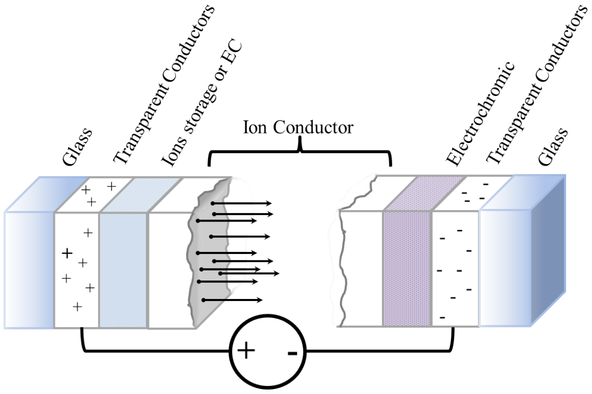

Figure 2.6: Typical layer structure of an EC device. Image redrawn from Granqvist (1995) with permission.

1. Transparent conductor: This layer is probably the most important part of an EC device and is attached of both glass sheet. ITO, AZO and SnO_2 have been extensively employed due to their good optical and conducting properties, but research for alternative materials is essential as high demand is increasing the cost of current materials. In this respect, conductive polymers (such as poly(3,4-ethylene-dioxitiophene), PEDOT) and carbon nanotubes, appear to be the viable alternatives;

2. Ion storage: This layer acts as a reservoir for the ions which are carried to and from the electrochromic material layer through the ions conductor layer. It is usually an EC material itself (which is anodic if the main EC material is cathodic and vice versa) and can be merged with the ions conductor layer.

3. Ion conductor: it is made of materials such as LiF of $LiNbO_3$;

4. Electrochromic materials;

5. Transparent conductor (the same as point 1).

Oxides of different transition metals, such as W, V, Ni, Mo or Ti, have been studied for their electrochromic properties. Among them, extensive studies have been carried out particularly on WO_3 (Bange, 1999; Granqvist, 2000) and $Ni(OH)_2$ (Estrada et al., 1988; Niklasson and Granqvist, 2007; Svensson and Granqvist, 1986). The former material shows a change in colouration (from transparent to deep blue) by effect of ion insertion as shown in Reaction 2.1:

$$\mathrm{WO_3 + xM^+ + xe^- \longrightarrow M_xWO_3} \tag{2.1}$$

where $1 < x < 0$ and M^+ can be an alkali, an alkaline earth metal or H^+. Tungsten oxide has been largely used as chromic material mainly because the high number of switching cycles that such materials can undergo (Nagai et al., 1999) and the good optical properties it shows (a reduction of 74% and 68% for T_{lum} and T_{sol}, respectively, have been achieved by Schlotter et al. (1994)). Also nickel hydroxide has showed good results so far. In contrast to WO_3, $Ni(OH)_2$ has been proven to undergo colour changing by ion extraction, as explained in Reaction 2.2 and Reaction 2.3:

$$\mathrm{Ni(OH)_2} \longleftrightarrow \mathrm{NiOOH} + \mathrm{H^+} + \mathrm{e^-} \tag{2.2}$$

$$\mathrm{NiO} + \mathrm{Ni(OH)_2} \longleftrightarrow \mathrm{Ni_2O_3} + 2\,\mathrm{H^+} + 2\,\mathrm{e^-} \tag{2.3}$$

Reaction 2.2 and Reaction 2.3 lead to grey and brownish colouration respectively. Optical properties of $Ni(OH)_2$ can be tuned by adding wide band gap metal oxides, improving the optical transmittance in the visible range of the solar radiation (Avendaño et al., 2004) when the electrochromic film is in the bleached state.

Recently, along with inorganic electrochromic materials, polymer based materials also starting to be employed. Polyaniline (PANI), for example, shows very good electrochromic properties as it turns from bleached to a coloured state (violet, ~600-700 nm) after changing its benzoid group into quinoid group following the application of an electrical voltage (Lacroix et al., 1989). Also, PEDOT has been employed as an electrochromic element as it switches from blue in its neutral state to transparent when it is oxidised (DeLongchamp et al., 2003; Kirchmeyer and Reuter, 2005; Kumar et al., 1998). The great advantage of polymer based materials in comparison with metal oxide electrochromics, is the easiness in modifying their optical properties by changing just the main chain and/or the pending group in the polymer structure (Roncali, 1997). On the other hand, they undergo UV degradation if exposed to solar radiation for an extended period of time, and this leads to a well-known yellowing in colouration.

Thermochromic Materials Thermochromics materials change their optical characteristics in response to variation in temperature. Compared to EC, they have the advantage to automatically regulate the incoming solar radiation when a certain temperature is reached on the glass surface. While this property is very efficient in granting an ideal thermal comfort, there is no way for the user to control the light income. As no electric voltage or ion transfer is required, such technologies have the advantage of consisting of just one layer, contrary to multilayer structures required for other smart glazing (Babulanam et al., 1987). Along with the good optical properties requirements, TC materials must be designed to work in a suitable range of temperatures for a building application. For this reason materials with a critical temperature T_c (the temperature at which the colouration changes) of approximately ~25 ℃ must be designed to obtain the ideal energy efficiency performance.

Among thermochromic materials, interested has been shown for fenestration covered with VO_2. This material shows a changing in optical and electronic properties following a phase transition above the critical temperature. Particularly, when $T > T_c$ the crystal phase change from a monoclinic, semiconductor and IR transmitting material to a tetragonal, metallic and, therefore, IR reflecting one (Morin, 1959). For its unique properties different studies were carried out to explore the potential of such materials for practical commercial applications (Babulanam et al., 1987; Jorgenson and Lee, 1986; Khan and Granqvist, 1989; Saeli et al., 2010). Pure VO_2 films show some defects for direct use in solar control devices. These films, show a very poor variation in their optical properties (less than 10% differences among the T_{sol} shown above and below T_c), a maximum T_{lum} of 40% and a typical T_c of approximately 70 ℃ for the bulky material (Morin, 1959), more than twice the desired one. Luminous transmittance can be slightly increased, as for metallic coating, by employing single or multiple layers of dielectric materials, such as SiO_2 (Lee and Cho, 2000), TiO_2 (Jin et al., 2003a), ZrO_2 (Xu et al., 2004) or ITO (Heinilehto et al., 2011). Since the visible absorbance in vanadium oxide is due to band-to-band transition, band gap widening induced by materials such as Mg, has been proven to linearly increase the T_{lum} of VO_2 up to a 10% for a sputtered deposited film (Mlyuka et al., 2009). Doping has been proven to be efficient also for reducing the critical temperature to a more suitable level for glazing application. Tungsten proved to be particularly efficient in this respect, being able to reducing the T_c of bulky vanadium oxide to approximately 25° C for ∼1% of dopant added. For thin film materials, other parameters such as thickness (Jepsen et al., 2006; Xu et al., 2005), nanocrystallinity (Whittaker et al., 2009), or mechanical deformation (Muraoka et al., 2002) can affect their thermochromic properties. Research in this field has moved towards using VO_2 nanoparticles (Dai et al., 2011; Lee and Cho, 2000) embedded in a polymeric matrix as they have been shown to increase light transmittance, increased modulation of solar radiation transmission and have a very strong absorption in the IR region (Li et al., 2010a).

2.4.4.2 Liquid Crystals and Suspended Particles Devices

Liquid crystal (LC) devices are among the leading technologies currently in use for smart-windows. They are similar to ECs, in as much as their optical properties can be changed by the application of an electric field. However, the way in which the optical properties influence the transmittance of light is completely different. Liquid crystals are often touted as the fourth state of matter, they have properties of both crystals (local order in the positioning of the molecules) and liquids (such as fluidity). Since, the optical properties of LC materials depends largely on the internal ordered structures, manipulation of the crystallinity of liquid crystals can be employed in building fenestration to achieve user controlled regulation over light and heat income. One such technology that takes advantage of LC properties is the polymer dispersed liquid crystals (PDLC) device. These have found widespread application as they are easy to prepare, show

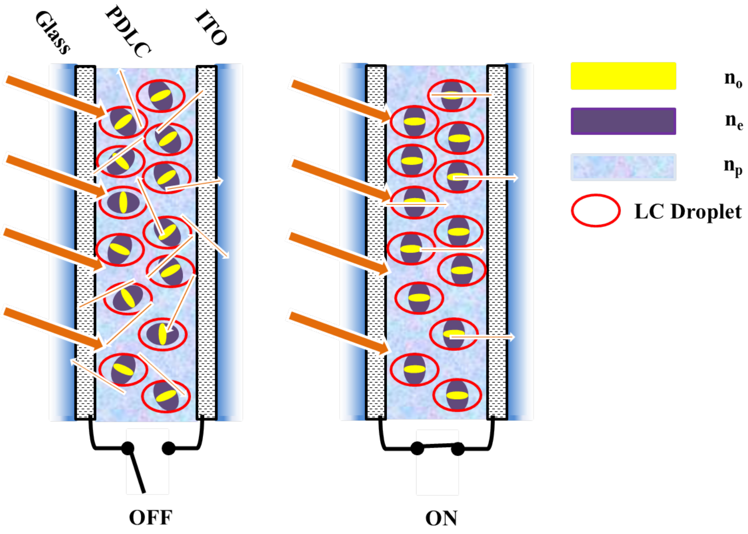

Figure 2.7: PDLC working scheme. When no electric current it is applied (OFF state) LC droplets phase are randomly orientated and solar radiation interacts randomly with n$_e$ and n$_o$ so it is scattered is all directions. When current it is applied, light interacts mainly with $n_o \approx n_p$ and therefore can be transmitted.

good optical properties and have long term durability (Park and Hong, 2009). These devices consist of small droplets of liquid crystalline material dispersed in a polymeric matrix. The matrix is sandwiched between two conductive substrates. These substrates are most commonly prepared from glass, but plastic can also be used; they are coated with a conductive layer, which is typically ITO. When an electric field is applied to the device, commonly referred to as the "ON state", the LC molecules align with the applied field resulting in a transparent window. Without the applied field, the "OFF state, the LC molecules are free to orientate in any direction. Due to the unique properties of LC materials they cause light to be scattered which results in an opaque window. In the ON state, the glazing shows high Tlum, that can reach values up to 65% in, while in the OFF state it drops to around 6% (see Figure 2.7). The advantages of PDLCs are its easy and cheap preparation (PIPS, Polimerisation Induced Phase Separation, is the most used protocol), and their long operative life. Disadvantages, on the other hand, include the haze present during the "ON state" (caused by the extraordinary refraction index still present in the PDLC droplets) and the need for a constant voltage applied to keep the transparent state on. Regarding the latter issue, PDLC materials have been developed to operate in reserve mode (current applied to keep the"OFF state"). However, their main problem is that the voltage that is needed to be applied to keep the OFF state is directly proportional to the temperature of the material, limiting the practical application of reverse PDLC as solar control material.

Suspended particle devices (SPDs) are the most commercially available smart-window technology (Mori and Mikami, 2012). SPD based fenestration work in a similar way to PDLCs, with particles suspended in a gel or a fluid between the two sheets of a double glazing window. When no electric field is applied, the particles (usually oblate particles of polyiodides or paraphathite of around 1 μm (Lampert, 1992)) are randomly distributed inside the matrix, blocking the incoming radiation. When an electric field is present the particles align themselves with the field and allow the light pass. SPDs are the only glazing technology that regulate the quantity of light transmitted, whilst not limiting the range of optical states to be transparent or opaque only (Sottile, 2005)(in the opaque state they are able to block up to 99.5% of incoming radiation). Furthermore, the colour change is very homogeneous even on a large area and the device can undergo a high number of ON-OFF cycles (Sottile, 2005).

2.4.5 Metal Nanoparticle-based Energy Saving Glazing

The commercial availability of smart-windows is still limited, despite the large amount of research in this field, particularly regarding the development of chromic materials. The main disadvantages of these technologies are the high cost of inorganic transparent conducting oxide, the UV degradation of the polymeric materials and the complexity of processes for preparing such devices.

Furthermore, the number of "ON-OFF" cycles of some of these materials are still far from making their employment convenient. Reflecting thin film coatings of both noble metals and semiconductor oxides, on the other hand, are largely employed, but recently some concerns started to emerge about the effects of the reflected radiation and glare; the former can cause discomfort in adjacent buildings and change the microclimate in the surrounding environment, while the latter can cause dangerous visual impairment (Shih and Huang, 2001).

Since the demand for efficient energy saving glazing is pressing, there is an increasing interest in absorbing devices made of metal nanoparticles (MNPs) embedded in a polymeric matrix. MNPs have been known for long due to their unique optical properties. These materials do show strong absorbance contrary to their bulky counterpart (Kelly et al., 2003). While spherical noble metal nanoparticles usually show intense colouration in the visible region, recent advances in controlling size and shape of nanoparticles allowed for finely tuning their absorbance to higher wavelengths (i.e. the NIR)

NIR absorbing gold nanorods dispersed in a poly(vinyl-alcohol)(PVA) matrix, for example, have recently been employed for window coatings by Stokes et al. (2010). These coatings result in very efficient absorbing of the IR radiation (approximately 60% of it is absorbed) and show a good T_{lum} (around 40%). Due to the high extinction coefficient of MNPs, high absorbance can be achieved by low concentration of particles, which can effectively reduce the cost of solar control coating. Compared to other technology, not only nanoparticles/polymer composites use smaller amount of absorbing materials (EC, TC or metal refractive materials need to be deposited as continuous film), but also they do not require expansive deposition techniques or post deposition processing (such as annealing). Xu et al. (2006) calculated that the cost of coating made using gold nanorods dispersed in a PVA matrix (0.26 g Au/m^2) would be of $\sim$ US\$ 3.76/m^2 compared to the average price of $\sim$ US\$ 100/m^2 of available technologies. The smaller amount of absorbing materials does not affect the efficiency of the coating as proved by Schelm et al. (2005). The dispersed LaB_6 nanoparticles he employed showed even an higher efficiency compared to an ITO based system. Until cheaper and longer lasting smart-windows technologies become available on the market, MNPs embedded in polymeric matrix appear to be the easiest and most convenient tool for cutting the energy requirement in both commercial and residential buildings.

2.5 Metal Nanoparticles

Over the last decade interest in nanotechnology has largely increased. The constant research for materials at the nanoscale and the control over their properties has led to the synthesis and characterisation of materials such as carbon nanotubes, polymeric and inorganic nanoparticles of both of metals and/or metal oxides semiconductors. Particularly, metal nanoparticles have received significant attention over other nanoscale systems, mainly due to their easy synthesis, modification and manipulation (Fedlheim et al., 2002). Furthermore, their unique optical and electronic properties have made them extremely appealing for application such as Surface Enhanced Raman Scattering (SERS) (Li et al., 2010b) and optics (Alschinger et al., 2003). Those properties usually lead to a strong coloration of MNPs solution that, in contrast to that of molecular dye, are not dependent on the chemical composition of the system but mainly on the geometrical parameters (such as shape and size), and for anisotropic particles, the orientation of different faces to the electromagnetic field (Kelly et al., 2003).

2.5.1 Synthesis of Metal Nanoparticles

Different ways of synthesising metal nanoparticles are available today, such as chemical reduction (Aiken III and Finke, 1999; Toshima and Yonezawa, 1998), photochemical decomposition (Kim et al., 2002b), electrochemical reduction (Zhu et al., 2001) and sonochemical methods (Salkar et al., 1999). As all these methods start from metal cations for building up the nanosized cluster of metallic atoms they are referred to as "bottom-up" approaches, in contrast to "top-down" techniques where the bulk materials are reduced to smaller sized stable particles (usually employed for oxide nanoparticles). Even if these methods employ different approaches for reducing the metal ions, they all have in common the two step mechanism of the particles formation (nucleation and growth) and the need for stabilizing agents.

2.5.1.1 Nucleation and Growth

Nanoparticle synthesis is a process involving two steps, starting with the formation of small nuclei followed by their growth. This two-step mechanism was firstly reported by La Mer and Dinegar (1950) (see Figure 2.8) for the formation of monodispersed hydrosol led by their increasing concentration in solution. In particular, La Mer pointed out that when the reagents' concentrations reached the supercritical value, insoluble nuclei started to form; as reagents were subtracted from the solution, the concentration reduced and nucleation blocked. This change in concentration drives the nuclei to growth and this process is led just by the diffusion of the reagent in solution. Even if this theory refers to the concentration-driven formation of colloids, it is commonly employed to explain the steps in nanoparticles synthesis undergo and how they can affect the quality of the final product. Indeed, if nucleation does not occur homogeneously over the system, then regions with simultaneous competitive nucleation and growth processes can be formed

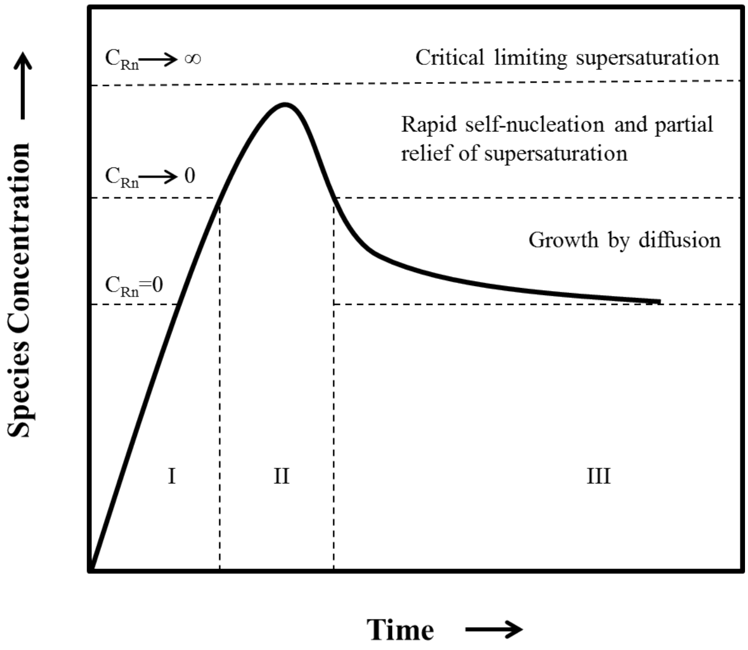

Figure 2.8: Change in concentration of species in solution during the formation of colloid as function of time. When the concentration it is near the supersaturation limit insoluble nuclei starts to form. When the concentration at which the nucleation rate (Rn) tends to zero (C_{Rn}) the particle start to growth. Figure adapted from La Mer and Dinegar (1950) with permission.

and this will affect the overall monodispersity (both in term of size and shape) of the particles.

2.5.1.2 Stabilizing Agents

Nanoparticles have been employed as catalysts due to their high surface to volume ratio and their high reactivity, which arises from high surface energy (Fischer et al., 2008). Even if these characteristics make MNPs very appealing in several applications, they, on the other hand, make these systems very unstable, and this leads to the spontaneous aggregation of nanoparticles and consequently loss of their properties. For these reasons a stabilizing agent is always required, despite the synthetic route employed.

Two strategies are commonly employed to avoid the aggregation of nanoparticle, as show in Figure 2.9:

1. Electrostatic stabilisation: Metal nanoparticles can be considered formed of a positive charged nucleus surrounded by a cloud of electrons. If charged molecules are present, dipoles are generated on the surface of metal nanoparticles due to charge repulsions. Although the total charge on the particles is still neutral, the presence of a dipole is enough to generate electrostatic repulsions and avoid particles aggregation;

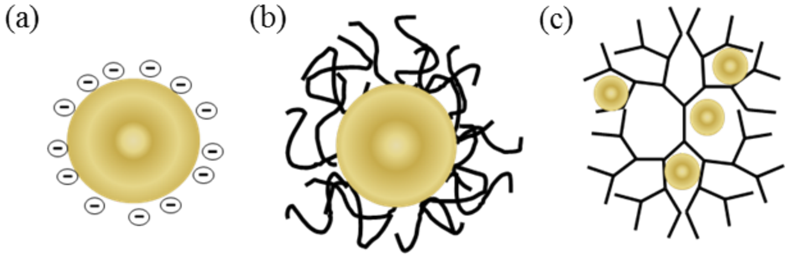

Figure 2.9: Nanoparticles stabilised with anions (Figure 2.9a), polymers (Figure 2.9b) and dendrimers (Figure 2.9c).

2. Steric stabilisation: In contrast to the previous technique, steric stabilisation does not change the electric properties of the single particle, but it creates a shell of very bulky molecules around the particle so that even if they are attracted to one another they cannot aggregate together. Polymers, both synthetic (Harris et al., 2003; Sakai and Alexandridis, 2005) and natural such as proteins (Sanghi and Verma, 2009) and surfactants, have been successfully employed to achieve the formation of stabile colloids in solutions, with poly(vinylpyrrolidone) (PVP), poly(vinyl-alcohol) (PVA) and cetyl trimethylammonium bromide (CTAB) among the most widely employed;

3. Dendrimers: I.e. repetitively branched molecules, are a self-standing group of steric stabiliser. In contrast to other steric stabilisers, dendrimers have the additional role of stabiliser and template for driving the size and shape of particles (Crooks et al., 2001). These branched macromolecules are particularly efficient in the preparation of nanostructured metallic particles because compared to polymers they show a very uniform size and structure, leading to very high reproducible synthesis of nanoparticles.

2.5.1.3 Chemical Synthesis of Nanoparticles

Chemical synthesis of metallic nanoparticles is most commonly carried out using the "bottom-up" approach. The are several advantages of this technique, e.g. starting from the wide array of chemicals that can be employed, and the low temperature usually required for such protocol and the cheap metal precursor. Furthermore, very reproducible and narrowly dispersed colloids can be prepared (Bönnemann and Richards, 2001). This kind of preparative procedure always requires, along with a metal precursor and a stabilizing agent, a reducing agent that is able to rapidly reduce the metal cations to zero valent clusters of metal. As pointed out by Leisner et al. (1996), the stronger the reducing agent is, the more homogeneous the seeds will form. The chemical preparation of a stable colloid of metal nanoparticle was first reported by Faraday (1857), but it was the method from Turkevich et al. (1951) which took the role of standard protocol in the preparation of nanoparticle by chemical reduction.

This method is based on the chemical reduction of a metal salt by trisodium citrate, which acts as both reducing and stabilising agent when added to a boiling solution containing the metal salt. Similar methods have been extensively used for the preparation of nanoscale colloidal particles, using alcohols as reducing agents and polymers, such as PVP and PVA as stabilizing agents (Hirai et al., 1998; Shiraishi and Toshima, 1999).

Chemical synthesis is powerful in the preparation of various shapes of nanoparticles, such as rods (Jana et al., 2001b), prisms (Ha et al., 2007) and cubes (Gao et al., 2012). These different shapes can be achieved by controlling different parameters such as the reaction temperature, the stabiliser type and its amount. Achieving highly monodispersed anistropic particles is more challenging compared to sphericals as the former usually requires preferential growth in some directions. “Seed-mediated growth” procedure was successfully employed to synthesise complex geometry particles as by removing the nucleation step when adding preformed seeds, better control can be achieved on the growth, without risk of competitive formation of other nuclei. Growth is started by reduction of the metal precursor by controlled addition of a mild reducing agent so that the growth (led by diffusion of ionic species in solution) is as more homogeneous as possible in the entire reaction vessel. Any change in the ratio of seed and metal ions can lead to different structures and shapes: this points out how this technique is strong for the production of anisotropic crystals. Nanorods (Nikoobakht and El-Sayed, 2003), nanoprisms (Sanedrin et al., 2005) and nanocubes (Zhang et al., 2010) have been successfully produced with this technique.

2.5.1.4 Photochemical and Sonochemical Synthesis of Nanoparticles

Photochemical methods for preparing nanomaterials show several advantages compared to traditional chemical methods. For example, the dose of irradiation can be easily tuned to affect the size and the shape of the colloid (Naghavi et al., 2010) and preparation of narrowly distributed particles can be achieved in homogeneously distributed irradiating field (Dong and Zhou, 2007). Furthermore, as irradiation usually does not generate heat, temperature sensitive materials can be employed in this reaction (Bárta et al., 2010). Metal reduction can be achieved directly by degradation of the metal precursor by light or by unstable species generated from the photolysis of water such as $H_2O \mapsto e^-$, $H^\cdot$, $OH^\cdot$, H^+, H_2O_2 and H_2 (Naghavi et al., 2010). The first two species, particularly, are very good for reducing metals due to their extremely low reduction potential (-2.87 and -2.3 V_{SHE} respectively). The reduction equations for the metal cations M^{n+} are shown in Reaction 2.4 and Reaction 2.5, respectively:

$$M^{n+} + ne^- \longrightarrow M^0 \tag{2.4}$$

$$M^{n+} + nH^\bullet \longrightarrow M^0 + nH^+ \tag{2.5}$$

As some of the species generated (such as $OH^{\cdot}$), in contrast to $H^{\cdot}$ and $H_2O \mapsto e^{-}$, are oxidisers, then species able to remove such materials must be added to reaction mixture. A widely employed technique is the addition of alcohol or formate anion in the reaction vessel as the reaction of these chemicals with $OH^{\cdot}$ not only reduce the oxidising power of the solution but also leads to the formation of strongly reducing species as shown in Reaction 2.6 and Reaction 2.7 for isopropanol and formate respectively.

$$(CH_3)_2CHOH + OH^{\bullet} \longrightarrow (CH_3)_2\dot{C}OH + H_2O \tag{2.6}$$

$$HCOO^{-} + OH^{\bullet} \longrightarrow COO^{\bullet -} + H_2O \tag{2.7}$$

The radical species generated in Reaction 2.6 and Reaction 2.7 have a reduction potential of -1.8 and -1.9 V_{SHE} respectively (Bárta et al., 2010). Different metals such as Ag (Huang et al., 1996), Cu (Bárta et al., 2010) and Au (Inasawa et al., 2003) have been successfully reduced to metal nanoparticles with this technique. The main issue of protocols based on photochemical method is the long time required for the completion of the reaction if the radiation source is not a special source, but just a standard UV source.

Sonochemical methods are based on similar principles photochemical methods. As for photochemical reactions, the nanoparticle generation is not due to the interactions with sonic waves but due to generation of reactive radical species. These radical species are generated by bubble cavitation in solution when intense ultrasounds are applied (Salkar et al., 1999). During cavitation, bubbles collapse generating very high temperature (up to 5000 K) and very high pressure (up to 1000 atm) for a very short time at the bubble-liquid interface. This rapid gradient formation in heat and pressure generates the radical species which are able to reduce the metal ions. Bubbles are also a source of improved mass and heat transport due to fluxes generated by temperature and pressure gradient present at the liquid-bubble interface (Suslick and Price, 1999). Instrumentation for ultrasound synthesis of nanoparticles require focused generation on sonic waves and therefore usually an acoustic horn (able to amplify the signal amplitude) and a cooling bath to avoid heating of the reaction solution (and therefore originate possible competitive reactions) are employed. Sonochemical assisted nanoparticles generation has been successfully employed in the synthesis of different metal nanoparticles, such as silver (Salkar et al., 1999) and gold amorphous nanoparticles (Okitsu et al., 2005) and also triangular prisms (Park et al., 2006).

2.5.1.5 Vapour Phase Formation of Nanoparticles

Vapour phase (VP) based protocols for the synthesis of nanoparticles have some differences compared to liquid phase reactions. Formation of nanoclusters is achieved when supersaturation is reached in the gas phase, and this leads to the spontaneous formation of seeds, followed by their growth. Once particles are formed they can coagulate together or sinter (coalesce), if temperature is high enough. Particularly, spherical particles are formed when coalescence is favourite instead of particles aggregating in loose open structure (Swihart, 2003). This agglomeration is due to the absence of a stabilizing agent, in contrast to what happens in wet chemical synthesis, where the amount and the type of protecting groups can be changed to modulate the properties of the particles.

The methods for preparing nanoparticles in the vapour phase can be divided into two groups depending on whether the metal precursors are in the solid or liquid phase. Among the former method, inert gas condensation is probably the most widely employed (Pérez-Tijerina et al., 2008). This method is based on the evaporation of the metal vapour from the heated bulk material, followed by condensation when mixed with a cooler inert gas. It has been proved that it is possible to tune the particle size distribution by modulating the mixing rate of the two vapour fluids.

Pulsed laser ablation (Dolgaev et al., 2002) and spark discharge generation are other methods that can be used for vaporised metal ions, an alternative to simple heating. The first technique employs a pulsed laser to generate vapours of metal; this method leads to the formation of very small amount of vapours in a very short period of time and has been employed in VP synthesis of nanocrystals that do not give good rate of evaporation at suitable temperature. The second method, on the other hand, involves the use of metal electrodes surrounded by inert gas, where voltage is applied to the electrode until the breakdown point, when sparks are generated. This method is able to generate small amount of highly dispersed particles and has been employed successfully in synthesising several metal nanocrystals.

Metal nanoparticles can also be generated starting from a solution of metal ions or from volatile precursors (Grodzicki et al., 2005), not just from the bulk solid materials. Chemical Vapour Synthesis (CVS) is a widely employed method in the industrial sector for preparing nanoparticles and depositing thin films (in which case it is called Chemical Vapour Deposition, CVD). Vapourisation of the inorganic precursor are carried out inside a hot-wall chamber where the supersaturation conditions are achieved and particles are formed. This method can also be used to form thin films. Reduction of the vapour phase precursors can be achieved by using a plasma, rather than an hot chamber, to generate more homogeneous heating. Other methods, on the other hand, can achieve the formation of particles by fast concentrating solution of the metallic precursors: spray pyrolysis, laser pyrolysis or plasma pyrolysis where droplets of metal precursor solution are nebulised and then concentrated by means of a heating source such as a hot chamber, or a pulsed laser or plasma. Flame can be used as well to generate particles from both vapour and liquid phase precursors. This method finds great success in industry and nowadays it is the most widely employed technique. The main disadvantage is the oxidising environment of the flames that limits its use mainly for the preparation of metal oxide nanoparticles.

Among all the methods listed, chemical synthesis was largely employed for synthesising silver triangular nanoparticles, thanks to the high control on their final geometry and the good monodispersity (both in terms of size and shape) (Aherne et al., 2008; Pastoriza-Santos and Liz-Marzán, 2002; Sun and Xia, 2003).

2.5.2 Optical Properties of Metal Nanoparticles

Metal nanoparticles have been used due to their optical properties for centuries. Owing to their nanoscale size, they show properties which are neither of the bulk materials nor of the molecules. Particularly, they show strong absorbance in the visible spectrum, a phenomenon known as Surface Plasmon Resonace (SPR). Because of the intense coloration of spherical gold (i.e intense red-purplish colour) and silver (bright yellow) nanoparticles, these materials where largely employed as dyes for glass objects (see Figure 2.10).

SPR can be explained by the collective resonance of the electrons when the nanoparticles are hit by the incident electromagnetic radiation. Despite the fact that

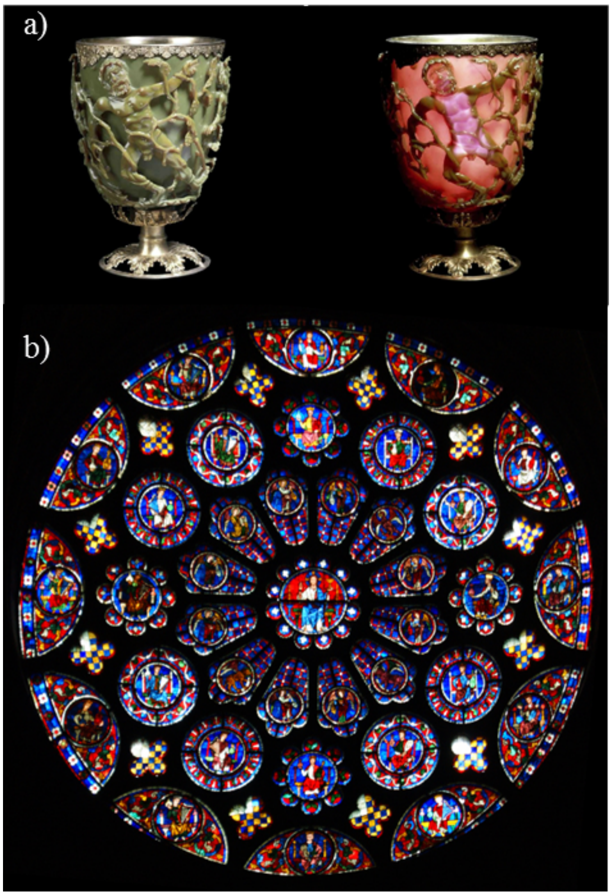

Figure 2.10: Dichroism effect in the Lygurcus Cup (4^{th} century BC , British Museum Figure 2.10a). The red coloration shown by the cup is due to the gold nanoparticles dispersed in the glass, while the yellow colour is due to light reflection by silver nanoparticles. Figure 2.10b shows the South Transept rose window in Chatres Cathedral (∼1225 AC, Paris) where noble metal nanoparticles were used to colour the glass frames.

metal nanoparticles have been largely employed as dyes for centuries their optical properties were not explained until 1908 when the first rigid treatment of their properties was explained by Mie (1908). Mie proposed a solution to Maxwell equations for spherical particle of any size (Maxwell equations were valid just with particles with negligible size compared to the incident radiation wavelength). By solving the Maxwell's equations, Mie was able to calculate the dielectric constant ($\varepsilon(\omega)$) for metal colloids and consequently, the cross section extinction (C_{ext})

2.5.2.1 Maxwell's Equations

Maxwell's equations (Maxwell, 1865) are a set of four equations that, by linking together the magnetic field (**B**), and the electric field (**E**), can explain all the phenomena of electricity and magnetism, such as the propagation of an electromagnetic field in an object. Maxwell's equation can be written in their differential forms as follow:

1. Gauss' Law for Electricity: The electric flux out of a closed surface is proportional to the charge enclosed by the surface

   $$\nabla \cdot \mathbf{D} = \rho \tag{2.17}$$

   where ρ is the current density of a free electron and $\mathbf{D} = \varepsilon_0 \varepsilon_\infty \mathbf{E}$ (with ε_0 and ε_∞ being the permittivity in the free space and the dielectric constant of the medium respectively) the electric displacement.

2. Gauss' Law for Magnetism: The magnetic flux out a surface is zero

   $$\nabla \cdot \mathbf{B} = 0 \tag{2.18}$$

   where $\mathbf{B} = \mu_0(\mathbf{H} + \mathbf{M})$ is the magnetic field. **M** and **H** are the magnetisation and the magnetic field strength respectively, while μ_0 is the permeability in the free space.

3. Faraday Law of Induction: The electromotive force induced by the changing in the magnetic field is equal to the negative value of the changing of the magnetic field itself with time

   $$\nabla \times \mathbf{E} = -\frac{\delta \mathbf{B}}{\delta t} \tag{2.19}$$

4. Ampere's Law: The strength of the magnetic field generated by an electric current is equal to the changing in the electric field with time

   $$\nabla \times \mathbf{H} = \mathbf{j} + \frac{\delta D}{\delta t} \tag{2.20}$$

   where **j** is the electrical current.

By using Maxwell's equations the dielectric constant $\varepsilon(\omega)$ can be defined by substituting Equation 2.20 in Equation 2.19 for calculating $\nabla^2 \mathbf{E}$:

$$\nabla^2 \mathbf{E} = +\mu_0 \sigma \frac{\delta \mathbf{E}}{\delta t} + \mu_0 \varepsilon_0 \varepsilon_\infty \left(\frac{\delta^2 \mathbf{E}}{\delta t^2} \right) \tag{2.21}$$

By taking the spatial and temporal components of the electric field as independent and **E** as periodical, it can be rewritten as a frequency dependent function by mean of Fourier transform as shown in Equation 2.22:

$$\nabla^2 \mathbf{E} = -\mu_0 \varepsilon_0 \omega^2 \left[\varepsilon_\infty + \frac{i\sigma(\omega)}{\omega \varepsilon_0} \right] \mathbf{E} \tag{2.22}$$

where ω is the frequency and $\sigma(\omega)$ is the frequency-dependent conductivity of the medium. The term between the square bracket is the frequency dependent dielectric constant when a wave is presence, $\varepsilon(\omega)$:

$$\varepsilon(\omega) = \varepsilon_\infty + \frac{i\sigma(\omega)}{\omega \varepsilon_0} \tag{2.23}$$

2.5.2.2 Drude's Model

Determination of $\varepsilon(\omega)$ and $\sigma(\omega)$ in media other than the free space is complicated. For metal, the Drude's model helps to calculate these parameters by giving a simplified explanation of electron motion. The Drude's model (Drude, 1900) is based on four assumptions:

1. Metals are formed by positively charged ions surrounded by a cloud of electrons;
2. Electrons are free and independent;
3. Electrons move as a whole cloud and act in phase;
4. Electrons interacts with positively charged ions only by instantaneous collision, the nature of which is not important for calculations.

Equation 2.24 describes the motion of electrons in a metal, where ν is the electron speed, m_e is the effective mass of electron, e is the electrons charge and Γ is the crystal lattice damping constant. :

$$m_e(\frac{d\nu}{dt}) + m_e \Gamma \nu = e\mathbf{E} \tag{2.24}$$

The second term, particularly, represent the viscous friction which arises from inelastic collision, phonon coupling or defects in the crystal lattice. As **E** can be expressed as a time harmonic function ($\mathbf{E}(\omega) = \mathbf{E}_0 e^{i\omega t}$) also ν can be expressed as sinusoidal function. Equation 2.24 can be written as:

$$(-i\omega m_e + m_e \Gamma)\nu_0 e^{-i\omega t} = e\mathbf{E}_0 e^{-i\omega t} \tag{2.25}$$

From Equation 2.25 ν_0 can be written as

$$\nu_0 = \frac{e}{m_e\Gamma - i\omega m_e}\mathbf{E}_0 \tag{2.26}$$

Drude's model also provides a relationship between **j** and **E** (Equation 2.27), where n is the electronic density.

$$\mathbf{j} = en\nu = \frac{ne^2}{m_e\Gamma - i\omega m_e}\mathbf{E}_0 = \sigma(\omega)\mathbf{E}_0 \tag{2.27}$$

From Equation 2.27 the frequency-dependent conductivity $\sigma(\omega)$ can be calculated (Equation 2.28):

$$\sigma(\omega) = \frac{ne^2}{m_e\Gamma - i\omega m_e} \tag{2.28}$$

By replacing Equation 2.28 in Equation 2.23 $\varepsilon(\omega)$ can be express as Equation 2.29 where $\omega_P^2 = ne^2/\varepsilon_0 m_e$ is the plasma frequency :

$$\varepsilon(\omega) = \varepsilon_\infty - \frac{\omega_P^2}{\omega^2 + \Gamma^2} + \frac{\omega_P^2\Gamma}{\omega(\omega^2 + \Gamma^2)} \tag{2.29}$$

2.5.2.3 Resonance Condition in Metal Nanoparticles

To understand how nanoparticles interact with the light, the condition of resonance of the light with the cloud of electrons has to be determined. Although the Drude's model can be used also for describing electron movement in metal nanoparticles, some consideration must be made:

1. $\rho = 0$ as in small particles the electronic density is not homogeneous;
2. Due to the small size, charges accumulate on the particle's edge.
3. Quasi-static Approximation: as nanoparticles are small compared to the wavelength, it can be assumed that all the electrons "feel" the same electric field and so the electric field is independent from the electron position.

As electrons displace from their starting positions, discrete charges are created on the surface of the particles (negative and positive). The presence of discrete charges on the surface of the particles results in a restoring force imposed on the electron. The Drude's equation (Equation 2.24) for the electron's motion on a nanoparticle can be written in a form that resembles the motion of a forced, damped harmonic oscillator :

$$m_e\frac{d^2x}{dt^2} + m_e\Gamma\frac{dx}{dt} + Kx = e\mathbf{E} \tag{2.30}$$

where K is the restoring force, x is the position of the oscillating cloud as described in Equation 2.31:

$$x = \frac{e\mathbf{E}}{m_e(\omega_R^2 - \omega^2 - i\Gamma\omega)} \tag{2.31}$$

Equation 2.31 shows how the electron displacement reaches the maximum when $\omega \simeq \omega_R$, with ω_R being the eigen-frequency of the system.

2.5.2.4 Mie's Theory and Optical Properties of Metal Nanoparticles

In 1908, Gustav Mie (Mie, 1908) was the first to describe the scattering and absorption of single, isolated particles by proposing a solution to Maxwell's equation. The method is valid for describing the scattering of a plane wave by a homogeneous, isotropic sphere, surrounded by a non-absorbing medium. Mie's theory leads to formulate the cross section extinction C_{ext} as:

$$C_{ext} = \frac{24\pi^2 R^3 \varepsilon_m^{2/3}}{\lambda} \frac{\varepsilon_2}{(\varepsilon_1 + 2\varepsilon_m)^2 + \varepsilon_2^2} \tag{2.32}$$

where R is the particles radius, λ the wavelenght of the incoming radiation, ε_m is the dielectric constant of the medium surronding the particles and ε_1 and ε_2 are the real and immaginary part of $\varepsilon(\omega, R)$.

Effect of the Surrounding Environment Equation 2.32 shows how the medium surrounding the metal nanoparticles has an effect on both the plasmon peak position and intensity.

Duval Malinsky et al. (2001), studied the effect of different solvent on the SPR of a silver nanoparticle array. By increasing the dielectric constant of the surrounding medium he proved that a linear relation exists between the peak maximum wavelength (λ_{max}) and ε_m. This relation is also shape dependent, i.e. oblate ellipsoids are less sensitive than truncated tetrahedrons to changes in the electronic environment.

Kelly et al. (2003), on the other hand, studied the effect of the substrate on the optical properties of silver nanospheres surrounded by a shell of mica and of truncated tetrahedrons sitting on a mica slab. For both cases a shift to higher wavelengths has been observed; particularly, in the former case, a linear trend has been reported as the coverage of the particles increases.

Not only the surrounding medium, but also the inter-particle distance can affect λ_{max} of the colloid solution. When clusters of particles are placed in closed proximity, the coupling between particles becomes very important. Su et al. (2003) reported the effect of intra-particle distances of the optical properties of elliptic gold nanodisks. Their calculations showed an exponential increase in the spectral position of λ_{max} as the inter-particle distance decreased.

Electronic Effects Equation 2.29 shows the dependence of $\varepsilon(\omega)$ on the plasma frequency ω_P which is a function of the electron density of nanoparticles n, as shown in Equation 2.33:

$$\omega_P = \sqrt{\frac{ne^2}{\varepsilon_0 m_e}} \tag{2.33}$$

As the electron density is a key factor in determining $\varepsilon(\omega)$, it is clear that everything that can increase or reduce n will have a strong impact on nanoparticles final optical properties. Particularly, the stabilisers used to prevent aggregation, strongly affect surface plasmon resonance as they i) change ε_m and ii) can donate/accept electrons to and from metal nanoparticles. Focusing on the second point, some examples are reported in literature: for example, Sherry et al. (2006) reported the shift to longer wavelength ($\sim$ 20 nm) for the SPR of a single silver triangular nanoprisms as trisodium citrate is replaced with 1-decanethiol. Moores et al. (2004), on the other hand shown how the use of phosphine as capping agent for gold nanosphere results in a shift to lower wavelenghts due to the π-accepting properties of these ligands.

Size and Shape Effects Equation 2.32 states the dependence of C_{ext} on the size of the particles expressed as their radius R. Although many studies have been carried out to predict how optical properties of metal nanoparticles varied as a response to the size variation, most of the results contradict with each other as some of them were predicting a red shift while other a blue shift when the size decreased. Experimental methods on the other hand, have resulted much more efficient in order to describe how the final SPR is affected by the size. In particular, for metal nanoparticles, two main trends can be highlighted:

1. Alkali Metal NPs: as the size of this particles decreases, a red shift of SPR is observed (and *vice versa*). This behaviour is due to the fact that by reducing the size of the cation core, the electron cloud can spill out of it and therefore moving the centroid of the fluctuating charge: this is analogous to using a spring with a weaker recall force, and this results in shifting the absorption to lower energy (i.e. longer wavelength);
2. Noble Metal NPs: compared to alkali metal nanoparticles, noble metals show an opposite trend. This is due to the presence of d electron which mutually induces a polarisation effect with the s one.

Modelling the effect of the shape on the SPR is still challenging. The main reasons are that: i) Mie's theory is valid just for a spherical particle, ii) Equation 2.32 is a first order equation and can only explain a first order oscillation (i.e. dipole), while with non-spherical particles multipole contributions start to consistently affect the optical properties of the nanoparticles. Commonly, in order to model the SPR of non-spherical particles, approximation methods are employed, of which the most popular is known as DDA (Discrete Dipole Approximation). This method consists of dividing the particles and the surrounding environment into small cubic elements, small enough to be consider dipoles, and each characterised by its position and polarizability. SPR on each element E_i results from the sum of the external electric fields (the radiation ones) and that generated by the oscillation of all the other element surrounding E_i. This method has been successfully employed for studying the optical properties of anisotropic metal nanoparticles such as rods, cubes, and triangular prisms.

2.5.2.5 Optical Properties of Silver Triangular Nanoprisms

Optical properties of silver triangular nanoprisms are far more complex than those of silver nanospheres, mainly due to their higher anisotropy and also due to the generally larger size of the prisms higher modes, can be observed, i.e. quadropoles. Figure 2.11a shows the optical spectra of silver nanoparticles in water. Each spectrum show the presence of four peaks which correspond to:

1. 770 nm: In-plane dipole resonance;
2. 470 nm: In-plane quadrupole resonance;
3. 410 nm: Out-of plane dipole resonance;
4. 340 nm: Out-of plane quadrupole resonance.

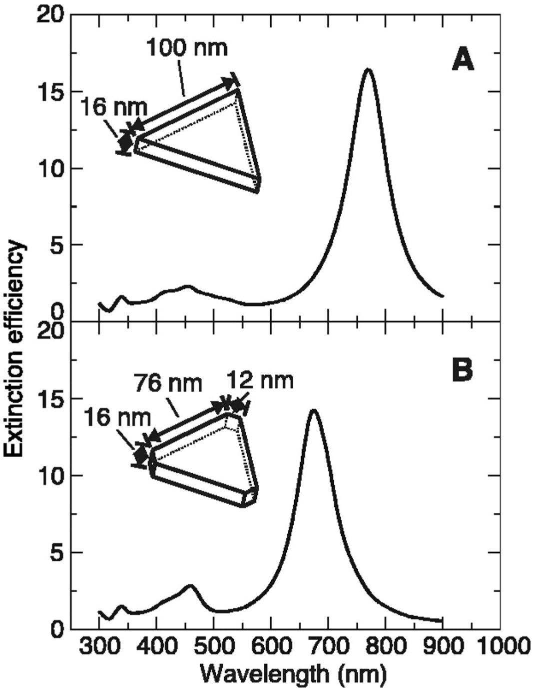

Figure 2.11: DDA simulations of two different triangular silver nanoprisms in water, as reported by Jin et al. (2001). Images reprinted with permission.

Experimentally, the peaks at 770 nm and 340 nm are the most characteristic peaks of silver nanoprisms as the one at 470 and 410 nm are usually present as a shoulder or not detectable at all. As for other noble metal nanoparticles, increasing the size of silver nanoprisms results in a red-shift of the SPR. Tips exert a great influence on the final plasmon resonance. In particular, Jin et al. (2001) observed how removing the tips causes a blue-shift of the in-plane dipole resonance of ∼100 nm. Sherry et al. (2006) demonstrated how sharper tips increased the broadness of the in-plane dipole resonance due to the well-known lighting-rod effect.

Chapter 3

Experimental

Contents

3.1 Introduction

In this Chapter, the experimental setups and the chemical syntheses employed are reported. The synthetic routes and the materials used were chosen in order to provide high quality coating, using cheap materials, low cost techniques and high control over particles properties. The Chapter is divided in four different Sections:

- Section 3.2 reports the batch synthesis of SNPs used for investigating their optical proprieties. The size and shape modification by mean of Cl^- and Au^{3+} ions, respectively, are also reported.
- Section 3.3 deals with the microfluidic preparation of silver nanoprisms. Section 3.3 covers the experimental setups used for the synthesis of SNPs, the process for the microreactors fabrication and the governing equations and boundary conditions used for computational fluid dynamic simulations. Section 3.3 also include the experimental setup used for the development of a microspectrophotometer for *in situ* monitoring of SNPs within a microreactor.
- Section 3.4 covers the reactions used for coating SNPs with a silica shell (SNPs@SiO_2) by sol-gel chemistry. The functionalisation of such shell with thiol and allyl moieties is also reported, along with analytical method for detecting their presence onto the particles surface, such as the Ellman test or thiol labelling with fluorescein-5-maleimide.
- Section 3.5 presents the synthesis of SNPs@SiO_2/PMMA composite materials, their characterisation and the calculation of the figure of merit for films of this material deposited on glass.

All Sections are structured as follow:

- Short introduction with justification of the experiments and targets;
- Chemicals and Materials;
- Characterisation Techniques and Equipment;
- Methods;
- Synthesis or Experimental Setups.

All reactions and experiment were carried out at, ambient conditions, room temperature and in air, unless specified. MilliQ water (18 MΩ·cm) was used for all the reactions. As yields of the reaction and the quantity (grammes) of the prepared particles are difficult to exthablish, they are not reported.

3.2 Batch Synthesis of SNPs

In this section the batch synthesis of SNPs and their size and shape modification by mean of Cl^- and Au^{3+} ions is reported. In particular the method proposed by Métraux and Mirkin (2005) (Section 3.2.4.1) was used for their preparation thanks to it short reaction time. The reaction consists in the formation of silver seeds by reduction of the silver precursor by $NaBH_4$ followed by re-oxidation (by H_2O_2) and re-precipitation on the already formed nuclei. Use of TSCD as stabilizing agent and the presence of twinned defects in the seeds drives the formation of flat triangular structure. Tuning of the their optical properties is granted by controlling the ratio between the silver precursor (i.e. silver nitrate) and the reducing agent (i.e. $NaBH_4$) and the good control over their optical properties. To modify the size of the particles by reaction with Cl^- (Section 3.2.4.2) the approach proposed by Cathcart et al. (2009) was adopted. Addition of KCl prior to the reduction with $NaBH_4$ reduce the solubility of Ag^+, leading to the formation of a reduced number of nuclei and to the formation of bigger particles. For the shape modification of SNPs, galvanic replacement with Au^{3+} was used. Both this methods require just small modification to the synthesis of SNPs, i.e. addition of small amounts of aqueous solutions to the reaction vessel, resulting advantageous for this research.

The targets of the experiments reported in this Section were to investigate both the optical properties of SNPs and to see how good the reaction proposed by Métraux and Mirkin (2005) is in controlling the final shape of the prisms. Furthermore the possibility of using Cl^- and Au^{3+} ions for modifying the optical properties of SNPs were investigated, with particularly interest on the reliability of such reactions.

3.2.1 Chemicals and Materials

Silver nitrate, trisodium citrate dihydrate (TSCD), potassium chloride and chloroauric acid were purchased from Sigma-Aldrich (UK).
Sodium borohydride was purchased from Acros Organic (Belgium).
Hydrogen peroxide was purchased from Fisher Scientific (UK).
TEM grids (Carbon on Cu, 400 mesh) were purchased from Agar Scientific (UK).

3.2.2 Characterisation Techniques and Equipment

3.2.2.1 TEM

TEM images were collected using a FEI Technai12 transmission electron microscope, with an electrons acceleration of 120 kV and a tugsten filament source.

3.2.2.2 Energy Dispersive X-ray Spectroscopy (EDAX)

EDAX spectra were collected with a FEI Technai12 transmission electron microscope.

3.2.2.3 Spectroscopy

UV-vis-NIR spectra (300-900 nm) were collected using a Cary Varian 300 Bio using a quartz cell (10 mm optical path).

3.2.3 Methods

3.2.3.1 Nanoparticles Purification

Nanoparticles can be purified by means of centrifugation (13,200 rpm for 15 minutes). After removal of the supernatant the particles can be redispersed in ethanol or water.

3.2.3.2 TEM Sample Preparation

In order to prepare samples for the transmission electron microscope, 10 μL of nanoparticle solution was drop cast on a TEM grid. The grid was then covered with a Petri dish to allow the solvent to evaporate.

3.2.3.3 Electron Microscopy Characterisation

The collected TEM images were analysed using ImageJ, an open source software for image analysis. After the images were processed, some parameters such as the area of the particles, their perimeter, the axes length (major and minor) of the fitting ellipse were obtained. The outputs provided was very useful for the calculation of large amounts of spherical or rod-shaped particles, though for particles with more complex geometry (such as triangles) they are not sufficient or not able to provide accurate measurements. In order to analyse the largest number of particles in a shorter time, further investigation was needed of geometrical descriptors in order to distinguish and discriminate the particles by their shape and, at the same time give the correct size of the edge of the particle. The first method was adapted from Igathinathane et al. (2008) where discrimination of different shape was carried out by employing geometrical parameters of the best fitting ellipse (the size of the two axes) and rectangle (the length and the height). Along with these parameters, the Feret diameter was employed for discriminating the different geometries, which represents the distance between two parallel tangent lines of the particle at an arbitrary angle (See Figure 3.1).

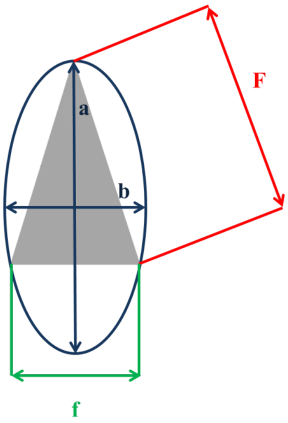

Figure 3.1: Different geometrical parameters for an object

In particular, the minimum Feret diameter (the shortest distance between two parallel tangent lines, f) and the maximum Feret diameter (the longest distance between two parallel tangent lines, F) are commonly taken in account. According to Igathinathane et al. (2008), three parameters are necessary to uniquely discriminate different shapes. These are:

1. Reciprocal Aspect Ratio (RAR): $\frac{a}{b}$
2. Rectangularity (RTY): $\frac{(\pi ab)}{4HW}$
3. Feret Major Axis Ratio (FMR): $\frac{F}{a}$

where a and b are the major and minor axes of the best fitting ellipse, H and W the height and the width of the bounding rectangle and F is the maximum Feret diameter. In particular, different triangular shapes are all identified by these values of RAR, RTY and FMR:

1. $0.115<\text{RAR}<0.991$
2. $0.110<\text{RTY}<0.517$
3. $1.295<\text{FMR}<1.351$

These values are very different from that of other shapes. In particular, circles are characterised by RAR=1, $0.750<\text{RTY}<0.889$ and $1.009<\text{FMR}<1.144$, respectively. These values are so different from that of triangles that only two of them are necessary to identify triangular nanoprisms uniquely. This methodology offers even a method to calculate the edge and width of the nanoparticles from a and b, through a correction parameter C, which was calculated from a template shaped to develop this method (the values of C are ~1.35 and ~1.165 for transforming the value of the major and the minor axes of the fitting ellipse to the major edge length and the height of the triangle).

Another method for discriminating triangles based on the minimum and the maximum Feret diameter and on the particles area (A) has been adopted by the work proposed by Rivollier et al. (2010). This method uses just two calculated values for isolating different shapes with a good resolution. Also, compared to the previous method, Rivolliers was able to recognise a wider amount of shape. The values taken into account in order to recognise the different shapes are:

1. Equilateral Triangularity (ET): $\frac{f^2}{(\sqrt{3}A)}$
2. Roundness (RD): $\frac{A}{\pi(a/2)^2}$

where A is the area of the nanoparticles given by Image J. The shape distribution as a function of ET and RD is shown in Figure 3.2. ET and RD are sufficient to roughly discriminate different shapes. The size of the triangles, in particular their edge, can be determined using the average value of the maximum and the minimum Feret diameter.

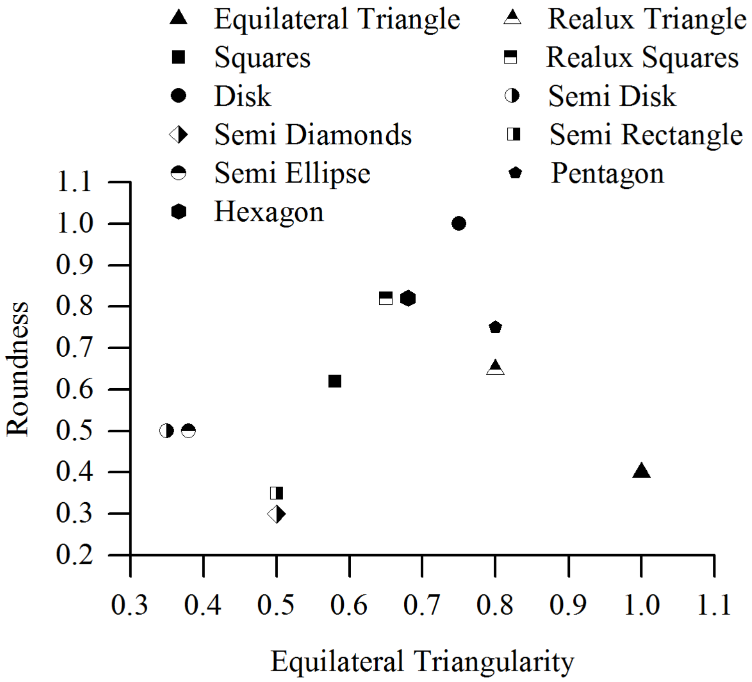

Figure 3.2: The different shape distribution for different values of equilateral triangularity and roundness. The figure shows how distinct the different shapes are when plotted as a function of these two parameters.

3.2.4 Syntheses

3.2.4.1 Synthesis of Silver Nanoprisms (SNPs) by Batch Reaction

In order to synthesise SNPs, the protocol proposed by (Métraux and Mirkin, 2005) was used. In a typical reaction, to a freshly prepared solution of $AgNO_3$ (20 mL, 0.1 mM, 2 μmol) a 30 mM solution of TSCD (1.2 mL, 36 μmol) was added. PVP (1.2 mL, M.W. 30 KDa, 0.7 mM, 0.84 μmol) could be added as well to the solution to grant extra stabilization of the forming particle. H_2O_2 (48 μL, 30% w/v, 422.2 mol) was added then the solution was left to stir for 5 minutes. Finally, a 0.1 M aqueous solution of $NaBH_4$ (0.2 mL, 20 μmol) was rapidly injected. The solution colour started to change from an intense yellow (typically shown by spherical particles) to a dark blue colour (characteristic of triangular silver nanoprisms). The reaction batch was stirred until no further change in colour could be observed. The solution was then centrifuged according to the purification procedure illustrated above and then stored in a fridge, where the colloid solutions were stable for months.

3.2.4.2 Size Modification of Silver Nanoprisms

The size modification of SNPs using chloride ions is based on the work of Cathcart et al. (2009). For modifying the size of silver nanoparticles, to a freshly prepared solution of $AgNO_3$ (20mL, 0.1mM, 2 μmol) a 30mM solution of TSCD (1.2 mL, 36 μmol) was added along with up to 44 μL of a 0.05M solution of KCl. To this solution H_2O_2 (48 μL, 30% w/v, 422.2 μmol) was added and then left to stir for 5 minutes. Finally, after the rapid addition of a 0.1 M aqueous solution of $NaBH_4$ (0.2 mL, 20 μmol) the solution was left stir for about 5 minutes, until the solution changed colour from a pale yellow to a light blue colour.

3.2.4.3 Shape Modification of Silver Nanoprisms

In order to modify silver nanoparticles into hollow triangular silver-gold alloys, to 1 mL of a freshly prepared Ag nanoprisms (prepared with and without PVP), 250 μL of different concentration of $HAuCl_4$ solution (0.125, 0.2, 0.3 mM) were added. The samples were briefly sonicated and then left to rest overnight.

3.3 Microfluidic Synthesis of SNPs

Use of microreactors has been proven successful in preparing a large number of metal colloids, with improved control over their final properties compared to traditional batch reactors. Experiments reported in this Section aim to investigate the feasibility of microreactors for the synthesis of SNPs. Section 3.3.6.1 reports the experimental setup used for the preparation of silver nanoprisms, while Section 3.3.6.2 reports the one used for investigating if bigger control can be exerted on size modification of SNPs by halide ions (i.e. Cl^- and Br^-). Computational fluid dynamic simulation were used to understand how the fluidodynamic of the system affected the concentrations of $AgNO_3$ and KCl (with interested in their ratio). In Section 3.3.6.3 the experimental setup for spectroscopic monitoring of SNPs formation within the microreactor is reported. For the synthesis of SNPs, PDMS/glass microreactors were employed, thanks to the easy preparation and low cost. For *in situ* spectroscopy a PMMA microreactor was built. PMMA was chosen due to his transparency in the visible and the absence of bubbles (which can be present in PDMS layers). High precision in manufacturing compared to glass (micromilling versus chemical etching) was another advantages. Different channel lengths were used to increase the reagents' residence time.

The targets of the experimental setups reported were to investigate if microfluidic can grant a better control over SNPs final size and shape and to understand how change in hydrodynamic parameters can affect them. In particulart the residence time of the particles inside the microreactor was tuned by changing the flow rate of the reagent inside the channel. The development of a microspectrophotometer aimed to produce a setup for absorbance measurments within a microreactor with no need for special channel designs (such as larger sections and/or optical elements).

3.3.1 Chemicals and Materials

Silver nitrate, trisodium citrate dihydrate (TSCD), trichloro(1H,1H,2H,2H)-perfluorooctylsilane, potassium chloride, potassium bromide, dimethylformamide and propylene glycol monomethyl ether acetate were purchased from Sigma-Aldrich (UK). Sodium borohydride was purchased from Acros Organic (Belgium).

Hydrogen peroxide, and isopropanol were purchased from Fisher Scientific (UK).

Polydimethylsiloxane (PDMS) monomer and curing agent were purchased from Dow Corning (USA). SU-8 2050 was obtained from Chestech (UK).

Silicon wafers, (100) or (111), were purchased from University Wafer (USA). PMMA sheets (1.5 mm thick) were purchased from Röhm (Germany). TEM grids (Carbon on Cu, 400 mesh) were purchased from Agar Scientific (UK).

The light source, detector (Avalight-Hal) and the optical fibres (FC-IR600-2-SMA) for the microspectroscopy experiment were purchased from Avantes, UK. The optics for the inlet and outlet tube were purchased from Edmund Optics, UK. The collimating tube was supplied by Avantes, UK. The microscope objective (RMS40X) and the fibre collimator (F220SMA-A) were purchased by Thorlabs, Germany, while the aspherical achromatic lens (NT49-664) was purchased by Edmund Optics, UK. The 60x microscope objective (RMS60X-PFC) was purchase by Thorlabs, Germany. For PMMA device fabrication a Protomat S100 micromiller and a LPKF Multipress (LPKF laser and electronics AG, Germany) were employed.

3.3.2 Characterisation Techniques and Equipment

3.3.2.1 TEM

TEM images were collected using a FEI Technai12 transmission electron microscope, with an electrons acceleration of 120 kV and a tugsten filament source.

3.3.2.2 Spectroscopy

UV-vis-NIR spectra (300-900 nm) were collected using a Cary Varian 300 Bio using a quartz cell (10 mm optical path).

In-line monitoring of the optical properties of SNPs produced within a microreactor a 10 mm optical path flow cell was used (model 73.65/Q from Starna Scientific, UK) which was connected to the exit fo the micro-reactor.

In-situ monitoring of the optical properties of SNPs while they were produced within the microchannel were carried out by collecting UV-vis-NIR spectra with a spectrophotometer, (Avalight-Hal, Avantes UK) coupled with a 10 W fan cooled tungsten halogen lamp spectrophotometer. The light was delivered with a FC-IR600-2-SMA optical fibre (Avantes, UK)

3.3.3 Methods

3.3.3.1 TEM Sample Preparation

TEM sample were prepared according to Section 3.2.3.2. TEM images were processed according to Section 3.2.3.3.

3.3.3.2 $NaBH_4$ Solution Preparation for Microreactor Experiments

$NaBH_4$ rapidly degradates in aqueous solutions, developing hydrogen. Although this phenomenon does not affect the hydrodynamic of mixing in a batch reactor, bubbles can alter it in the confined space of a microreactor. Reducing the spontaneous formation of hydrogen can be achieved by preparing a basic, alcoholic solution of $NaBH_4$.

The protocol for solution preparation followed that described by Shalom et al. (2007). Briefly, 1 mL of a 0.01 M solution of sodium borohydride (prepared by dissolving 0.038 g of $NaBH_4$ in 70 mL of MilliQ water and 30 mL of 1 M of NaOH) was added to 32 mL of a 0.1 M isopropanolic solution of $NaBH_4$.

3.3.4 Microreactors Fabrication

3.3.4.1 PDMS/Glass Microdevices Fabrication

In order to prepare a hybrid PDMS/Glass microdevice a positive mold made of SU-8 on silicon wafer was prepared according to Microchem website (Microchem (2014)). Prior to depositing SU-8 on the silicon wafer, the substrate was cleaned with piranha solution, followed by isopropanol and MilliQ water rinsing, and then dried in an oven overnight. SU-8 (1 mL/25mm of substrate diameter) was deposited on the substrate and then spun with the following setting:

1. 500 rpm (acceleration 100 rpm/s) for 10s;
2. 3,000 rpm (acceleration 300 rpm/s) for 30s;

The substrate was then put on a hot plate and left at 65 ℃ for 5 minutes and then at 95 ℃ for 20 minutes. Once the substrate had cooled to room temperature, the mask with the desired design was placed on the SU-8 film and kept in place with a glass slide, tightened with clamps to the silicon wafer. The substrate was placed on a stand at 5 cm of distance from the light bulb of a UV lamp (100 W, λ= 365 nm) and irradiated for 30 seconds to start the polymerisation of the SU-8. After irradiation, the sample was put on a hot plate and left at 65 ℃ for 5 minutes and then at 95 ℃ for 20 minutes.

In order to remove the un-reacted SU-8, the silicon substrate was dipped in propylene glycol monomethyl ether acetate for ~20 minutes and then rinsed with isopropanol. The clean substrate was dried overnight at 100 ℃.

Subsequently, the mold was covered with a layer of a 10:1 (w/w) PDMS precursor and curing agent mixture and heated for 1 h at 80 ℃ for the polymer to cure. The PDMS sheet with the microchannel architecture fabricated on the surface was then removed from the mold and permanently bonded to a glass slide after oxidizing its surface with a plasma treatment for 30 seconds. Following the bonding of PDMS sheet to the glass layer, the channel wall was functionalized with a solution of trichloro(1H,1H,2H,2H)-perfluorooctylsilane (5% v/v in dimethylformamide) to make the channel surface hydrophobic in order to reduce the interaction between silver cations and hydroxyl groups on the glass surface.

3.3.4.2 PMMA Microdevices Fabrication

After the disegn, the geometry of the microdevice was imported to the micro-mill software and then cut out from the PMMA sheet. A PMMA sheet (1.5 mm thickness)

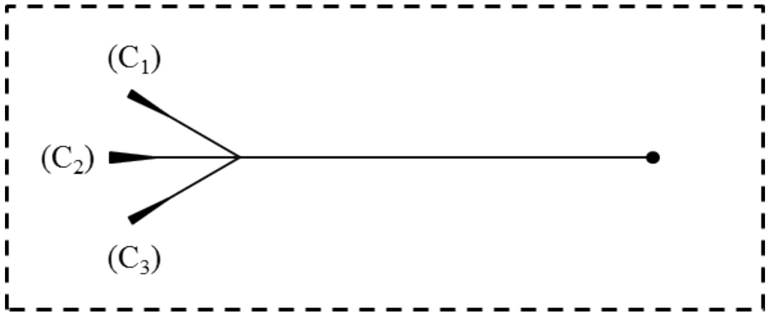

Figure 3.3: PDMS/Glass microreactor scheme used for the synthesis of SNPs. Microchannel dimensions are 150 μm×50 μm×3 cm (width×depth×length).

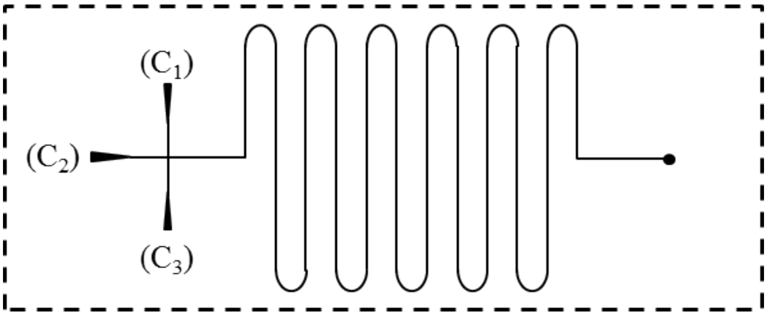

Figure 3.4: PDMS/Glass microreactor scheme used for the modification of SNPs with halide ions. Microchannel dimensions are 150 μm×50 μm×35 cm (width×depth×length).

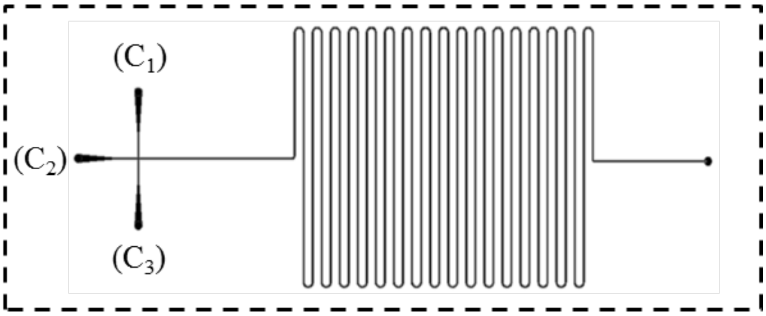

Figure 3.5: PMMA microreactor scheme. Microchannel dimensions are 210 μm×300 μm×108 cm (width×depth×length).

with the geometry milled on it was then bound to smooth sheet, according to Ogilvie et al. (2010). Briefly, the face of the PMMA sheets that have to be bound were exposed to chloroform vapours and then pressed together for 1 minute by hand. The weakly bounded polymer sheet, were then pressed with a clamp and heated for 30 minutes to secure them.

3.3.4.3 PDMS Mold Preparation

In order to prepare thicker films, a mold made out of PDMS have been prepared by casting a thin film of 10:1 PDMS precursor:initiator solution in a Petri dish and let it cure in the oven at 80 ℃ for a couple of hours. After removing the film from the dish (∼2 mm thick) and cutting 1 cm×1 cm holes, it was placed on clean glass slide and carefully attached to it, while paying attention that no air bubbles were left. The glass slide is then place on a hot plate at 50 ℃ for 30 minutes to improve adhesion. Once the glass slide got cold again, polymer solutions can be cast in the mold holes.

3.3.5 Computational Fluid Dynamic (CFD) Simulations

A two-dimensional (2D) numerical model was developed in order to investigate the fluid dynamics and mass transfer processes within the fluidic domain. Particularly CFD were used to study the how the fluidodynamic mixing affects the relative concentrations of $AgNO_3$ and KCl when mixed inside the microreactor.

3.3.5.1 Mesh design

ICEM® 14 (Ansys Inc., US) was employed for geometry design and mesh construction. Model geometry corresponded to that of a commercially-available T-junction (model V100-T®, from Upchurch Scientific). The channel length is 3.098 mm, while the channel internal diameter is 1.016 mm. The geometry was meshed using quadrilateral elements, where the mesh element size was set to 0.02 mm.

3.3.5.2 Governing Equation

The following mass conservation (Equation 3.1) and momentum conservation (Equation 3.2) equations were solved over the computational flow domain, using Ansys Fluent® 12.1 (Ansys Inc., US), where $\mathbf{v}$, ρ_f, μ and P represent fluid velocity, density, dynamic viscosity and pressure, respectively:

$$\nabla \cdot (\mathbf{v}) = 0 \tag{3.1}$$

$$\frac{\delta \mathbf{v}}{\delta t} + \rho_f \mathbf{v} \cdot \nabla \mathbf{v} = -\nabla P + \mu \nabla^2 \mathbf{v} \tag{3.2}$$

The mass transfer of $AgNO_3$ and KCl in water was modelled, by solving the species conservation equations (Equation 3.3) over the computational flow domain, where $M_{f,i}$ is the mass fraction of species i:

$$\frac{\delta(\rho_f M_{f,i})}{\delta t} + \nabla \cdot (\rho_f \mathbf{v} M_{f,i}) = -\nabla \cdot \mathbf{J} \tag{3.3}$$

$\mathbf{J}$ is the diffusion flux and is defined by:

$$\mathbf{J} = -\rho_f D_i \nabla M_{f,i} \tag{3.4}$$

where D_i is the mass diffusion coefficient for the species i. The diffusion coefficient of $AgNO_3$ and KCl in water were obtained from the literature and were set to 1.7×10^{-5} m^2/s and 1.9×10^{-5} m^2/s, respectively (Harned, 1954). The working fluid was assumed to be incompressible and Newtonian, with a density of 1000 Kg/m^3 and a dynamic viscosity of 0.001 Pa·sec. The flow was assumed to be steady and laminar.

3.3.5.3 Solution Methods

The Semi-Implicit Method for Pressure-Linked Equations (SIMPLE) algorithm was employed for solving the governing equations. Using this method:

1. An approximation of the velocity field is obtained by solving the momentum equation. The pressure gradient term is calculated using the pressure distribution from the previous iteration or an initial guess

2. The pressure equation is formulated and solved in order to obtain the new pressure distribution

3. Velocities and pressures are corrected and a new set of conservative fluxes is calculated

3.3.5.4 Boundary Conditions

In all cases examined, channel walls were assumed to be rigid with a no-slip flow boundary condition imposed on each wall. A velocity boundary condition was applied at the inlet sections. Mean velocity values were selected in order to reproduce the experimental conditions. The outlet was set to a zero pressure boundary.

3.3.6 Experimental Setups

3.3.6.1 Microreactor Synthesis of Silver Nanoprisms

A schematic of the experimental setup is shown in Figure 3.6. The micro-reactor was placed on an inverted microscope (Olympus IX70) stage with a CCD camera (QICAM Fast, Qimage, Canada) coupled to the microscope for real time monitoring of the fluidics. The reagent were injected into the channel with syringe pumps. The outlet channel was connected to a 1 mL volume, 1 cm optical path flow cell for collection of UV-vis spectra. A schematic of the setup is shown in Figure 3.6.

In order to synthesise SNPs in a microreactor, a solution (A) of $AgNO_3$ (36 μM), TSCD (6.5 mM) and H_2O_2 (76 μM) and a solution (B) made of 200 μL $NaBH_4$ (0.1 M

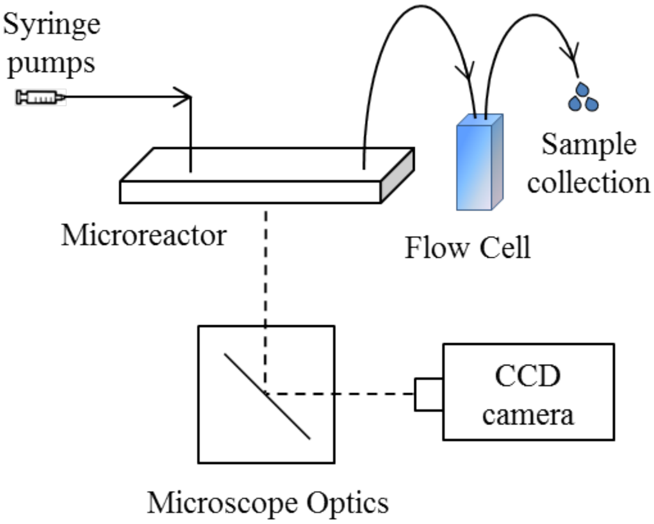

Figure 3.6: Experimental setup for the synthesis of SNPs within a microreactor

prepared according to Section 3.3.3.2) and 5.5 mL of MilliQ water were injected through the lateral channels (Figure 3.3, inlet C_3 for solution A and inlet C_1 for solution B) by means of syringe pumps. The solutions were injet with a flow rate V_1 for solution A and a flow rate V_3 for solution B. Additionally, MilliQ water was injected through inlet C_2 at a flow rate V_2 in order to i) dilute the two solutions from C_1 and C_3 to the desired concentration level, and ii) act as spacer between the two solution streams containing the reactants as they would otherwise react rapidly at the focused interface resulting in clogging or fouling at the channel junction. The solutions were injected at different total flow ratios (V_{tot}=V_1+V_2+V_3) (from 2.41 to 3.41 mL/h) by keeping the water flow constant at 1.41 mL/h.

3.3.6.2 Modification of SNPs with Halides Using a Microreactor Setup

A schematic of the experimental setup is shown in Figure 3.7. PTFE tubes with an internal diameter of 750 μm were employed for injecting the solution in the device (Microreactor 1). A PTFE tube with the same internal diameter and 1 m length was also used either as outlet or to connect it to a flow cell (10 mm optical path) for the in-line monitoring of absorbance.

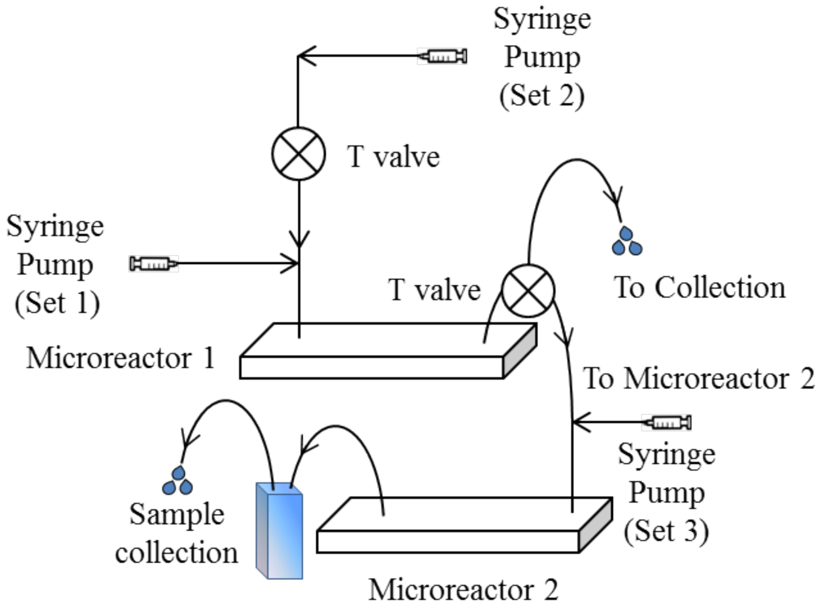

Figure 3.7: Experimental setup for the modification of SNPs with different halides ions (i.e. Cl^- and Br^-). Inlet of Microreactor 2 are named C_4, C_5 and C_6, corresponding to C_1, C_2 and C_3 in Microreactor 1, respectively. The outlet solution from Microreactor 1 can be either collected or transferred in Microreactor 2 for further modification with KBr.

The PTFE tube entering into C_3 was connected to a T-valve used for switching between a solution of silver nitrate, TSCD, H_2O_2 (Solution A) (OFF position) and a mixed solution of former reagents with KCl (Solution B) (ON position). The two solutions were injected in T_1 and T_2 (the right and left inlet of the valve), respectively, by Syringe Pump Set 2. The reagents mixed in the T-valve were then flushed in the channel through the inlet C_3. The outlet solution from Microreactor 1 was either collected in an Eppendorf vial or transferred via the central inlet into Microreactor 2 for the modification of the synthesised nanoparticles with KBr (which was introduced through the lateral channel of Microreactor2).

3.3.6.3 *In-situ* Microspectroscopy

A schematic of the experimental setup is shown in Figure 3.8.

The microreactor was placed on the microscope stage and the light source holder height was adjusted to launch the beam waist at its thinnest cross-section through the centre of the channel. A 60× microscope objective was used to focus and collect the maximum of the light passing through the microfluidic channel. A custom assembly of lenses and a sub multi assembly (SMA) fibre coupler were fixed in a concentric outlet tube which was attached to the side port through a C-mount adapter and directly connected to the spectroscopy detector with an optical fibre.

For absorbance measurements, 100 scans were taken and averaged for each measurement in order to reduce the background noise. Background spectra were collected at

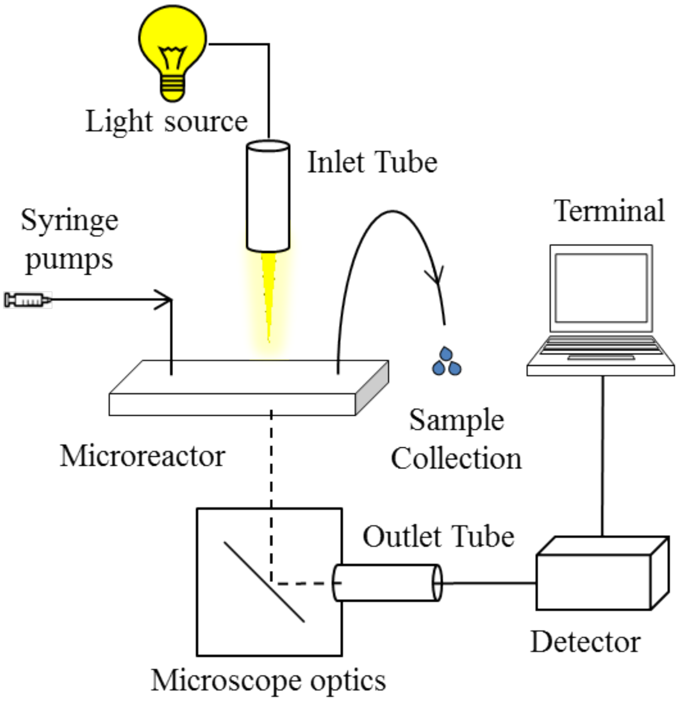

Figure 3.8: Experimental setup for microspectroscopy experiments

different points along the channel with water flowing through the reactor. The spectra were averaged in order to obtain a baseline valid for the entire length of the channel.

3.4 Synthesis of SNPs@SiO$_2$

Silica shells surrounding a metal nanoparticles can improve the stability of the metallic core (i.e. avoid aggregation), shift their absorbance (to higher wavelengths for SNPs) and allow for functional groups to be attached covalently to the particles surface. Section 3.4.4.1 reports the use of a modified Ströber method for the coating of SNPs with a silica shell. The method was adapted from the one proposed by Xue et al. (2007). This method was used as starting point not only for the coating the particles but also for attaching functional moieties such as thiol and allyl groups, as reported in Section 3.4.4.2 and Section 3.4.4.3, respectively.

The aims of these synthesis were to provide a reliable path for the production of stable SNPs. The presence of functional groups on their surface could also improving the dispersion of this material in an organic matrix. In particular, grafting the particles to polymer chains could avoid problems such as aggregation, which could negatively affect the problem of both the organic host and the inorganic filler.

3.4.1 Chemicals and Materials

Silver nitrate, trisodium citrate dihydrate (TSCD), tetraethyl orthosilicate (TEOS), allyltriethoxysilane (ATES), (3-mercaptopropyl)trimethoxysilane (MPTMS), (3-mercaptopropyl)triethoxysilane (MPTES),16- mercaptohexadecanoic acid (MHA), 5,5'-dithiobis(2-nitrobenzoic acid), fluorescein-5-maleimide and ethylenediaminetetraacetic acid (EDTA) were purchased from Sigma-Aldrich (UK). Sodium borohydride was purchased from Acros Organic (Belgium).

Hydrogen peroxide, and ethanol were purchased from Fisher Scientific (UK).

TEM grids (Carbon on Cu, 400 mesh) were purchased from Agar Scientific (UK).

3.4.2 Characterisation Techniques and Equipment

3.4.2.1 TEM

TEM images were collected using a FEI Technai12 transmission electron microscope, with an electrons acceleration of 120 kV and a tugsten filament source.

3.4.2.2 Energy Dispersive X-ray Spectroscopy (EDAX)

EDAX spectra were collected with a FEI Technai12 transmission electron microscope.

3.4.2.3 Spectroscopy

UV-vis-NIR spectra (300-900 nm) were collected using a Cary Varian 300 Bio using a quartz cell (10 mm optical path).

Fluorescence emission spectra were acquired using a Cary Eclipse fluorescence spectrophotometer using a 10 mm optical path quartz cell.

IR spectroscopy was performed on a Nicolet 380 FT-IR equipped with a diamond crystal Smart Orbit for ATR experiment.

3.4.3 Methods

3.4.3.1 Nanoparticles Purification

Nanoparticles can be purified according to Section 3.2.3.1. Nanoparticles coated with a silica shells can be dried in a vacuum concentrator and then redispersed in water or ethanol.

3.4.3.2 TEM Sample Preparation

TEM sample were prepared according to Section 3.2.3.2. TEM images were processed according to Section 3.2.3.3.

3.4.4 Syntheses

3.4.4.1 Coating of Silver Nanoprisms with SiO_2 ($SNPs@SiO_2$)

To 1 mL of Ag nanoprisms, 20 μL of a 1mM ethanolic solution of MHA (20 nmol, final concentration in solution 19.6 μM) was added. After vigorously shaking the sample for few seconds, it was left to rest for 3 minutes. The SNPs solution was then centrifuged at 13,200 rpm for 15 minutes and re-dispersed in an ethanolic 0.5 mM solution of TEOS, under gentle sonication. To the solution, 155 μL of a 20% v/v solution of dimethylamine (DMA) was added and then the sample was left to stir for 1 hour. The sample was then centrifuged at 13,200 rpm for 15 minutes and re-dispersed in EtOH under gentle sonication (2 times).

3.4.4.2 Functionalisation of $SNPs@SiO_2$ with Thiol Groups

To the solution of SNPs and TEOS, prepared following the procedure in Section 3.4.4.1, 57 μL of an ethanolic solution of MPTES (10 mM, final concentration in solution 0.5 mM) was added after 1 hour and then left to stir for another 2 hours. The solution was then centrifuged at 13,200 rpm for 15 minutes and re-dispersed in EtOH under gentle sonication (2 times). MPTMS may be used instead of MPTES under the same experimental conditions.

3.4.4.3 Functionalisation of SNPs@SiO$_2$ with Allyl Group

Regarding the functionalisation with allyltriethoxysilane, co-condensation of different ratios of TEOS and ATES (from 100% TEOS/0% ATES, to 0% TEOS/100% ATES) in the same experimental condition of Section 3.4.4.1 for the condensation with just tetraethyl orthosilicate were used in order to coat nanoparticles with a functionalised silica shell.

3.4.4.4 Ellman Test

To 250 μL of a nanoparticle solution of which the unknown thiol concentration must be determined, 2.5 mL of a sodium phosphate buffer solution, final pH 8, containing 1mM EDTA were added. 50 μL of 10 mM of 5,5'-dithiobis(2-nitrobenzoic acid)(Ellman reagent) were injected into the mixture, which was then left to react for 15 minutes, before analysing by UV-vis spectroscopy.

3.4.4.5 Thiol Group Labelling

Labelling of thiols on the particle surface was carried out by re-dispersing the functionalised nanoparticles in a sodium phosphate buffer, pH 7.5. 100 μL of a 5 mM solution of fluorescein-5-maleimide (excitation 492 nm, emission 515 nm) was added and the resulting solution was left overnight. Unreacted fluorescein-5-maleimide was removed by centrifugation and the precipitate was washed, two times, before spectroscopy measurement.

3.5 Synthesis of SNPs@SiO$_2$/PMMA composites

This Section reports the synthesis and characterisation of SNPs@SiO$_2$/PMMA composite materials. These where tested as potential energy saving glazing by depositing a thin layer onto a microscope slide and measuring the drop in transmittance in the vis-NIR region. The composite were prepared according to Section 3.5.4.1, employing a standard radical polymerisation.

The targets of this section were to synthesise composite materials with nanoparticles prepared according to Section 3.4.4.3 well dispersed in the polymeric matrix (PMMA), thanks to a "grafting through" approach.

3.5.1 Chemicals and Materials

Silver nitrate, trisodium citrate dihydrate (TSCD), methyl methacrylate (MMA, with $<$ 30ppm monomethyl ether of hydroquinone (MEHQ) as inhibitor), tetraethyl orthosilicate (TEOS), allyltriethoxysilane (ATES) and 16- mercaptohexadecanoic acid (MHA) were purchased from Sigma-Aldrich (UK). Sodium borohydride was purchased from Acros Organic (Belgium).

Azobisisobutyronitrile (AIBN) was purchase from Molekula (UK). Hydrogen peroxide, ethanol, methanol, toluene and chloroform were purchased from Fisher Scientific (UK). Poly(acrylic acid) (PAA), MW ∼50000, was purchased by Polyscience Europe (Germany).

TEM grids (Carbon on Cu, 400 mesh) were purchased from Agar Scientific (UK).

All the chemical were used as received with exception of methyl methacrylate (see Section 3.5.3.2) which was purified in order to remove the polymerisation inhibitor.

3.5.2 Characterisation Techniques and Equipment

3.5.2.1 TEM

TEM images were collected using a FEI Technai12 transmission electron microscope, with an electrons acceleration of 120 kV and a tugsten filament source.

3.5.2.2 Spectroscopy

UV-vis-NIR spectra (300-900 nm) were collected using a Cary Varian 300 Bio using a quartz cell (10 mm optical path).

UV-vis-NIR spectra (300-2500 nm) were collected using a Jasco V-570 Spectrophotometer. The glass slide with the deposited polymer film were attached directly to the cell holder with tape, with the polymer film facing the incoming beam.

IR spectroscopy was performed on a Nicolet 380 FT-IR equipped with a diamond crystal Smart Orbit for ATR experiment.

^{1}H Nuclear Magnetic Resonance (NMR) spectra were acquired with a 400 MHz Bruker DPX-400 spectrometer.

^{13}C Solid State NMR spectra were acquired wiht a 400MHz Bruker spectrometer.

3.5.2.3 Size Exclusion Chromatography (SEC)

Size exclusion chromatography was performed with a Viscotek GPCmax cromatograph coupled with a Water 410 differential refractive index detector, using a flow rate of 1mL/min.

3.5.2.4 Thermogravimetric Analysis (TGA)

Thermogravimetric analysis was performed using a Mettler Toledo TGA/SDTA 851e thermogravimetric analyser. The sample were analysed under flowing Ar (65 ml/min) using a temperature ramp rate of 10 ℃/min.

3.5.3 Methods

3.5.3.1 Nanoparticles Purification

Nanoparticles can be purified according to Section 3.2.3.1. Nanoparticles coated with a silica shells can be dried in a vacuum concentrator and then redispersed in water or ethanol.

3.5.3.2 MMA Purification

Before using MMA for the synthesis of SNPs@SiO_2/PMMA the polymerization inhibitor, MEHQ, must be removed. In order to efficiently remove the inhibitor, MMA must be washed ~5-6 times with a 0.5 M solution of NaOH. MMA was then dried with Na_2SO_4, filtered and then stored at +4 ℃.

3.5.3.3 Solid State NMR Sample Preparation

A solution of SNPs@SiO_2/PMMA composite was centrifuged and the surfactant was then removed. The precipitate was redisperse in chloroform and spun down again. This process was repeated until no more PMMA signals were observed in ^{1}H NMR. The precipitate was then redisperse in chloroform and then few drops of the solution were added inside the NMR rotor. The rotor is then placed in a vacuum concentrator for the solvent to evaporate.

3.5.3.4 TEM Sample Preparation

TEM sample were prepared according to Section 3.2.3.2.

To prepare TEM samples of the spun polymer films a different approach was adopted, i.e. a self-standing polymer film was prepared. To prepare the self-standing polymeric film, a 5% w/v solution of polyacrylic acid was spun onto a glass of slide clean according to Section 3.5.3.5 at 3,000 rpm for 15 seconds. The film was then dried on a heating plate at 120 ℃ for 2 minutes.

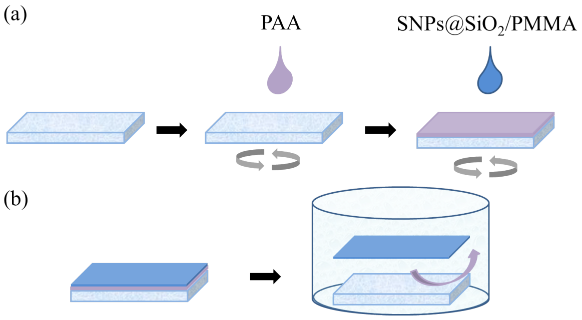

Figure 3.9: Preparation of self-standing films of SNPs@SiO_2/PMMA to be deposited on TEM grids. Once a PAA layer is deposited on a clean glass slide, SNPs@SiO_2/PMMA is spun on it and let dry (Figure 3.9a). The coated slides were then dipped in water until complete dissolution of the PAA layers and complete detachment of the SNPs@SiO_2/PMMA self-standing film (Figure 3.9a).

This process offers a smooth surface (Root Mean Square (RMS) roughness of 0.28 nm, according to Linder et al. (2005)). SNPs@SiO_2/PMMA nanocomposite films were then spun coated on the PAA-coated glass slide from a toluene solution and then dried in air. Once the film was dry, the slide was dipped in water until complete dissolution of the PAA layer (see Figure 3.9). The self-standing polymer films floating on the water surface it can be then directly collected on the TEM grids.

TEM images were processed according to Section 3.2.3.3.

3.5.3.5 Glass Slide Cleaning

Microscope slides (1 cm×1 cm) were washed with isopropanol under sonication for 10 minutes. The slides are then rinsed with ethanol and MilliQ water and then dried overnight in the oven.

3.5.4 Synthesis

3.5.4.1 Synthesis of SNPs@SiO_2/PMMA Composites with Different Initiator Percentage

To ∼0.75 mL of MMA purified according to Section 3.5.3.2 a same amount of toluene was added, along with different percentage of AIBN (1, 2, 4 and 6% w/w). To this solution, different percentages of silver nanoprisms (0, 0.1, 0.2 and 0.5% w/w) dispersed in 200 mL of EtOH were mixed with the monomer solution. The flask was wrapped in aluminium foil and degassed with Ar in order to remove O_2 from the solution. After 30 minutes the aluminium foil was removed and the solution irradiated with a UV lamp (100 W, λ=365 nm). After two hours, the solution was added dropwise into ice cold methanol for the polymer to precipitate. The polymer was then filtered and washed several times with cold methanol to remove unreacted monomer and toluene.

Chapter 4

Synthesis, Modification and Characterisation of Silver Nanoprisms

Contents

4.1 Introduction

Synthesis of anisotropically shaped crystals such as rods (Nikoobakht and El-Sayed, 2003), cubes (Sherry et al., 2005), prisms (Sun and Xia, 2003) or more complex geometries such as multipods (Chen et al., 2003) attracted much attention. Compared to spherical particles these materials show more complex electronic and optical properties which could be used for improving a wide range of application such as SERS (Surface Enhanced Raman Scattering) (Mulvihill et al., 2010), bio-labeling (Kabashin et al., 2009), optics (Torres et al., 2007) and photovoltaics (Kulkarni et al., 2010). Furthermore, their preparation has been a driving force in the investigation of the shape-related properties and the mechanism ruling the assembly of metal ions in such different geometries (Hao et al., 2004). Among anisotropic particles, rods (Dai et al., 1995; Yu et al., 1997) were the first to attract considerable attention due to the good controllability and reproducibility of their synthesis. In contrast to spherical particles, the UV-vis spectrum of these materials shows two absorbance bands in the visible region corresponding to two different directions in which the electron cloud can be polarized (i.e. the two axis of the rod), contrary to the single sharp peak usually shown by silver and gold nanospheres.

Along with rods other two classes of anisotropic nanomaterial have also been studied systematically in the last decade, i) "platonic solid" shaped nanoparticles and ii) triangular nanoprisms, as they show a high-yield and reproducible synthesis. In particular, the latter class (both of gold and silver) has recently found applications in several fields, such as catalysis (Yu et al., 1997), optical bandpass (Torres et al., 2007), SERS application (Cui et al., 2008) and fluorescence enhancer (Munechika et al., 2010). Several examples have been reported for preparing metal triangular nanoprisms, but batch chemical methods are the most employed. Jin et al. (2001) were the first to propose a reliable and reproducible synthesis of these colloids based on the photoconversion of silver nanospheres into triangular prisms in the presence of trisodium citrate and bis(p-sulfonatophenyl)phenylphospine dihydrate dipotassium salt. When the solution of spherical nanoparticles is irradiated with a 40 W fluorescent light, its colour starts to slowly change from a bright yellow to a dark blue: after 70 hours no more changes were observed and stable triangular colloids were formed. Similarly, Sun and Xia (2003) proposed the growth of nanoprisms from small silver nanospheres by irradiation of a 20 W halogen lamp in the presence of PVP (poly(vinylpyrrolidone)) and trisodium citrate for 40 hours. Millstone et al. (2006) employed a seed-mediated synthesis for the preparation of triangular gold nanoparticles. By adding different amounts of gold seeds to a solution of a metal precursor (i.e. $HAuCl_4{\cdot}3H_2O$) a mild reducing agent (i.e. ascorbic acid), NaOH and CTAB (as surfactant) they showed the efficiency of this method in controlling the edge length, and therefore, the possibility of finely tuning the opto-electronic properties of these colloids.

Aherne et al. (2008) employed a similar method for the synthesis of SNPs by growing them from silver seeds added to a solution of silver nitrate in the presence of poly(sodium styrenesulphonate) (PSSS) and ascorbic acid as the reducing agent.

Compared to the methods proposed by Jin et al. (2001) and Sun and Xia (2003), in which the change in nanoparticle geometry was promoted by light irradiation, the kinetics of the chemical induced seed mediated growth was faster and makes this method more appealing for industrial application. Even if the reaction proposed by Aherne et al. (2008) was faster and showed a good monodispersity, the requirement of a two-step reaction for the formation of such particles could be a limitation in their large scale production. For this reason the investigation of a single step method for preparing silver nanoprisms has been a hot topic over the last few years. In particular, Pastoriza-Santos and Liz-Marzán (2002) proposed the synthesis of silver nanoprisms in DMF in the presence of PVP; DMF was used both as solvent and as reducing agent when it was heated up to its boiling point. The main disadvantage of this method was the small grade of monodispersity which could be achieved by this method, as proven by the broad peaks of the SPR in the visible spectra. This polydispersion, in terms of both size and shape, is confirmed by TEM microscopy which shows the simultaneous presence of spheres and triangles.

A more reliable method for producing nanoprisms of silver was proposed by Métraux and Mirkin (2005), who investigated the formation of SNPs in the the presence of trisodium citrate dihydrate, PVP, $NaBH_4$ and H_2O_2 without the need of heating. By changing the amount of the reducing agent (i.e. $NaBH_4$) and H_2O_2 the final dimensions of the nanoparticles can be tuned (both in terms of edge length and thickness). The geometrical parameters of SNPs can also be modified by adding ions to the precursor solution either before or after the formation of nanoparticles. Among these ions, halide anions, such as Cl^-, Br^- or I^- have been extensively employed for modifying both the size and shape of noble metal nanoparticles (Millstone et al., 2008; Wiley et al., 2004; Zhao et al., 2012). Particularly, Br^- ions are able to round the less stable faces of silver nanoparticles at low concentrations (i.e. the tips) and to drive their growth to three dimensional shapes such as triangular bipyramids and cubes at higher concentrations if added to preformed silver nanoparticles (Cathcart et al., 2009). Cl^- ions, on the other hand, can lead to the growth of silver colloids if added to the precursors solution, but can also etch SNPs edges if added once the prisms have formed (An et al., 2008), acting in a similar way to the bromide ions. Iodine (An et al., 2008) showed a similar behaviour to that of Br^- but, as its effect is difficult to control, it is not commonly employed for tuning the geometrical properties of SNPs.

Not only anions were used in the modification of silver nanoparticles but also cations. Contrary to the mechanisms that rule the sculpting effect of halide ions the modification of nanoparticles geometry is not due to precipitation and complexation of silver ions and atoms by ions. The driving force in this process is the galvanic replacement of the nanoparticle metal by ions of another metal added into solution. This process usually leads to monometallic or bimetallic hollow structures as reported for the formation of Pd-Ag (Chen et al., 2005), Pt-Ag (Chen et al., 2005) or Pd-Au (Teng et al., 2008) nanostructures.

In this Chapter the formation of silver nanoprisms based on the protocol proposed by Métraux and Mirkin (2005) has been studied and its reproducibility has been evaluated by mean of UV-vis spectroscopy and TEM microscopy. Particularly, effects of PVP on the final physical properties of the nanoparticles has been investigated and compared with particles synthesised without it. Furthermore, modification of SNPs size via Cl^- induced growth and the formation of triangular hollow alloys of silver and gold have been studied in order to tune the optical properties of silver nanoprisms. In particular, increasing the size and/or creating a hollow structure can move the in-plane dipole to lower energies. Different concentrations of both Cl^- and Au^{3+} have been employed and the formed particles have been characterised with both UV-vis spectroscopy and transmission electron microscopy.

4.2 Results and Discussion

4.2.1 Batch Synthesis of Silver Nanoprisms

4.2.1.1 Reaction Mechanism and Flat Triangular Prisms Formation

Single step production of SNPs as reported by Métraux involves i) the rapid reduction of silver ions by $NaBH_4$ resulting in the formation of quasi-spherical seed which ii) are etched by oxidation of silver by H_2O_2, as reported in Reaction 4.1 and Reaction 4.2:

$$\mathrm{NaBH_4 + 8\,AgNO_3 + 4\,H_2O \longrightarrow Na[B(OH)_4] + 8\,Ag^{(0)} + 8\,HNO_3} \tag{4.1}$$

$$\mathrm{2\,Ag^{(0)} + H_2O_2 + 2\,H^+ \longrightarrow 2\,Ag^+ + 2\,H_2O} \tag{4.2}$$

It is notable to observe that these two reactions show different kinetics, mainly due to the negative charge present on BH_4^-, which reacts with the positively charged metal ions faster than H_2O_2, which in water is stable in a neutral form. This difference in reactivity is such that the reduction of the metallic ions is instantaneous, while the further growth caused by hydrogen peroxide can take up to half an hour (when PVP is present). The reaction can be easily monitored by visual inspection due to the changing of colouration of the reagent solution. As soon as sodium borohydride is added, the solution turns yellow and then the colouration gradually changes (due to the changing in the geometry of particles in solution) until a blue colouration is reached.

Citrate ions play a vital role in the synthesis of triangular shaped particles as they act as a stabilising agent, but also as a buffer for neutralizing the nitric acid developed by the reduction of the silver ions by $NaBH_4$, as shown in Reaction 4.3.

$$\mathrm{Na_3C_3H_5O(COO)_3 + HNO_3 \longrightarrow Na_2HC_3H_5(COO)_3 + NaNO_3} \tag{4.3}$$

TSCD has been largely employed in the synthesis of different metal nanoparticles as an electrostatic stabiliser. Regarding silver nanoparticles stabilisation with TSCD, *ab initio* calculation showed that TSCD binds stronger to the (111) faces of the nanocrystals than to the (100) faces. This selective coordination is due to the matching between the geometries of the citrate ions and the silver crystal lattice (Aherne et al., 2008; Sun et al., 2003). As the (111) faces show a triangular symmetry, they are expected to match the threefold symmetry of the trisodium citrate ions more than the square symmetry present on to the 100 faces. Due to this matching, it has been shown that citrate ions bind to (111) faces with all their carboxylic groups, while the (100) faces are bonded with just two of them (the hydroxyl group does not binds to any face due to its short length) and this results in a higher stability of the (111) faces over the (100) faces. This difference in stability is one of the driving forces in the synthesis of anisotropic particles, such as triangular nanoprisms. The formed seeds undergo oxidation and etching by H_2O_2 which result in the destruction of the least stable geometry, while the most stable one is left as the product; in this particular case only triangles, truncated triangles and hexagons are observed.

The presence of planar defects in the nanocrystals' structure is also an important factor in the selective growth of SNPs and in particular it helps to explain why the particles tend to grow in two dimensions rather than three. Aherne et al. (2008) tried to explain this behaviour by studying the presence of defects in the lamellar structure of stacked (111) planes. Particularly, those defects result in the presence of hcp layers between the characteristic fcc layers of silver. As the hcp structure is not native in silver crystals, these layers will be less stable and therefore more reactive towards the growth process. Considering the silver nanoplates as shown in Figure 4.1, where a hcp layer is sandwiched between two fcc layers of differing size, it is possible to understand the reason of the growth to a triangular final shape: as the layers of fcc structure have different size, it is clear that three of them will be less stable ((100) bigger faces plus hcp layer, U) while three of them will be more stable ((111) bigger faces, S). As shown by the arrow in Figure 4.1, the U faces are the ones that grow faster than the others and this leads to a final triangular shape.

PVP is a polymer that is able to coordinate to the nanoparticles with the lone pairs presents in the pending group of the polymeric chain (i.e. 2-pyrrolidone) particularly with the carbonyl groups, which is preferred to the nitrogen (Jiang et al., 2004; Mdluli et al., 2011). Even if PVP preferentially binds to the (111) face of silver seeds, as citrate does, its coordination is not responsible for the formation of the triangular shaped as proven by the fact that nanotriangles cannot be formed in the absence of TSCD. Although PVP does not have an effect on the final shape, its addition can influence the kinetics of the transformation from isotropic (i.e. spheres) to anisotropic nanoparticles as confirmed by the longer time required for the particle solution to change its colour from yellow to blue.

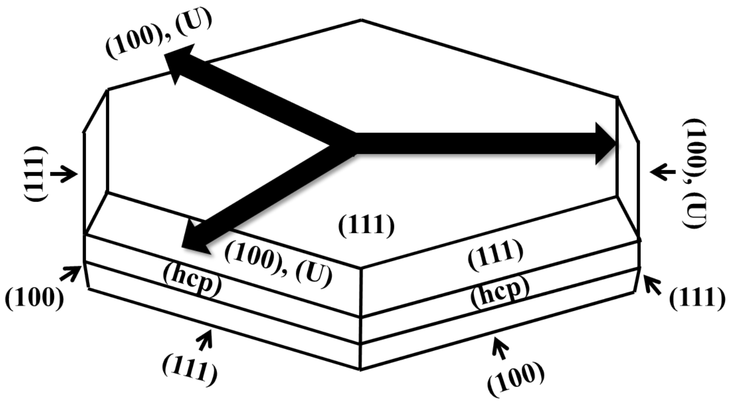

Figure 4.1: The different faces of the crystal and the hcp layers are shown. Arrows indicate the different growth directions of the seeds. Figure re-adapted from Aherne et al. (2008) with permission.

4.2.1.2 Optical Properties of Silver Nanoprisms

As for other metal nanoparticles, optical properties are a direct reflection of size and shape (and their monodispersion) of silver nanoprisms. In the case of spherical nanoparticles the interpretation of their visible spectra and their correlation to the geometry of the colloid in solution is quite simple; their optical properties depend on such few parameters that are commonly employed to have roughly estimation of their size and their concentration. However, for anisotropic particles, this linking is more complicated due to the more complex shape, for which the more parameters (both geometrical and electronic) must be taken in account for calculating the final optical properties. .

Furthermore, compared to spheres, SNPs anisotropically interact with the light and therefore final optical properties are affected from the direction from which it interacts with them. This results in more than one absorbance peak in the visible spectra. Regarding silver nanoprisms, their optical properties have been extensively studied in recent years. Particularly, Kelly et al. (2003) described the optical properties of silver triangular nanoprisms by means of DDA (Discrete Dipole Approximation) calculation and identified four typical peaks in the optical spectra of SNPs. In particular, two peaks were identified around 670 and 460 nm, corresponding to the in-plane polarization (dipole and quadrupole respectively) and other two peaks at 430 and 335 due to the out of plane polarization (dipole and quadrupole respectively). These peaks have been calculated from a truncated prism (10 nm snips) with an edge length of 100 nm and a thickness of 16 nm, to resemble the presence of triangles and truncated triangles in a common nanoprisms solution.

Yang et al. (2009), on the other hand, studied the optical properties of triangles with high aspect ratio (calculated as (Edge Length)/ (Thickness)) achieving similar results. Although it is complex to use the visible spectra of triangular prisms to obtain information about nanoparticle concentration in solution, they are still useful to get a good estimation of the quality of the final product (in terms of size and shape distribution) and of the average size as a sharp peak (the in-plane dipole is commonly monitored, being the most intense) at low energies is an indicator of good monodispersity of the prepared colloid. Regarding the spectral position/size correlation, Shuford et al. (2005) calculated the dependence of the spectral position in term of edge length (L) and thickness (Tk), as shown in Equation 4.1.

$$\lambda_{max} = 33.8\frac{L}{Tk} + 418.8\ [nm] \tag{4.1}$$

Several values of the maxima of the dipole in-plane absorbance and of the FWHM of different sample are shown in Figure 4.2a and Figure 4.2b respectively, in order to evaluate the reproducibility of the synthesised nanoparticles. As can be seen in Figure 4.2, nanoparticles prepared in the presence of PVP generally show the in-plane dipole peak at higher wavelength compared to that prepared without PVP.

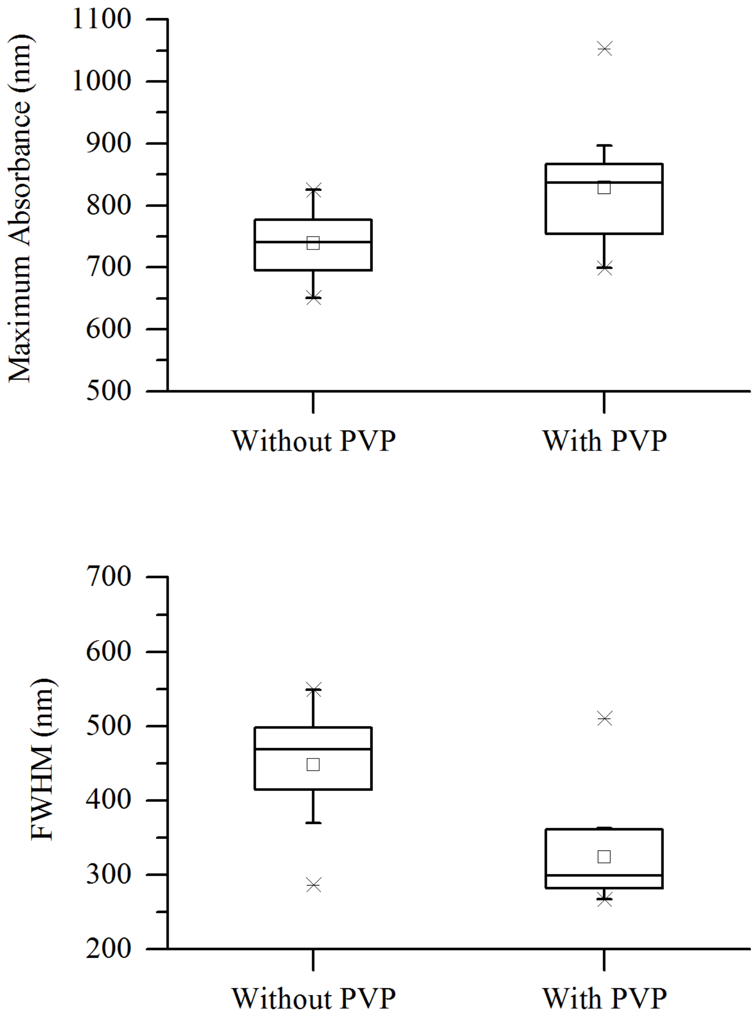

Figure 4.2: Maxima (Figure 4.2a) and FWHM (Figure 4.2b) for different samples prepared without (▼) and with (■) PVP. The spectra from which this data are extrapolated are shown in Appendix A.1.

Regarding the broadness of the peak, silver nanoprisms stabilised with both the citrate and PVP, show a sharper absorbance peak due to the in-plane dipole surface plasmon resonance, and this is usually a sign of a narrower distribution in the particles geometry. In Figure 4.3, two typical spectra for nanoparticles prepared with and without PVP are shown.

As nanoparticles synthesised with PVP generally show a more red-shifted peak of the dipole in plane resonance, experiments were carried out to observe how its presence, and in particular its different concentration in solution, can affect the final spectral properties. In this regards, no change in the spectral position of silver nanoparticles have been reported by (Métraux and Mirkin, 2005), but only an increased stability of the so-formed colloid. In the present study the four different samples were prepared by reducing the volume of the precursor solutions (i.e. the solutions of $AgNO_3$, TSCD, $NaBH_4$ and H_2O_2) and increasing the 0.7 mM PVP solution volume in order to change just the

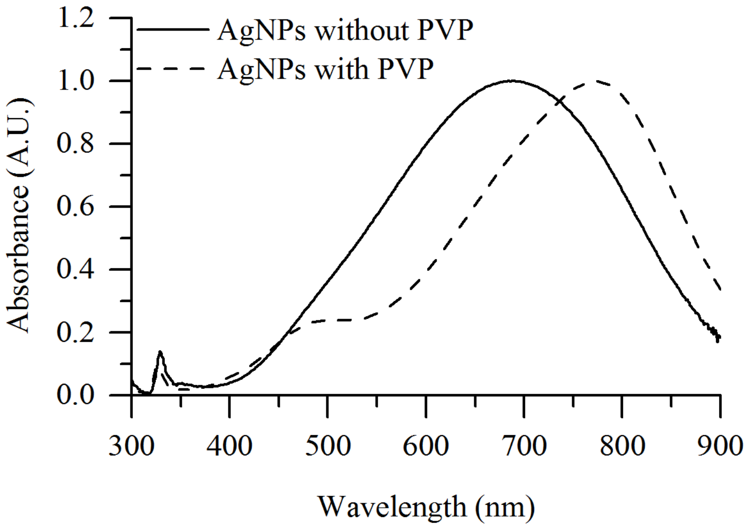

Figure 4.3: The different faces of the crystal and the hcp layers are shown. Arrows indicate the different growth directions of the seeds. Figure re-adapted from Millstone et al. (2006).

polymer concentration. The experimental conditions for testing different concentration of PVP are reported in Table 4.1.

Sample	**Reagents Solution Volume [mL]**	**PVP Solution Volume [mL]**	**[PVP][mM]**
A	5.25	0	0
B	4.95	0.3	0.04
C	4.65	0.6	0.08
D	4.35	0.9	0.12

Table 4.1: Four sets of different experimental conditions for the results shown in Figure 4.4. The volume of the reagents solution (excluding PVP) was changed in order to keep their concentration constant.

The polymer solution was added to the solution of silver nitrate, trisodium citrate, and hydrogen peroxide and stirred for 5 minutes after which a solution of sodium borohydride was rapidly injected. The reacting solution was stirred vigorously until no further change in colouration was observed. As expected, the reaction time increased along with the concentration of PVP due to the extra stabilisation given by the presence of the polymer.

Figure 4.4 shows the effect of different concentrations of poly(vinylpyrrolidone). As it is seen, the spectra of sample B ([PVP]=0.04 mM) and of sample C ([PVP]=0.08 mM) show a red-shift of the in-plane dipole resonance. Particularly, it is possible to observe a neat change in spectral position for B and C compared to A. Regarding the difference between B and C, it is possible to see how the latter is still more red-shifted than the former, marking a trend in the relation between the spectral position and the concentration of the stabilising agent. Along with this change in optical properties

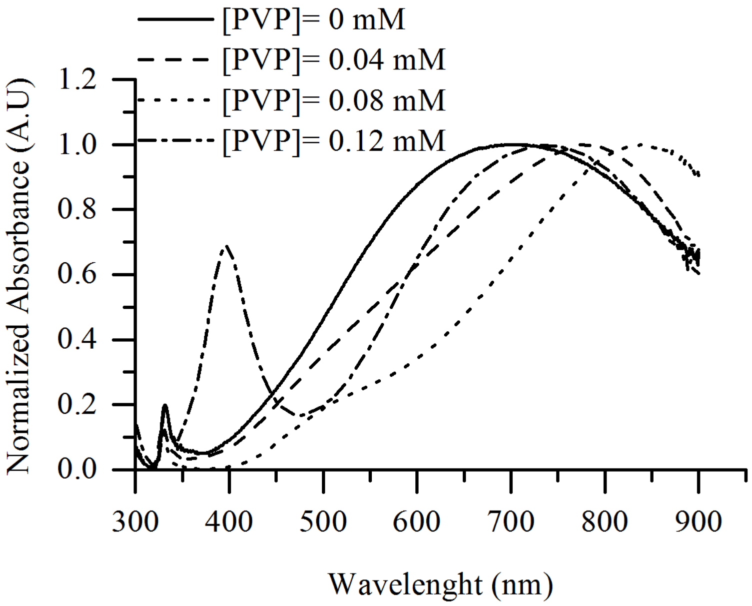

Figure 4.4: Effect of different concentration of PVP on optical properties of SNPs.

changing in the shape of the peaks can also be observed. Particularly, it is possible to observe a sharpening of the peak compared to the one synthesised without extra stabilisation due to the polymer. Furthermore, the presence of a small shoulder between (approximately) 430 and 470 nm could be noticed. This shoulder is likely due to the simultaneous presence of the peaks of the out-of-plane dipole resonance and the in-plane quadrupole resonance, respectively. These peaks are not always visible as the in-plane dipole resonance peak (i.e. the peak at lower energy) shows a notable broadness if the nanoprisms are not homogeneous in size and shape and this broad peak can overtake these smaller ones.

When the concentration of PVP increases up to 0.12 mM (Sample D), the optical spectra of silver nanoparticles show a sharp peak around 400 nm and no shift of the in-plane dipole band. The peak ~400 nm can be attributed to the presence of an high number of silver nanospheres along with nanoprisms in solution, due to the high stabilisation of spherical colloids that are not able to undergo the transformation from sphere to prisms. This phenomenon has not previously been observed by Métraux and Mirkin (2005) as they limited their research to concentrations of PVP not higher than ~0.1 mM.

4.2.2 Size and Shape Modification of SNPs

As reported in Section 2.5.2, optical properties of metal nanoparticles can be affected by different parameters. Their size, for example, can affect the spectral position of their absorbance peak. SNPs λ_{max}, for example, shifts to higher wavelength as the edge length of the prisms increases. Shape, on the other hand, not only affect the λ_{max} but also the number of peaks due to the resonance of both dipoles and multipoles (quadrupoles) with the interacting light. Shifting SNPs' λ_{max} to higher wavelength (NIR) can be achieved both way, as reported in the following Sections.

4.2.2.1 Effect of Cl$^-$ on Silver Nanoprisms Size

Halide ions can interact with the metal nuclei of silver nanoparticles and modify their optical properties by changing their geometry. In particular, previous studies reported that chloride ions generally led to a size increase of silver nanoprisms, while the addition of bromide ions reduced their size and led to a modification of the geometry, converting them from prisms to other three-dimensional structures (Cathcart et al., 2009). It is understood that the halides interaction with the core of nanoparticles follow two different patterns, depending on which of them is employed and at which point of the reaction it is added (i.e. before or after the reduction of the metal precursors). Particularly, using chloride ions, two opposite effects can be achieved due to the different behaviour of Cl$^-$ ions towards Ag$^{(0)}$ atoms; i) at high concentration the chloride ions act as complexing agent and they can remove the metal atoms form the nanoclusters while ii) at low concentration, on the other hand, chloride ions bind with the silver cations in solution. The latter interaction is particularly influential during the formation of the nanoparticles, where chloride ions can exchange with the counter ions of the silver precursor (see Equation 4.4). This leads to the precipitation of silver due to the lower solubility constant (K$_s$) of AgCl compared to that of the inorganic precursors employed for preparing the nanocolloids.

$$\mathrm{AgNO_3(K_s{=}5.86\times10^{-4}) + KCl \longrightarrow AgCl(K_s{=}1.56\times10^{-10}) + KNO_3} \qquad (4.4)$$

As AgCl is poorly soluble in water, Ag$^+$ concentration in solution is massively reduced. Due to its lower concentration, the number of nuclei formed during the reduction of Ag$^+$ is drastically reduced. When AgCl finally dissolves, the reduced Ag$^+$ released in solution grows on the surface of the preformed nuclei. As the nuclei concentration in solution is lower compared to reactions carried out without chloride ions, the final nanoparticle dimensions (i.e. the triangles edges) are larger.

In order to observe the effect of different concentration of chloride ions on the final optical properties of silver nanoprisms, different volumes of KCl (0.05 M) were added to the solution of silver nitrate, trisodium citrate and hydrogen peroxide before adding the reducing agent. The first attempt was tried by adding 15 μL of potassium chloride to 5.312 mL of the reagents. The final concentration of KCl was chosen to give the maximum red-shift of the plasmonic band of silver nanoprisms. According to the literature this can be achieved when concentration of potassium chloride is ~0.15 mM Cathcart et al. (2009). To observe the reliability four samples were prepared and UV-vis

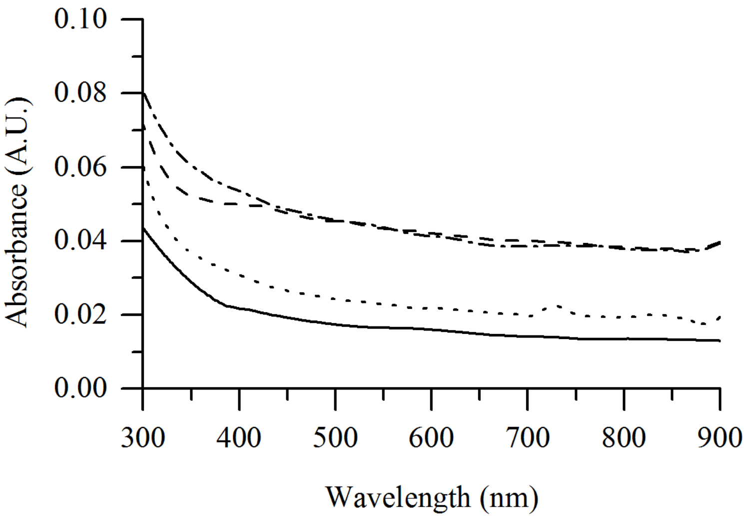

Figure 4.5: UV-vis absorbance spectra for samples prepared with different volumes of KCl are shown. The small peak around 700 nm present in the spectra of sample B it is due to noise and not because of nanoparticles surface plasmon resonance.

spectra were collected. As it is shown in Figure 4.5 the collected spectra do not show any absorbance.

Particularly, the intense dipole in-plane resonance present at low energies vanishes completely from the spectra in the region between 300 and 900 nm and the spectra show no possible trend that can suggest the presence of any peaks at higher energy (i.e. the spectra are completely flat). At a higher energy, the absorbance spectra show a very steep slope, starting at ∼600 nm, likely due to the high scattering of the solution which is possible to observe also by visual inspection, as the solutions appears opalescent. This scattering is due to the excessive formation of AgCl in the solutions. This precipitation is also the possible reason for the lack of absorbance in the spectra, as no nanoparticles are formed.

In order to tailor the concentration of KCl so that no precipitation of silver chloride was observed, different volumes of KCl (0.05 M) were added to the reagents solutions, as reported in Table 4.2

Sample	**KCl 0.05 M [μL]**	**Final [KCl] [mM]**
A	5	0.047
B	10	0.094
C	15	0.140
D	20	0.187

Table 4.2: Volumes of 0.05 M solution of KCl used for samples reported in Figure 4.6

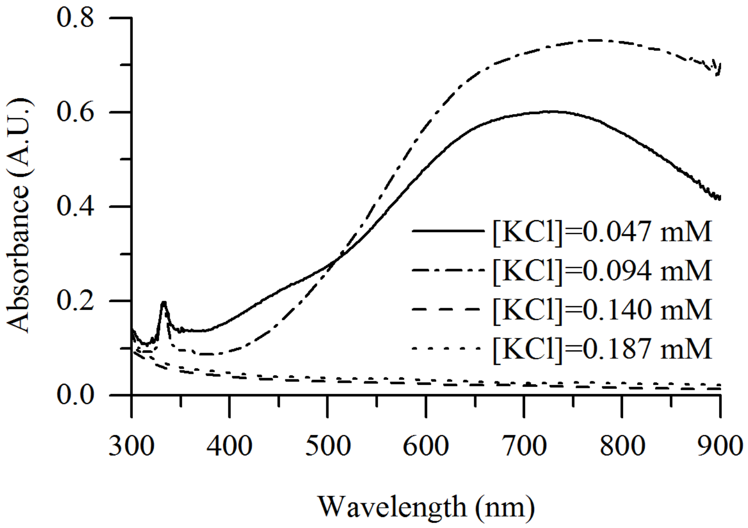

Figure 4.6: Absorbance spectra for samples prepared with different volume of KCl (0.05 M), as reported in Table 4.2.

As can be seen in Figure 4.6, by reducing the concentration of potassium chloride in solution, the absorbance spectra show an intense peak in the NIR region. Particularly, both Samples A (5 μL) and B (10 μL) show an intense peak around 720 nm and around 770 nm, respectively. As also noticed, the absorbance spectra are very broad with comparison to the spectra prepared in the absence of chloride ions presented in Figure 4.3. The spectra of samples C (15 μL) and D (20 μL), on the other hand, do not show any peaks. Intermediate concentration of KCl was used in order to determine if there was any linear relation between the concentration of Cl^- and the optical response of nanoparticles. The concentrations used are reported in Table 4.3.

Sample	**KCl 0.05 M [μL]**	**Final [KCl] [μM]**
A	11	103.3
B	12	112.7
C	13	122.1
D	14	133.4

Table 4.3: Volumes of 0.05 M solution of KCl added to a nanoparticles solution

The general trend of the spectral maxima for different concentration is reported in Figure 4.7. As it is possible to see, Samples A and B usually show absorbance (usually above 900 nm) at higher wavelength than Samples C and Sample D, but sometimes a complete disappearance of the SPR is observed.

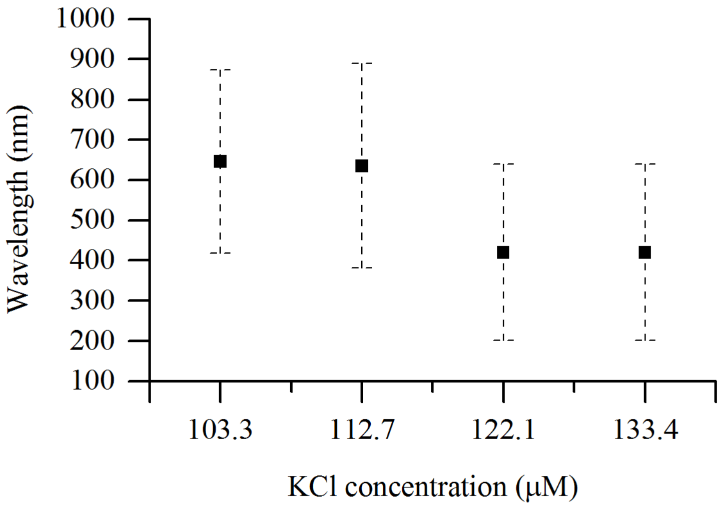

Figure 4.7: Average $\lambda_{(max)}$ of samples prepared with different concentrations of KCl, as reported in Table 4.3. The spectra of modified silver nanoparticles used for calculating these samples are reported in Appendix A.3

4.2.2.2 Effect of Au^{3+} Ions on Silver Nanoparticles Shape

Not only can the presence of halide ions modify the final shape of the nanocrystal, but also the presence of other noble metal ions such as gold, can affect the shape of silver nanoparticles by subtracting silver atoms from the original nanoparticles structure. The driving force for this process in (called galvanic replacement) is the oxidation of silver atoms by gold ions in the solution as illustrated in Equation 4.5:

$$3\,Ag^{(0)} + Au^{3+} \longrightarrow 3\,Ag^{+} + Au^{(0)} \tag{4.5}$$

Due to the higher reduction potential of gold ions (0.99 V_{SHE} for the redox couple $AuCl_4^-/Au$) compared to the one of silver (0.8 V_{SHE} for Ag^+/Ag) the atoms in the nanocluster return back to the solution as ions. Gold ions on the other hand start to deposit on the surface of the former particles until no further oxidation of silver is possible. In order to study the effect of the galvanic replacement on the final optical properties of SNPs, different amounts of a 10 mM $HAuCl_4$ solution were added to 1 mL of silver nanoparticles solution prepared without PVP. The volumes of gold solution added are reported in Table 4.4.

Sample	**Volume of $HAuCl_4$ 10 mM solution [mL]**	**Final [Au^{3+}] [mM]**
A	0.01	0.09
B	0.02	0.19
C	0.04	0.38
D	0.06	0.56
E	0.08	0.74

Table 4.4: Different volumes of $HAuCl_4$ (10 mM) employed for the modification of silver nanoprisms

As soon as the gold solution was added, the colouration of the silver colloid solutions vanished in all the samples. Leaving the samples to rest overnight in the dark, the colour of the solution changed again and it was possible to observe the appearance of a peak around ~580 nm (see Figure 4.8). Along with this peak it was possible to observe a steep slope in the ultraviolet region. As the optical spectra do not show any of the optical properties of the silver nanoprisms, lower concentrations of gold have been employed to better understand the effect of Au^{3+} on silver colloid.

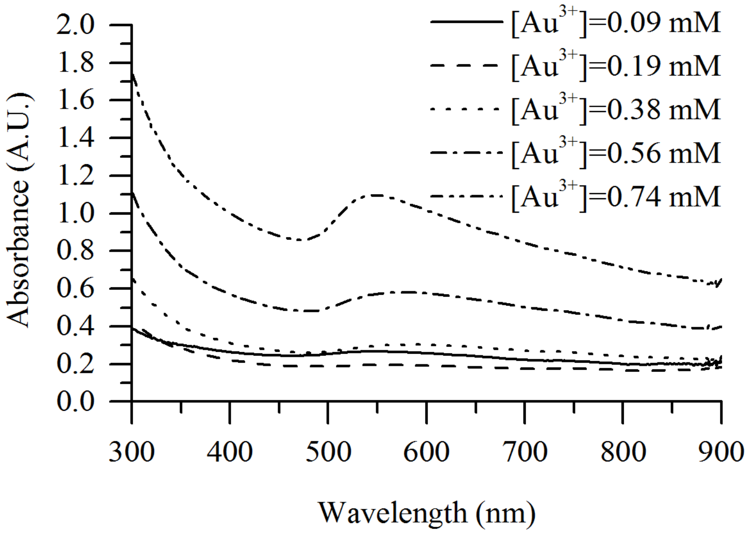

Figure 4.8: UV-vis spectra of AuAg nanohollows formed by adding a solution of $HAuCl_4$ (see Table 4.4).

Different volumes of 10 μM $HAuCl_4$ solution were added to 1 mL of silver nanoparticles solution, as reported in Table 4.5. As shown in Figure 4.9, by reducing the starting concentration of the gold solution, a more moderate effect is observed on the UV-vis spectra of SNPs. As $[Au^{3+}]$ increases, the in-plane dipole resonance shifts to higher wavelength; along with the shift in spectral position also a broadening of the peak is observed.

Sample	**Volume of $HAuCl_4$ 10 μM solution [mL]**	**Final $[Au^{3+}]$ [μM]**
A	0.01	0.09
B	0.02	0.19
C	0.04	0.38
D	0.06	0.56
E	0.08	0.74

Table 4.5: Different volumes of $HAuCl_4$ (10 μM) employed for the modification of silver nanoprisms.

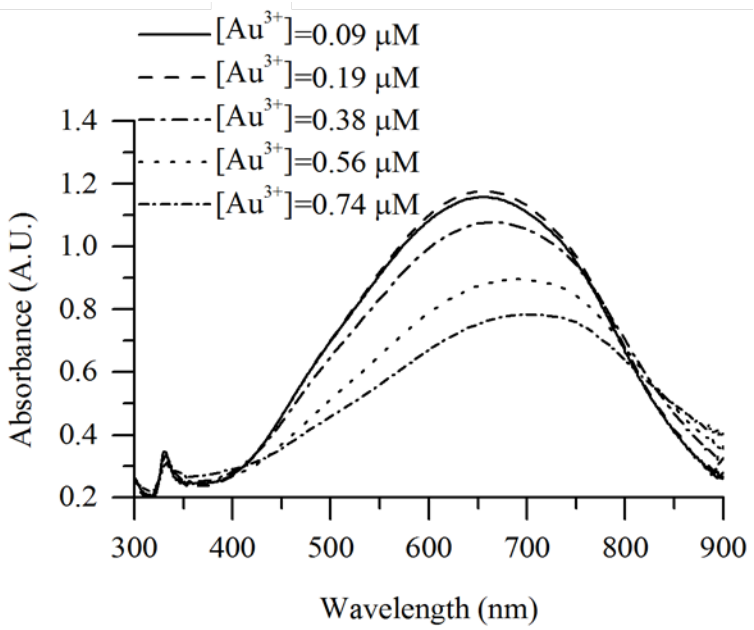

Figure 4.9: SPR decrease of silver nanoparticles prepared with different volumes of $HAuCl_4$, as reported in Table 4.5.

The concentration of the gold was further increased and the same experimental conditions were applied both with and without PVP added during the synthesis of silver nanoprisms, as reported in Table 4.6.

As soon as the solutions were added to the different samples it was possible to observe the vanishing of colouration. Depending on the presence of PVP, the nanoparticles showed a different shape after the addition of gold. The spectra in Figure 4.10a,

Sample	**Volume of $\mathbf{HAuCl_4}$ 10 μM solution [μL]**	**Final [$\mathbf{Au^{3+}}$] [mM]**
$\mathrm{A/A_{PVP}}$	250	0.125
$\mathrm{B/B_{PVP}}$	250	0.200
$\mathrm{A/A_{PVP}}$	250	0.300

Table 4.6: Different concentration of Au^{3+} (same volume) added to a solution of nanoparticles prepared without (samples A-C) and with PVP (samples $\mathrm{A_{PVP}}$-$\mathrm{C_{PVP}}$); the spectra of these samples are shown in Figure 4.10a and Figure 4.10b respectively.

which are from nanoparticles prepared without PVP, do not show a particular trend as the concentration of gold increases.

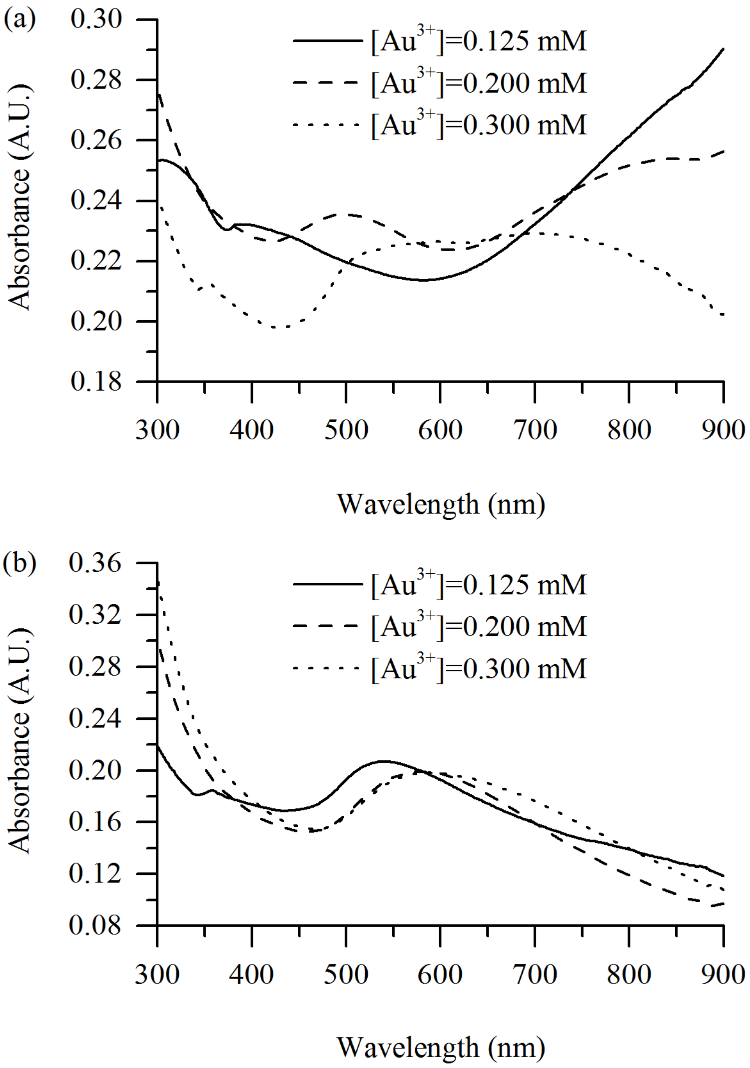

Figure 4.10: Samples prepared according to Table 4.6. Figure 4.10a shows the spectra of samples prepared without PVP, while spectra shown in Figure 4.10b refer to samples prepared with PVP

The spectra shown in Figure 4.10b, on the other hand, show a red-shift of the peak at ~600 nm as the concentration of gold increases. Furthermore, a broadening of the peaks is observed from sample A_{PVP} and sample C_{PVP}.

4.2.3 TEM Analysis

4.2.3.1 SNPs TEM Images

The results of image analysis carried out according to the method presented in Section 3.2.3.3 are shown in Figure 4.11. As shown, samples prepared with PVP show a narrower size distribution compared to the one synthesised without it.

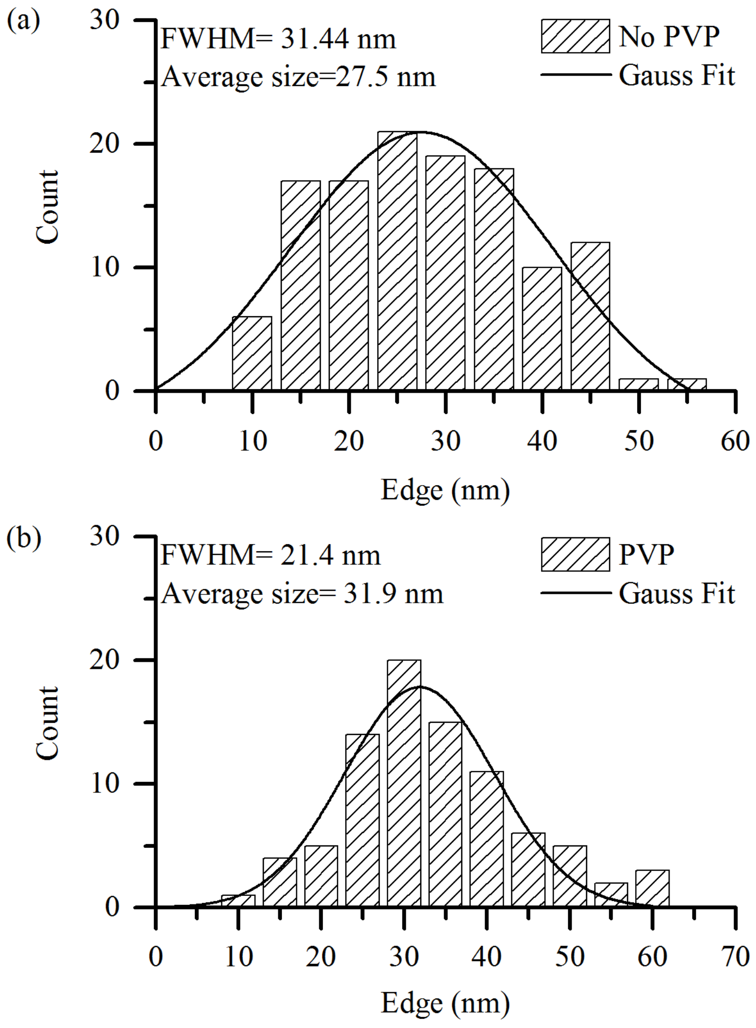

Figure 4.11: Size distribution of particles calculated with (a) and without PVP (b) are shown. It is possible to see how the FWHM of the first one is bigger compared to the one of the second; with regard to the average size of prisms, the second, on the other hand, is around 4 nm bigger than the first. Some of the images used for calculating these histograms are shown in Figure 4.12, while the whole set of pictures are shown in Appendix A.2.

Only the method proposed by Rivollier et al. (2010) was successful in discriminating triangular shaped particles as the use of the method proposed by Igathinathane et al. (2008), did not lead to good results since the parameters employed were not able to identify properly the triangular nanoparticles among all the particles present in the TEM images even when they were insulated from other particles and with an evident triangular shape.

Furthermore, it was possible to observe differences in the actual size of the edge length. In particular, a significant increase in the average edge length can be appreciated for particles prepared with the addition of poly(vinylpyrrolidone) as expected from the graph shown in Figure 4.2. Image analysis of the particles also gave an important information about the shape of the particle synthesised which resulted in mainly equilateral and realux triangles, with very curvy tips: the high presence of relaux triangles can also be an explanation of the reason why the method proposed by Igathinathane et al. (2008)

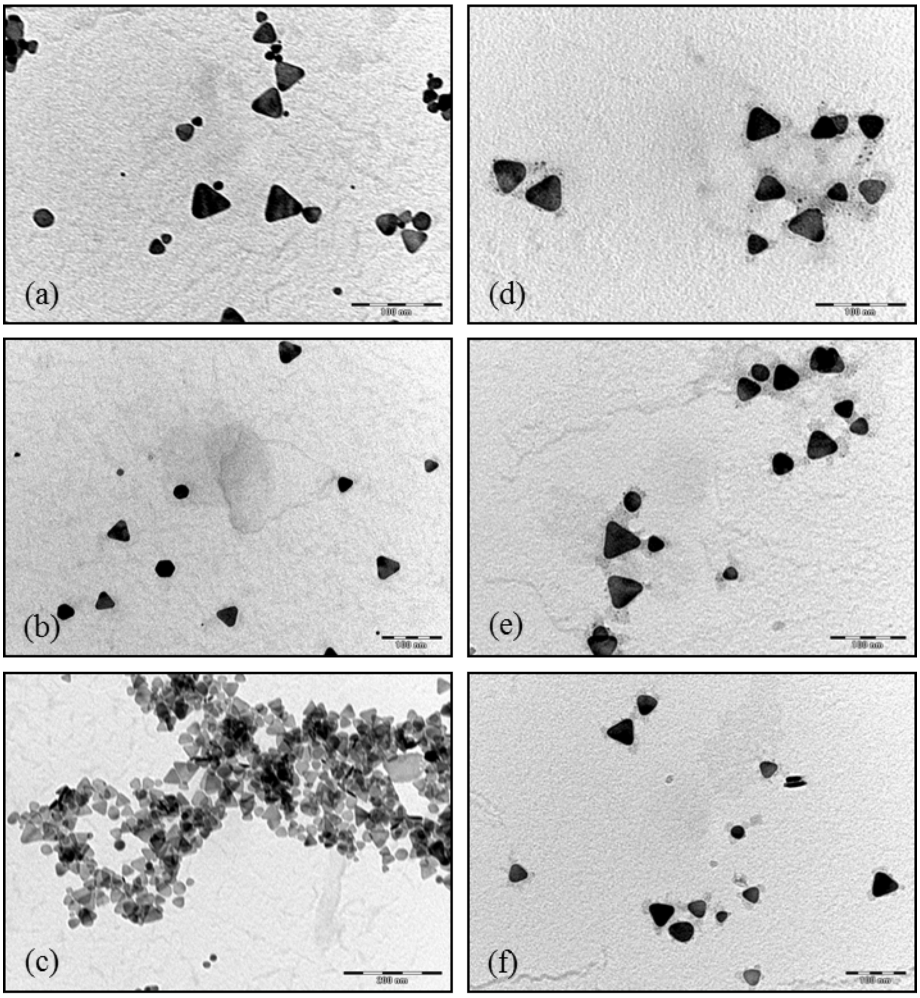

Figure 4.12: TEM images for particles prepared without (Figure 4.12a-Figure 4.12c) and with (Figure 4.12d-Figure 4.12f) PVP are shown. The scale bar is 100 nm except Figure 19c where it is 200 nm. The full set of pictures is shown in Appendix A.2.

was not efficient in identifying the correct shape. This geometry has very curvy edges and it can be easily confused with a circle if the parameters used are not good enough in discriminating these shapes.

4.2.3.2 Modified SNPs TEM Images

By examining TEM images of samples prepared with different amounts of Cl^- two main conclusions can be drawn in terms of the edge length of the prisms and variation of the tips' sharpness. Regarding the prisms edge it was possible to observe a large increase in length as the concentration of KCl in the solution increased. In particular, the edge length changed from a minimum of ~80 nm when $[Cl^-]=103.3$ M to a maximum of ~300 nm when $[Cl^-]=122.1$ μM, while no particles were observed when $[Cl^-] \geqslant 133.4$ μM as expected from the UV-vis spectra which showed no absorbance above that concentration due to the formation of AgCl. As the size of the triangular nanoprisms increased their density on the grids reduced. This was due to the fact that the number of prisms was reduced, along with the reduced numbers of nuclei with the precipitating effect of chlorine.

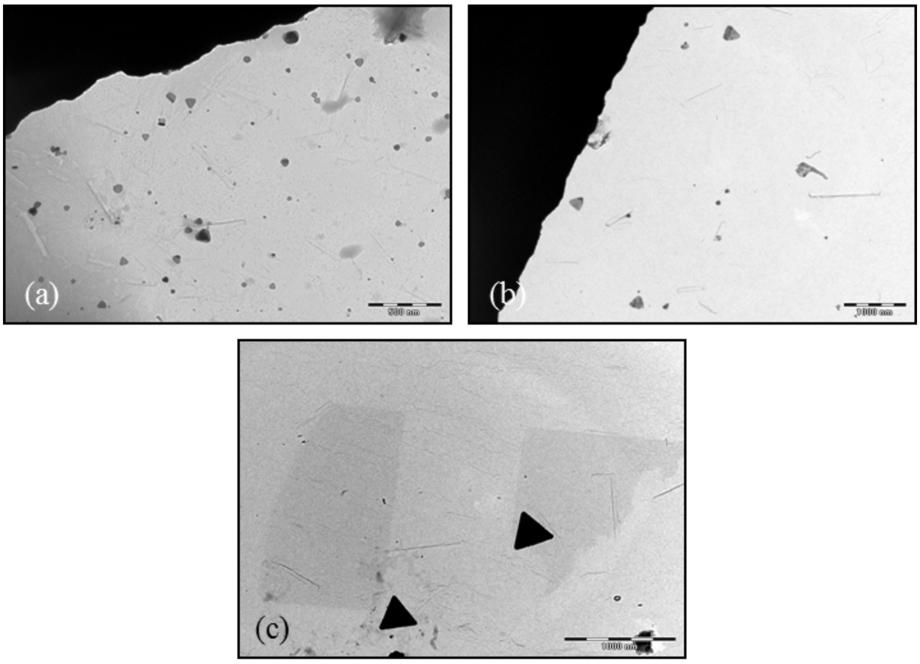

Figure 4.13: TEM images of samples prepared with different amount of chlorine (11,12,13 μL respectively). The scale bar is 500 nm for Figure 4.13a and 1000 nm for Figure 4.13b and Figure 4.13c.

According to Shuford equation (Shuford et al., 2005), this change in edge size was responsible for the red shift of the SPR of the nanoprisms solution. The addition of chloride had an effect on the prisms tips as well. In particular, it was possible to observe how it became sharper as the KCl concentration increased. In Figure 4.13 it is possible to observe how the tips of the particles change to a round shaped one (that is also the most commonly found in nanoprisms prepared in the absence of any halide) to a very neat sharp one. This sharpness had an effect on the optical properties of the prisms. Particularly, DDA calculation showed that the sharpness of the tips affected the bandwidth of silver nanoprisms, i.e. the sharper the tips the broader the peak of the in-plane dipole resonance (Sherry et al., 2006), due to the "lightning rod effect" on the tips of the nanocrystals.

TEM images for the sample specified in Table 4.6 have been collected and are shown in Figure 4.14.

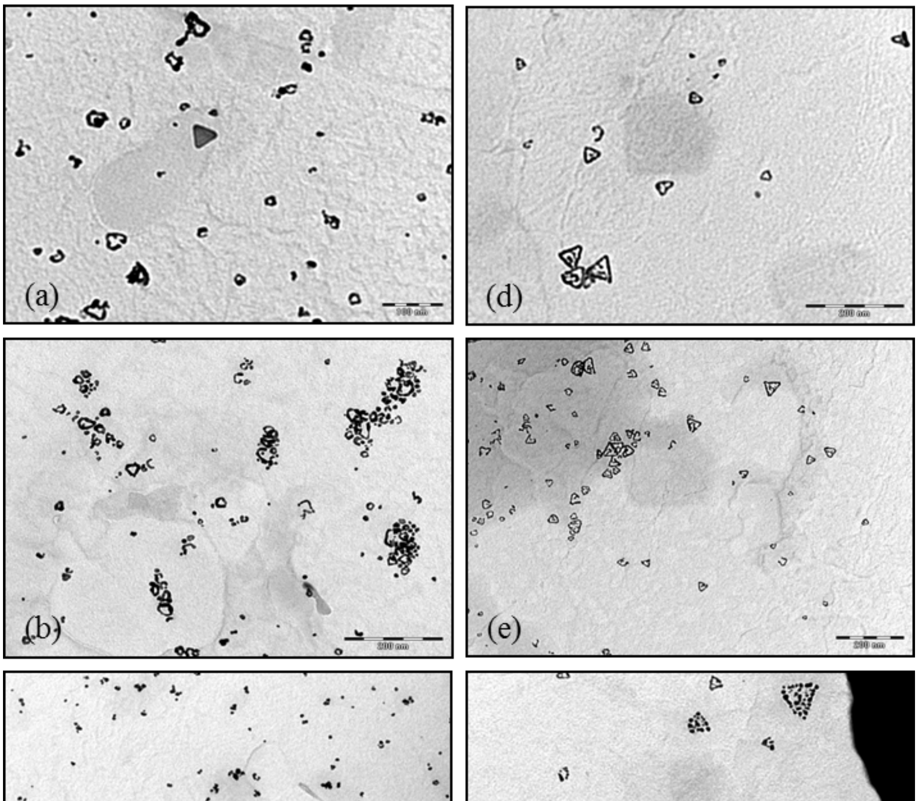

Figure 4.14: Series of TEM images of nanohollow prepared with different concentrations of gold solution as reported in Table 4.6 . Figure 4.14a-Figure 4.14c are the images of sample A-C, while Figure 4.14d -Figure 4.14f are the images of sample A_{PVP}-C_{PVP}

As Figure 4.14a-Figure 4.14c show, the addition of gold ions effectively removed the silver from the nanoparticles but the triangular geometry was lost. Regarding the TEM images in Figure 4.14d-Figure 4.14f, triangular geometry remained, even when the concentration of gold was very high. At the same concentration, i.e. Sample C/C_{PVP}, the particles prepared without the addition of PVP completely lost their original shape and just small spheroids were left.

Figure 4.14 shows the ratio between the counts of AgL and AuM transition collected with energy-dispersive X-ray spectroscopy (EDAX).

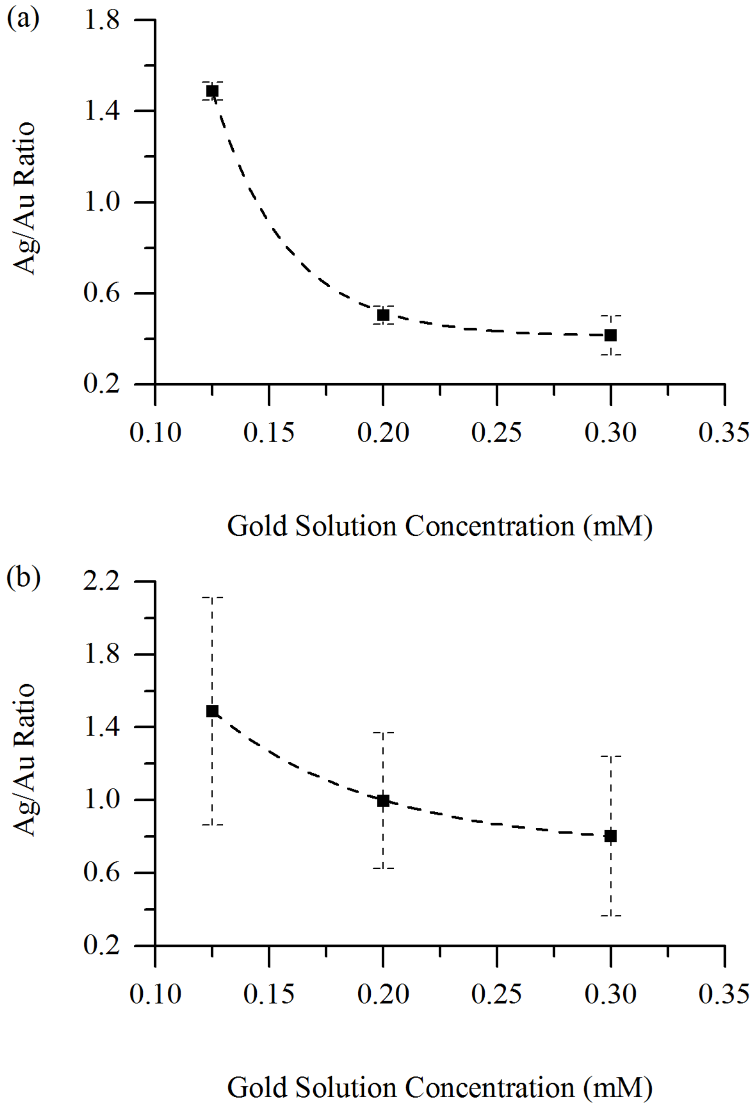

Figure 4.15: Ratio of counts of AgL and AuM transition collected with energy-dispersive X-ray spectroscopy. Figure 4.15a refers to nanoparticles prepared in absence of PVP, while Figure 4.15b refers to nanoparticles prepared with PVP. EDAX spectra used for calculating these values are shown in Appendix B.2

As it is possible to see, when the concentration of the gold solution increases the ratio gets smaller; as only metallic gold is present in the samples used for EDAX the decay of Ag/Au ratio is an indication of the galvanic replacement. An important conclusion, which found a correlation in the TEM images of Figure 4.14, is that nanoparticles not protected with PVP lose silver much faster than that with the extra protection of the polymer; these results in the complete consumption of silver colloids and only gold spheroids are left.

4.3 Conclusions

A method for preparing silver nanoparticles has been studied and evaluated for their potential application in the production of the energy saving nanoprisms. Particularly, the effect of PVP on their final geometry, and therefore on their final optical properties, has been investigated both with spectroscopy and electron microscopy techniques. PVP was found to have a consistent effect on the final shape, size and distribution of the particles. In particular, a red-shift in the spectral position and a narrowing of the band were observed when extra stabilisation was introduced to the system by addition of the polymeric stabiliser. To investigate if there was any correlation between the concentration of poly(vinyl(pyrrolidone)) and the optical properties of the nanoparticles, spectra of different samples were collected, by changing the concentration of PVP while keeping other concentration constant (i.e. concentrations of trisodium citrate dihydrate, silver nitrate, hydrogen peroxide and sodium borohydride). In the collected samples a move to lower energy and a narrowing in the in-plane dipole surface plasmon resonance were observed until the final concentration of PVP was kept under 0.12 mM. Above this concentration the presence of a peak at around 400 nm was observed due to the too high stabilisation of the particles that avoided them to be completely etched by hydrogen peroxide. TEM image analysis showed that the triangle prepared were mostly equilateral or realux triangles with rounded tips. Edge calculation, on the other hand, showed that the particles prepared with PVP had a narrower size distribution and longer edges. This was reflected in the narrower and more red-shifted band in the visible absorbance spectra.

Different routes for the modification of silver nanoparticles was examined in order to tune their optical properties as far as possible in the NIR region. Particularly, the effect of chloride ions on the final shapes of the silver colloid was studied. It was found that adding these ions led to the formation of larger nanoparticles by reducing the numbers of nuclei in solution. As TEM images suggested, the addition of Cl^- also encouraged the formation of sharper tips which can cause the broadening of the SPR due to lighting rod effect. Unfortunately, this methodology was not as reliable as suggested by the high standard deviation shown in Figure 4.7. The difficulty in controlling the final shift in the spectral position may arise from the small volume of KCl solution added to the nanoparticles precursor solution and to the sensitivity of the system to small changes in chloride ion concentration.

Along with size modification, the modification of SNPs to Au/Ag nanohollows by galvanic replacement was also carried out. UV-vis spectra collected showed a general red-shift of the surface plasmon resonance of the nanoparticles when low concentrations of $HAuCl_4$ were used, while a change in the shape of the spectra was also observed when larger amounts of chloroauric acid were injected in the nanoparticles solution. Effect of poly(vinylpyrrolidone) on the final nanoparticles shape were examined as well: TEM images collected for these samples showed that generally SNPs modified in presence of PVP appeared to better retain the initial triangular shape.

In summary, the preparation procedures studied here demonstrated their feasibility for synthesising nanoparticles with the required optical properties for application in fenestration. Unfortunately, the resulting particles showed high deviations in terms of both shape and spectral position of the surface plasmon resonance. Clearly, this is a critical issue for large scale production of these materials, and needs further investigations.

Chapter 5

Microfluidic Synthesis of Silver Nanoprisms

Contents

Parts of this chapter were published as:

- Carboni, M., Capretto, L., Carugo, D., Stulz, E. and Zhang X. (2013), Microfluidic-Based Continuous Flow Formation of Triangular Silver Nanoprisms with Tunable Surface Plasmon Resonance. Journal Material Chemistry C, 1:7540 - 7546
- Zmijan, R., Carboni, M., Capretto, L., Stulz, E. and Zhang X. (2014), *In situ* microspectroscopic monitoring within a microfluidic reactor. RSC Advances, 2014, 4 (28), 14569 - 14572.

5.1 Introduction

Although the synthesis and characterisation of anisotropic nanomaterials has increasingly attracted attention in a wide range of research fields, there still remain challenges for the synthesis of nanoparticles with precise control and tailoring of stable geometries (e.g. prisms (Liu et al., 2005), cubes (Peng et al., 2012) and stars (Nehl et al., 2006)) in order to achieve geometry-dependent characteristics in a reproducible and predictable manner. This becomes more difficult for large-scale production where these challenges should meet the requirements of sustainable processes using low cost precursors, simple processes and reducing the amount of waste (Cui et al., 2009). In addition, the most commonly used batch processes including dry and semidry methods (e.g. plasma, flame, aerosol, spray and pyrolysis), which are currently employed in the industry, suffer from the lack of monodispersity and control over the reaction steps (Ould-Ely et al., 2011) including nucleation and/or growth (La Mer and Dinegar, 1950; Turkevich et al., 1951).

Recently, microfluidic reactors have been proposed as a tool to potentially overcome the limitations commonly associated with macroscale production of a range of nanoparticles (e.g. polymeric (Capretto et al., 2011), metal (Lin et al., 2004; Song et al., 2004; Wagner and Köhler, 2005) and oxide (Frenz et al., 2008)). The interest in translating conventional synthesis to microreactors stems from the unique characteristics provided by such micro-scaled devices. These include the quick response of the system to variation in the experimental boundary conditions, improved handling of smaller volumes, more efficient heat and mass transfer, and highly controllable and tunable mixing compared to batch reactors (Jensen, 2001). In addition, microfluidic reactors can be employed as investigation tools (Sounart et al., 2007; Zinoveva et al., 2007), given the possibility of online process monitoring and integration with sensors and control units (Jensen, 2001).

Previous studies have demonstrated that by precisely controlling the experimental parameters, such as mixing and residence time, the two steps (i.e. nucleation and growth) that lead to the formation of nanoparticles can be identified, isolated and manipulated (Sounart et al., 2007). Various types of metal nanoparticles (e.g. platinum, silver and gold) have been produced successfully in microchannels, leveraging the faster mixing (Song et al., 2004; Wagner and Köhler, 2005) and control over heat exchange (Chan et al., 2003; Lin et al., 2004) which lead to the production of highly mono-disperse isotropic particles (i.e. spheres). Particle analysis has shown that the dimensional standard deviation of metal nanoparticles produced with microfluidics is reduced by approximately 20% compared to batch systems (Song et al., 2004; Wagner and Köhler, 2005). It has been suggested that the more homogenous diffusion of the reagent obtained inside the microreactor, the more uniform and efficient nucleation is granted, which is crucial for the subsequent growth phase, leading to a narrower distribution in both particle size and shape.

However, the production of anisotropic materials represents an additional challenge, which is commonly tackled by the use of specific ligands for selectively blocking the growth of some faces of the growing crystal (Wang et al., 2007; Weng et al., 2008). Due to the precise control required over nucleation and growth steps, a seed-mediated approach is usually employed in order to bypass the nucleation step and to simplify the overall procedure (Jana, 2005; Jana et al., 2001a). Regarding SNPs, their size control in batch synthesis is achieved through changing the concentration of the reducing agent ($NaBH_4$) whilst keeping the concentrations of the other reagents constant (Métraux and Mirkin, 2005) or by adding halide ions (Cl^- and Br^-) to finely tune their size and shape (Cathcart et al., 2009). Alternatively, a seed-mediated approach can be used to exert control over the final absorption of silver nanoprisms: by changing the concentration of the seed different size of prisms can be achieved (Aherne et al., 2008). This approach has been successfully reproduced using flow reactors (Knauer et al., 2012; Knauer and Khler, 2013) where an effect similar to the one observed in the batch synthesis on the optical properties of silver nanoprisms can be achieved. Although seed mediated approaches are the most widely used to prepare silver nanoprisms in microreactors, the combination of microstructured reactors and efficient LED illumination was also successfully applied for synthesising nanoprisms of enhanced homogeneity (Silvestrini et al., 2013).

In this Chapter, the development of a microfluidic-based process for the direct synthesis (i.e. without seed-mediated growth) of silver nanoprisms in a continuous flow format using a flow focusing microreactor, by varying major microfluidic parameters only, namely flow rate ratio (R) and total flow rate (V_{tot}) is presented.

The aim of this research is to investigate the effect of controlling the hydrodynamics (i.e. the mixing) on the final shape and size distributions of SNPs. Control of the reagent's mixing in a batch reactors is hard and when very fast reaction are involved (such as the reduction of silver by $NaBH_4$) it can lead to the formation of species gradients in the reactions vessel. This is particular problematic when the reactions consist of two almost simultaneous steps, negatively affecting the homogeneity of the final products. Not just the microfluidic setup could help to improve SNPs quality, but also to achieve a better control over small volumes of reagents, such as the volume of KCl solution used in Section 4.2.2.1. In this Chapter a new experimental setup for the modification of SNPs with halide ions is proposed. The modification of the prisms with Cl^- is confronted with a similar reaction carried out in a batch reactor, while for the modification with Br^- kinetic studies where conducted. To monitor SNPs formation, a novel absorbance detection system based on an inverted microscope coupled with a UV-vis-NIR micro-spectrophotometer for spatially-resolved spectroscopy measurements at any point of interest along the microfluidic channel has been developed and validated against a benchtop spectrophotometer.

5.2 Results and Discussion

5.2.1 Microreactor Synthesis of Silver Nanoparticles

SNPs were synthesised according to Section 3.3.6.1. With this experimental setup, it was observed that a stable flow focusing was achieved within the main reaction channel, and the use of water as the central spacer stream effectively avoided the immediate clogging of the channel (Figure 5.1). By varying the lateral inlet flow, the chemical composition of the reaction system was adjusted as desired.

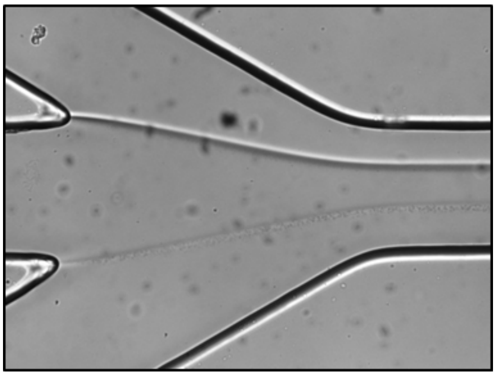

Figure 5.1: Laminar flow at the flow focusing junction for a V_{tot}=3.41 mL/h

Compared to the study with batch method (Métraux and Mirkin, 2005) more attention was taken in preparing the $NaBH_4$ solution. To reduce the spontaneous production of hydrogen in water, an alcoholic basic solution was prepared according to the method proposed by Shalom et al. (2007) (see Section 3.3.3.2). Differing from the original method, the pH was adjusted by varying the amount of NaOH used. Notably, a higher pH resulted in the production of solely nanospheres or a complete impairment of the nanoprecipitation process (i.e. no particles formed in this case).

In order to assess the effect of pH of the reducing agent solution on SNPs formation, experiments were first carried out in a batch reactor and UV-vis spectra were collected. Silver nanoprisms were synthesized according to the published procedure by Métraux and Mirkin (2005) with increasing volumes of 0.01 M basic solution of $NaBH_4$ added to the final reducing agent solution, see Section 3.3.3.2.

As shown in Figure 5.2, as the volume of the basic solution increases, the optical absorbance moves to shorter wavelengths typical of spherical silver nanoparticles.

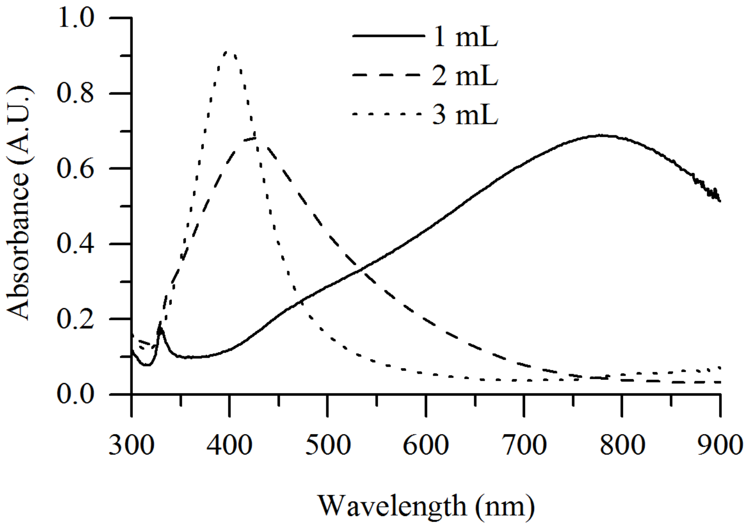

Figure 5.2: Absorbance spectra acquired for nanoparticles solution prepared by adding different volumes of 0.01 M solution of $NaBH_4$ to the final reducing solution (final volume 33 mL for all three samples).

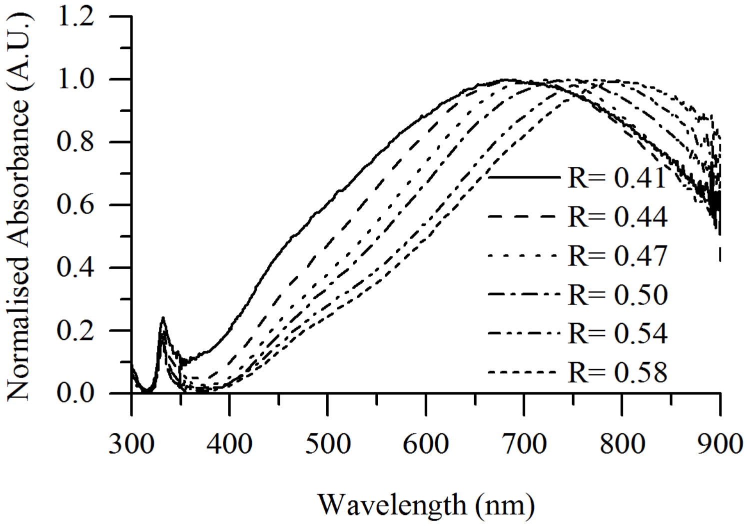

Figure 5.3: Normalised UV-vis spectra of silver nanoprisms obtained under different flow conditions where R represents the flow rate ratio of central flow over total flow rate (V_2/V_{tot}), with central flow rate (V_2) kept constant at 1.41 mL/h.

Figure 5.3 shows the absorbance spectra of the silver nanoprisms obtained with the inline UV-Vis spectrophotometer under different flow conditions, with R ranging from 0.41 to 0.58. R represents the flow rate ratio of central flow over total flow rate V_2/V_{tot}, with constant central flow rate V_2 at 1.41 mL/h.

These flow conditions were selected for the concentration of reagents inside the microreactor to reflect the chemical conditions employed in the batch experiments by Métraux and Mirkin (2005). As can be seen from Figure 5.3, all six spectra show a single maximum absorbance peaks which shifts from 690 nm to 796 nm, with increasing R from

0.41 to 0.58. It should be noted that a small peak at an identical position of 340 nm appears in all spectra, which may be attributed to the out-of-plane quadruple resonance effect which is significantly weaker than the main absorbance band due to the in-plane dipole surface plasmon resonance (Kelly et al., 2003). Previous studies have suggested the in-plane dipole resonance is a good indicator of general nanoprisms geometries. Its redshift, particularly, is correlated with increased edge length (Jin et al., 2003b; Métraux and Mirkin, 2005). The results shown in Figure 5.3 suggest that by adjusting the flow conditions different sizes of nanoprisms can be obtained.

It is generally understood that the process of silver nanoprisms formation involves two steps including i) the reduction of $AgNO_3$ by $NaBH_4$ to form and grow silver seeds in the presence of the stabilizing agent TSCD, and ii) the chemical oxidation of $Ag^{(0)}$ induced by hydrogen peroxide to etch the silver nanoparticles formed. With the selective adsorption of citrate ions on the (111) surface of Ag seeds, the most stable shape of prism (or triangular platelet) in solution is achieved (Callegari et al., 2003; Métraux and Mirkin, 2005; Sun et al., 2003), which is largely attributed to the kinetic factors of the fast growth along the planar twinning defects Aherne et al. (2008). Previous studies with a traditional batch synthesis method showed that the growth phase took approximately 30 mins when PVP is added for additional stabilisation. When only citrate is present, on the other hand the growth process require $\sim$5 minutes (Métraux and Mirkin, 2005). In our microfluidic approach, the residence time of reagents within the reaction channel was in the range 0.23-0.34 s under the flow conditions described above, indicating a significant increase in the reaction kinetics due to faster mixing compared to bulk reactions (Capretto et al., 2011).

5.2.1.1 TEM Image Analysis

Representative TEM images are shown in Figure 5.4 .

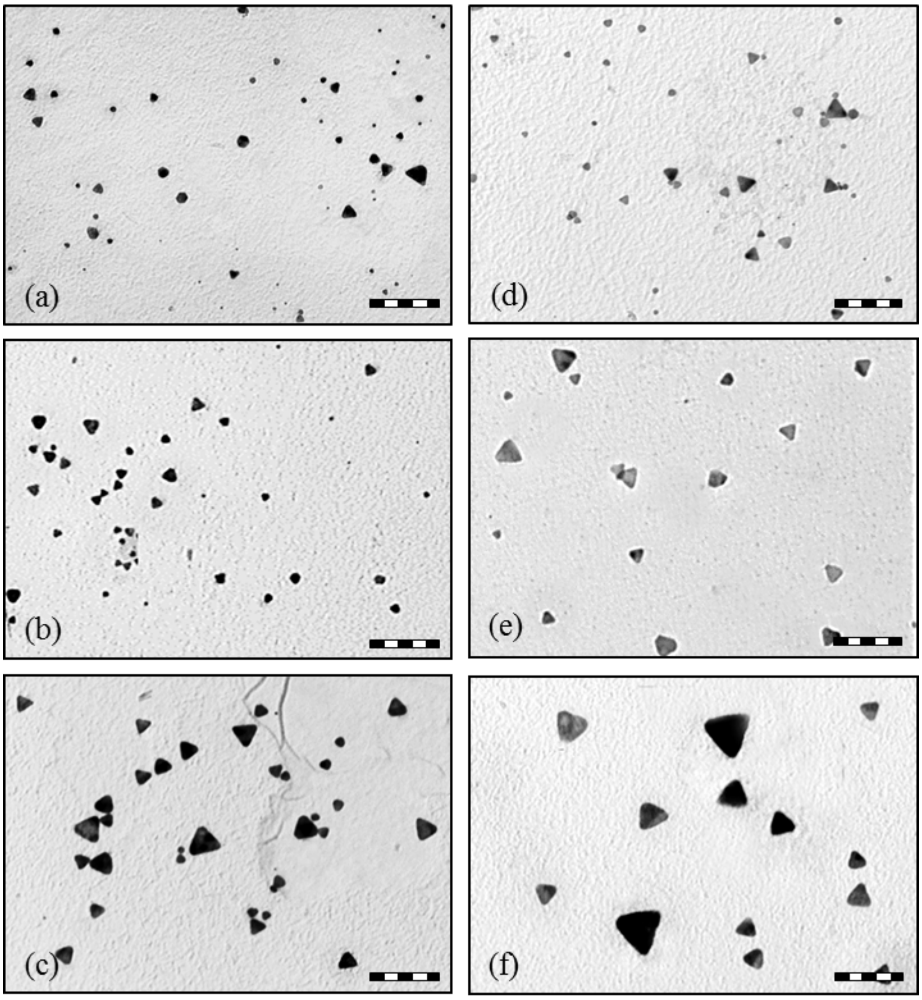

Figure 5.4: TEM images of silver nanoprisms at different flow rates (a) 3.41 mL/h, (b) 3.21 mL/h, (c) 3.01 mL/h, (d) 2.81 mL/h, (e) 2.61 mL/h, (d) 2.41 mL/h. The scale bar is 200 nm for all pictures.

Image analysis results are illustrated in Figure 5.5 for nanoprisms average edge length (Figure 5.5a) and triangular nanoprisms percentage (Figure 5.5b) at different flow rate ratios; the percentage is related to the overall particle composition including spheres and other geometries. The corresponding absorbance band position and FWHM at different flow rate ratios are also plotted for correlation.

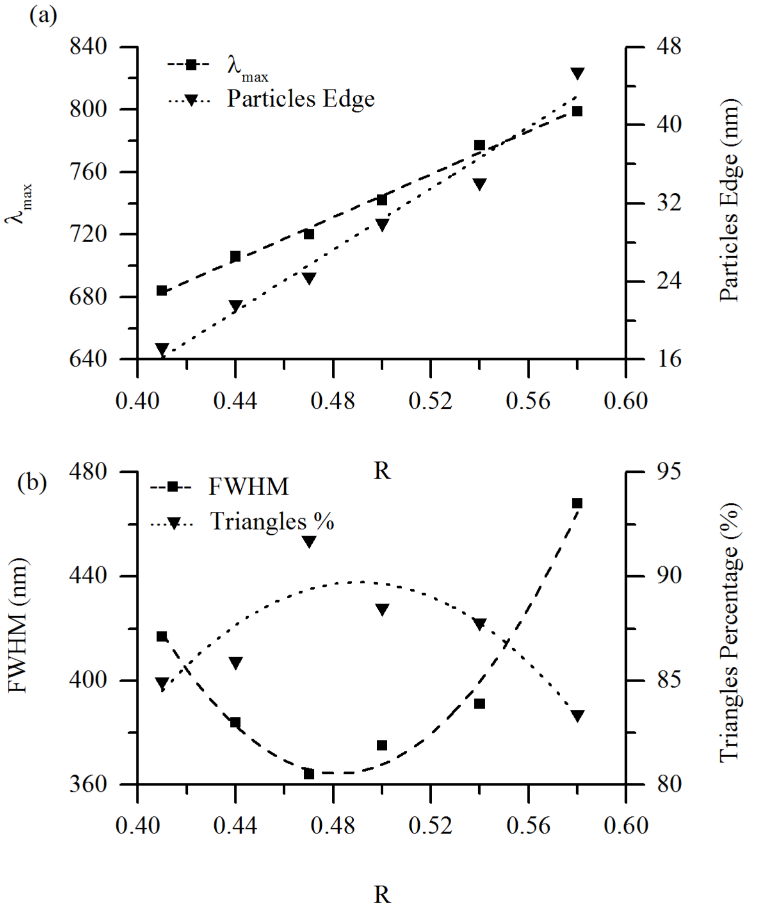

Figure 5.5: (a) Nanoprisms edge length and corresponding absorbance band peak position at variable R. (b) Percentage of nanoprisms and corresponding FWHM at variable R.

Figure 5.5a shows a growth of the prisms edge length from 18 nm to 46 nm with increasing R from 0.41 to 0.58, following an approximately linear relationship. Notably, the absorbance band position shifts following a similar linear trend. This correlation of nanoprisms geometries with their optical response agrees well with that observed by Shuford et al. (2005), who found that the absorbance band position of nanoprisms was proportional to prism edge length (L) and inversely proportional to prism thickness (Tk). Using Shuford's Equation (Equation 4.1) with the prism edge lengths obtained (Figure 5.5a), the prism thickness was calculated. It was found that the minimum average thickness of prisms was 2.3 nm when L=18 nm, and the maximum was 3.6 nm when L=46 nm. This suggests that the shift of the spectral position shown in Figure 5.3a is largely due to the increase in the prisms edge length (∼156% max increase) with smaller changes in their thickness (∼56.5% max increase).

Figure 5.5b depicts the percentage of nanoprisms in whole samples and their absorbance band FWHM at different flow rate ratios. It shows that both percentage of nanoprisms and FWHM are significantly influenced by the flow conditions. In the operation R range, the percentage of nanoprisms initially increases with increasing R, reaching a maximal percentage of 92% at R=0.47, and then decreasing when R>0.47. At the same time, the change in absorbance band FWHM shows an opposite trend, initially decreasing with increasing R, reaching a minimum FWHM of 360 nm at R=0.47, and then increasing when R>0.47. As the absorbance spectral position and its broadness depend on the size and shape distribution of the nanoparticles, the results demonstrate the capability of the microreactor for the controllable production of nanomaterials by adjusting microfluidic operational parameters.

As described above, the results shown in Figure 5.3 were obtained at variable flow rate ratio. R was varied by changing the flow rates of two lateral streams while keeping the central flow rate constant. This resulted in both flow rate ratio R and total flow rate V_{tot} changing simultaneously; the higher R, the lower V_{tot}. Within the continuous flow reaction channel, the change of R altered the width of the flow streams and consequently chemical composition in the microenvironment where nanoparticles formed and grew. At the same time, V_{tot} determined the overall residence time (RT) of reactants passing through the whole reaction channel volume (V), $RT = V/V_{tot}$. In the microfluidic reactor system, both mixing and reagents concentration profiles are dynamic, and the synergistic effect of R and V_{tot} add extra dimensions to the complexity of the system.

5.2.1.2 Effects of Varying Microfluidic Parameters

The effect of two key parameters (i.e. R and V_{tot}) was examined by keeping one of the two variables constant whilst varying the other parameter. Based on the experiments described above, three values of R (i.e. 0.41, 0.50 and 0.58) were selected and at each value the total flow rate V_{tot} was varied in the range 2.41-3.41 mL/h.

As shown in Figure 5.6a, for a given V_{tot} the spectral position of the maximum absorbance shifts to higher wavelength as R increases, indicating an increase in particle size according to Shuford et al. (2005). As discussed above, within the microscale reaction channel changes in the chemical composition of the microenvironment were facilitated through the diffusive mixing process across the three laminar flow streams.

At lower R levels, the central spacer flow stream becomes relatively narrow thus the system requires shorter time for complete mixing (i.e. faster mixing) (Capretto et al., 2011). Subsequently, the resulting chemical composition of the microenvironment affects the kinetics of nanoprisms formation steps, including super-saturation, nucleation and growth.

In general, faster mixing increases the super-saturation rate and thus the kinetics of both nucleation and growth (Schwarzer and Peukert, 2004). It was found in previous studies that the nucleation step was influenced more significantly by an increased super-saturation rate leading to the formation of a higher number of small nuclei, and vice versa (Schwarzer and Peukert, 2004). Therefore, at higher R levels, the slower mixing process and the associated chemical composition within the microenvironment are favorable for the bigger size and triangular shaped nanoparticles to form, resulting in the spectral redshift, as observed in the experiments and coherently with Shuford calculation.

The results depicted in Figure 5.6b show that at the different R values investigated the broadness of the spectral band in terms of FWHM decreases with decreasing V_{tot} in the higher V_{tot} range (3.41→2.81 mL/h) and reaches a minimum at V_{tot}=2.81 mL/h, which is followed by an increase with lowering V_{tot}. As V_{tot} determines the reagents residence time within the reaction channel, the lower V_{tot} generally provides a longer residence and reaction time creating a microenvironment for the formation of SNPs with smaller FWHM, as shown in Figure 5.5b. On the other hand, Munechika et al. (2007) suggested that a rising percentage of triangular nanoprisms could result in an increase in radiation damping. Thus, an increase in FWHM is observed in the lower V_{tot} range (2.81→2.41 mL/h) with more triangular nanoprisms produced, as confirmed by TEM analysis (Appendix B.1). Overall, this demonstrates that the size and shape

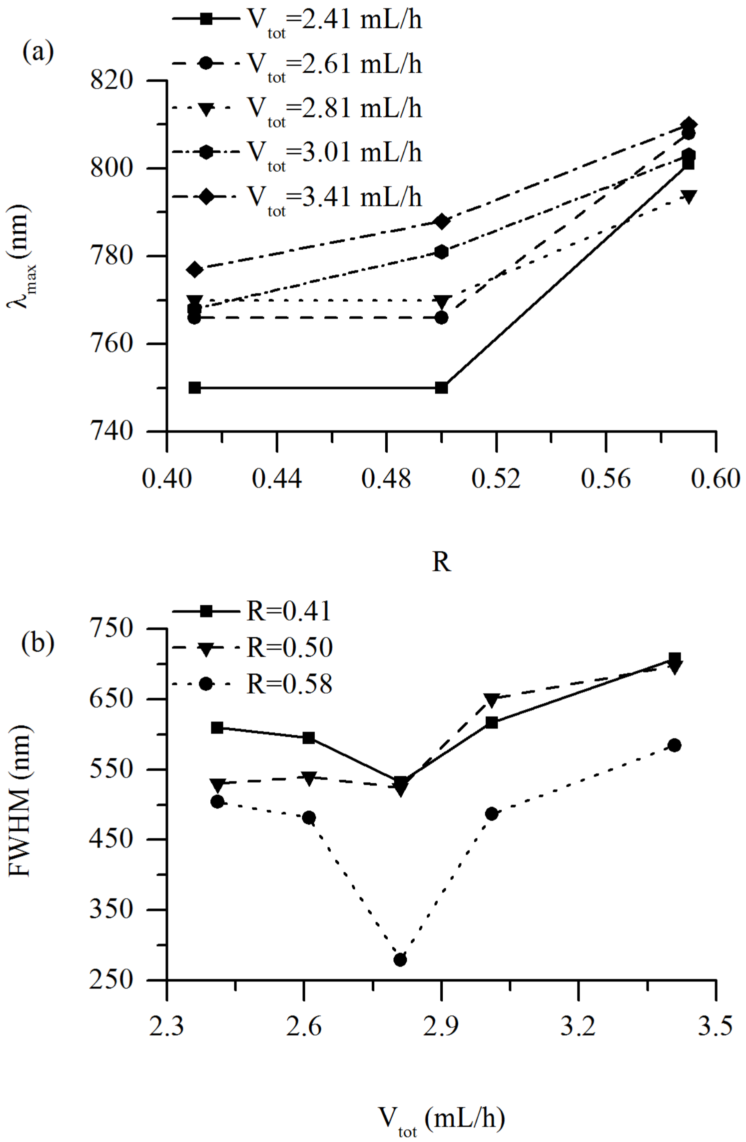

Figure 5.6: Changes in (a) absorbance spectral position and (b) spectral band broadness by changing R and V_{tot}, respectively.

distribution can easily be tuned to the desired specifications, simply by adjusting the operational parameters.

For comparison, experiments using a conventional batch reactor were also performed at the same reagent concentrations employed in the microfluidic reactor, as detailed in the Supplementary Information. Briefly, the results showed that the reagent concentrations affected the spectral band position (λ_{max}) and broadness (FWHM) in a random way, where no clear trend of effect was observed. Clearly, the dynamic conditions are crucial for the reproducibility of the SNPs characteristics and cannot be achieved in the same manner under bulk conditions (Section 5.2.1.3).

5.2.1.3 Batch Synthesis Comparison

In order to asses if the results were due to different reagents' concentration or microfluidic parameters, experiments using a conventional batch system were performed for comparison, at the same reagent concentrations employed in the microfluidic-based reactor system. The batch synthesis was carried out using an adapted published procedure (Métraux and Mirkin, 2005) and reported in Section 3.2.4.1. The concentrations of reagents summarized in Table 5.1 were chosen to reproduce the concentrations in the microreactor at different V$_{tot}$ (from 3.41 mL/h, Sample 1, to 2.41 mL/h, Sample 6). The resulting changes in the absorbance spectra (spectral position and peak broadness) from the product colloids prepared according to Table 5.1 are illustrated in Figure 5.7.

Sample	**[AgNO$_3$] [mM]**	**[TSCD] [mM]**	**[H$_2$O$_2$] [mM]**	**[NaBH$_4$] [mM]**
1	0.12	2.09	0.047	1.16
2	0.11	2.00	0.045	1.11
3	0.10	1.90	0.043	1.05
4	0.01	1.78	0.040	0.99
5	0.09	1.64	0.037	0.91
6	0.08	1.48	0.033	0.82

Table 5.1: Concentration of the reagents used for replicating the microfluidic conditions at different total flow rate in a batch reactor.

Figure 5.7 shows that the reagent concentrations affected the spectral band position (λ_{max}) and broadness (FWHM), however, no clear trend was observed between these parameters. In particular, the spectrum of sample 4 shows an additional narrow and intense peak at about 400 nm indicating a high concentration of spherical particles, which is reflected in a characteristic absorption in that spectral region. The differences between batch and microfluidic systems suggested that, compared to the bulk solution concentration, the control of the fluid dynamic conditions which governed the mixing process and the chemical microenvironment played a crucial role for the production of nanoparticles with tunable characteristics.

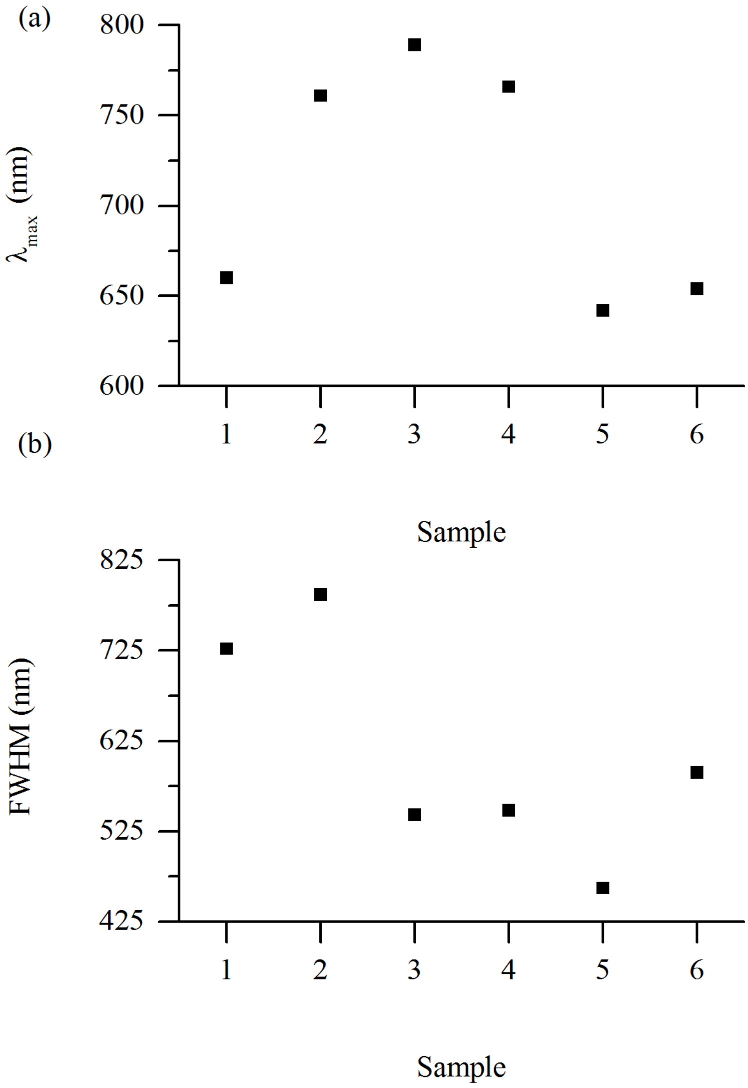

Figure 5.7: (a) λ_{max} and (b) FWHM at different reagent concentrations, as reported in Table 5.1.

5.2.1.4 Microreactor Robustness Test

In order to test the robustness of the microreactor system for long time performance, experiments were carried out by monitoring the reaction channel optically, and the reaction product spectroscopically. For monitoring microchannel fouling, microscope images were acquired every 15 mins by focusing at the bottom wall of the channel. The monitoring of the produced nanoparticle colloid system was performed by collecting UV-vis spectra at intervals of 1 min.

In Figure 5.8a the evolution of the position of the absorbance peak maximum, λ_{max}, and FWHM over time is shown. The trend of the spectral maximum reached a stable stage after an induction period of ~25 mins, which was mainly due to time needed for flushing the spectrometer flow cell with a much larger volume than the microreactor priming volume. The FWHM profile instead displays a slightly decreasing trend over time. The standard deviation calculated for the maximum wavelength is 40 nm over the whole period of the experiment, which is 9.2 nm if the induction stage is excluded. The same calculation performed on FWHM data revealed a standard deviation of 15 nm after the induction stage. Thus, the spectroscopic monitoring results together with microscopic observation demonstrate that the microreactor developed is robust, enabling a long-term stable process for nanoparticle synthesis in a continuous flow format.

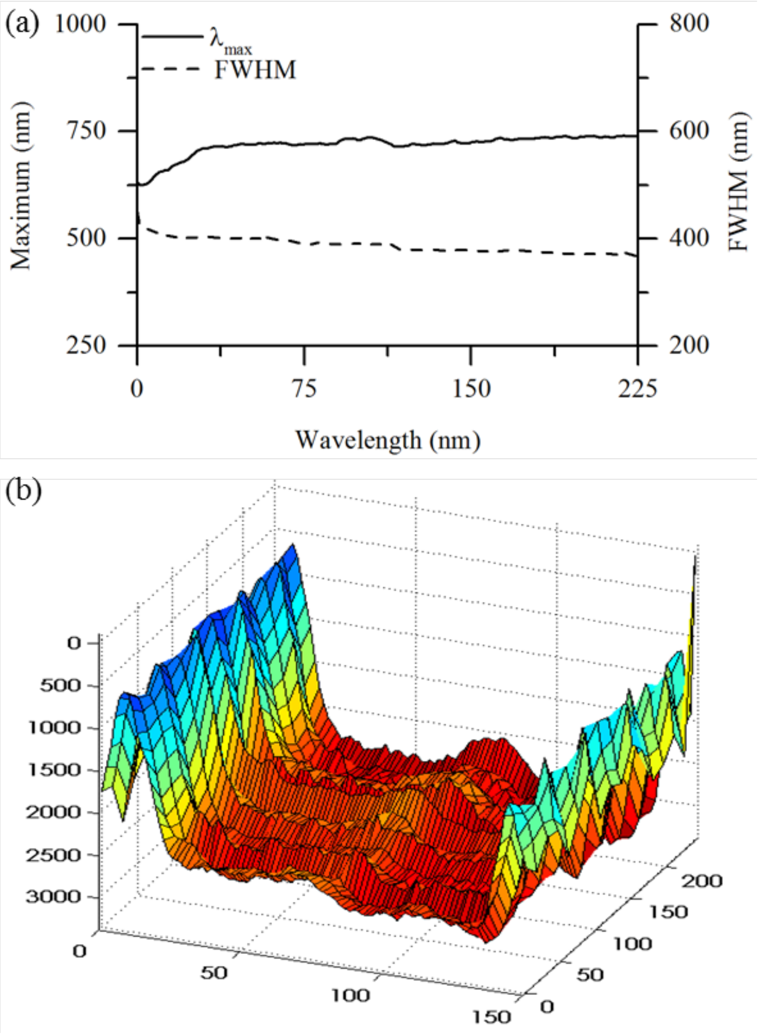

Figure 5.8: (a) Profiles of spectral peak maxima (—) and FWHM (- - -) over the experiment period.(b) Surface plot showing the temporal evolution of the grey level intensity recorded at the channel junction.

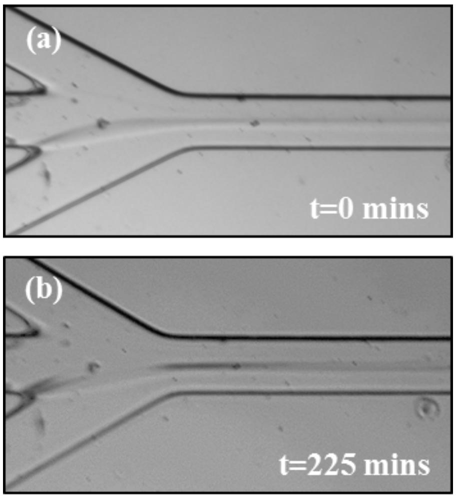

Figure 5.9: Microscope images of the microchannels at the region of interest at (a) t=0 min, and (b) t=225 mins.

The time evolution of the fouling process at the region of interest was quantified by measuring the grey level intensity of each pixel on the images. The results are illustrated in Figure 5.8b as surface plot which shows the change on channel surfaces of both side and bottom walls over the experiment period. The results confirm that no significant fouling took place within the microreactor channel during the extended run (up to 225 minutes).

Figure 5.9a and Figure 5.9b show the microscopic images of the microchannel at the beginning of the experiment (t=0 min) and after 225 minutes run, respectively. As can be seen, no fouling was present at t=0 min. With the experiment running, a thin grey line appeared in the center of the channel suggesting some minimal precipitation and aggregation at the channel surface (Figure 5.9b). There was no fluidic disturbance caused by the attached layer which is in the micron range thickness and is confined to a very limited area.

In order to verify the effect of the hydrophobic coating in preventing channel fouling, a microfluidic experiment was carried out in a non-functionalized reactor. For monitoring microchannel fouling, microscope images were acquired every 15 minutes by focusing on the channel bottom wall across the channel junction area (i.e. where the three streams joined). As shown in Figure 5.10a, the grey level intensity inside the channel rises very rapidly as a consequence of precipitation of silver nanoparticles. Figure 5.10b shows the fouling inside the channel. On the top part small agglomerates of silver are clearly recognizable.

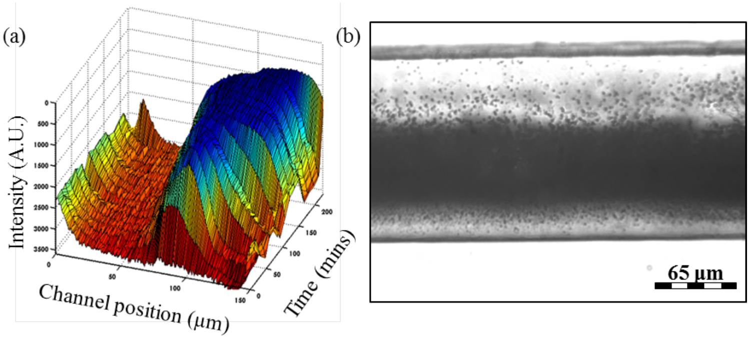

Figure 5.10: (a) Surface plot showing the temporal evolution of the grey level intensity along the channel. (b) Details of the precipitate are illustrated at higher magnification. Images were acquired using an inverted microscope (IX71, Olympus Corporation, Japan) and a bright field illumination.

5.2.2 Modification of Silver Nanoprisms Inside a Microreactor with Halide Ions

5.2.3 Modification with KCl

In order to modify the geometrical properties of silver nanoparticles, the precursor of the silver nanoparticles was injected in the microreactor with a flow ratio of 0.5 (V_2/V_{tot}), based on the previous experiments (Section 5.2.1.1) which showed that at this flow ratio a good distribution in size and shape could be achieved. In particular, V_1 and V_3 were chosen to be 2 mL/h, while V_2 was chosen to be 4 mL/h. The higher flow rate are due to the longer length of the channel and its geometry.

The reagents were kept to flow inside the microreactor until a stable UV-vis spectra was obtained, indicating that the microdevice was fully operative (i.e. no air bubble in the tubing as the reagents fill them, replacing water). Prior to the addition of chloride ions in the reagent solutions, the T valve was left in the OFF position (see Figure 5.11b) in order to avoid contamination of the silver nitrate solution with chloride, which could be washed away from the front of the stationary KCl solution. Spectra of nanoparticles suspension prepared with this microreactor showed a nice sharpness of the in-plane dipole resonance, confirming its abilities in producing high quality silver nanoparticles. In order to inject chloride ions into the microreactor, the valve was turned to the ON position and the system was left to settle for 5 minutes after starting the pumping of the KCl solution (0.1 mM) and before starting the collection of silver nanoparticles suspension.

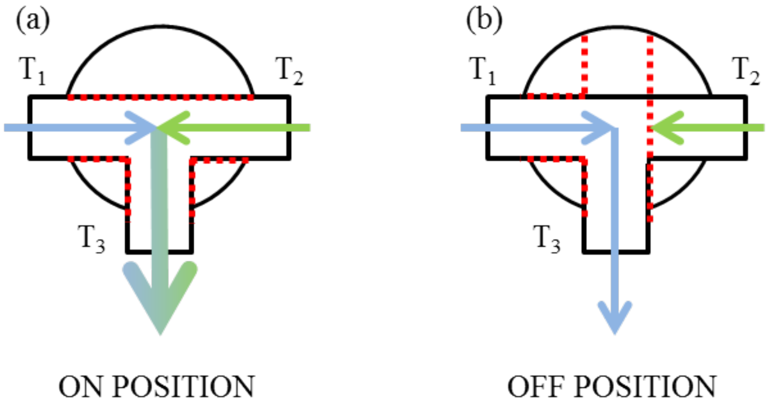

Figure 5.11: Valve geometry for the (a) ON and the (b) OFF position. From T_1 the solution of $AgNO_3$, TSCD and hydrogen peroxyde were injected, while from T_2 the KCl solution was flushed in the channel. T_3 connect the T-valve to the channel.

In order to examine the effect of an increasing concentration of chloride ions on the final spectral position of SNPs absorption, the flow rate of KCl (V_{T2}) was increased from 2 to 6 mL/h, while keeping the flow rate of silver nitrate, V_{T2} (as well as the $NaBH_4$, V_3), and water, V_2, constant at 2 and 4 mL/h, respectively. A starting flow of 2 mL/h for the KCl solution was chosen in order to start under identical fluidic conditions for both reagents and in particular to have a symmetrical stream in the channel. The spectral shift of the nanoparticles spectra after the addition of chloride ions are shown in Figure 5.12a.

Another effect of the microfluidic synthesis over the final optical properties was the significantly reduced standard deviation of the final optical properties of the prepared colloids, making this method much more reliable than the batch process. This was an indication of the reliability of the method compared to other methods reported in the literature.

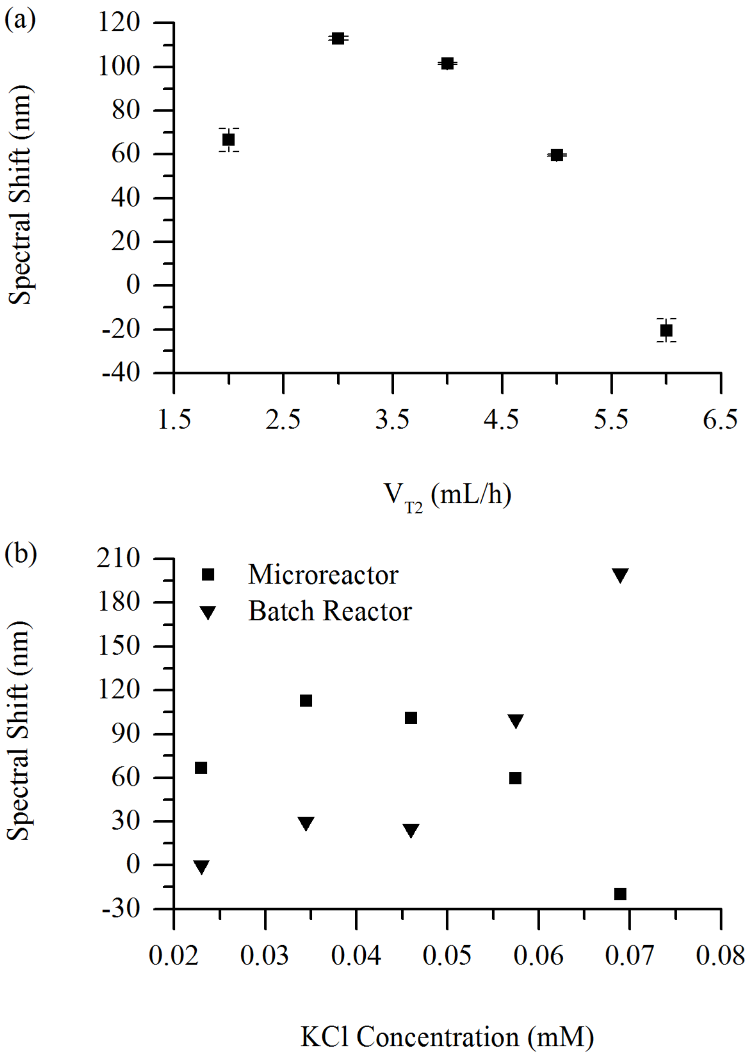

Figure 5.12: (a) Trend of the spectral shift with different V_{T2} and (b) comparison of the trend in a microfluidic and in a batch reactor.

5.2.3.1 Computational Fluid Dynamic Simulations

To better understanding the effect of chloride ions on the optical and geometrical properties of silver nanoparticles, computational fluid dynamic (CFD) simulations were performed according to Section 3.3.5. Particularly, the CFD simulations focused on understanding the concentration of the two species at the outlet of the T-valve. The calculations presented in Figure 5.13 gave some useful information:

1. The real concentration of KCl at the outlet of the T-junction was higher compared to the calculated one.

2. The real concentration of $AgNO_3$ was lower that the ideal one before its addition in solution.

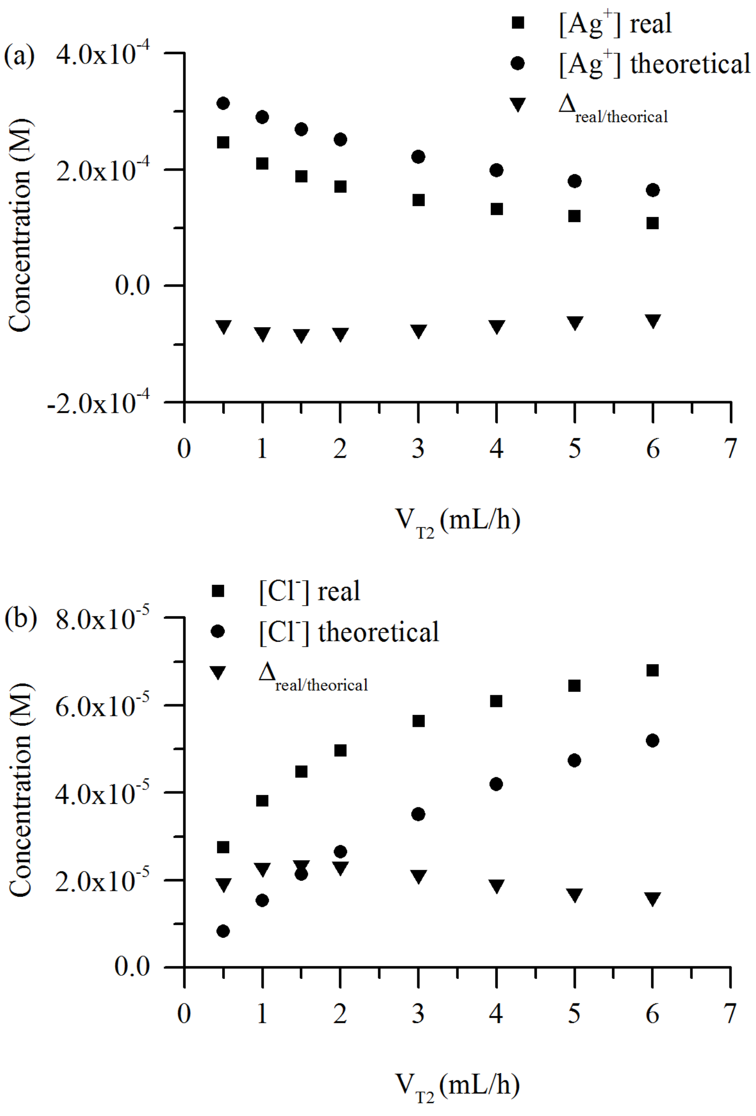

Figure 5.13: Trend for the real and the theoretical concentration of (a) silver and (b) chloride ions.

These two points could be due to fluidodynamic effects, in particularly the asymmetric shape of the flow and the diffusion of the reagents inside the channel. Notably, the ratio between $[Ag^+]/[Cl^-]$ was much lower when compared to that of the same reaction carried out in a batch reactor as shown in Figure 5.14. This difference was useful for explaining the higher redshift of the first three points in Figure 5.12b, as a lower $[Ag^+]/[Cl^-]$ ratio gave a higher concentration of chloride ions and therefore a higher shift of the final dipole.

The ratio of $NaBH_4$ to Ag^+ could affect the final optical properties of silver nanoprisms. In order to observe how the ratio between the final concentrations of the reagents changed with the change of V_{T2}, CFD was performed to investigate the diffusion of species at the focusing for T_2, flow ranging from 2 to 6 mL/h, while flows of T_1, C_2 and C_3, on the other hand, were kept constant at 2, 4 and 2 mL/h, respectively.

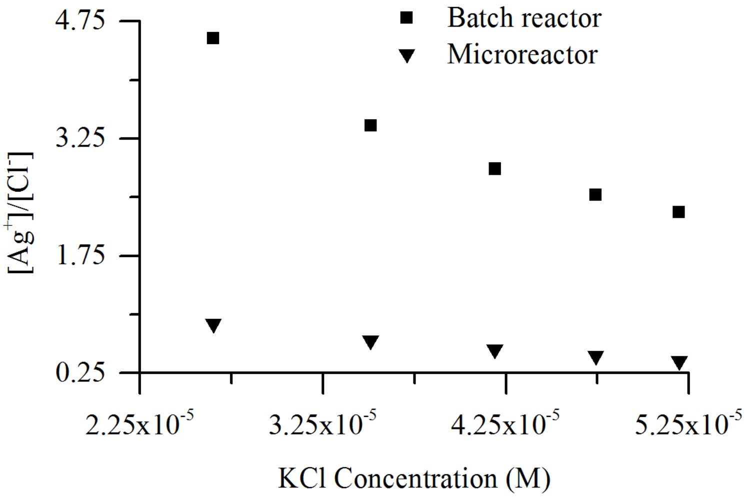

Figure 5.14: Ratio of $[Ag^{+}]/[Cl^{-}]$ in a batch and microreactor. Batch data from Cathcart et al. (2009).

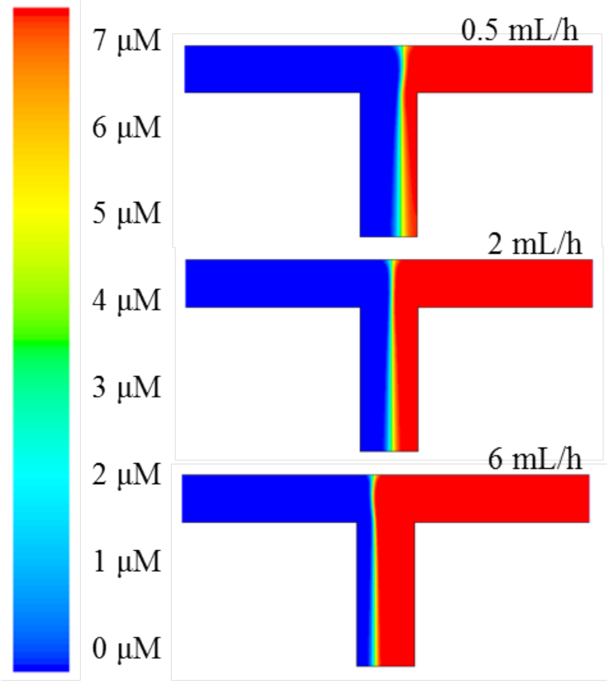

Figure 5.15: Contours of potassium chloride concentration, at different V_{T2}.

The diffusion coefficient of $NaBH_4$ employed for these calculations was 3.5×10^{-9} m^2/s (Chatenet et al., 2009). The mesh size was 0.02 mm as for the previous calculations.

Figure 5.16 shows the trend of the ratios of Ag^{+}/Cl^{-} and $(Ag^{+}\text{-}Cl^{-})/(BH_4^{-})$. The latter particularly shows how the ratio between the reducing agent and the inorganic precursor change after the subtracting effect of the chloride ions. This was important, as the greater the $(Ag^{+}\text{-}Cl^{-})/(BH_4^{-})$ value, the larger the colloid formed. This was true also in the absence of chloride ions and it was therefore important to understand how the particles' shape changed prior to the further growth due to silver ions release from AgCl in solution. It was also shown that the trend of the two ratios decreased for both

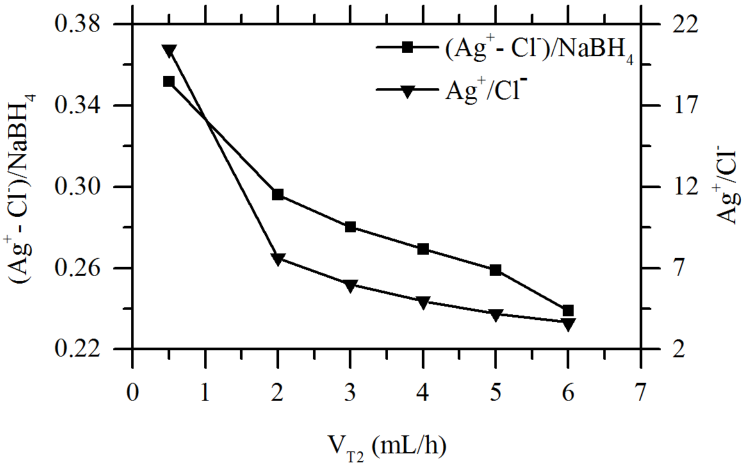

Figure 5.16: Changing in the Ag^+/Cl^- (■) and $(Ag^+\text{-}Cl^-)/(BH_4^-)$ (▼) as a function of changing in V_{T2}.

of them, with Ag^+/Cl^- showing a bigger change from the first and the second point of the series. In order to match the trend of spectral shift shown in Figure 5.12a, the trend of $(Ag^+\text{-}Cl^-)/(BH_4^-)$ should change its slope at 4 mL/h, leading to the formation of smaller colloid and therefore to more blue-shifted optical absorbance.

As the trend of the optical shift in Figure 5.12a was present when experiments were carried out by changing V_{T2} from both 0.5 to 6 mL/h and vice versa, this effect could not be due to fouling in the channel, otherwise differences in the spectra collected in the two different experimental setups would be observed.

An explanation could be found by taking into account the interparticles spacing and the effect that overlapping electronic fields had on the final optical properties of metal nanoparticles. Indeed, although the Mie theory is quite good in describing the optical properties of nanoparticles, it just takes into account a single, isolated particle. In real systems, instead, particles instead can aggregate and interact with other particles in solution. In particular the oscillating electrons on one particle can sense the electron field generated by the coherent oscillation of electron on near particles. This effect usually leads to a redshift of the peak as the particles distance decreases and to a blue shift when it increases. In this case, as the increase of V_{T2} dilutes the final solution of nanoparticles, the final optical properties can be affected by the increasing interparticles distance, i.e. the optical spectra blue shifts.

To confirm that the shift in the spectral position was due to chemical action of chloride ions and not just to the different concentrations of the precursors with the extra addition of solvent when KCl was added, experiments were carried out using just MilliQ water instead of KCl solution. Figure 5.17 presents the data collected under the same experimental conditions when water was used instead of chloride solution.

As shown, the trend of the shift followed a random pattern, confirming that chloride ions had an effect in changing the optical response of the nanoparticles. Unfortunately, these experiments also pointed out that the blue shift of the last two samples was not due to

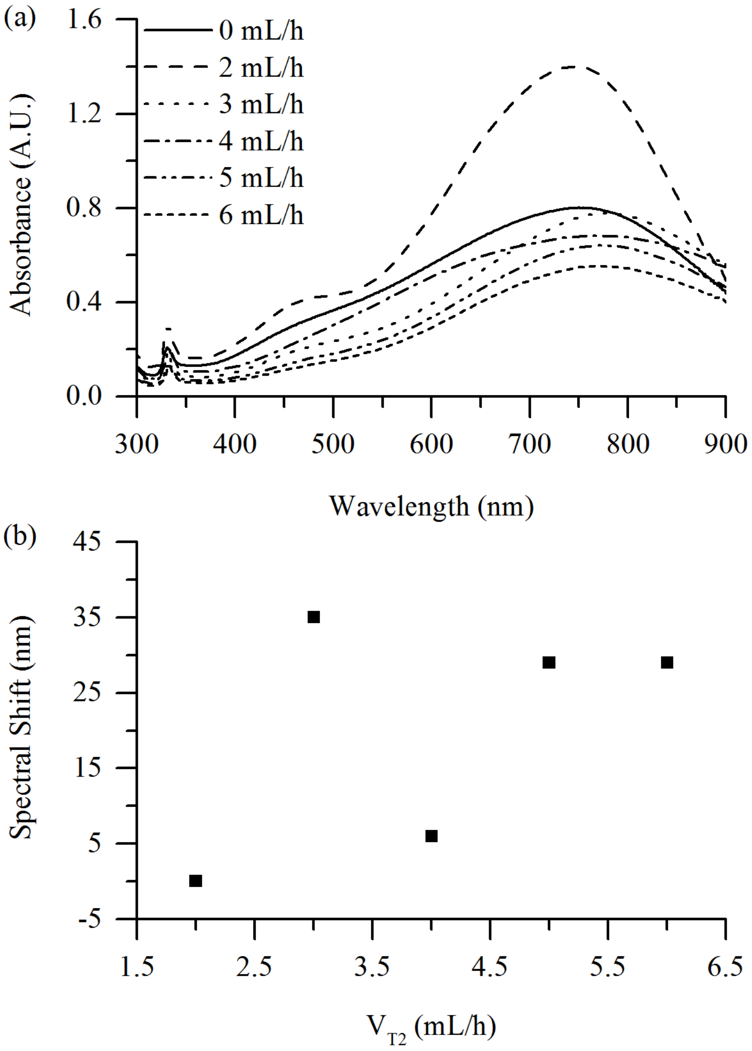

Figure 5.17: (a) UV-vis spectra and (b) spectral shift for sample prepared flushing water through V_{T2}, changing its flow rate from 2 to 6 mL/h

the interparticles distance changing, as otherwise the same effect would be observed also in these experiments. When no KCl was present all the silver ions react instantly with $NaBH_4$ in a short space-temporal windows and this could allow them to aggregate and form larger nuclei

5.2.4 Modification with KBr

Microreactors can be used in order to modify particles by post-synthetic etching of particles with Br^-. Bromide ions are indeed able to remove silver from the colloid, starting from the tips (which are the more reactive parts of the nanoparticles), and slowly round them until a final circular shape is reached. This change in the geometries has a clear effect on the SPR, because the more the particles shape changes from triangular to discs, the more λ_{max} shifts to shorter wavelength. A good indicator of this transformation is the disappearance of the peak at ~350 nm which is characteristic of triangular nanoprisms.

Compared to the modification of nanoparticles with chloride ions during their formation, the post synthetic modification of SNPs with bromide ions does not suffer from reliability problems that can be caused by the fouling of silver colloids on to the channel surface as the preformed particles are more stable and do not interact with the OH groups on the glass wall surface.

To estimate the effect of the bromide ions, a KBr solution (0.001 mM) was injected in C_4 and C_6 (see Figure 3.7) while the central flow was injected with a constant flow in C_5. This experimental setup was chosen in order to replicate experimental conditions reported in the literature (Tang et al., 2009). In particular, the flow of the central stream used in the experiment was chosen to be 8 mL/h (in order to mimic the outlet flow of Microreactor 1 when no KCl is flushed), while the lateral streams were varied from 4.3 to 5.5 mL/h (0.6 mL/h steps). As the change in the spectral proprieties was not instantaneous, the reacting solution was left to react overnight and monitored with spectroscopy. The results are shown in Figure 5.18.

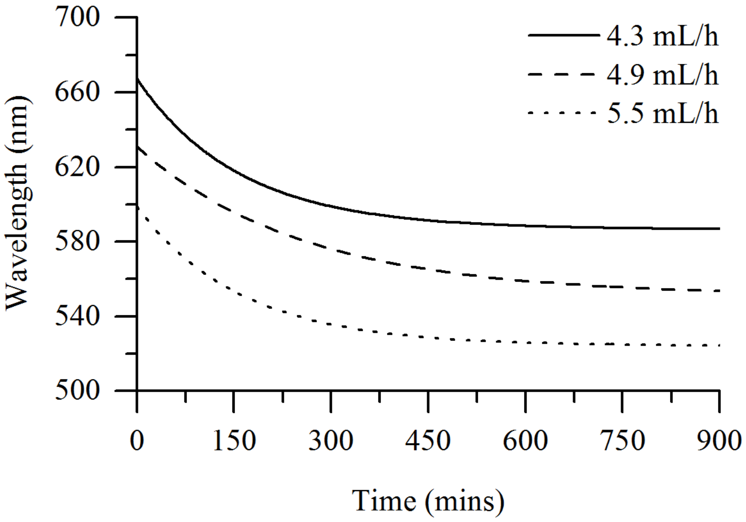

Figure 5.18: Spectral shift versus time of nanoparticles etched with different amounts of bromide ions.

As seen in the figure, when the flow rate of bromide solution is increased, the spectral position of the SPR shifted to shorter wavelength. After the minimum wavelength, a plateaux was reached indicating that no more etching of particles occurred in solution. Monitoring of changing in absorbance intensity could be used to study the kinetics of etching and make a comparison with data reported in the literature. In order to monitor the changes, volumes of potassium bromide solution (see Table 5.2) were injected in C_4 and C_5, with a constant flow of 2.1 mL/h. The central stream flow, on the other hand, was 8.5 mL/h. Furthermore, the length of the outlet PTFE tube was cut to just 1.5 cm in order to reduce the residence time of the reacting solution inside the microreactor.

Sample	**[KBr] in the syringe [mM]**	**[KBr] in the channel [mM]**
1	0.20	0.1
2	0.42	0.2
3	0.83	0.4
4	1.25	0.6
5	1.7	0.8
6	2.09	1

Table 5.2: Concentrations of KBr used for collecting kinetic data for the etching of silver nanoparticles.

All samples prepared with this method showed the same absorbance in the yellow region of the visible spectra. This suggested that the concentration of KBr in the reactor was too high and its effect on the particles was so strong that it was impossible to discriminate different effect between the different samples. Even when the concentration of the bromide solutions was reduced 100 times, Sample 5 and Sample 6 already showed a yellowish colouration when collected, giving no useful information about the absorbance shift.

To overcome this problem the flow rates of both the KBr solution and the SNPs solution were doubled to halve their residence time in solution. The samples collected this time appeared to be suitable for measuring the kinetic constant as when they were collected they still showed a blue colour. The main issue of this technique was that during the collection of the samples in the vial prior to the UV-vis spectra collection the solution kept reacting creating a gradient inside the vial between particles reacted for different times. For this reason the data collected with this method were not convincing and further investigations are required in order to determine proper kinetic values.

5.2.5 *In-situ* Microspectroscopic Monitoring within a Microfluidic Reactor

With recent advances in microfluidic technology, microreactors have proven to be an excellent platform not only for carrying out chemical reactions, but also for real time monitoring of reaction progress in order to elucidate the reaction mechanism and kinetics. As reactions evolve along the whole microchannel length, all the chemical species are present simultaneously at different points along the channel allowing detection of reaction progress in a spatially-resolved format. In particular for the formation of nanoparticles, changes in optical properties of the reaction system can act as direct indicators

---

The optical setup here reported was developed by R. Zmijan, University of Southampton.

for the transition from seeds to the final desired nanoparticles (Salvati et al., 2005). Unfortunately due to the resulting short optical path length of microchannels, this method becomes problematic where low absorbances are to be detected.

Although successful attempts have been made to increase the optical path length, e.g. by increasing microchannel dimension for a selected section, or adding optical elements for multi-pass spectroscopy (Rushworth et al., 2012; Yue et al., 2012), they generally limit the detection to specific points of the channel.

In our optical setup, on the other end, a 10 W tungsten halogen lamp was used as the light source linked through an optical fibre (i.d. 600 μm) to an inlet tube which held a collimating lens (focal length 25 mm) and an aspherical achromatic lens (focal length 40 mm) (Figure 5.19a). This setup allowed us to focus the divergent light from the inlet tube to pass the microfluidic channel at its thinnest beam waist, without the need of optical elements or wider channel portions on the microreactor. An other assembly of lenses was connected to the side port of the microscope to focus the light in the detector optical lenses (Figure 5.19b).

With this setup a minimum integration time of 1.050 ms was reached, which is the lower limit of the detector, but sufficient for the light source to almost reach the

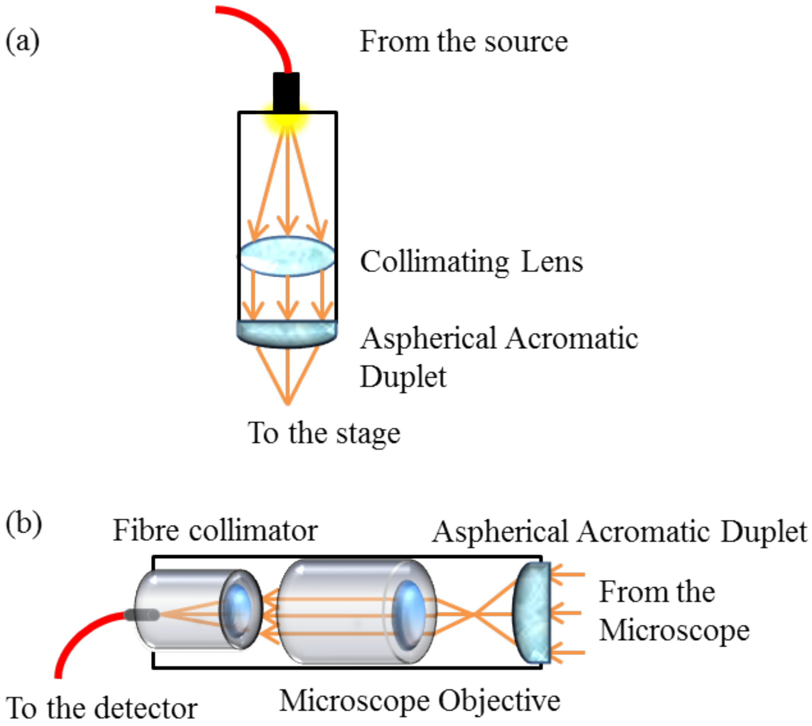

Figure 5.19: (a) Optics of the inlet tube used for focusing the diffusing light from the optical source to the microscope stage. (b) show the schematic of the outlet tube connetcted to the side port of the microscope. The light is first compressed by the aspherical achromatic lens and the microscope objective and then focused in the optical fibre by a collimator.

saturation limit with the built-in zoom of the microscope (1.6×) and the 60× objective (see Appendix B.2).

The size of the light spot (250 μm) compares well with the width of the microfluidic channel (210 μm) which grants an excellent space resolution, and the spot can be moved precisely to the selected point of interest along the microchannel with the X-Y microscope stage.

For the precise light delivery to the detector, the microscope condenser lens holder was replaced with a custom assembly that held the inlet tube in alignment with the optical axis of the microscope objective.

5.2.5.1 System Validation

The developed system was validated against a conventional bench spectrophotometer by measuring the absorbance of solutions at known concentration levels. Figure 5.21 shows sample spectra collected from aqueous tartrazine solutions in a concentration range of 20-100 μM passing through the microreactor channel. For comparison, spectra collected from samples with the same concentrations using the benchtop spectrometer (with a 1 mm optical path) are also displayed.

As can be seen from Figure 5.21a, the spectra collected from the microreactor match very well with that from the spectrometer cuvette by taking the different path lengths into account (i.e. 300 μm for microreactor, and 1 mm for spectrometer cuvette); all spectra exhibit a maximum absorbance peak at ∼425 nm (Jain et al., 2003). In addition, the limit of detection (LOD) was found to be 20 μM for tartrazine solution in the microreactor. For a similar application Waechter et al. (2009) achieved an LOD of 5 μM, however, with more complex techniques employed, including a fibre-loop ring-down spectrophotometer and a diode laser system.

To quantify the system, the extinction coefficient of tartrazine was determined using λ_{max}=∼425 nm (Figure 5.21b). The response is linear in the range of 30-100 μM,

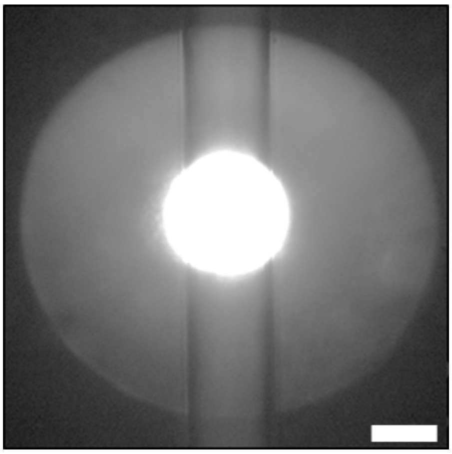

Figure 5.20: Focused light spot on the microfluidic reactor channel (scale bar: 200 μm).

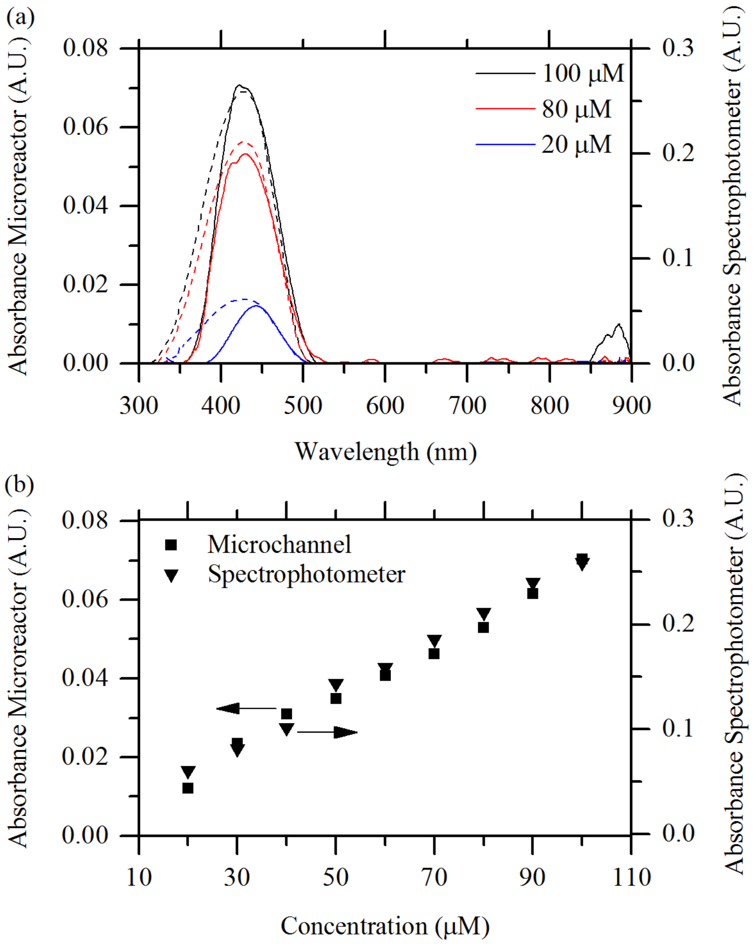

Figure 5.21: (a) Absorbance spectra collected with the microscope-coupled spectrophotometer from the microreactor (—), and with the bench spectrophotometer (- - -). (b) Absorbance of tartrazine solution measured with the microscope-coupled spectrophotometer (■), and with the bench spectrophotometer (▼) at a wavelength of 425 nm.

and the obtained value of ε=2.3×10^4 M^{-1}cm^{-1} agrees well with measurements using a standard spectrometer and with literature values (Waechter et al., 2011).

Analogous results were obtained using copper nitrate trihydrate (10-50 mM) at λ_{max}=~809 nm (see Figure 5.22). The validation performed using copper nitrate trihydrate solution showed a good agreement between the two instruments. The LOD was calculated to be of 10 mM (which was higher than using tartrazine solution, due to the lower ε of this species compared to tartrazine). Even in this case the spectra show a good overlapping by taking into account of a different optical pathlength (l=10 mm) of the spectrometer cuvette. Thus the system yields valid numbers over a detection range of at least 400-800 nm.

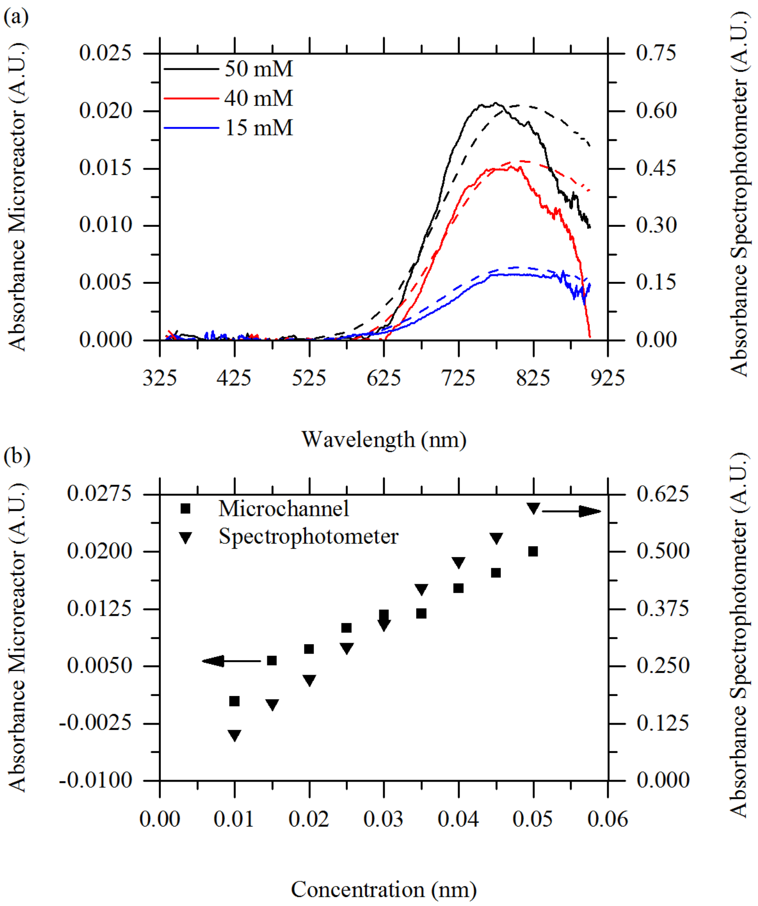

Figure 5.22: (a) Absorbance spectra collected with the microscope-coupled spectrophotometer from the microreactor (—), and with the bench spectrophotometer (- - -). (b) Absorbance of copper nitrate solution measured with the microscope-coupled spectrophotometer (■), and with the bench spectrophotometer (▼) at a wavelength of $\sim$809 nm.

5.2.5.2 Nanoparticles Formation Monitoring

Following the validation of the system, we used the setup to monitor the formation progress of silver nanoprisms within the microfluidic reactor shown in Figure 3.5, prepared according to Section 3.3.6.1. The flow rates of the three streams were optimised to be 1.4 mL/h for both C_1 and C_3, and 2.4 mL/h for C_2 due to the different size and geometry of the microreactor.

It is generally understood that following the mixing of the reagents under these conditions, the formation and growth of silver nanoprisms takes place along the microreactor channel (Knauer et al., 2012). Also, the absorbance spectral position (λ_{max}) and its broadness depend on the size and shape distribution of the nanoparticles (Aherne et al., 2008). Therefore, by monitoring the spectral and absorbance changes at different points along the microreactor channel, the formation process and associated rapid changes in size and shape of silver nanoprisms could be spatially resolved.

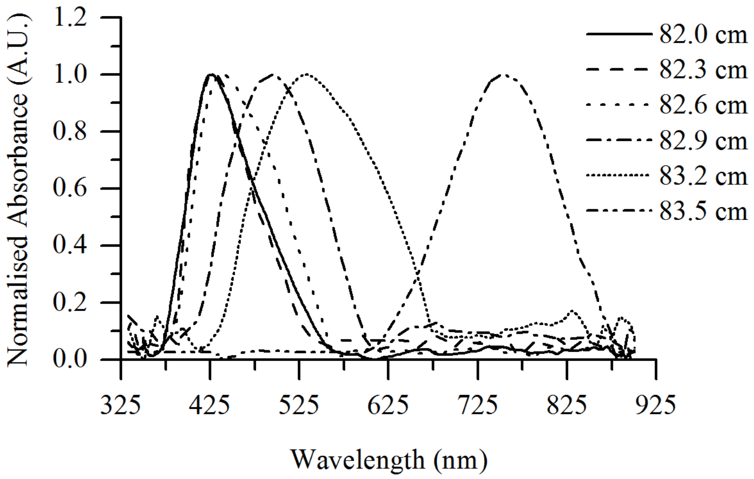

Figure 5.23: Spectral position shift of the absorbance band as a result of detection at different points along the channel.

Figure 5.23 shows the optical absorbance spectra taken from the reaction solution within the microreactor with the incident light beam focused at the middle plane of the microchannel at different positions along the channel.

It is interesting to note that the change occurs in a very short part of the channel, while the spectral properties do not change before or after these points. Beyond the point of 83.5 cm no spectral shifts were observed indicating the formation of a stable colloid systems. The long persistence (several minutes) of the yellow solution indicating spheres were also observed in batch reactors, followed by a rapid colour change to give prisms (Métraux and Mirkin, 2005). However, in the microreactor system this process took place in a much shorter time period. The first stage lasted for about 35 seconds (i.e., the residence time at the point of 82 cm) rather than minutes, and rapid change occurred within one second (from the point of 82 cm to 83.5 cm). The mechanism for this significantly faster kinetics within the microreactor is still unclear, and would need further investigation.

5.2.5.3 Single Point Experiments

Once the region of the channel, after which no more changings were observed, was identified, the total flow rate V_{tot} was varied in order to monitor how it affected the optical properties of SNPs. Figure 5.24 shows a clear red-shift of the optical absorption in response to V_{tot} variations (while keeping C_2 at a constant flow rate of 2.4 mL/h). Particularly, reducing V_{tot} from 5.6 mL/h (C_1=C_3 =1.6 mL/h) to 5.2 mL/h (C_1=C_3=1.4 mL/h), the positions of the absorption bands shift from 753 to 834 nm, respectively.

These data confirm that fluidodynamic parameters can affect the final optical properties of SNPs as already observed in Section 5.2.1.

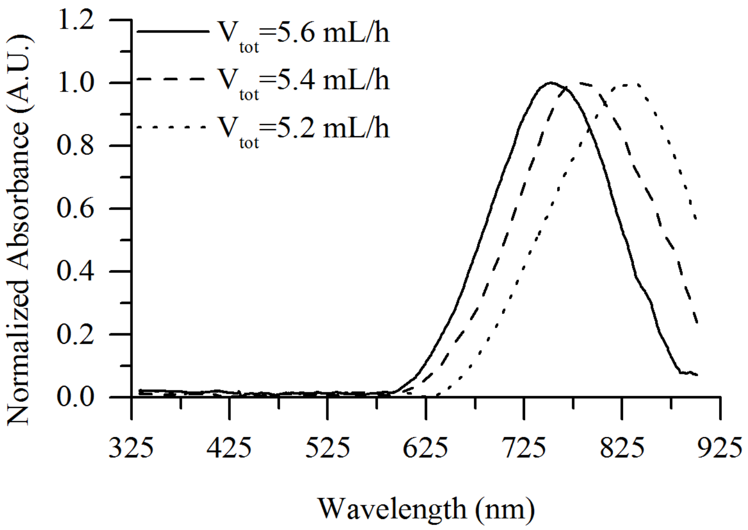

Figure 5.24: Spectral position shift of the absorbance band as a result of different flow rate in the later channel.

5.3 Conclusions

A novel microfluidic reactor design for the synthesis of triangular silver nanoprisms is presented, and the effect of different fluidic conditions on the characteristics of the produced nanoparticles has been studied. We have demonstrated that the flow rate ratio and the total flow rate can be adjusted independently to control the spectral position and the peak broadness of the absorbance spectra of the nanoparticles. By varying both parameters simultaneously, fine tuning of the optical properties can be achieved. In order to demonstrate that this effect is not due to the effect of different concentration of reagents inside the channel, batch experiments were carried out, showing that controllable changes in optical properties are due to the microfluidic conditions and cannot be replicated in a batch reactor. To the best of our knowledge, this is the first time that the optical properties of triangular shaped silver nanoprisms can be tuned in a microreactor without a seed mediated approach. The reactions carried out in the microreactor showed a faster kinetics than the traditional batch reactor, as nanoparticles are formed in seconds rather than minutes. TEM analyses were carried out to compare the spectrophotometric characteristics with the particles shape and size distribution. Image analysis of the TEM pictures showed that the redshift in the spectral position was due to an increase in the edge length, while the narrowing of the peak is related to the increase in the percentage of triangular shaped particles. Though particles obtained from seed-mediated approach showed a better quality, our setup allowed a good degree of controllability, reproducibility and shape selectivity by using a very simple micro-reactor design. Furthermore, the device was tested over a long period of time to prove its robustness and its potential industrial applications; the data collected demonstrate that the device was capable of synthesizing homogenous nanoparticles over a long period of time with reduced clogging owing to hydrophobic functionalisation of the internal walls of the channels.

A microreactor for the *ante* and *post* synthesis modification of silver nanoprims with halide ions was developed. Particularly, the particle size could be modified by adding KCl to the $AgNO_3$ solution before its reduction with sodium borohydride. By increasing the flow rate of the chloride solution it was possible to appreciate a significant red-shift of the in-plane dipole resonance while KCl flow rate being greater than 4 mL/h led to a spectra shift to blue. CFD simulations for monitoring the changes of species concentration in solution as V_{T2} changed revealed that this change in the trend of the spectral position shift could be due to change in the ratio between the inorganic precursor and the reducing agent. Experiments using water instead of KCl solution suggested that the trend of the red-shift could be a combined effect of diffusion and concentration of reagent. Post modification of the nanoparticles synthesised in the first channel was carried out with KBr by mixing the particles and the bromide ions in a following microchannel. Changes in the spectral position were monitored by cyclic spectroscopy and could be used for determining the kinetic constant of the etching of silver nanoprisms. Unfortunately, the large volume of the UV-vis cell and the introduction time prior to their collection did not lead to reproducible results. These experimental setups allowed reducing the standard deviation in the spectral shift of nanoparticle due to halide ions making their use a reliable way to control the final shape of these particles.

To monitor the shape and size changing during nanoparticles formation, a unique microscope-coupled microspectrophotometer for *in situ* monitoring of reaction evolution within a microfluidic reactor was developed. Collimating the light by use of a custom-made set of lenses allowed the light to be focused in small spots, and short integration times were reached along with excellent spatial resolution. The add-on optics had no effect on the use of the microscope, and the system serves well for both spectra and image acquisition. Reducing the fibre diameter, smaller spot sizes could be achieved, which may improve the spatial resolution of the measurements in the channel, however, this result in an increase of the integration time (as the light source intensity decreases with smaller fibres). Validation against conventional spectroscopy, demonstrated that the application of the system to successfully monitor the shape and size evolution of silver nanoprisms during their formation within a microfluidic reactor. This could provide crucial information for further design and control of production of nanoparticles with desired geometries and properties (Shestopalov et al., 2004). The system will be useful for a wider range of spectroscopic measurements, avoiding complex designs of integrated micro-optics into the microfluidic devices.

Chapter 6

Coating and Functionalisation of SNPs by Sol-Gel Chemistry

Contents

6.1 Introduction

Coating of metal nanoparticles with SiO_2 has always been a hot topic since Liz-Marzàn first proposed the stabilization of gold with silica, using (3-aminopropyl)-trimethoxysilane as a primer for starting the growth of the silica shell on the metal surface (Liz-Marzán et al., 1996). Silica shell around the metallic core acts as protecting agent, with some advantages compared to other stabiliser, such as the chemical inertness of SiO_2, its optical transparency and the possibility of functionalise the surface owing to the well-known sol-gel chemistry.

The sol gel process is a well-known reaction in which a colloid solution of alkoxysilane (such as TEOS, and also others like tetramethyloxysilane, TMOS) acts as precursors for forming a network of silicon atoms connected each other through O-Si-O atoms (gel). This method is based on the hydrolysis and condensation of the alkoxysilane (Si-OR) groups as shown in Figure 6.1. These processes are catalysed by acids and base, respectively. The sol-gel method can also be used to easily prepare silica spheres with the diameter of a few nanometres by a reaction commonly known as the Ströber method (Giesche, 1994).

This protocol consists of a sol-gel reaction carried out by diluting the alkoxysilane precursor in an excess of water, into which EtOH and NH_3 (the catalyst) are added and the resulting solution is left stir. The Ströber method has been largely employed also for the preparation of (metallic core)/(silica) ($M@SiO_2$) nanostructure. The silica particles present in solution, indeed, can deposit on the metal nanoparticles surface and there coalesce in bigger structure, forming the external shell.

Most of the methodologies found in the literature for coating metal nanoparticles take advantages of primers with two different functional groups to improve the deposition of tetraethyl orthosilicate (TEOS) on particles surface and allow the silica shell to grow. These primers are usually organosilanes with amino (Liz-Marzán et al., 1996; Ung et al., 1998), (-NH2) or thiol (-SH) (Cui et al., 2011; Kobayashi et al., 2004) groups on one side to from strong interactions with the positive charged metal cores, while the other side carries alkoxy groups which can undergo the sol-gel process with TEOS particles in solution. Advances in nanotechnologies have led to the development of methods for

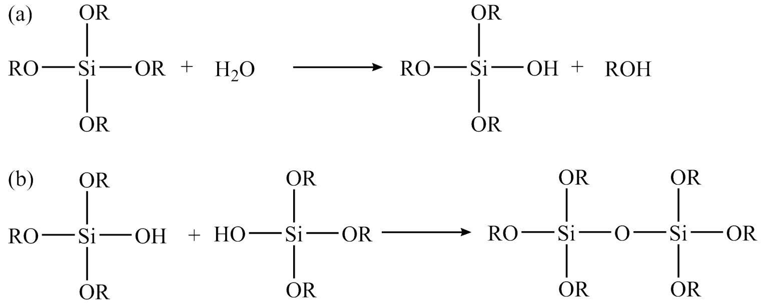

Figure 6.1: Sol-gel process. Figure 6.1a shows the hydrolisation of TEOS while Figure 6.1b shows its condensation.

directly coating metal nanoparticles without the need of using coupling molecules to enhance the deposition of the silica particles, and direct coating of gold nanospheres (Lu et al., 2002), silver nanoparticles (Graf et al., 2003) and silver nanowires (Yin et al., 2002) have been reported in the literature.

In this chapter, coating of triangular silver nanoprisms is presented. Particularly, the attention has been focused on the effect of different bases on the final thickness of the shell and the final shape of the metallic core. Time of the reaction has been taken into account as well. The functionalisation of the so-formed particles (SNPs@SiO_2) has been performed using three different organosilane, i.e. (3-mercaptopropyl)trimethoxysilane (MPTMS), (3-mercaptopropyl)triethoxysilane (MPTES) and allyltriethoxysilane (ATES) and characterised with several techniques including UV-vis, fluorescence, IR spectroscopy and TEM.

6.2 Results and Discussion

6.2.1 TEOS Coating of Silver Nanoparticles

Compared to other metal nanoparticles, the coating of silver nanoparticles with silica is more difficult to achieve, mainly due to the $Ag^{(0)}$ instability in the presence of ammonia or ammonia based catalyst commonly employed to accelerate the hydrolisation of silica precursors (such as TEOS). This instability is often observed by the damping of the plasmon resonance of silver nanoparticles in the presence of NH_3; this phenomenon can be explained by the aerial oxidation of metallic silver in the presence of ammonia, as shown in Reaction 6.1:

$$4\,Ag^{(0)} + 8\,NH_3 + O_2 + 2\,H_2O \longrightarrow 4\,Ag(NH_3)_2^{+} + 4\,OH^{-} \tag{6.1}$$

The solubilisation of silver bring to the formation of transparent ammonia complex and, therefore, to a reduction of the intensity of the particles absorbance in the visible range (Kobayashi et al., 2005; Ung et al., 1998). Using bulkier ammonia based catalyst, such as methylamine (MA) and dimethylamine (DMA), on the other hand, led to a similar phenomenon, but in this case the plasmon damping was due to a reduction of the surface charge on the particles (Ung et al., 1997). This phenomenon was due to the absorption of catalyst onto the surface of the particles (Ung et al., 1997, 1999), and therefore depended on the size of the catalyst, i.e. the bulkier the molecules, the less that can be absorbed onto the surface of the colloid. It was reported the reduction of the damping from around 50% to ~13% when a bulkier base such as MA was used instead of ammonia. Use of DMA drops the damping to ~0%. This method, unfortunately, was proven to be ineffective in coating triangular silver nanoprisms, as significant etching and aggregation of the silver core was observed even when working with a lower concentration of DMA (Xue et al., 2007).

In order to achieve coating of SNPs without affecting their optical properties (i.e. avoiding etching and aggregation) an additional stabilisation was needed. In particular, MHA was proven to be particularly efficient in protecting the particles surface from DMA, blocking it from reaching the surface. MHA was very suitable for passivating silver nanoparticles as it bound very strongly to them thankfully to the SH group on one end of its long alkylic chain. The carboxylic group on the other end of the chain, instead, kept the particles soluble in water (Xue et al., 2007). When MHA surrounded the prisms the dielectric constant around the particles changes (i.e. it increases), a change in the optical properties could be also observed as the plasmon band moved to higher wavelengths (Kelly et al., 2003; Xue et al., 2005).

Figure 6.2 shows the spectral shifts of nanoparticles protected with different volumes of MHA. As shown, the red-shift varies from a maximum of ~24 nm to a minimum of ~14 nm, when the largest volume of MHA is added. The small differences in the spectral position of nanoparticles indicate that the original concentration is sufficient to give a good coverage of the particles surface.

As MHA was added as an ethanolic solution, experiments to prove that the red-shift was not due to the presence of EtOH were carried out. Spectral shifts with different concentrations of EtOH are shown in Figure 6.2. As shown by spectral shifts in Figure 6.2, the addition of EtOH does not significantly affect the spectral position of the intense dipole absorption of the nanoparticles, as expected.

Regarding the choice of catalyst, it was reported that the bulkier the ammonia based catalyst the less was the damping of nanoparticle absorbance (Kobayashi et al., 2004). Particularly, DMA proved to be efficient for catalysing the hydrolisation of TEOS for forming a shell around both spherical and triangular particles. To confirm if a base bulkier than DMA could lead to even better results, different concentrations of

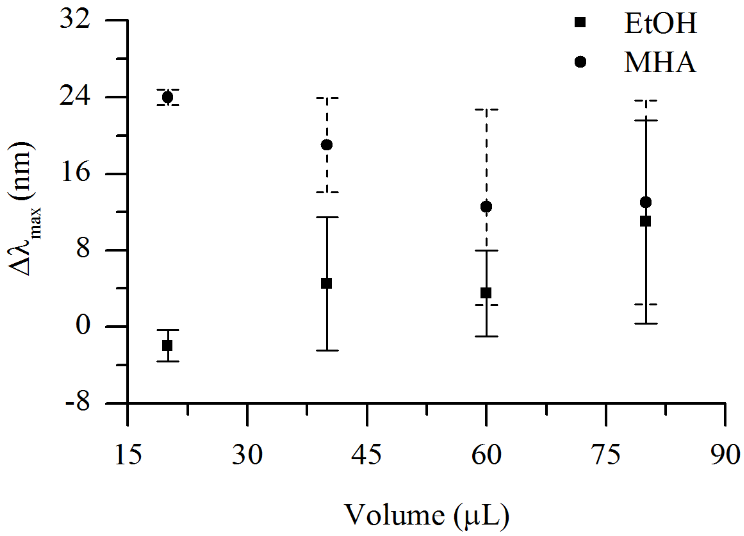

Figure 6.2: Red-shift of nanoparticles λ_{max} when different volumes of EtOH (■) and MHA (●) are added.

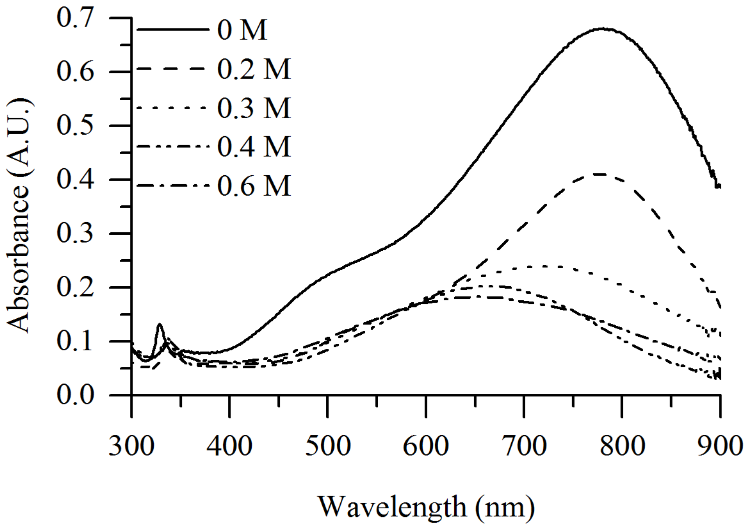

Figure 6.3: Effect of different concentrations (0 (—), 0.2 M (- - -), 0.3 M (· · ·), 0.4 M (··-··) and 0.6 M (·-·)) of DEA on the final SPR of nanoparticles. As the concentration increases, the absorbance is damped and the maxima wavelength moves to higher energies.

diethylamine (DEA) were used and the effect of the plasmon resonance of the prims was monitored by UV-vis spectroscopy. Figure 6.3 shows that the spectra of particles prepared with different concentrations of DEA show a blue-shift of their spectral position as the base concetration increases. The maximum concentrations was choosen to be similar to the concentration of DMA used by Xue et al. (2007).

In contrast to the red-shift observed with the silica shell formation around the silver nanoparticles core (Xue et al., 2007), the blue-shift observed in the presence of DEA, could be due to the etching of silver nanoparticles. This etch could be due to the fact that diethylamine is a stronger base than DMA (pK_b=2.91 and pK_b=3.36, respectively). As reported in the literature (Shabbeer et al., 2012), the presence of strong base in silver nanoparticles solution could bring to the solubilization of $Ag^{(0)}$ and therefore to the distruction of the metallic core. This effect was shown even for lower concentration of DEA (<0.2 M), as shown in Figure 6.3.

Regarding the use of DMA as catalyst, better results could be achieved. The spectral position of in-plane dipole resonance of SNPs moves to up 70 nm when the nanoparticles are redispersed in a solution in TEOS, as shown in Figure 6.4. The final red-shift is due to the effect of both MHA passivation and silica coating. According to the literature Xue et al. (2007) this shift can be related to a shell thickness of round 15 nm. Different experiments have shown that the shift of the plasmon resonance is not always observed as a consequence of the formation of the silica shell. For this reason different concentrations of silver nanoparticles solution were used in order to identify the experimental condition for which the maximum red-shift was achievable.

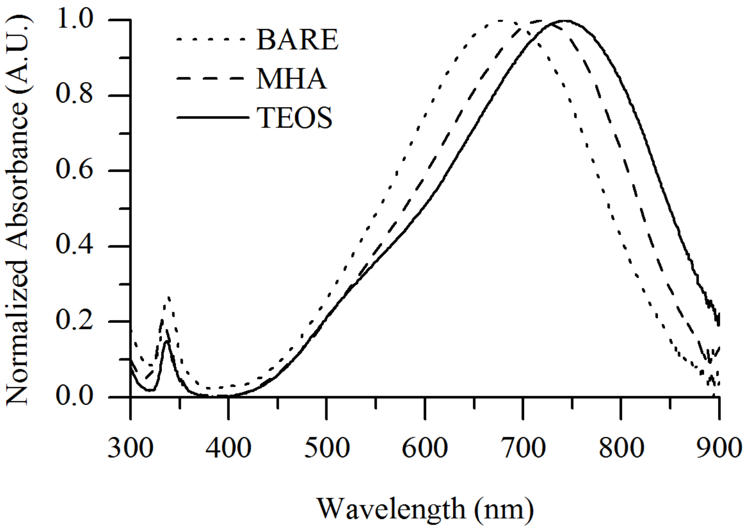

Figure 6.4: Typical red-shift of bare silver nanoprisms SPR (···) after the addition of MHA (- - -) and TEOS (—).

As estimating the concentration of triangular particles could be difficult, the absorbance value was taken into account as indicator of the concentration of particles in solution. The different experimental conditions and the red-shift achieved after the addition of MHA (ΔA) and after the formation of the silica shell (ΔB) are shown in Table 6.1

Absorbance [A.U.]	$\Delta\lambda_{max}$ **MHA[nm]**	$\Delta\lambda_{max}$ **TEOS [nm]**
0.2	22.0	38.0
0.3	28.0	48.0
0.4	31.5	44.0
0.5	24.0	36.0
0.6	24.5	40.0
0.7	38.0	28.7
0.8	30.0	37.0
0.9	38.5	37.0
1.0	36.5	24.0

Table 6.1: Different spectral position of the in-plane dipole absorbance for different concentrations of nanoparticles, reported in function of their absorbance, (a) after the addition of MHA and (b) after the formation of the silica shell.

By plotting the data of Table 6.1 ($\Delta\lambda_{max}$ MHA and $\Delta\lambda_{max}$ TEOS) versus the absorbance of the starting silver nanoparticles solution, two different trends can be observed (Figure 6.5). Particularly, the shift caused by the addition of MHA shows a general increase as the absorbance of SNPs get higher. The change in spectral position caused by the formation of the silica shell, on the other hand, shows a decrease from the Absorbance=0.2 to Absorbance=1.

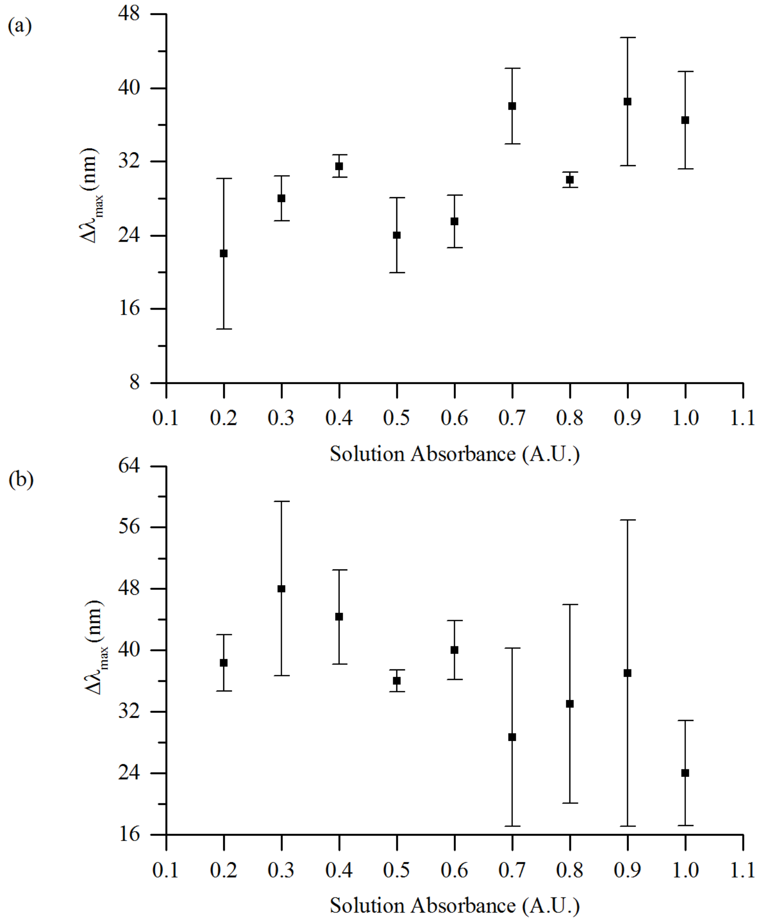

Figure 6.5: Different spectral position of the in-plane dipole absorbance for different concentration of nanoparticles (reported in function of their absorbance) after the addition of MHA (Figure 6.5a) and after the formation of the silica shell (Figure 6.5b).

This trend could be due to the fact that at lower concentration of nanoparticles, the thickness of the silica shell is bigger (for a constant concentration of TEOS solution). An issue of this method is the lack of reproducibility (particularly in terms of spectral position) after the formation of the silica shell. As even by changing the initial concentration of nanoparticles this effect was always present, a study on the reaction was carried out. Previous studies, show that the formation of the silica shell did not completely isolate the internal core from chemicals (Xue et al., 2007), and therefore, the basic environment of the reaction batch could affect the final optical properties (both the absorbance intensity and the spectral position) by etching the silver core. In order to monitoring the change of the maximum wavelength, different reaction times were employed. The experiments were carried by using nanoparticles prepared with and without PVP, to check if the extra stabilisation offered by the polymer during the synthesis of nanoparticles could grant better results.

Figure 6.6 shows the trend of both systems for reactions carried out for one, two and three hours, respectively. The first point of each data set represents the wavelength

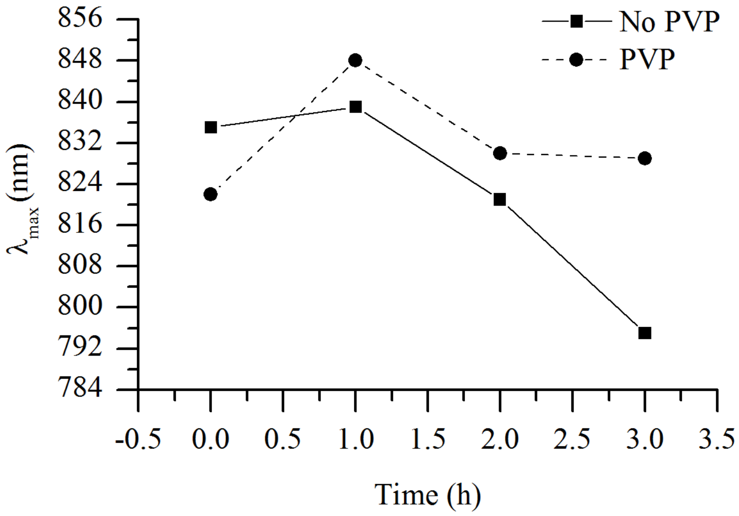

Figure 6.6: Spectral position of samples prepared with different spinning time, with (●) and without (■) PVP.

of the starting solutions. As shown, when the reaction time was increased, absorbance maximum changed; the shift either decreased or increased, according to Figure 6.6. The third and the fourth point of the series of particles prepared without PVP, moved to shorter wavelength than the starting one. The explanation of this phenomenon must not be found in a possible effect of PVP, which is indeed replaced by MHA, which has stronger interaction with the metallic particles. Figure 6.6 shows that the maximum shift is achieved after one hour of reaction for both experimental setups.

6.2.1.1 TEOS Coating TEM Images

The formation of the silica shell by condensation of TEOS around metal nanoparticles was monitored by electron microscopy. Figure 6.7 shows different images of silver nanoprisms coated with silica, using DEA as catalyst. The coating was far from the smooth and homogeneous compared to literature results (Xue et al., 2007). Particularly, no formation of silica shell was observed when [DEA]<0.4 M (Figure 6.7b). When higher base concentrations were used TEM shows the formation of a coating around SNPs core. Notably, in the images the edges of SNPs@SiO_2 are rough, in contrast to the smooth one reported by Xue et al. (2007). This could be due to high pH of the solution as suggested by Lu et al. (2004) who reported that an high pH could lead to faster the rate of growth of SiO_2 particles than the nucleation one. This lead to the formation of bigger particles which cannot pack properly on the nanoparticles surface. TEM images confirm what UV-vis analysis suggested; DEA is not a good catalyst for the formation of silica shell around silver nanoparticles.

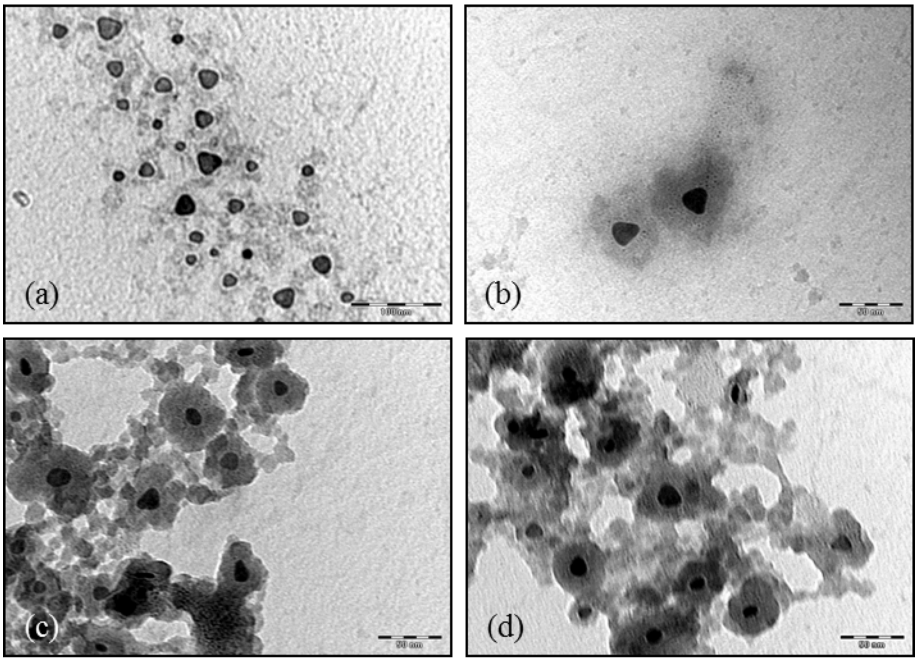

Figure 6.7: Nanoparticles prepared with different concentrations of DEA (see Figure 6.3). The scalebar is 50 nm, except for Figure 6.7a where is 100 nm.

When dimethylamine was used to catalyse the formation of silica shell, results were better than that obtained using DEA (see Figure 6.8).

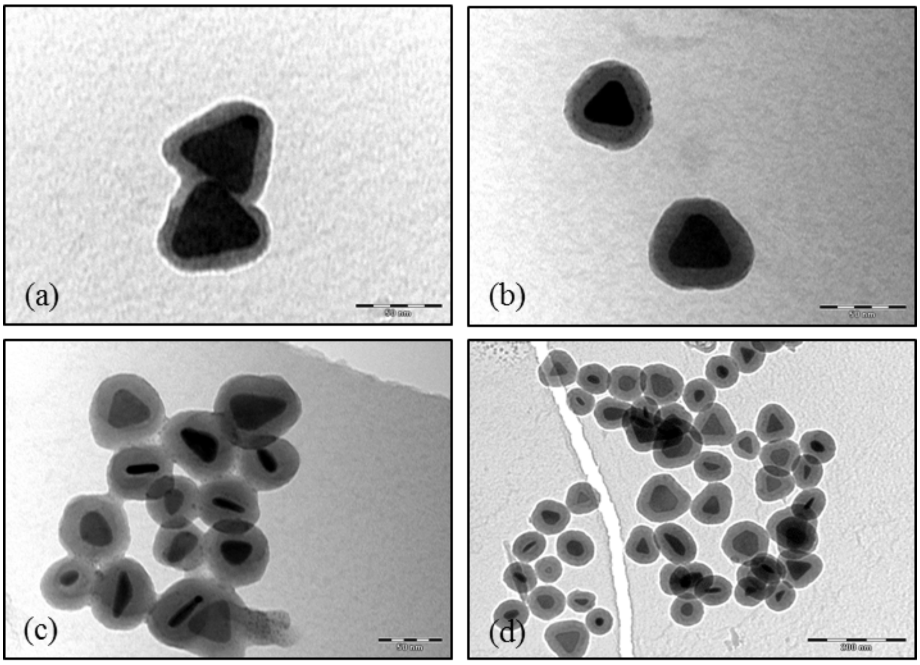

Figure 6.8: Examples of silver nanoparticles covered with silica shell. The scale bar is 50 nm for all the pictures with exception of Figure 6.8d, for which is 200 nm.

As indicated by the shift of the plasmonic band at higher wavelength, the formation of the coating was complete and similar to that reported in the literature. In particular, working with the TEOS concentration herein reported (0.5 mM), the average shell thickness obtained was ∼18 nm which was consistent with the magnitude of the optical shift. In contrast to that prepared with DEA, the outer surface of SNPs@SiO_2 was very smooth and the external shapes clearly resembled the geometry of the internal metallic core.

Regarding the effect of the reaction time on the final shape of the metallic core surrounded by the silica shell, TEM images were collected from samples prepared (with and without PVP) leaving the reaction to take place for one, two and three hours, respectively. In order to understand how the core shape was affected by reacting time, the percentage of triangles over other shapes was calculated. The results are reported in Figure 6.9.

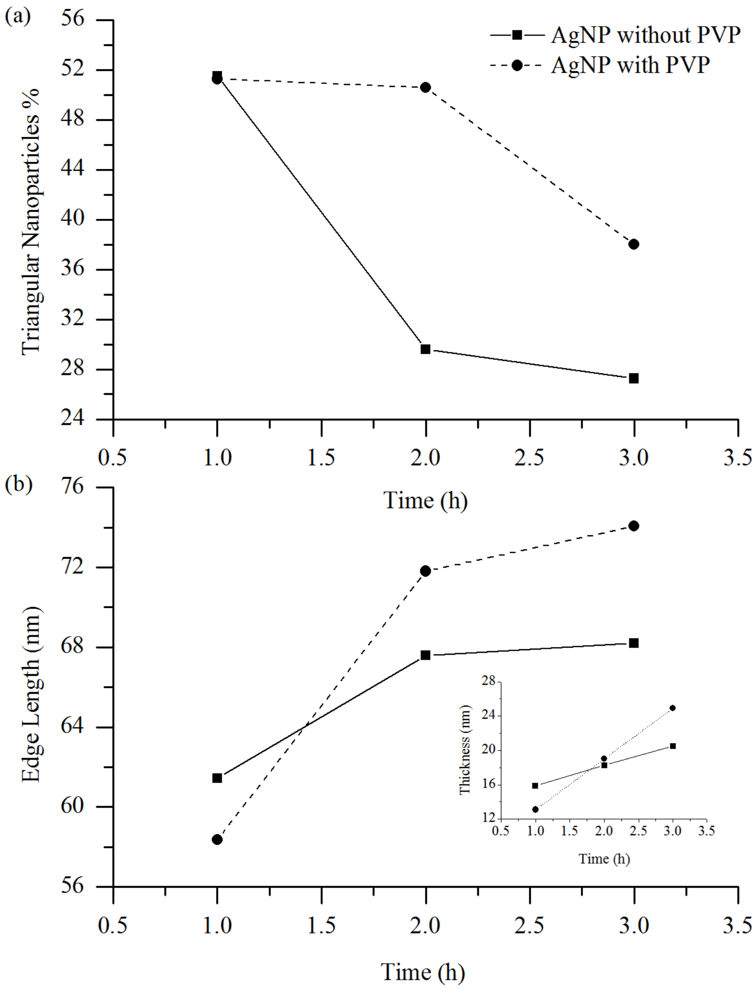

Figure 6.9: Spectral position of samples prepared with different spinning time, with (●) and without (■) PVP.

As shown in Figure 6.9, the longer time the reaction was carried out the smaller the percentage was for SNPs prepared in the absence of PVP, dropping from ∼50% with 1 hour reaction to less than ∼30% with 3 hours reaction. The size of both core and the core/shell was determined by using ImageJ and the results are shown in Figure 6.9. The trend of core/shell edge plotted versus time shows that the thickness of the particles increases when increasing time. This growth could be due to factors from both the deposition of other silica nuclei on the existing one, and the reduction of the internal core edge (see Figure 6.9b inset).

6.2.2 Thiol Functionalisation of SNPs@SiO_2

Coating of metal nanoparticles with a layer of silica adds new reactive site on the outer surface of those materials. Particularly, the presence of SiOH and Si-OR brought by the condensation of orthosilicate around the metallic core, makes them a good substrate for sol-gel reactions, opening to a wide range of possible functionalisation with several organosilanes and leaving intact the optical properties of the silver core. In order to study the functionalisation reaction for the system herein presented, condensation of organosilane with a thiol moiety (MPTES and MPTMS) was carried out. The first method tried to stick this functional group onto the silica was a co-condensation of the organosilane along with the TEOS.

Before the addition of MPTES (or MPTMS), TEOS was left to react for 2 hours to get a layer of silica already formed in order to grant the deposition of this material on the outer surface of the particles. Condensation of the organosilanes was catalysed by the DMA still present in solution. Contrary to other organosilanes, which condensation onto the silica shell stopped the growth by replacing the Si-OR and Si-OH with organic moieties, thiol deposited on SNPs@SiO_2 led to further growth of the shell thickness due to the formation of S-S bridges in the basic reaction environment. This change could be used for monitoring the functionalisation of the silica shell. Unfortunately, it was not easy to observe changes in spectral position due to change in shell thickness. For this reason 5,5'-dithiobis-(2-nitrobenzoic acid) (Ellman reagent) was employed to monitor the presence of SH groups on nanoparticles' surface. This reagent reacts specifically with thiol as the reaction led to the release in solution of a very intense yellow dye (absorbance at 412 nm) which could be used to monitor the exact concentration of SH in solution.

Figure 6.10 shows the reaction scheme of Ellmans reagent with thiols and the calibration curve prepared with different concentration of MHA. The sample was prepared with MPTES and the analysis with this method shows the absence of any absorbance around 412 nm. This lack in reactivity shown by the Ellman's reagent could be caused by:

1. Absence of thiol group on the silica shell (due to poor reactivity of MPTES or too a short reaction time);

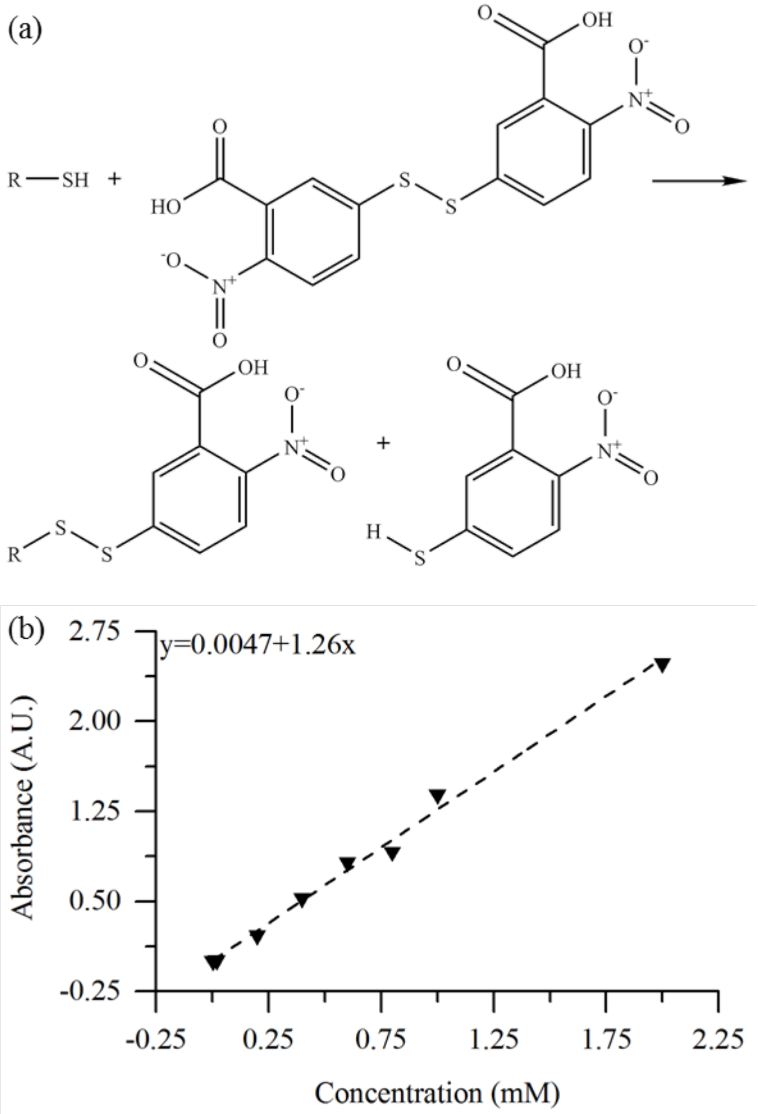

Figure 6.10: (a) Reaction scheme of the Ellman reagent in the presence of thiol and (b) the calibration curve of the absorbance versus the thiol concentration.

2. Formation of thiol bridges onto the nanoparticles surface;

3. Low concentration.

Regarding the first point listed above, more reactive MPTMS was employed instead of MPTES. No improvement was observed in the optical response of the Ellman reagent. Furthermore, the absorbance in the UV region of the spectra was the only one observed. Different reaction times were tried as well. However, protocols reported in the literature were found not to be useful as mixed information indicated different times as necessary for functionalise the surface of silica particles.

Xue et al. (2007), for example, stated that one hour was sufficient to achieve a good functionalisation and Claesson and Philipse (2007) reported an even shorter time (i.e. 40 minutes), while much longer times were reported by Yang et al. (2005) , that was up to 7 hours. In order to understand how the reaction time can affect the final coverage of SNPs@SiO_2 with thiol, three different samples (reaction times 2, 24 and 48 hours respectively) were prepared. Similar to the previous experiment, the Ellman's test showed no response to the prepared particles. Suspecting that the base used for catalysing the functionalisation might not be sufficient to grant a good functionalisation and that the simultaneous presence of MPTES/MPTMS and TEOS might affect the yield of the final coverage with thiol, post-functionalisation of the formed shell was examined using a stronger base as catalyst. In particular, after one hour SNPs@SiO_2 was spun down (30 minutes at 13,000 rpm, 2 times) and re-dispersed in an equal volume of solutions of MPTMS and/or MPTES (both 1 mM). To these samples, different volumes of NH_4OH (35% w/v) were added with the amount shown in Table 6.2:

Sample	**Volume of NH_4OH, (35% w/v) [nm]**
A	60
B	70
C	80
D	90
E	100

Table 6.2: Volumes of NH_4OH (35% w/v) used to catalyse the functionalisation of the silica shell surrounding the particles.

The samples were left to react for 48 hours followed by examination. It showed the samples were losing their colouration with just scattering present when UV-vis spectra were collected, for the samples prepared with both MPTMS and MPTES. This vanishing of colouration (also the vanishing of absorbance) could be caused by the interaction of the metallic core and the base while the scattering may be due to the condensation of the alkoxysilane and the formation of the S-S bridges on the silica particles, leading to the formation of big silica particles.

Regarding formation of thiol bridges onto the nanoparticles surface, it may relate to the possible formation of thiol bridges both during the deposition of the organosilane on the surface and during the Ellman test (which was performed in basic conditions). Regarding the latter point, $NaBH_4$ (0.1 M, 10 μL) was added prior to the addition of the Ellman reagent in order to cleave thiol bonds that could be formed after the re-dispersion of SNPs@SiO_2 in the buffer for the Ellman test. Even this measure did not improve the identification of the functional moiety that should be present on the surface of the core/shell particles. Regarding the former point, comparison between acid and basic catalysis was carried. Use of acid catalyst could indeed avoid the formation of S-S bridges, leaving -SH on the particles surface. In this respect, reactions with different amount of acid (i.e. acetic acid, 20% v/v in water) and the base (i.e. DMA) were carried out, as reported in Table 6.3.

Sample	**Volume of Acetic Acid, (20% v/v)** [μL]	**Volume of DMA, (20% v/v)** [μL]	**Catalyst Concentration** [M]
A	33	25	0.11
B	66	50	0.22
C	133	100	0.44
D	200	150	0.66
E	266	175	0.88
F	333	200	1.1
G	400	250	1.3

Table 6.3: Volume of acetic acid (20% v/v) and DMA (20% v/v) used to catalyse the condensation of organosilane on the silica surface.

Even under this working condition, no presence of -SH was detected with the Ellman's test. As all the methods tested did not exhibit to good results, the third point of the list (i.e. concentration of thiol too low) could be the cause of failure of the Ellman test. For this reason, a different approach for detecting the functionalisation of SNPs@SiO_2 was employed by monitoring the change in concentration of MPTMS/MPTES left in the reacting solution after the precipitation of the particles. According to the calibration curve plotted (Figure 6.10b) the concentration of two unreacted organosilanes in the surfactant are ~0.26 mM and ~0.11 mM for MPTMS and MPTES, respectively. These results showed the reactivity of the thiol precursors under the experimental conditions and the better reactivity of MPTES compared to MPTMS. The limitation of using this protocol was the difficulty to understand whether the organosilane reacted with the alkoxy groups present on the silica shell or it reacted with the silanes present in solution. In order to understand if there was any thiol sticking on the particles, a thiol specific fluorescent label (i.e. fluorescein-5-maleimide (Bigelow and Inesi, 1991)) was used.

Particularly, three samples prepared with MPTMS and MPTES (a TEOS sample was prepared as blank) were left to react for different times (2, 24 and 48 h) to identify if the reaction times affected the final -SH density on the colloid surface, by taking emission intensity as an indicator of this parameter. An example of the collected spectra is shown in Figure 6.11. The most valuable result was the difference in emissivity shown between functionalised samples and non-functionalised one (which showed no emission). The main disadvantage of this protocol is the difficult in precipitating the particles from the fluorescein solution (prepared using DMF as solvent). Particularly, during the centrifugation several particles stay suspended in solution, as shown by the visible spectra of the precipitate, which shows a significant decrease in absorbance.

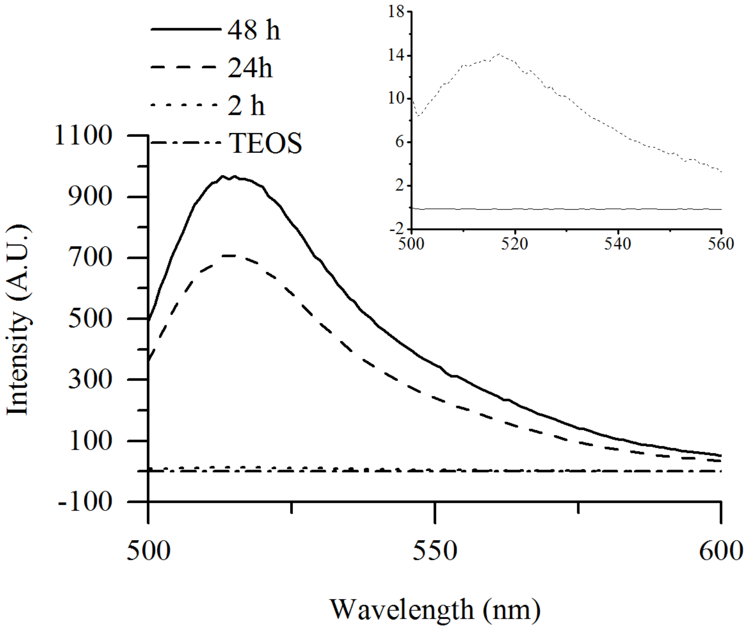

Figure 6.11: Fluorescence emissivity of samples functionalised with thiols, and let react for different times. The inset shows the emissivity for the sample let react for 2 hours and for the sample non functionalised.

6.2.2.1 Infrared Characterisation of Thiol Coating

As thiols coating showed a characteristic weak but very sharp peak in the infrared (~2550 cm^{-1}) due to the S-H stretching, samples were prepared for IR characterisation.

All spectra (the ones prepared with 10 μL and 25 μL are overlapped) show a broad peak around 1045 cm^{-1} due to the stretching of Si-O-Si, but no reflectance is present for the S-H stretch for any of the samples, as shown in the inset of Figure 6.12.

6.2.3 Allyl Functionalisation of SNPs@SiO$_2$

Functionalisation of particles with organosilanes bearing allylic moieties could be helpful in the preparation of nanocomposites as these groups could polymerise along with the polymer monomers in order to covalently link the particles to the polymeric matrix. As a starting point, same experimental conditions were used as that for the functionalisation with thiols (see Section 3.4.4.2). The functionalised samples were concentrated and dried by centrifugation in vacuum and then used for IR characterization but no typical peaks of the allyl group were observed.

As the presence of allylsilane is able to stop the growth of the silica shell, co-condensation of TEOS and ATES was examined, by adding allyltriethoxysilane simultaneously with TEOS. Carrying out the reaction with different ratios of TEOS and ATES, the presence of C=C groups on the surface could be detected by means of UV-vis spectroscopy. In particular, as the fraction of allylsilane increased, the external shell became

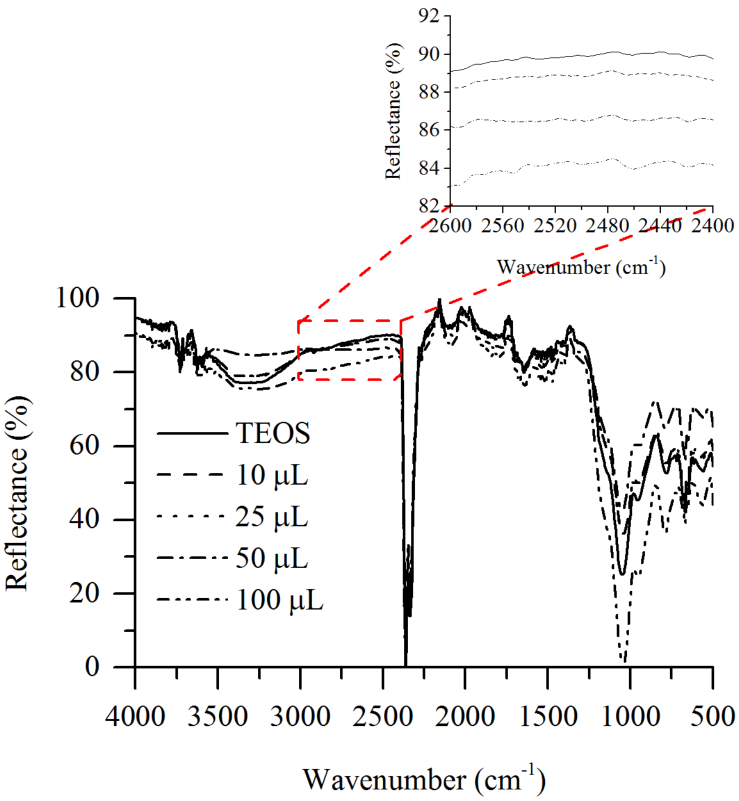

Figure 6.12: IR spectra of SNPs@SiO$_2$ prepared with different volumes of MPTES. Inset show the region where S-H peaks should be.

thinner and the red-shift caused by it was reduced. As shown in Figure 6.13, as the ratio TEOS/ATES became smaller, the final red-shift tended to be smaller as well.

As further proof of the functionalisation, polymerisation reactivity of functionalised and non-functionalised particles was investigated by using AIBN as radical initiator. The first test was carried out with thermal activation of AIBN (i.e. 80 ℃). To 1 mL of each sample, 0.1 mL of 1% w/v ethanolic AIBN solution was added and the samples were then placed in a thermomixer and left to react overnight at 80 ℃.

Then, the UV-vis spectra were collected showing a change in the spectral position, but the link between the TEOS percentage and the λ_{max} observed in the sample prior the to polymerisation was not observed anymore. This might be associated to the long exposure to high temperature which could have altered the nanoparticles properties, in particular the geometry and the silica coating. As AIBN could be activated even by light irradiation, two samples (100% TEOS and 80% TEOS/20% ATES respectively) were prepared by adding the same amount of AIBN (1% w/v in EtOH) and exposing them to UV irradiation for 2h. To these samples, 10 μL of ATES were added before starting the polymerization, in order to add a monomer for polymerization in the reacting solution and to observe if the functionalisation had a real effect on the final products. The samples showed in both cases the presence of a blue suspension. UV-vis spectra were taken after the polymerisation showed no differences between the two samples. This similarity could be due to the presence of a great amount of polymers which could have surrounded indiscriminately the particles of both samples. For these reasons, the same experimental conditions were applied, this time without adding the ATES to samples.

Figure 6.14 shows the final effect of UV exposure and the differences between the two samples. In particular, the presence of allylic moieties on the surface of the particles brought to the formation of aggregates, which was not observed for particles coated just with silica. The UV-vis analysis of the two samples showed a difference in the spectral position after the polymerization. In particular, the red-shift of the sample without allylsilane was bigger than that shown when ATES was present on the particles surface.

6.2.3.1 TEM Analysis of Functionalised Particles

As the UV-vis analysis carried out with different TEOS/ATES ratio suggested, the presence of a different amounts of organosilane brought a different thickness of the

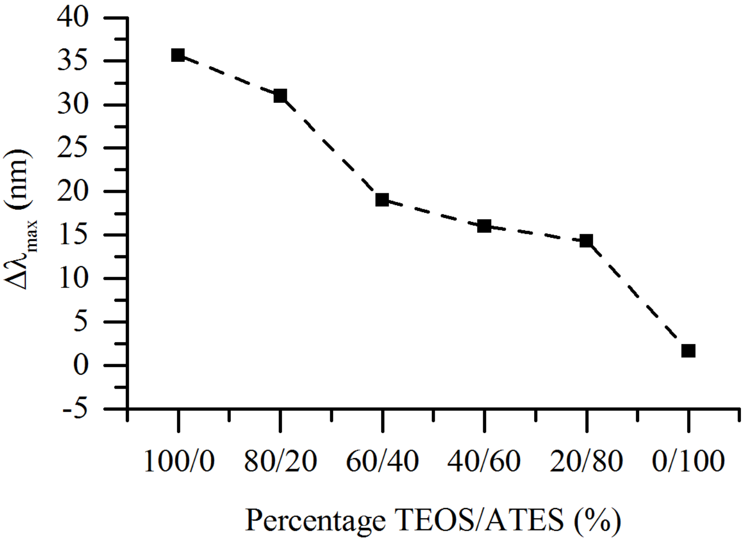

Figure 6.13: Different spectral position of SNPs@SiO_2 prepared with different ratio TEOS/ATES

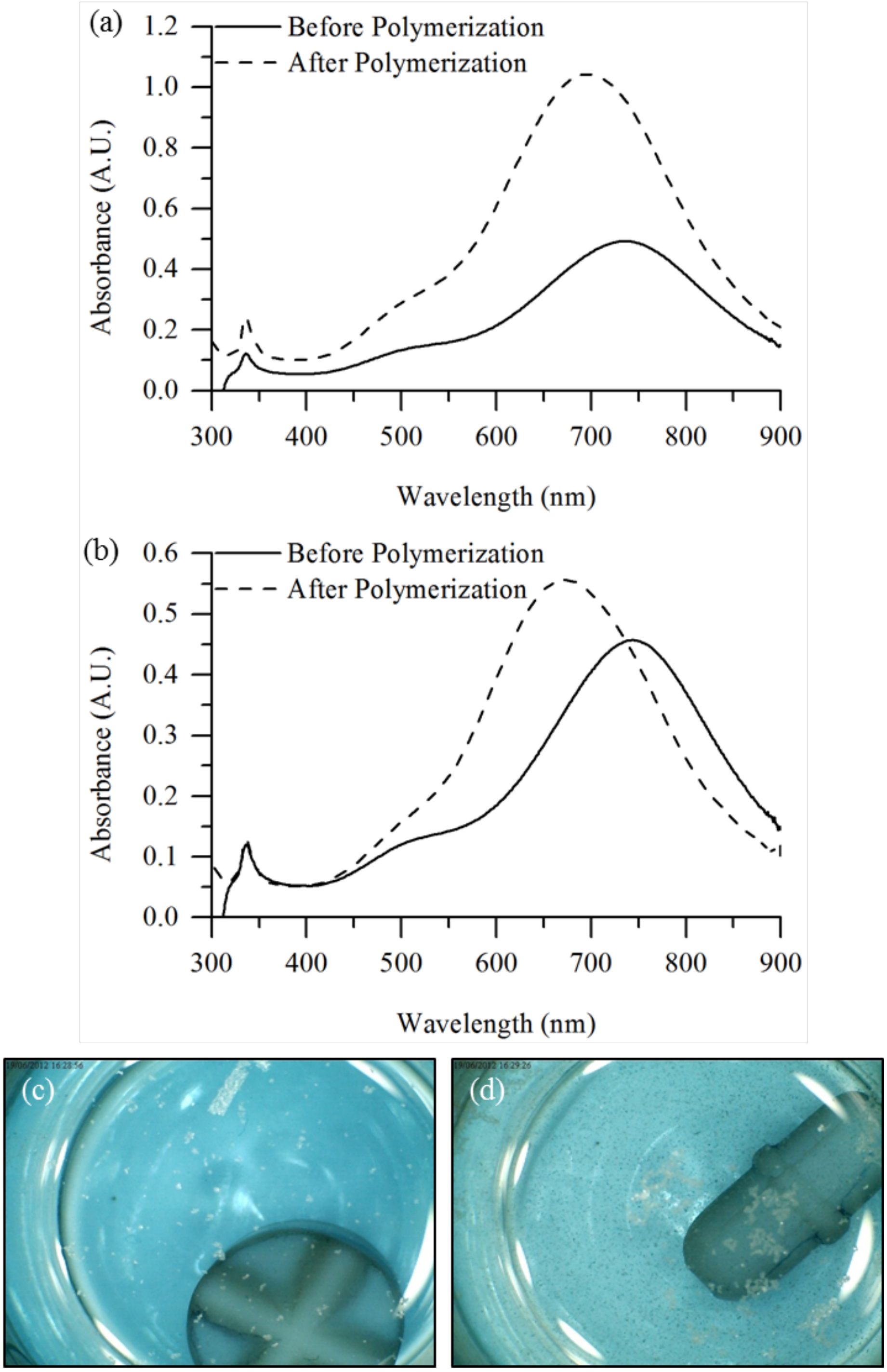

Figure 6.14: Change in the spectral position before and after irradiation with UV light in presence of AIBN for particles (a) without and (b) with allyl group on the surface. Figure 6.14c and Figure 6.14d show the solutions used for the experiments. Particularly is possible to observe the presence of darker agglomerate in Figure 6.14d.

external silica shell. TEM images confirmed this assumption, as shown in Figure 6.15. It was shown that the presence of silica around the particles (very clear in Figure 6.15a) decreased until vanishing completely (Figure 6.15f).

For the particles shown in Figure 6.15, EDAX data have been collected in order to evaluate the ratio between Si and Ag for samples prepared with different ratio of TEOS/ATES added to the nanoparticles solution. Figure 6.16 shows the different ratios between Si and Ag counts for particles prepared with different TEOS/ATES ratios.

As shown, as soon as the ATES is added the amount of Si is drastically reduced. This decreasing trend persists as higher amounts of ATES are added. The high standard deviation of the first point could be due to formation of large aggregate of silica formed along with the shell around the particles and that could precipitate with SNPs@SiO_2 during the purification procedure. This effect is reduced in the other samples, where the presence of ATES could have led to the formation of smaller particles which can stay in suspension during the centrifugation. The data used for these calculations are shown in Appendix C.1.

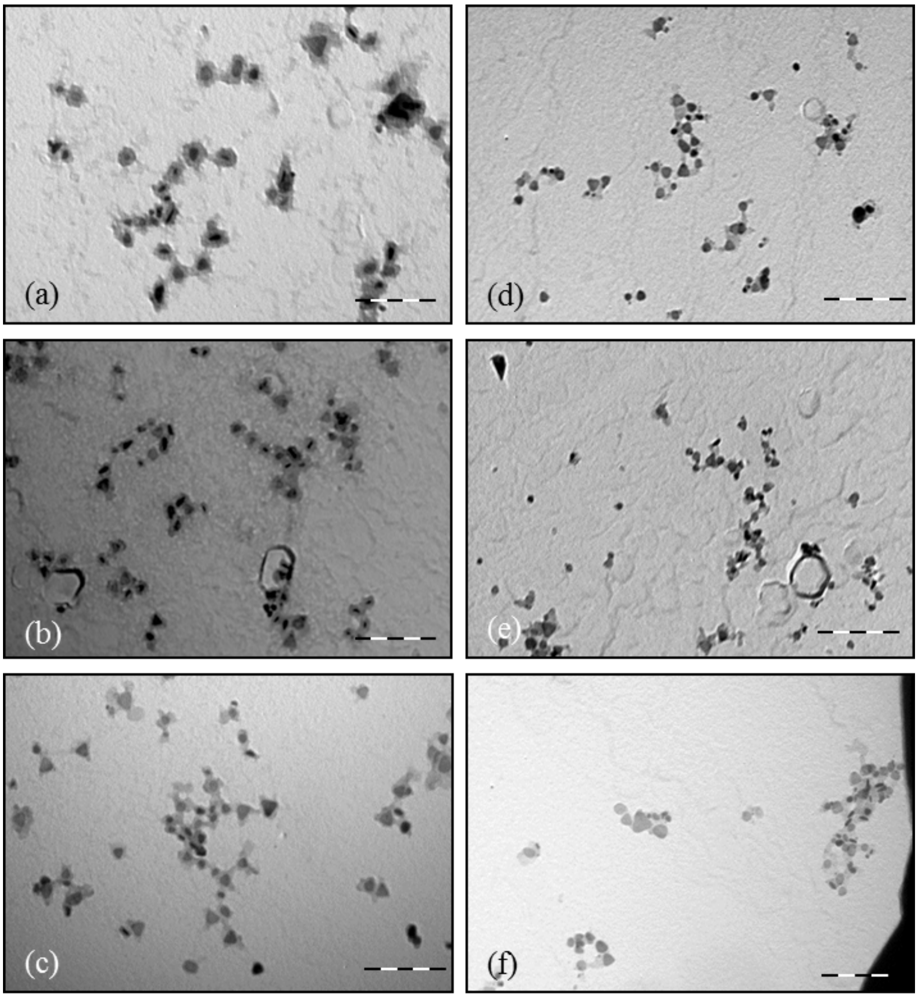

Figure 6.15: Nanoparticles coated with different ratios of TEOS/ATES, starting from 100% TEOS/0% ATES (Figure 6.15a) to 0% TEOS/100% ATES (Figure 6.15f). The scale bar is 200 nm for all the pictures.

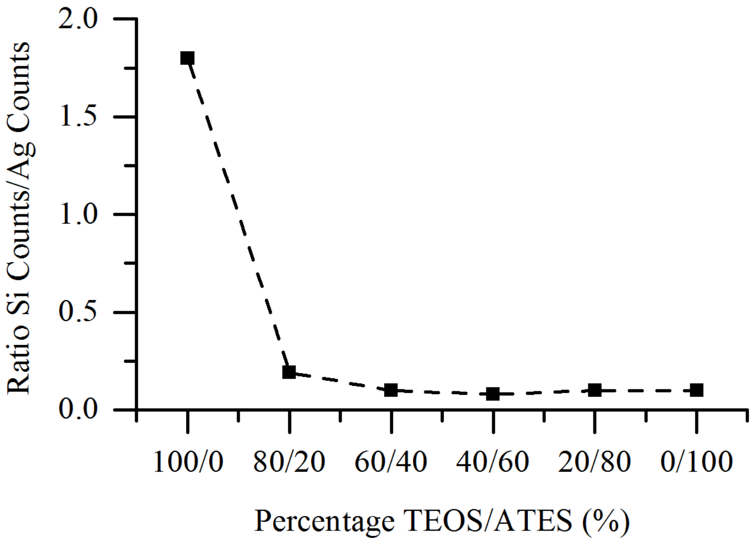

Figure 6.16: Ratio between the counts of Si and Ag collected for samples with different ration of TEOS/ATES

6.3 Conclusions

The coating of silver nanoparticles with SiO_2 has been carried out. This coating increases the chemical stability of the silver nanoparticles without drastically changing the optical properties of the nanoparticles. Furthermore, the coating also adds reactive sites on the surface of the nanoparticles, i.e. alkoxy and hydroxy groups, which allow further modification thanks to the well-known sol-gel chemistry. The so prepared particles have been functionalized with thiol groups by reaction between SNPs@SiO_2 and MPTMS and MPTES. The particles have been characterized by mean of Ellman test, reaction with thiol-specific fluorescein and with infrared spectroscopy. This method showed the efficiency of the functionalisation, but they are not reliable methods for giving a quantitative estimation of the thiols density of particles surfaces.

Functionalisation of nanoparticles has been carried out also with allyltriethoxysilane. Different thickness of the shell can be achieved by changing the ratio TEOS/ATES, achieving at the same time functionalisation with allyl groups. This new functional groups on the surface can be used as a starting point for following polymerization of the particles, which, in absence of a monomer, happens only when the polymerisation is carried out with the samples functionalised with ATES. These functionalised particles can be used in the preparation of composites with polymers, such as PMMA, forming covalent bonding with the polymer networks.

Chapter 7

SNPs@SiO$_2$ Embedded in a PMMA Matrix for Energy Saving Glazing

Contents

7.1 Introduction

Composite materials made of a polymeric matrix filled with inorganic nanoparticles (namely nanocomposite materials) have attracted attentions for potential applications in several fields, such as optical biosensors (Srivastava et al., 2014), colour filters (Carotenuto et al., 2000), fire retardant (Cárdenas et al., 2013) or solar cells elements (Kwong et al., 2004). Nanocomposite materials exhibit the mechanical properties of the organic network, which can act as an elastic and robust host for the inorganic filler. Furthermore, the low cost and processability of polymers, make them an ideal support for a wide range of applications. Nanoparticles, on the other hand, can add their opto-electronic properties to their organic guest. Components of composite materials can affect each properties; for example, addition of fillers can alter the mechanical properties of the polymer (Martin-Gallego et al., 2013), while the change in the dielectric constant ε of the surrounding medium can shift the optical absorbance of the embedded nanoparticles (Vodnik et al., 2009).

Recently, composite material films made of a polymer matrix and metal nanoparticles have found application as innovative coatings for energy saving glazing (Schelm and Smith, 2003; Stokes et al., 2010). In contrast to other methods, such as chromic materials or suspended particles devices, the composites are very cheap to produce and deposit even on a large area. Furthermore metal nanoparticles are more robust than organic dyes which often suffer from UV light degradation. Schelm and Smith (2003) were the first to study the use of these nanocomposite materials for an NIR blocking application in building fenestration. They reported the use of LaB_6 dispersed in a poly(vinylbutyral) (PVB) matrix and sandwiched between two slides of glass. Stokes et al. (2010), on the other hand, studied the quality of Au nanorods/PVA composites. In both cases preformed nanoparticles were dispersed in polymer solutions. Due to the different characteristics of the organic and inorganic environment, forming composite by simple blending of the two components can result in the formation of nanoparticle aggregates, which can led to phase separation and a change in the optoelectronic properties of the nanoparticles and in the mechanical properties of the organic host. For these reasons several methods have been studied for improving the mixing of the two components.

Particularly, grafting methods have been found to be efficient for the formation of nanocomposite with well dispersed filler. These methods are commonly divided in “grafting to”, “grafting from” and “grafting through”. In “grafting to” method polymer chains are attached to functional groups on the particles surface. This method, however, leads to a low grafting density as the more polymer chains get attached to the surface, the more difficult it is for other chains to get to the particles surfaces due to steric effects.

“Grafting from” methods, on the other hand, aims to functionalise the particles surface with polymerisation initiator groups and disperse them in a monomer solution. The polymerisation starting from the surface leads to high grafting density. The main disadvantage of this methodology is the change in initiator concentration with the change in filler percentage. This makes it very difficult to determine if the differences in the properties of the polymer are due to the differences in the filler percentage or in the polymer initiator concentration.

The third option, "grafting through", consists of adding polymerisable groups on the surface of nanoparticles. The particles are mixed in the monomer solution along with a polymerisation initiator. This method brings to a high grafting density, but as consequences of the polymerisable group on the surface, formation of crosslinked polymer is possible.

In this chapter, the formation of SNPs@SiO$_2$/PMMA nanocomposites by a "grafting through" approach is presented. The allyl groups present on the silica shell can polymerise along with the MMA monomer and permanently link them to the polymer chain, creating stable and robust composite materials. PMMA was chosen as polymeric

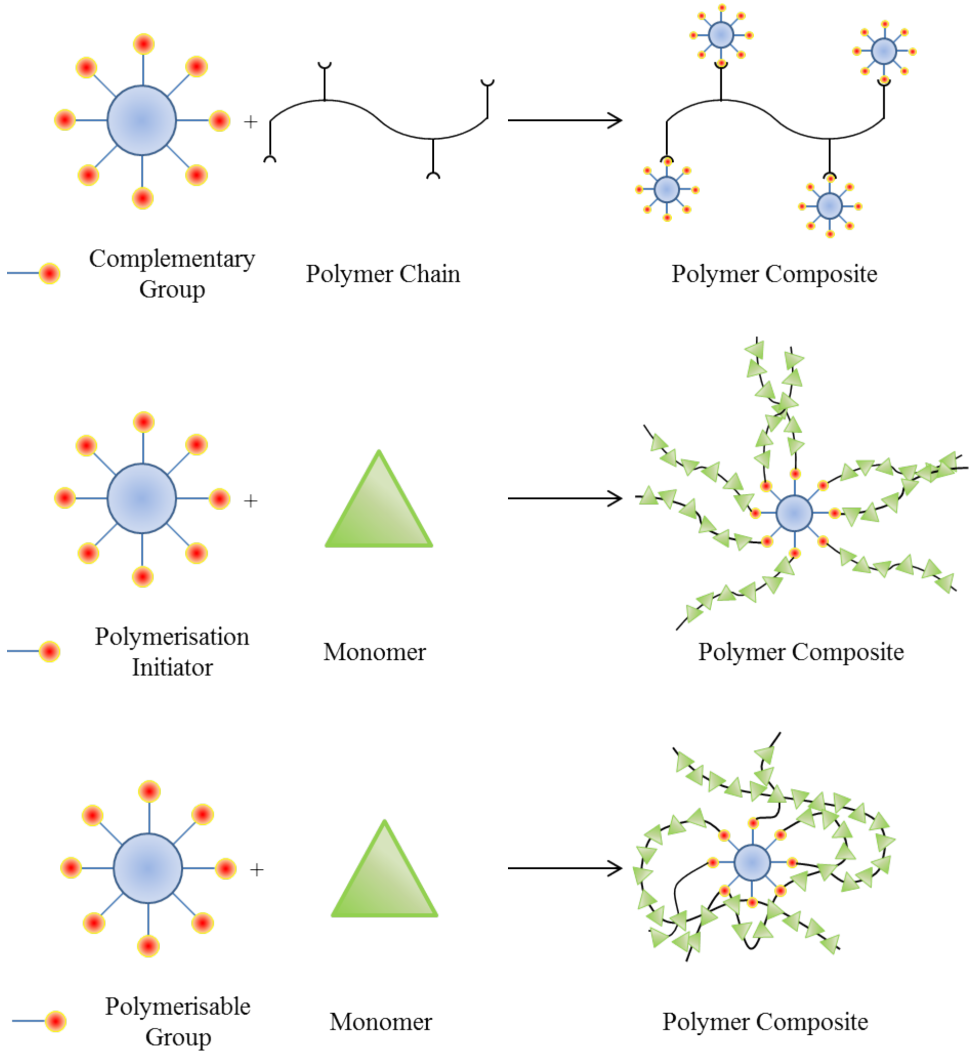

Figure 7.1: Schematic of (a) "grafting to", (b) "grafting from" and (c)"grafting through" methods.

host as it does not show yellowing due to aging and due to its robustness to outdoor conditions. The nanocomposites were prepared with a different percentage of radical initiator (1,2,4 and 6%) and of inorganic filler (0.1, 0.2 and 0.5% respectively) then characterised by means of NMR, GPC, IR, TGA and TEM. The so prepared composites were deposited onto glass slide and their efficiency in selective absorbing the NIR portion of the spectrum without affecting the transmittance of the visible radiation was evaluated.

7.2 Results and Discussion

The synthesis of SNPs was carried out according to Section 3.5.4.1. The reaction scheme of the radical polymerisation initiated by AIBN is shown in Figure 7.2. UV irradiative cleavage of the N=N bond generates two 2-cyanoprop-2-yl radicals which can react with the C=C bond of MMA; the new radicals can then propagate the polymerisation by reacting with:

1. Another MMA molecule;
2. An allyl group attached onto SNPs@SiO$_2$ silica shell.

Notably, during the filtration of the polymer to remove unreacted monomer and toluene, no leak of silver nanoparticles in the washing solution was observerd. Absence of SNPs@SiO$_2$ in the washing solution was proved by concentrating it and collecting UV-vis spectra: no peaks typical of SNPs were observed, meaning that all the nanoparticles were trapped in the polymeric matrix. To evaluate the effect of silver nanoprisms amount (namely 0, 0.1, 0.2 and 0.5%) on the chain length of polymer prepared with different AIBN concentration (0, 1, 2, 4, 6%), SEC measurement were carried out according to Section 3.5.2.3. Particularly, two parameters were evaluated, namely M_n and M_w. M_n is particularly useful to evaluate properties which are not dependent on the size of molecules but just to their numbers in solution, such as colligative properties while M_w is useful for evaluating properties which are dependent on the size of molecules in solution such as light scattering.

The first parameter M_n, defined in Equation 7.1, is the number average molecular weight. N_i is the number of molecules with molecular weight M_i.

$$M_n = \frac{\sum_{i=1}^{\infty} N_i M_i}{\sum_{i=1}^{\infty} N_i} \tag{7.1}$$

Equation 7.2, on the other hand, shows the formula for calculating M_w, namely the weight average molecular weight. :

$$M_w = \frac{\sum_{i=1}^{\infty} N_i M_i^2}{\sum_{i=1}^{\infty} N_i M_i} \tag{7.2}$$

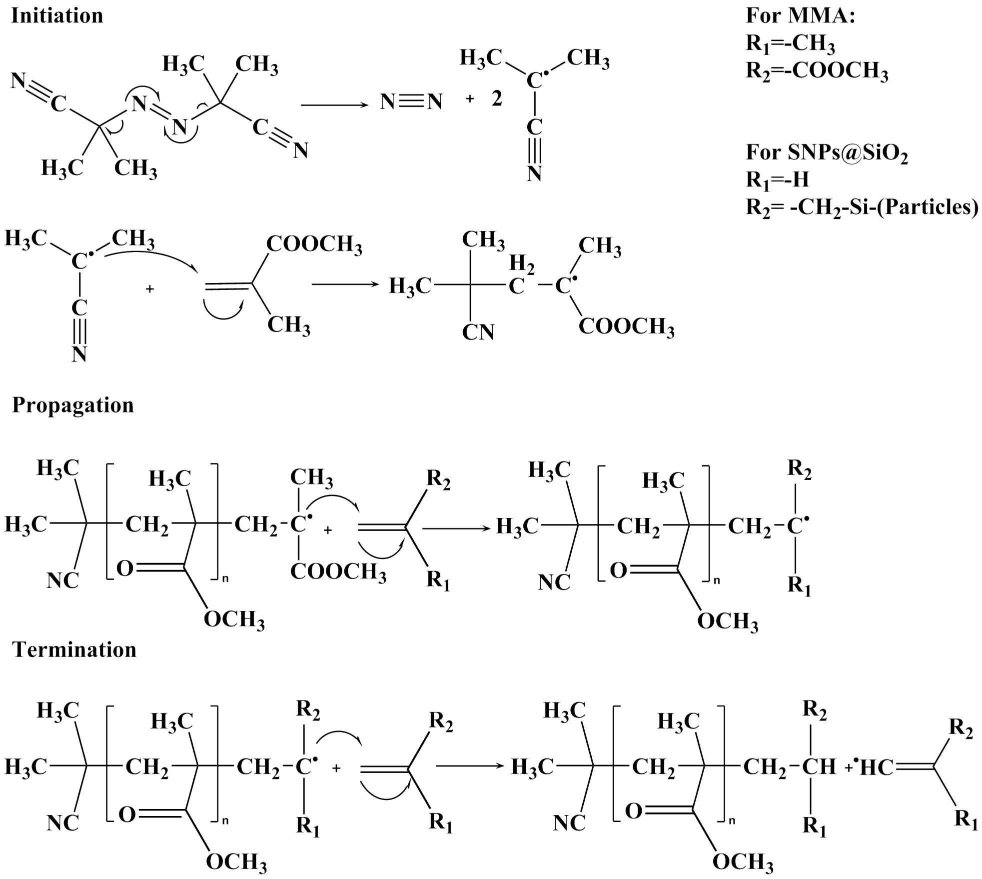

Figure 7.2: Scheme of MMA polymerisation activated by AIBN. The reaction is started by the UV irradiation cleavage of the radical initiator.

Graphs in Figure 7.3 show the trend of M_n and of M_w for different AIBN concentrations and filler volumes. As shown in Figure 7.3a, addition of silver nanoparticles affects the M_n but although all the composites with different filler volumes shows differences from the pure PMMA, no clear trend can be identified. Only the addition of small percentages of nanoparticles (0.1%) seems to have a clear effect on the M_n, namely showing higher values than that of the pure polymer. This could be due to grafting of the nanoparticles to the polymer chains: the lower concentration of SNPs, and therefore of additional polymerisable groups, can bring to the formations of longer linear chains. These seems to be valid also for higher percentage of radical starters, while the M_n of pure polymer decreases, as expected. The same observations can be made also for M_w.

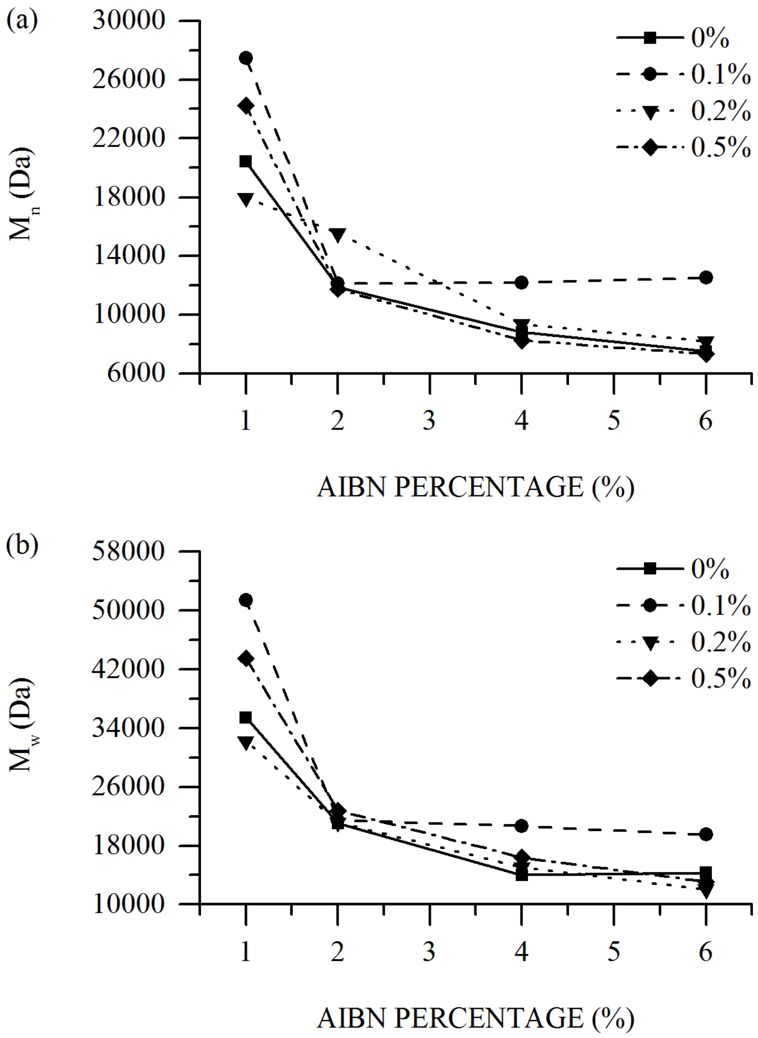

Figure 7.3: (a) M$_n$ and (b) M$_w$ calculated for polymers composite prepared with different concentration of AIBN (1, 2, 4, 6% w/w) and for different filler percentages (0, 0.1, 0.2 and 0.5% w/w).

7.2.1 Thermogravimetric Analysis

To observe the effect of filler volume on the thermal properties of the composite materials, thermogravimetric analysis (TGA) was carried out according to Section 3.5.2.4. The samples were acquired for polymers prepared with 1% AIBN and different amounts of SNPs (0, 0.1, 0.2, 0.5%). Thermal degradation of PMMA usually involves several steps (Kashiwagi et al., 1986). The first step, ∼165 ℃, involves the scission of the head-to-head linkages. The large steric hindrance and the inductive effect of the ester groups makes them less stable than the head-to-tail and tail-to-tail linkages. The second degradations steps, ∼270 ℃, is due to the radicals degradation generated by the presence of saturated groups at the end of the polymer chain which can be generated by polymerisation termination due to disproportion. Their presence involves the homolytic scission β to the vinyl group (Ferriol et al., 2003).

The third peak at ∼360℃, i.e. is the random scission along the polymer chain, represents the degradation mechanisms that have a greater effect on the thermal decomposition of PMMA. The random depolymerisation of PMMA chain is generated from side group scission rather than from the main chain (Manring, 1991). Figure 7.4a and Figure 7.4b show the TGA analysis and their first derivate (dTGA) for samples prepared with constant AIBN concentration (1%) and different filler percentages (0, 0.1, 0.2 and 0.5% w/w), respectively.

Focusing on the first and second peak, it is possible to observe that increasing the percentage of filler, the dm/dT (change in mass with temperature) decreases. The random chain scission on the other hand, increases with SNP content.

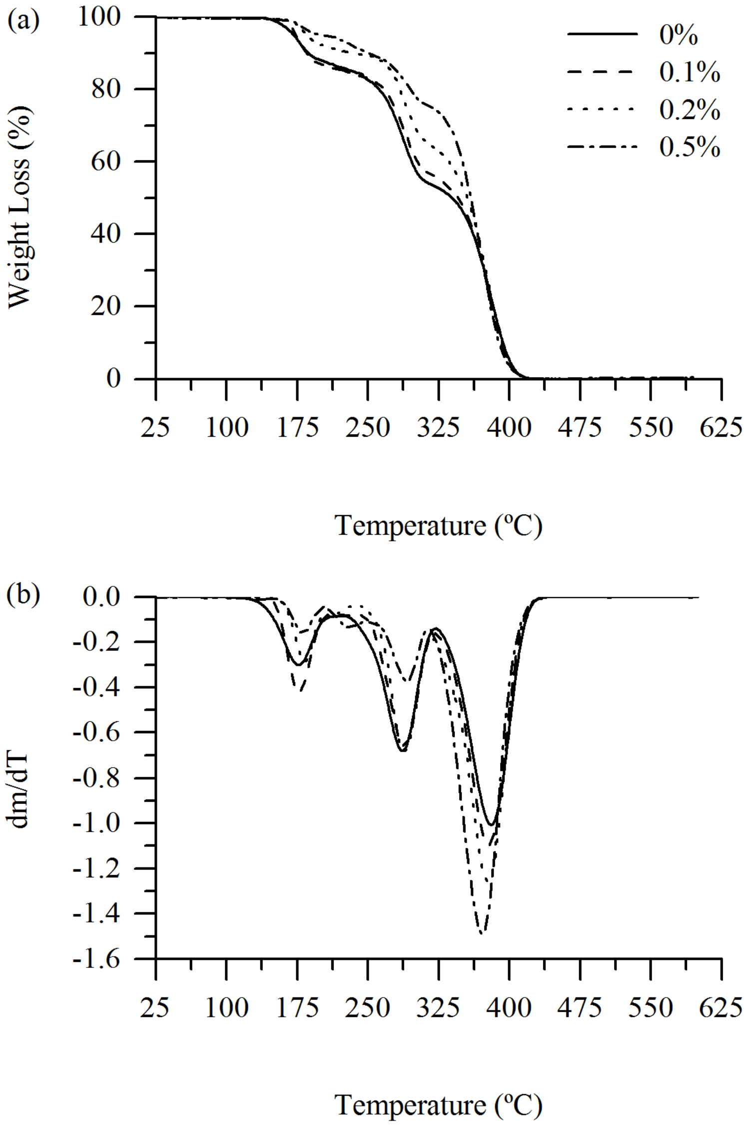

Figure 7.4: (a) TGA and (b) dTGA measured for polymers composite prepared with different filler percentages (0, 0.1, 0.2 and 0.5% w/w) and 1% AIBN.

The trends of the first two peaks could be due to the effect of the SNPs@SiO$_2$ on the polymeric chain, i.e. affecting the head to tail configuration (reduction of head-to-head linkages) and the number of unsaturated ends in the polymers.

Regarding the third peak, Vodnik et al. (2009) reports the effect of incorporating bare silver spherical silver nanoparticles into preformed PMMA on the thermal degradation of the polymeric matrix. As the filler content increases the thermal stability of the polymer chain versus random scission increases as well. Since the random scission is initiated by any reaction able to generate radicals (head-to-head linkage, scission β to the vinyl group at unsaturated ends and impurities) it has been proposed that silver nanoparticles can have some inhibiting effect on some stage of the degradations process. A similar effect was observed by Aymonier et al. (2003) for the degradation of Pd/PMMA composites.

Figure 7.4 shows that grafting increasing amounts of SNPs@SiO$_2$ to the polymeric matrix has an opposite effects on the thermal properties of PMMA. In particular for highly loaded composites, the degradation temperature decrease by $\sim$10 ℃. This effect therefore must be caused by the effects that the allyl groups attached on the nanoparticles could have on the polymer chains and on the radical degradation of the polymers.

7.2.2 Infrared Spectroscopy of SNP@SiO$_2$/PMMA Composites

Figure 7.5 shows the IR spectra collected for SNPs@SiO$_2$(- - -), PMMA($\cdots$) and SNPs-@SiO$_2$/PMMA(—). The IR spectrum of SNPs@SiO$_2$ shows typical peaks of ATES and of the silica shell. The peak at 1049 cm^{-1} is due to the Si-O stretching while the peaks at 795 cm^{-1} is due to the Si-C stretching. The two small peaks at 2919 and 2850 cm^{-1} are due to the C-H stretching of the CH$_2$ on the allyl chain. The groups corresponding to =C-H bending should be present between 1009-675 cm^{-1}, but as they are weak peaks they may be cover by the more intense peaks due to the silica shell. The broad peak at 3228 cm^{-1} is due to -OH groups on the silica shell. The IR spectrum of PMMA, on the other hand, shows peaks for C-H stretching vibrations of -CH$_3$ and -CH$_2$ groups (2989, 2946 and 2838 cm^{-1}) the C=O stretch (1720 cm^{-1}), bending of -CH$_3$ (1430 cm^{-1}). Peaks at 1184 and 1141 cm^{-1} are due to the ester C-O stretch while the small peaks at 983, 836 and 744 cm^{-1} are due to =C-H bending.

IR spectrum of SNPs@SiO$_2$/PMMAcomposites shows the same peaks as the pure PMMA. This could be due to the low concentration of silver nanoprisms inside the polymeric matrix. These results were achieved not only with ATR-IR spectroscopy but also using KBr pellets and by casting CHCl$_3$ solution of the composites on NaCl disks.

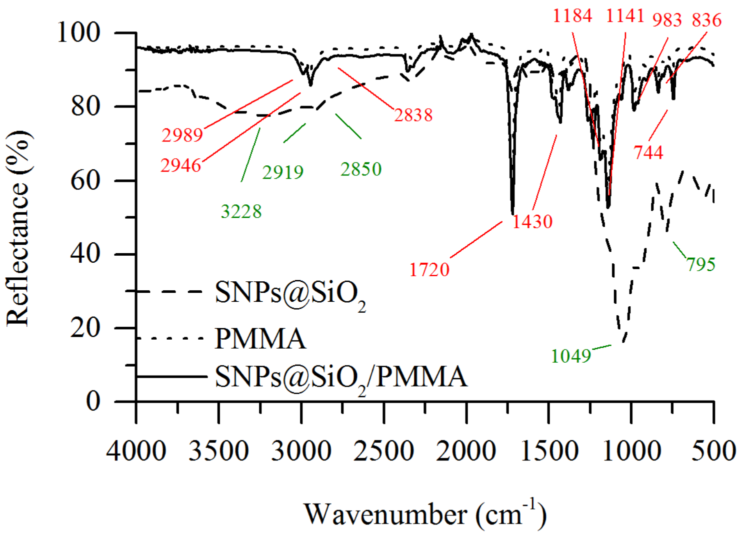

Figure 7.5: IR spectrum collected for SNPs@SiO$_2$(- - -), PMMA(···) and SNPs@SiO$_2$/PMMA (—)

7.2.3 Polymer Tacticity by NMR Spectroscopy

Tacticity, i.e. the arrangement of the successive configurational repeating units (the monomers) in the main chain of a polymer, is an important parameter that can affect polymer properties, such as glass transition temperature, T_g (Gourari et al., 1985), thermal degradation (Kitayama et al., 1989) and applications (Tung and Lu, 2006). Figure 7.6 shows the three possible orientations of the polymer's side chains. Isotactic polymers are composed of chains with side groups oriented all in the same direction, while a syndiotactic polymer has an alternate repetition of the pending groups. In an atactic polymer, on the other hand, there is no specific orientation of the side groups. To better describe the reciprocal stereochemistry of polymer units, the orientation of diads (groups of two monomers) inside a triad groups of three monomers can be used. In particular a isotactic is described by two meso diads (mm), a syndiotactic by two racemo diads (rr), and an atactic (also called heterotactic when analysed as triad) by a meso and a racemo diad (mr or rm). As the various conformations are not equally populated, motion of the polymer chains do not cancel these differences. NMR is a very powerful technique for studying the tacticity of polymers. In particular, Bovey and Tiers (1996) extensively studied PMMA and the effect of tacticity on its spectrum. They focused the attention on the chemical shift of the α-methyl group for iso-, syndio and heterotactic configuration (using chloroform as solvent).

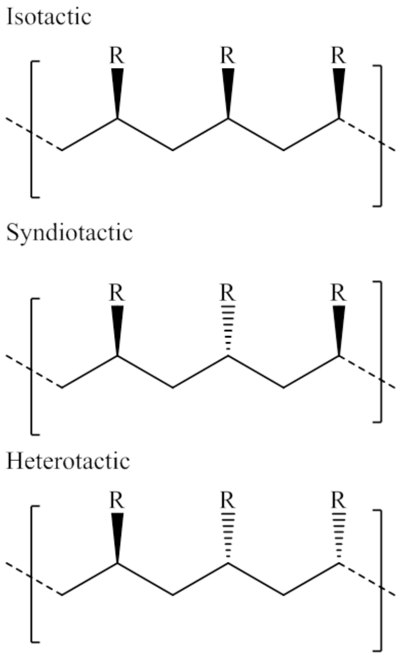

Figure 7.6: Different orientation of the side chain for iso-, syndio- and heterotactic triads.

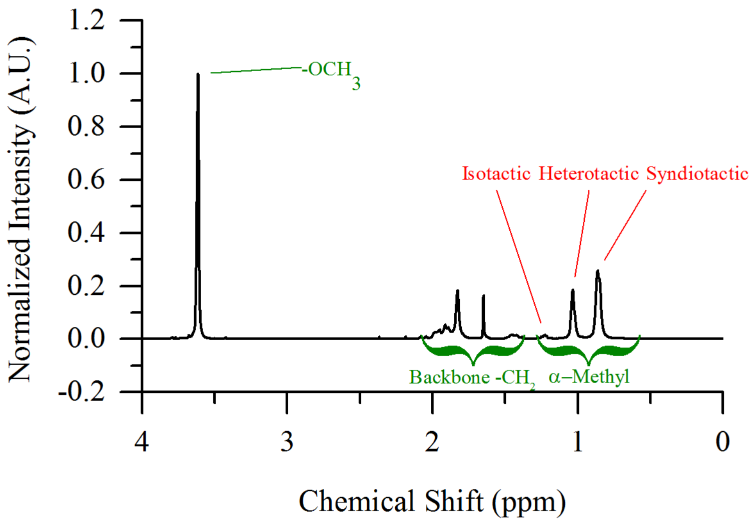

Figure 7.7: Characteristic NMR spectrum of PMMA in chloroform.

The spectrum in Figure 7.7 displays the three peaks for the syndiotactic (rr), heterotactic (rm) and isotactic (mm) configurations at 0.78, 0.95 and 1.15 ppm, respectively. This difference in the chemical shift is due to the magnetic field experienced by the α-methyl groups due to the strong magnetic anisotropy of the ester carbonyl group.

Interestingly, polymer tacticity also affects the signal of the methylene groups in the polymers chain. Their resonance is a single peak in a fully syndiotactic polymer as both protons over the time must experience the same magnetic environent. In an isotactic chains, instead, the two protons will be differently shielded and, therefore, a fourfold resonance is expected. These differences are observed in the several number of peaks observed in the -CH$_2$- region.

Figure 7.8 shows the percentage of the different tacticity calculated for polymers prepaperd with a different concentration of AIBN and silver nanoprisms. It is possible to observe that the radical initiator has a major effect on the reciprocal orientation of the side groups which is similar for polymer prepared with different amount of inorganic fillers. In particular, it is possible to notice a clear trend for the mm configuration, which percentage increases with AIBN concentration.

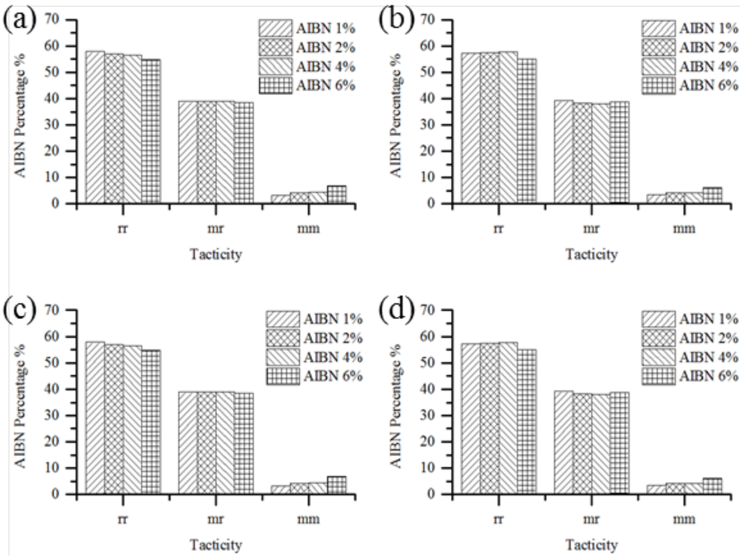

Figure 7.8: Percentage of different tacticity for polymer prepared with (a) 0%, (b) 0.1%, (c) 0.2%, (d) 0.5% SNPs w/w dispersed in the polymeric matrix.

Table 7.1 shows the percentage of mm configuration for different concentration of AIBN and SNPs. The data show that the lower the SNPs amount, the more the mm percentage differs from the one of the pure PMMA for high percentage of AIBN (i.e. 4% and 6%).

AIBN [%]	**mm Percentage [%]**			
	0% SNPs	**0.1% SNPs**	**0.2% SNPs**	**0.5% SNPs**
1	3.19	3.5	3.25	3.524
2	3.85	3.94	3.84	4.148
4	5.17	4.82	5.02	5.396
6	6.49	5.7	6.2	6.644

Table 7.1: Percentage of mm configuration for different percentages of AIBN radical initiator and SNPs.

7.2.4 Attachment of PMMA on SNPs@SiO$_2$

To prove effective attachment of PMMA on SNPs@SiO$_2$ surfaces, experiments were carried out to remove physisorbed chains and observe if any polymer is left attached to the particles.

In order to remove the polymer that was non-covalenty bond to the silica shell, 6.5 g of polymer composite were dispersed in chloroform and centrifuged at 13,000 rpm for 30 minutes. After removing the surfactant, the precipitate was redispersed in chloroform and centrifuged again. In this way only the covalently bond chain will remain in the precipitate while the other will be removed with the surfactant. The solvent was then removed from the surfactant to control the amount of polymer removed from the solution. These steps are repeated until no more polymer is extracted from the surfactant.

Fraction	**Polymer Weight [g]**
1	6.4630
2	0.0251
3	0.0090
4	0.0017
5	0.0012
6	0.0000

Table 7.2: Weight of polymer collected from the surfactant of different fraction of SNPs@SiO$_2$/PMMA.

Table 7.2 shows the decrease in polymer weight collected from different fractions of centrifuged SNPs@SiO$_2$ solution. As shown, most of the polymer is removed during the first centrifugation of the solution. This can be expected considering the low amount of SNPs@SiO$_2$ dispersed in the polymeric matrix (0.5% w/w in this case). To prove that no further polymer was present in the vial, ^{1}H NMR spectra were collected for all the fractions. Spectra in Appendix D.1 show that after the fourth fraction no more PMMA peaks were observed in solution. It should be noted that peaks at lower ppm values, on the other hand, are due to some plasticisers leached from the Eppendorf vials.

Figure 7.9 shows the ^{1}H NMR spectrum of SNPs@SiO$_2$/PMMA collected in CDCl$_3$. As shown in the picture (and the inset), the NMR spectra shows the characteristic peaks of α-methyl groups and of the -OCH$_3$ but not the peaks of the backbone -CH$_2$- groups. This could be due to the fact that nanoparticles are not fully soluble in solution and they form a solid phase inside the NMR tubes. For this reason, solid state NMR was carried out on a 20 mg sample of SNPs@SiO$_2$/PMMA prepared according to Section 3.5.3.3.

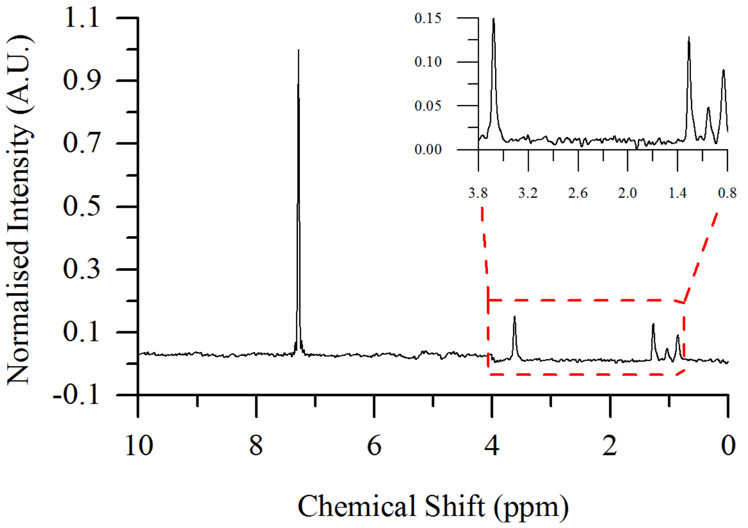

Figure 7.9: Proton NMR spectra of PMMA on SNP@SiO2 surface after removing of physisorbed polymer by centrifugation (see Table 7.2)

Figure 7.10 shows the ^{13}C NMR spectrum of the composite materials. The five peaks highlighted in Figure 7.10 correspond to the five different carbons in the polymer chains; particularly the peak at 13.6 ppm corresponds to the α-methyl groups, that at 30.4 ppm to the quaternary carbon, while the peak at 40.2 ppm is due to -CH$_2$- carbons resonance. Peaks at 47.4 and 173.6 ppm correspond to the -OCH$_3$ and the carbonyl carbons, respectively. These data confirm the presence of polymeric chains on the surface of the particles, proving that the particles are not just physisorbed on SNPs@SiO$_2$, but also covalently bonded to it.

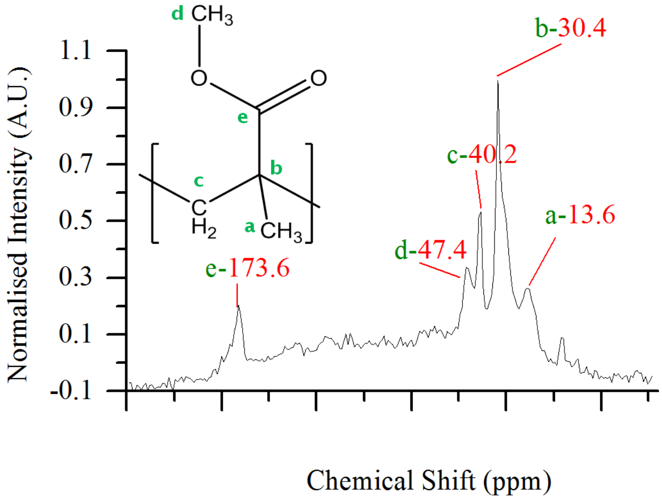

Figure 7.10: Carbon NMR spectra of PMMA on SNP@SiO2 surface after removing of physisorbed polymer by centrifugation

The precipitate used for collecting NMR spectra were also used for collecting TEM pictures which are shown in Figure 7.11. All the pictures show a strand connecting different aggregates of silver nanoparticles. Although the image can suggest the presence

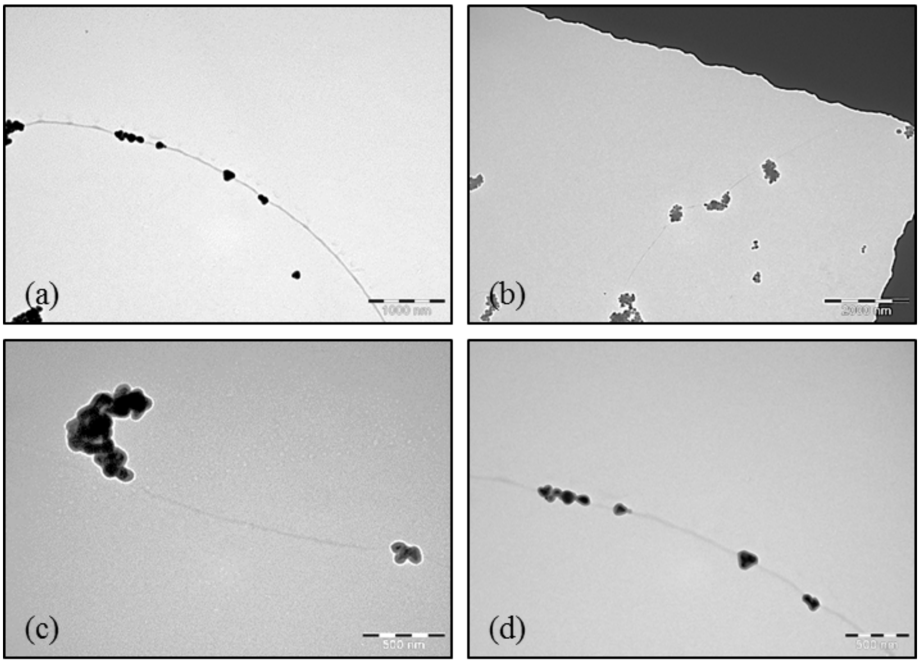

Figure 7.11: TEM picture of SNP@SiO$_2$/PMMA to which the physisorbed polymer has been removed. The scale bar is 200 nm for Figure 7.11(c) and Figure 7.11(d) while for Figure 7.11(a) Figure 7.11(b) the scale bar is 1000 and 2000 nm, respectively. Larger images are shown in Appendix D.2

of a PMMA strand entering and exiting the cluster of nanoparticles, the coffee-spot shape of the strand itself suggest that the polymer strand may actually be a trace of the solvent evaporation.

7.2.5 Deposition of SNPs@SiO$_2$/PMMA Thin Films

Silver nanoparticles embedded in the polymeric matrix can be used as NIR radiation absorbing materials. In order to prove the efficiency of SNPs@SiO$_2$/PMMA films as an efficient energy saving material for glazing, thin films of the composite solution prepared at different concentration (10, 15, 20 and 30% w/w) of composite with different concentration of silver nanoparticles (0.1, 0.2 and 0.5%) in toluene, were deposited on a 1cm×1cm glass slide, prepared according to Section 3.5.3.5. Few drops of the polymer solutions were drop-cast on the glass surface and then spun at different speeds (from 500 to 4,000 rpm) for 1 minute, with an acceleration equal to half the revolution speed per second.

Figure 7.12 shows the minimum transmittance for different polymer solutions loaded with various amounts of inorganic filler. As expected, by increasing the amount of SNPs@SiO$_2$ the transmittance in the NIR region decreased, reaching a minimum of ~54% per film spun at 500 rpm containing 0.5% of nanoparticles. Notably, for all the samples, spinning at more than 500 rpm resulted in very high values of transmittance due to the low thickness of the film and therefore cannot be efficiently used as energy saving materials.

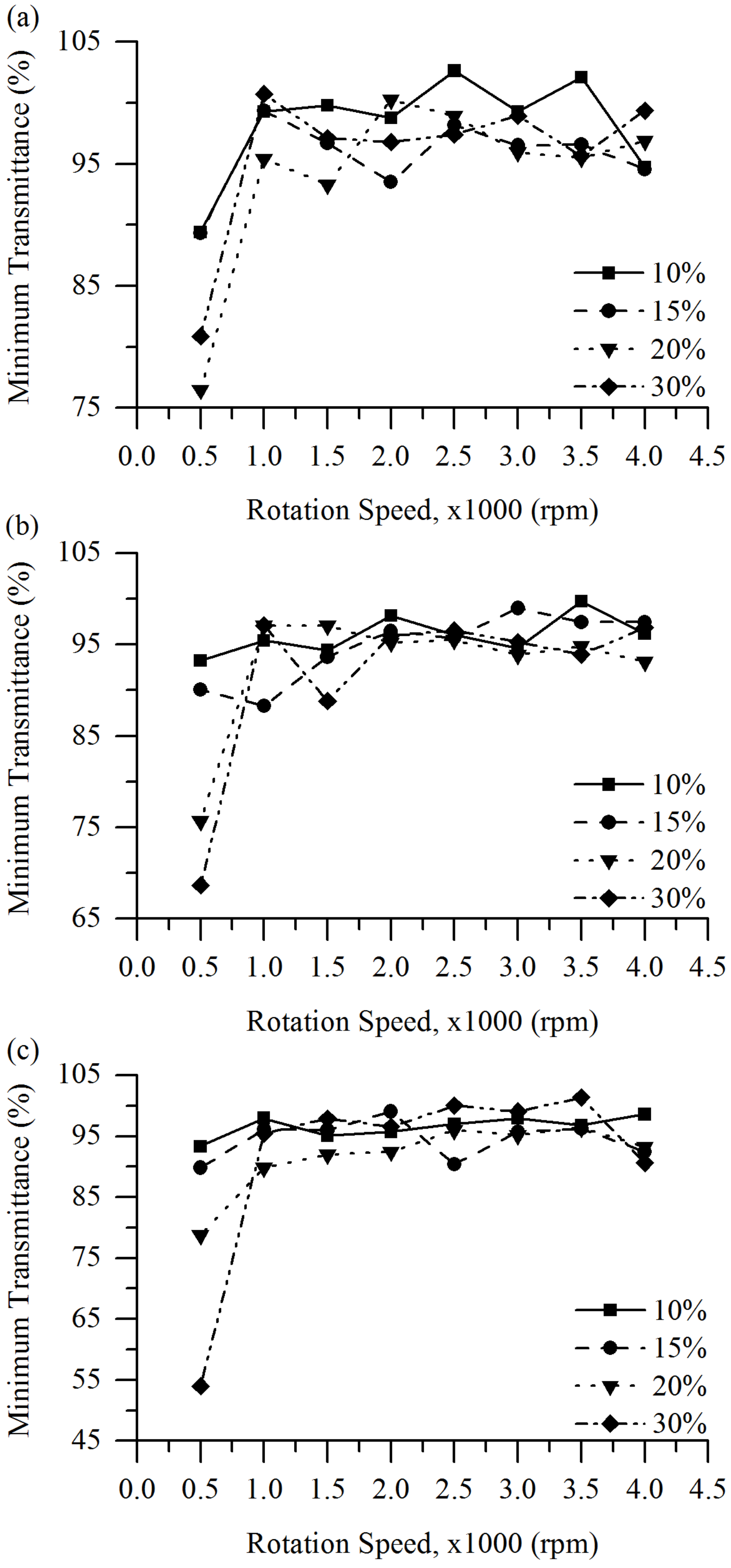

Figure 7.12: Minimum transmittance measured for polymer loaded with (a) 0.1, (b) 0.2 and (c) 0.5% of inorganic filler. For each graph the trend of polymer solution with increasing concentration (10, 15, 20 and 30% w/w) is shown.

Spinning the film at lower speed did not lead to better results as it did not allow to the polymer solution to uniformly spread on the glass surfaces. Particularly a donut-shaped film was obtained when the film was deposited at low speed. Also the use of very concentrated solution led to non-homogeneous coatings as polymer filaments were radially dispersed from the glass slide edges.

7.2.6 Thin Film TEM Images

Although the spinning of polymer solutions did not appear to be a good way to deposit the composite solution for the fabrication of energy saving coatings on glass, it was usefully employed to easily preparing self-standing films for TEM imaging, without the need of using microtomy. TEM samples were prepared according to Section 3.2.3.2. To efficiently prepare the samples, only films spun at high speed were employed (i.e. $\geqslant$1,500 rpm) in order to obtain a thin and homogeneous film.

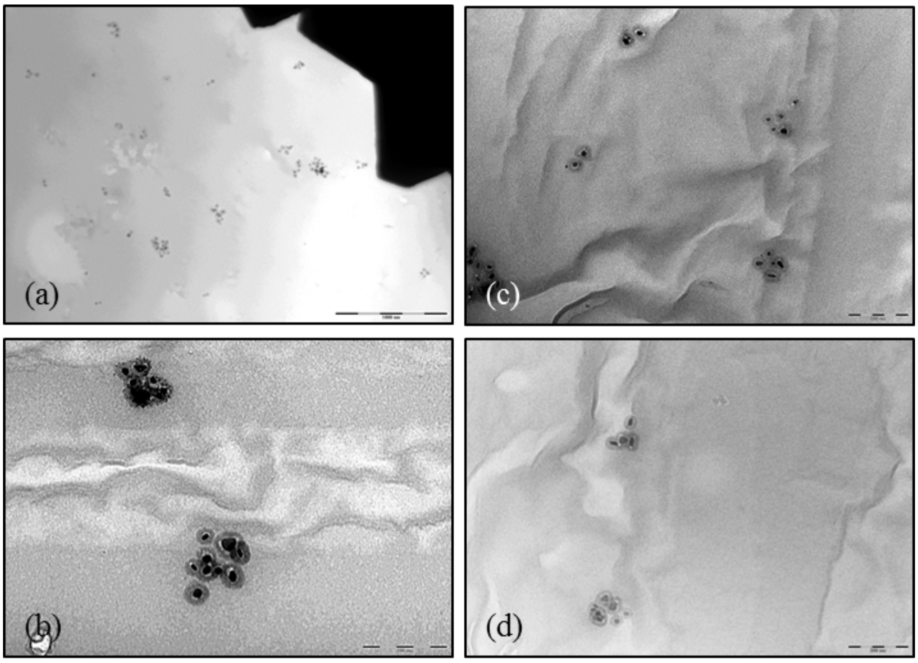

Figure 7.13: TEM images of SNPs@SiO$_2$/PMMA composite. The scale bar is 200 nm, except for Figure 7.13(a) for which in 1000 nm.

Figure 7.13 shows pictures collected for SNPs@SiO$_2$/PMMA composite. Although it is possible to clearly see the presence the nanoparticles embedded in the polymer film, the presence of the polymer film itself reduces the quality of the images making it difficult to clearly see the silica shell. Figure 7.13(a) shows a wide panoramic of the particles dispersed in the organic matrix. SNPs@SiO$_2$/PMMA are well dispersed in the PMMA film, even if they tend to form small clusters (generally less then ten silver nanoprisms). Figure 7.13(b)-Figure 7.13(d) show more details for the nanoparticles. Particularly, it is possibly to detect the silica shell. Thanks to its presence metal nuclei to not coalesce.

Furthermore, they cannot affect each other optical and electronic properties due to near field effect.

7.2.7 Deposition of SNPs@SiO$_2$/PMMA Thicker Films

As the film was deposited by spin coating method, they did not show any notable absorbance in the NIR range due to their thinness. Thicker films were deposited in order to evaluated the efficiency of these nanocomposites coatings. To prepare thicker films, polymer solutions were cast in a glass/PDMS mold prepared according to Section 3.3.4.3. The solutions were prepared using chloroform as solvent. An attempt to use toluene as the solvent resulted in very thick films (approximately 1.5 mm) with a fragile honeycomb structure. To make the film more homogeneous, the mold holes were covered with a clock slide to slow down the evaporation of chloroform; polymer solutions evaporated without the clock glass show a cracked and corrugated surface. After leaving the polymer solution to rest overnight the PDMS film can be peeled off and the higher edges on the side of the film can be removed by cutting them with a scalpel. The polymer film were prepared using a 20% solution of SNPs@SiO$_2$/PMMA loaded with different amounts of silver nanoparticles (0.1, 0.2 and 0.5%): use of more dilute solutions resulted in peeling of the PDMS film due to infiltration between the glass slide and the PDMS film while using polymer concentration >20% results in film with a very intense colouration (almost pitch black), which could not be used for obvious reasons.

Two different sets of SNPs@SiO$_2$ were prepared and used as inorganic fillers.

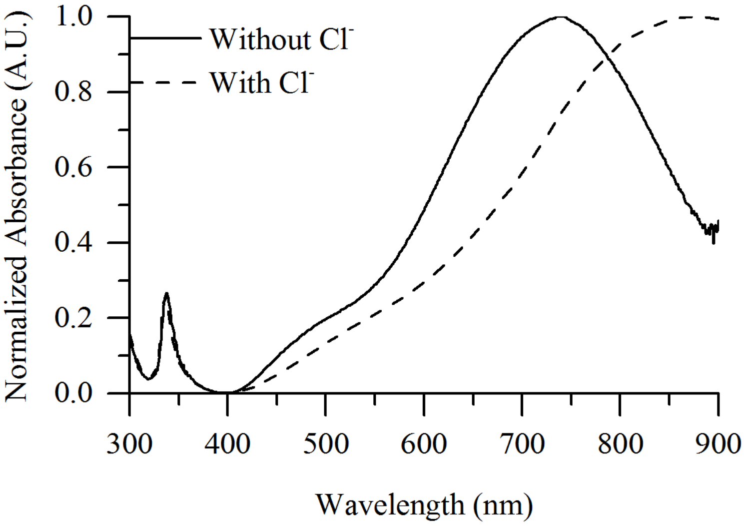

Figure 7.14: Optical absorbance of silver nanoparticles prepared with(- - -) and without (—) chloride ions.

The first set was prepared according to Section 3.2.4.1 (SET 1) while the second was prepared in the presence of Cl$^-$ ions (SET 2), according to Section 3.2.4.2. The particles of both sets were then coated with a TEOS:ATES (80:20) shell according to Section 3.4.4.3. The optical spectra of the two sets of SNPs@SiO$_2$ are shown in

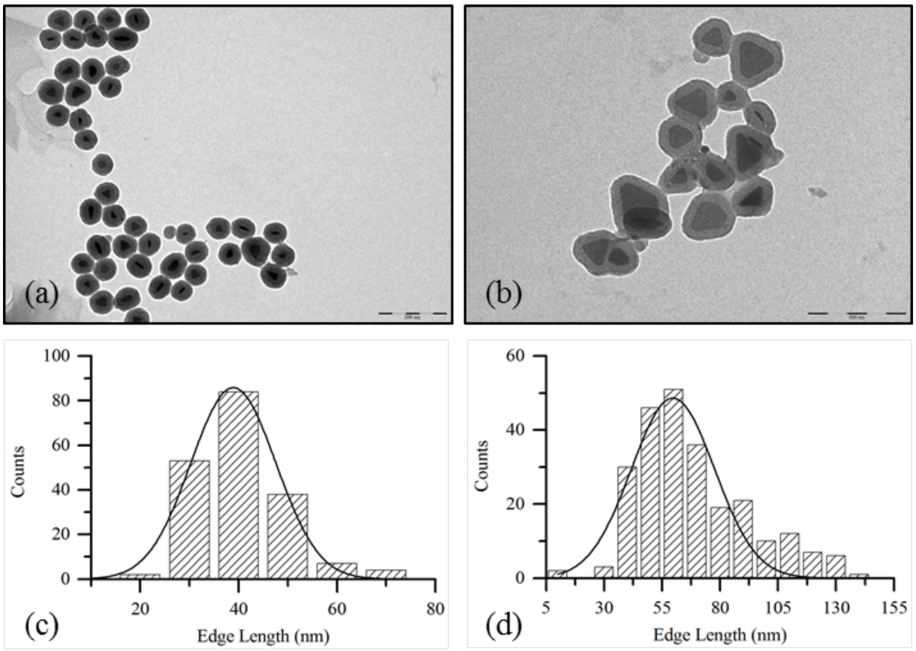

Figure 7.15: TEM images of SNPs@SiO_2 prepared (a) without and (b) with Cl^-. The size distribution for the two sets of nanoparticles are shown in Figure 7.15(c) and Figure 7.15 (d), respectively.

Figure 7.14. As expected, particles prepared in the presence of chloride ions show a broader peak at higher wavelength due to the larger size and the sharper tips of the triangles.

TEM pictures were acquired for both the sample sets in order to measure their size distribution and the average edge length. Figure 7.15 shows images of SET 1 and SET 2 particles (Figure 7.15(a) and Figure 7.15(a) respectively). The particles size is ∼38 nm for SNPs@SiO_2 SET 1 and ∼60 nm for nanoparticle SET 2.

The films prepared with the PDMS/glass mold (2mm depth) have a thickness of ∼0.8 mm. While this thickness is good for composite prepared with 0.1 and 0.2%, the UV-vis-NIR spectra of SNPs@SiO_2/PMMA loaded with 0.5% of inorganic filler signal was saturated in most of the UV-vis range. For this reason, thinner films were prepared by casting only the amount of composite solution necessary to cover the bottom part of the mold. With this method ∼0.1 mm films were prepared. With this thickness no saturation of the signal was observed.

Figure 7.16(a) and Figure 7.16(b) show the transmittance of SNPs@SiO_2/PMMA composite prepared with SET 1 and SET 2, respectively. All the spectra, with exception of the polymer one, show four peaks. The two peaks at shorter wavelength (<1000 nm) correspond to the absorbance of the inorganic nanoparticles, while the one at longer wavelength are due to the organic matrix. The lowest transmittance of both the composites correspond to the in-plane dipole resonance of the SNPs; for SET 2 particles, this peak is broader than that of SET 1 due to the sharper tips of the triangular nanoparticles.

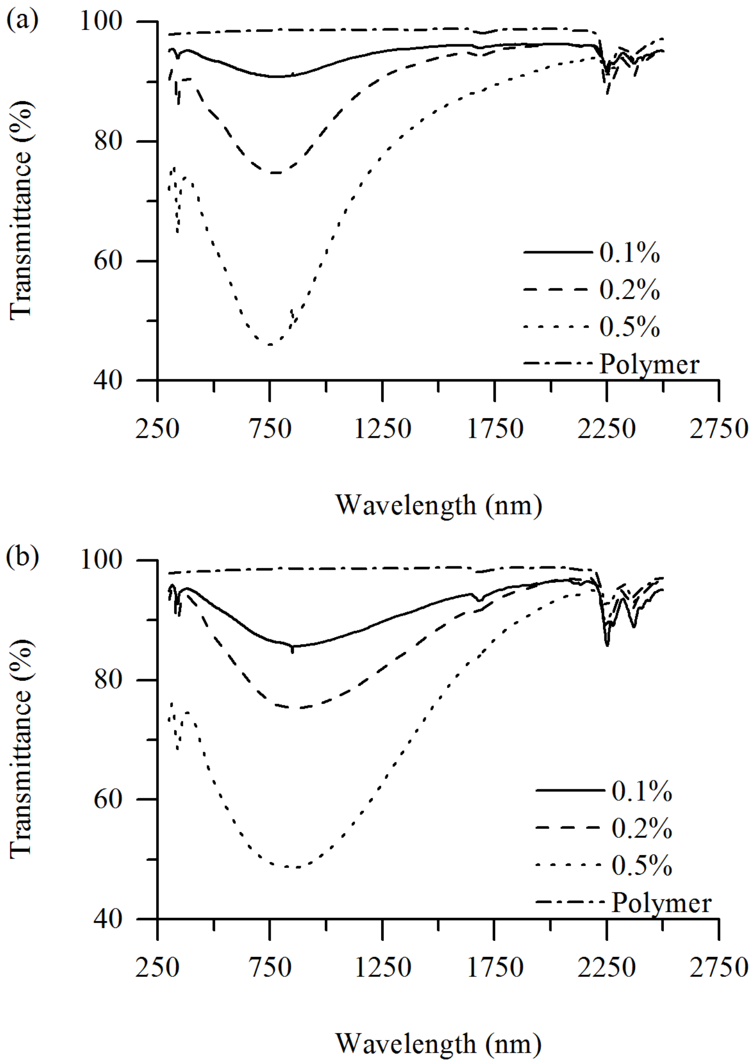

Figure 7.16: UV-vis-NIR transmittance of composite prepared with (a) SET 1 and (b) SET 2 of SNPs@SiO$_2$. Each graphs show the different transmittance for 0.1 (—), 0.2 (- - -), 0.5% (···) and for the pure polymers (-·-·-).

To evaluate the potential of these materials as energy saving materials, the ratio between the transmittance of visible light (T$_{lum}$) and the transmittance of total solar radiation (T$_{sol}$) was taken into account as a figure of merit (FOM) to evaluate how efficient these materials could be in absorbing the NIR part of radiation without affecting the visible light income. T$_{lum}$ and T$_{sol}$ are defined in Equation 7.3 and Equation 7.4, respectively.

$$T_{lum} = \frac{\int T(\lambda)S(\lambda)Y(\lambda)d\lambda}{\int S(\lambda)T(\lambda)d\lambda} \tag{7.3}$$

$$T_{sol} = \frac{\int T(\lambda)S(\lambda)d\lambda}{\int S(\lambda)d\lambda} \tag{7.4}$$

S(λ) and Y(λ) correspond to the solar irradiance and the optical response at wavelength

λ. S(λ) and Y(λ) values used for calculation were obtained from American Society for Testing and Materials (ASTM) and from Stockman and Sharpe (2000). The ideal value of this FOM would be 2.08, corresponding to a material absorbing all the NIR radiation while letting pass all the UV and visible light, but usually values above 1 are considered good (Stokes et al., 2010). Table 7.3 shows the values of T$_{lum}$, T$_{sol}$ and FOM for samples prepared with both sets of particles and for samples reported in literature for gold nanorods (Au NRs) in PVA (Stokes et al., 2010) and for LaB$_6$ nanoparticles (LaB$_6$ NPs) dispersed in poly(vinylbutyral)(PVB) (Schelm et al., 2005). As the final concentration of gold nanorods in PVA was not reported, Pane 1 and Pane 2 were used as in the original paper. Pane 1 and Pane 2 refer to NRs with maximum absorbance at 768 and 834 nm, respectively.

	Sample	**Thickness (mm)**	**T$_{lum}$**	**T$_{sol}$**	**FOM**
SET 1	0.1%	0.1	0.927	0.929	0.997
	0.2%		0.816	0.830	0.982
	0.5%		0.575	0.619	0.928
SET 2	0.1%	0.1	0.909	0.899	1.011
	0.2%		0.895	0.893	1.003
	0.5%		0.586	0.601	0.975
	PMMA	0.1	0.983	0.979	1.000
Au NRs	Pane 1	0.8	0.37	0.37	1.000
	Pane 2		0.30	0.29	1.030
LaB$_6$ NPs	0.020%	0.8	0.624	0.366	1.705
	0.025%		0.575	0.314	1.705
	0.030%		0.530	0.274	1.934

Table 7.3: Figure of merit for SNPs@SiO$_2$/PMMA filled with different percentage of SET 1 and SET 2 nanoparticles. FOM for Au NRs and LaB$_6$ NPs reported from Stokes et al. (2010) and Schelm et al. (2005) were reported for comparison.

Data in Table 7.3 show that the FOM of composite materials prepared with both SET 1 and SET 2 SNPs@SiO$_2$ (see Figure 7.17) give similar or lower values compared to both Pane 1 and Pane 2. SET 1 and SET 2 FOM are both smaller than the figure of merit of films prepared with LaB$_6$ NPs.

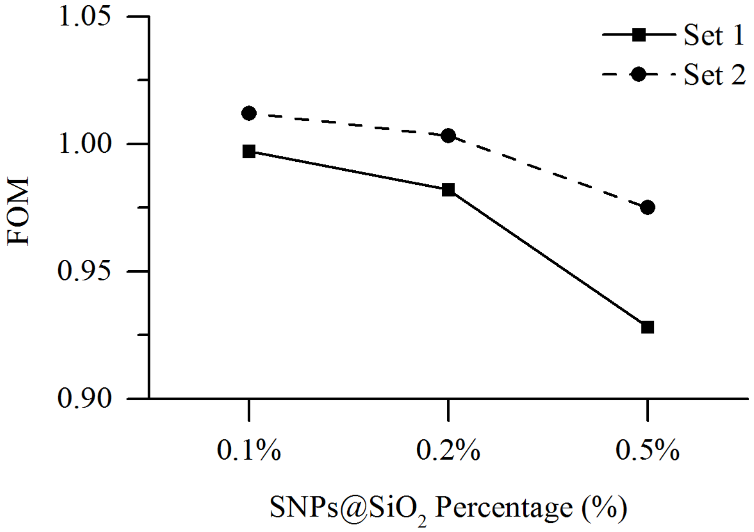

Figure 7.17: FOM for particles prepared with SNPs@SiO$_2$ from SET 1 (■) and SET 2 (●) as reported in Table 7.3.

As the films prepared with our composite were 0.1 mm thick while both Au NRs and LaB$_6$ NPs were ~0.8 mm thick, films of similar thickness were prepared using a concentration of 0.1 and 0.2% w/w SNPs@SiO$_2$ dispersed in PMMA. 0.5% concentration was not used as the composite signal saturated the spectra.

	Sample	**Thickness (mm)**	**T$_{lum}$**	**T$_{sol}$**	**FOM**
SET 1	0.1%	0.8	0.410	0.416	0.985
	0.2%		0.541	0.567	0.953
SET 2	0.1%	0.8	0.517	0.487	1.063
	0.2%		0.463	0.453	1.022

Table 7.4: Figure of merit for thicker films of SNPs@SiO$_2$ prepared with concentration of 0.1 and 0.2% w/w of inorganic filler.

The FOM of these samples are reported in Table 7.4. Increasing the thickness of the composite film resulted in better figure of merit for samples prepared with SET 2 particles. Even with thicker films, FOM of all the samples prepared with LaB$_6$ show higher values. This is mainly due the very intense absorbance of the polymer matrix in the near infrared and also in the visible region of the spectra (minimum transmittance ~70% vs. ~100% of PMMA). This is reflected in the FOM of the pure PVB which was calculated to be ~1.2 which is itself higher than all the samples prepared with both SNPs@SiO$_2$ and Au NRs.

Although the concentration of SNPs@SiO$_2$ dispersed in the polymer matrix is low (0.1% or 0.2% as in the composite podwer, as the solvent dries out), the transmittance spectra shown in Figure 7.16 remark how they can efficiently block the incoming radiation. Efficiency evaluation, (by calculation of the SHGC) for similar systems were reported by Schelm et al. (2005) and (Stokes et al., 2010). SHGC values in the range of 0.618-0.466 for LaB6 NPs (0.010% and 0.030% particles weight) and of 0.66-0.62 for AuNRs (Pane 1 and Pane 2 respectively). These values are comparable with an ITO based coating (0.683) and do not depend from the orientation of the nanoparticles with respect to the incoming radiations (contrary to the LC system). Although performances of nanoparticles coating can be improved by increasing the concentration of nanoparticles in the polymer matrix, these can also lead to (i) strong colouration in the visible and (ii) depletion of the optical properties due to phenomena such as near field effect and/or particles aggregation. The presence of the silica shell surrounding the silver core can prevent aggregation of the absorbing nuclei in our system and the interaction between the electronic fields of each particles. Improvement of the FOM could be achieved by increasing the size of the triangular prisms or the thickness of the silica shell in order to shift the dipole in-plane resonance at higher wavelength although this could cause haze in the glazing due to scattering.

7.3 Conclusions

In this chapter preparation of SNPs@SiO$_2$/PMMA composite was shown. Nanoparticles were covalently linked to the polymeric matrix using the grafting through method. Namely, allyl groups on the particles surface were polymerised along with the monomers. The effect of particle load on M_n and M_w was studied by means of GPC. Although an effect on both properties was observed for all particle loadings, no clear trend was observed, with the exception of 0.1% for which M_n and M_w show higher values the pure polymers. TGA and dTGA of pure polymers and composite showed that increasing the percentage of particles in the organic matrix the temperature of random scission linearly shifts to lower temperatures. This effect is in contrast with previous results for bare silver nanoparticles disperse in a PMMA network, meaning that the trend is due to the effect of the grafting of the particles as allyl groups are attached to the silica shell surrounding the metallic core. To prove the grafting of the polymer to the C=C groups, SNPs@SiO$_2$/PMMA solutions were centrifuged in order to remove the physisorbed polymer chains. ^{1}H NMR and ^{13}C solid state NMR show the presence of PMMA on the particles' surface. Also, TEM pictures of the precipitate suggest the embedding of the SNPs@SiO$_2$/PMMA in the polymer chain Further characterisation of these materials with atomic force microscopy (AFM) could help proving the presence of a polymeric network between the particles.

To test the efficency of SNPs@SiO$_2$/PMMA, two different approaches were tried, (i) deposition of a thin film by spin coating and (ii) casting of thicker film using a PMDS/glass mold. Films obtained with the first method showed very high transmittancwe, except when slow spinning speed were used which resulted in a thick and non-homogeneous film. Thicker films, on the other hand, showed reduced transmittance in the region of interest. FOM were calculated for two different sets of particles embedded in the polymeric matrix, SET 1 and SET 2, absorbing at ∼740 and ∼880 nm. Composite made with SET 2 particles showed higher values compared to films prepared with gold nanorods dispersed in PVA of similar thickness, while composite prepared with SET 1 particles, FOM<1 were obtained for samples prepared with all the different concentration of SNPs@SiO_2. Although further characterisation is needed, the results presented in this chapter clearly suggest the potential application of silver nanoprisms as coating for energy saving glazing.

Chapter 8

Concluding Remarks

Reducing radiation heat transfer through a building's windows has emerged as a key factor to reduce energy demand and CO_2 production. Although several technologies have been developed in recent years, no real marketable energy saving windows coating exists as their high production cost and their limited life time is a limiting factor in their diffusion.

In this study we investigated the feasibility of novel materials. i.e. metal nanoparticles/polymer thin film, as a cheap and robust technology potentially to be commercialised on a large scale. Particularly, we investigated the potential application of triangular silver nanoprisms as dye due to the low absorbance in the visible portion of the spectrum compared to other colloid studied for energy saving glazing, such as gold nanorods and LaB_6 nanoparticles.

The aims of the thesis were:

- To study the optical properties of SNPs, in particularly the possibility to tune their plasmon surface resonance to higher wavelength;
- To functionalise the particles with a silica shell to avoid aggregation of the metal nuclei and add functional groups onto their surface;
- To improve the dispersion of SNPs in the polymer matrix;
- To evaluate the proprieties of the composite as energy saving material;
- To provide a more reliable synthesis of SNPs, with good control over the final size and shape, even for large volumes of particles.

To investigate the optical properties of silver nanoprims two different approaches were adopted. The first approach was to modify their optical properties by modifying their size using Cl^- ions while the second was to change both the shape and composition of the colloid by galvanic replacement of silver by Au^{3+} ions. Although both approaches lead to a large shift to higher wavelength of SNPs' maximum absorbance, a lack of reproducibility was observed, as proven by the high standard deviations, in particularly for the modification with Cl^-.

Coating of the particles with a silica shell was achieved using a modified Ströber method. Particularly TEOS condensation was catalysed using DMA, in order to prevent the etching of Ag^0 from the colloid due to the formation of ammonia salt. Furthermore, the stabilizing agent (TSCD) was replaced with MHA to grant further stabilisation. The reaction lead to the formation of the a smooth and thick shell around SNPs, as shown by TEM images. Addition of functional groups onto the particles' surface was achieved using simultaneous condensation of TEOS and ATES in order to provide allyl group onto the particles' surface. Co-condensation was chosen over post-functionalisation as allows for simpler characterisation. The thinner shell formed when higher amount of allytriethoxysilane replaced TEOS during the sol-gel process can indeed be detected with TEM, UV-vis spectroscopy and EDAX, while the presence of allyl group on the particles

surface is hard to detect do to the small amount attached to the metal nanoparticles' surface.
To improve the dispersion of SNPs@SiO_2 in the polymer matrix (i.e. PMMA) a "grafting through" approach was adopted. Thanks to the allyl groups onto the surface of SNPs@SiO_2, the particles can be incorporated directly in the polymer matrix. This can avoid the formation of two phases in the polymer blend, i.e. particles's aggregates surrounded by the polymer. TEM images show a good distribution of SNPs@SiO_2 when the particles are grafted to polymer matrix.

In order to provide a more reliable synthesis of SNPs, even for larger volumes of particles, a microreactor was developed for the continuous flow production of such colloids. In particular, by controlling the microfluidic parameter (i.e. RD, R, V_{tot}), tailoring of SNPs size and shape distribution, and therefore on the particles optical properties was achieved. Micro-reactors were also successfully employed to modify the size of SNPs by mixing chloride to nanoparticle precusors solution by means of a T-valve prior to the micro-reactor inlet. Results achieved with this method led to a much more reproducible output and reduced the standard deviation of the final λ_{max}. By *in series* connecting a second micro-reactor, modification of preformed SNPs using bromide ions was achieved. As halide ions are not only know to change the size of silver particles but also to sculpture their shape, the use of a microfluidic setup that combine the ability of both chloride and bromide ions can lead to the formation of a very wide range of different anisotropic particles just by modifying the flow rate of reagents inside the reactor.

Compared to the studies of Schelm et al. (2005) and Stokes et al. (2010), this thesis work reports improvements for application of metal nanoparticles as NIR absorber for energy saving glazing application. The use of SNPs with their strong absorbance in the NIR and weak colouration, is a step closer to the production of glazing able to reduce the heat income and to still provide good illumination. Furthermore, coating of the metallic core with a silica shell bearing allyl moieties lead to several advantages, such as:

- Aggregation of the metal nuclei can be avoided, even at high load, leaving their optical properties unchanged;
- The distribution of particles is improved inside the polymer matrix, with no formation of aggregates;
- Particles can be dispersed also in organic solvents, allowing the use of polymers more resistant to outdoor condition/humidity.

In order to provide efficient coatings, a good control over the final shape and size of SNPs must be exerted, to reduce the broadness of the absorbance band (i.e. absorbing just in the NIR portion of the solar spectrum). Although use of microreactors for scaling up chemical syntheses still presents several limitations, a microfluidic approach can result more efficient than traditional batch reactor in the preparation of nanoparticles, as high control over the mixing is required for producing high quality materials. Compared to a traditional batch reactor the use of a microfluidic, showed several improvements. The first advantages is the control over the fluidodymanic of the whole process, in particularly on the particles' nucleation and growth. Changing in the diffusion-driven mixing of the reagent allowed for a precise control over size and shape of the particles. In particular at lower R, faster mixing was achieved (narrower water stream), increasing the supersaturation rate and thus the kinetic of both nucleation and growth (the faster the supersaturation, the smaller the particles). Although control over size and shape of SNPs is possible also in batch, our microfluidic approach do not requires changing in the chemical composition, as otherwise reported from Métraux and Mirkin (2005). Another advantage of our system is the possibility to synthesise SNPs over a long period of time (∼4 hours) with limited changes in the optical properties (λ_{max} and FWHM) and therefore in the particles size and shape distribution.

The work reported in this thesis offer a complete approach for the production of highly competitive coatings, both in term of cost (cheap reagents and low cost production techniques) and quality (sharp absorbance peak moved to higher wavelengths).

Although the results reported in this thesis are encouraging, we believe that further characterisation of our coating could strengthen them and push these composite materials a step closer to market commercialisation. In particularly we think that their mechanical properties should be investigated, with focus on their adhesion and resistance to outdoor conditions. Both points will help to better understand if these materials can find real application in everyday use (i.e. they will last enough to be cost efficient or they will need to be frequently replaced). The studies here reported mainly focused on investigating the optical properties of SNPs@SiO_2/PMMA composite as potential energy saving coatings. Although the calculated FOM shows good result compared to similar systems, studies on their real efficiency in reducing the cooling load in a building should be carried out in order to give a complete picture of the characteristics and advantages of these materials. In particular study on the SHGC (or SC) must be the central aim of future works, with an extensive modelling of their effect on the heat income in buildings.

Even if nanomaterials are founding application in several everyday objects, the possible risks associated with their possible realise are still object of concern. For this reasons we think that focus should be put in studying possible leaking of nanomaterials from the polymer matrix. Although a recent study prove the very low rate of leaking of nanomaterials from a building façade (Al-Kattan et al., 2013), assessing the environmental risk of these materials is a fundamental step for them to be part of the solution and not of the problem.

Appendix A

A.1 UV-vis Spectra of SNPs

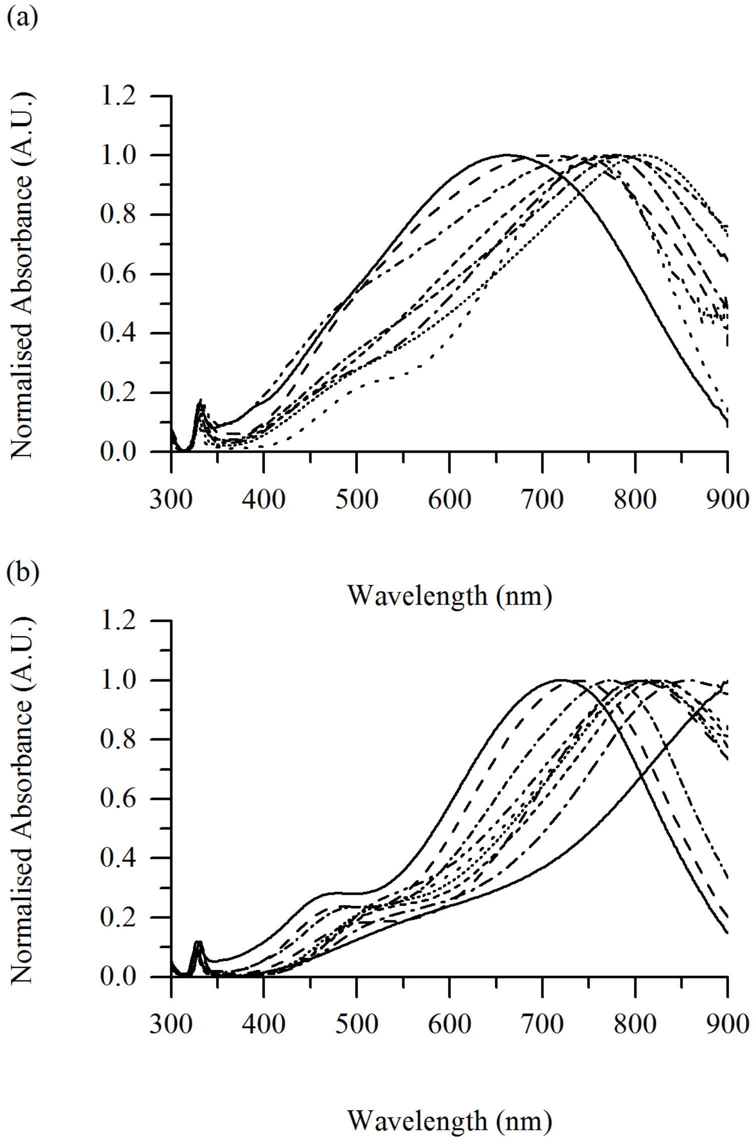

Figure A.1: Spectra of SNPs prepared with (a) citrate only and (b) with PVP

A.2 TEM Picture of Silver Nanoprisms

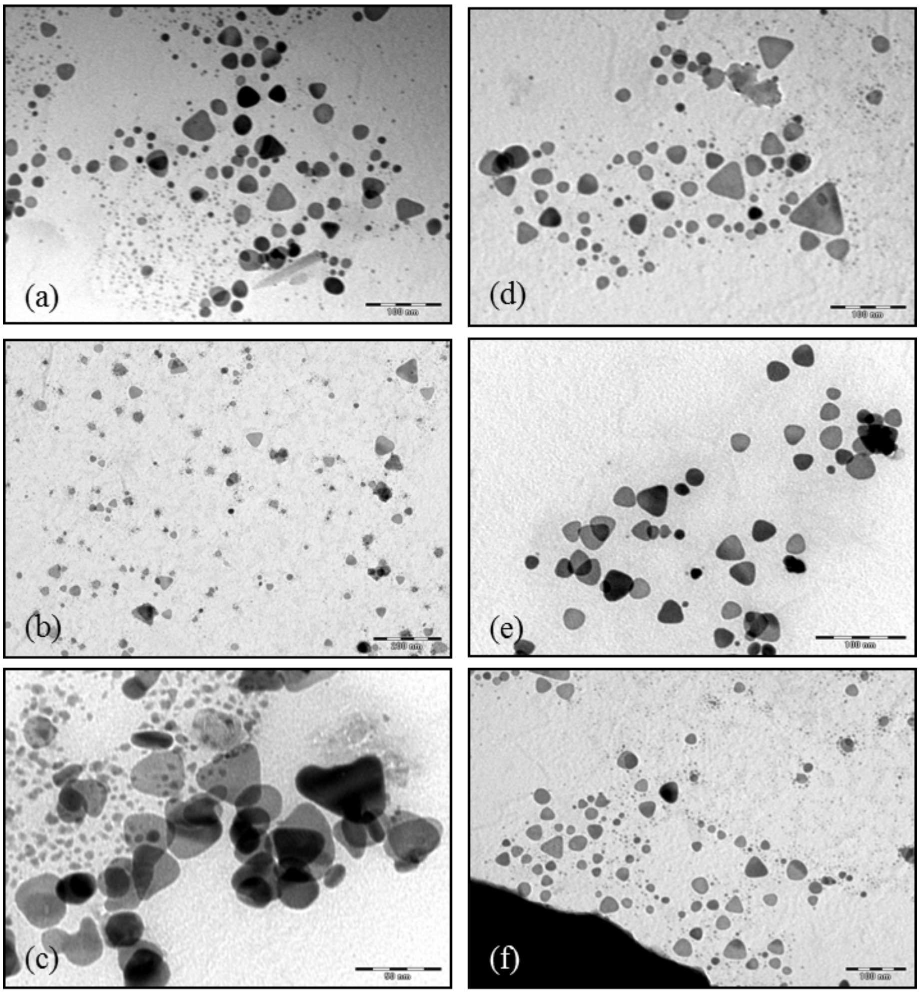

Figure A.2: TEM images of silver nanoprisms prepared in absence of PVP. The scale bar is 100 nm for all pictures, with the exception of Figure A.2b and Figure A.2c for which is 200 nm and 50 nm, respectively.

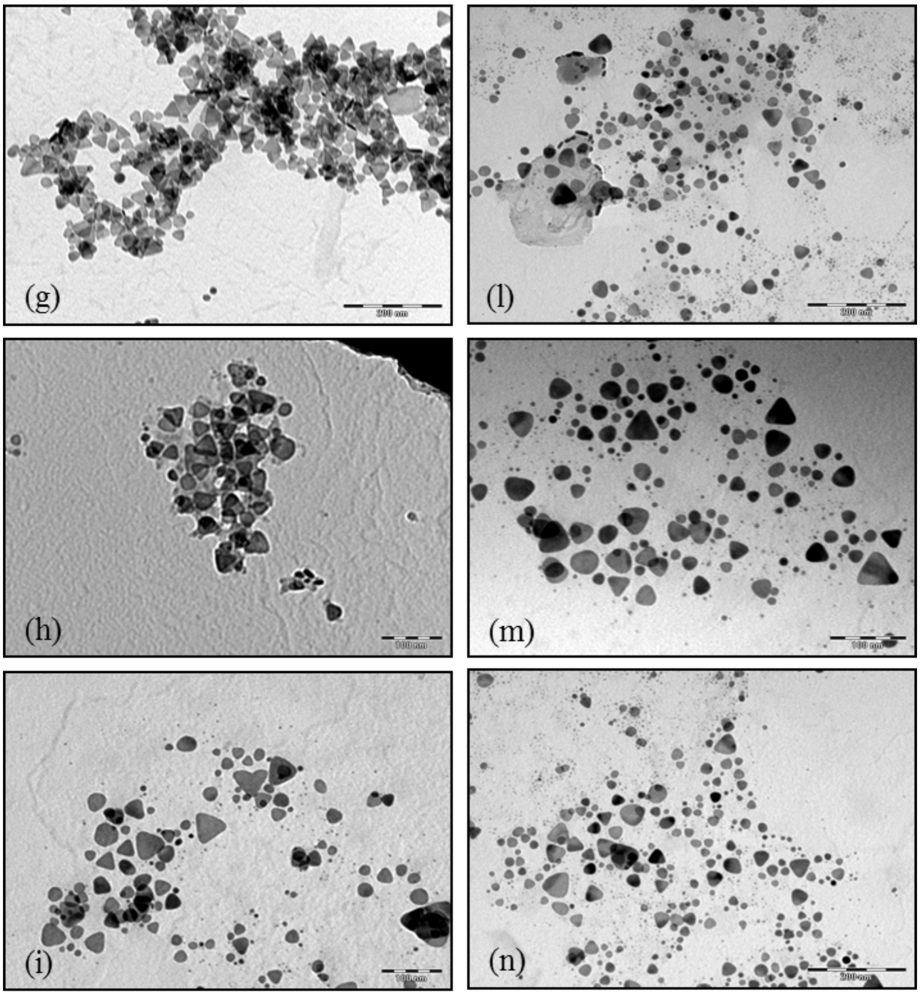

Figure A.3: Continues from Figure A.2. TEM images of silver nanoprisms prepared in absence of PVP. The scale bar is 100 nm for all the pictures, with exception of Figure A.3g, Figure A.3l and Figure A.3n for which the scale bar is 200 nm.

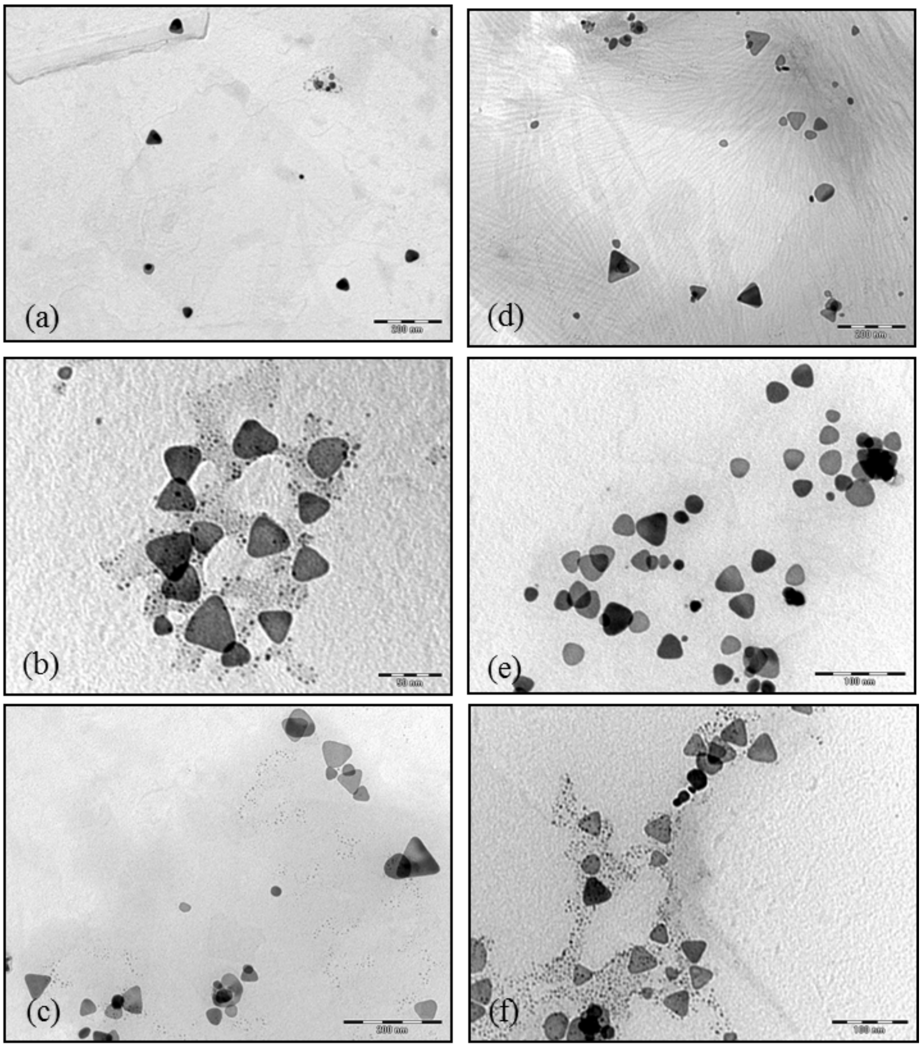

Figure A.4: TEM images of nanoprisms prepared with PVP. The scale bar is 200 nm for Figure A.4a, Figure A.4c and Figure A.4d, 100 nm Figure A.4e and Figure A.4f and 50 nm for Figure A.4b

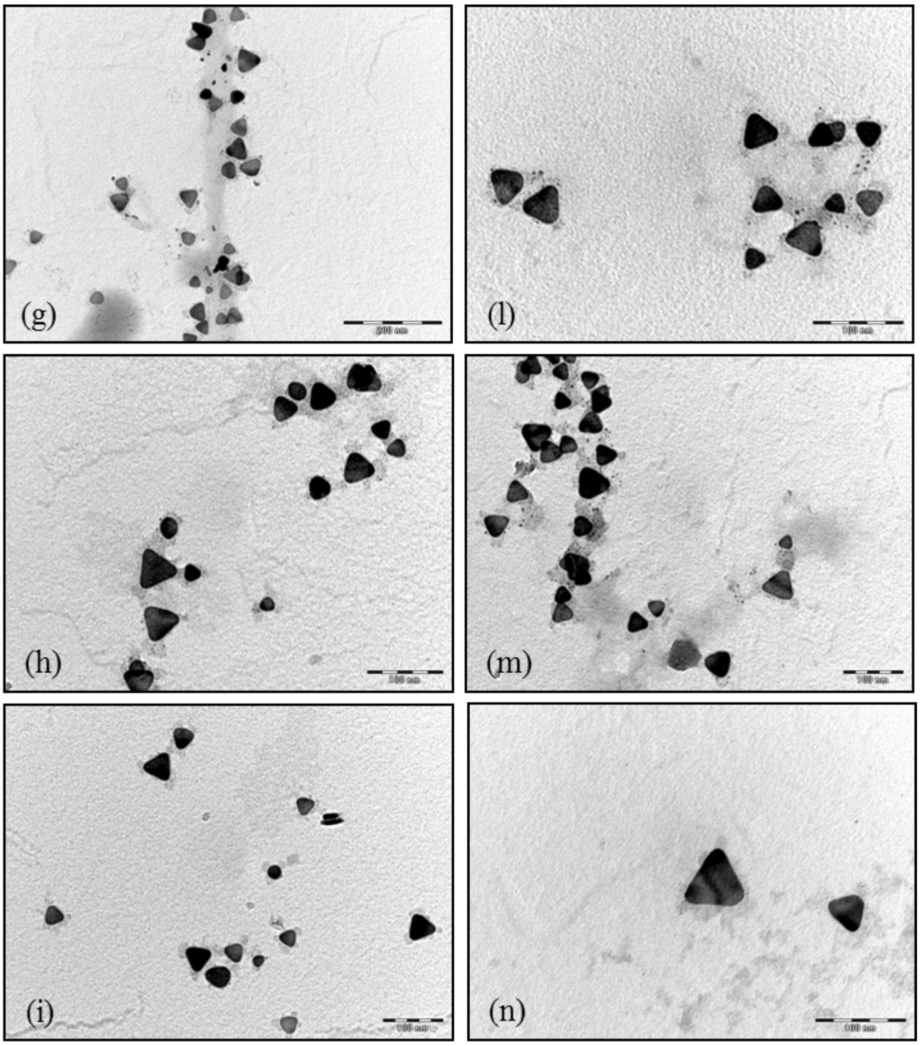

Figure A.5: Continues from Figure A.4. TEM images for nanoprisms prepared with PVP. The scale bar is 100 nm for all the pictures, with the exception of Figure A.5g for which is 200 nm.

A.3 Collection of UV-vis Spectra Prepared with Different Amount of KCl

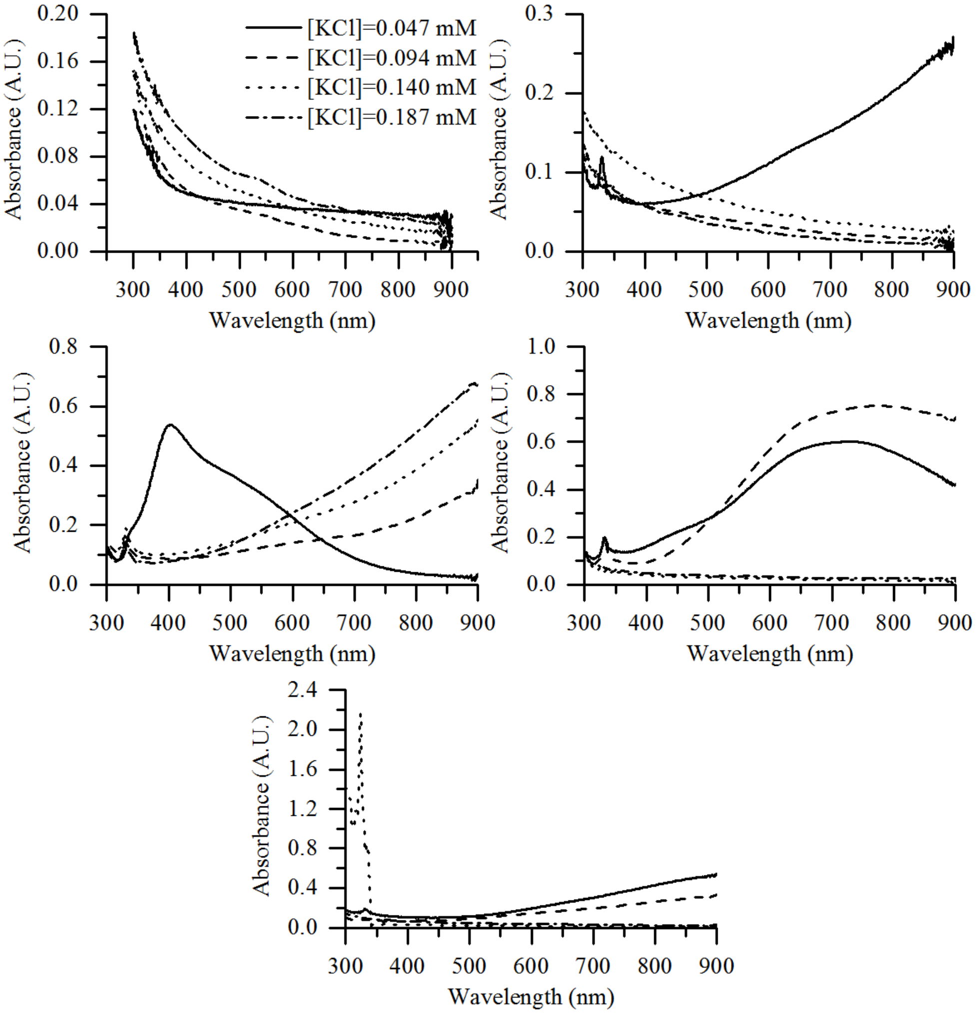

Figure A.6: Spectra used for calculating the standard deviation of samples prepared with different concentration of KCl.

A.4 EDAX Spectra

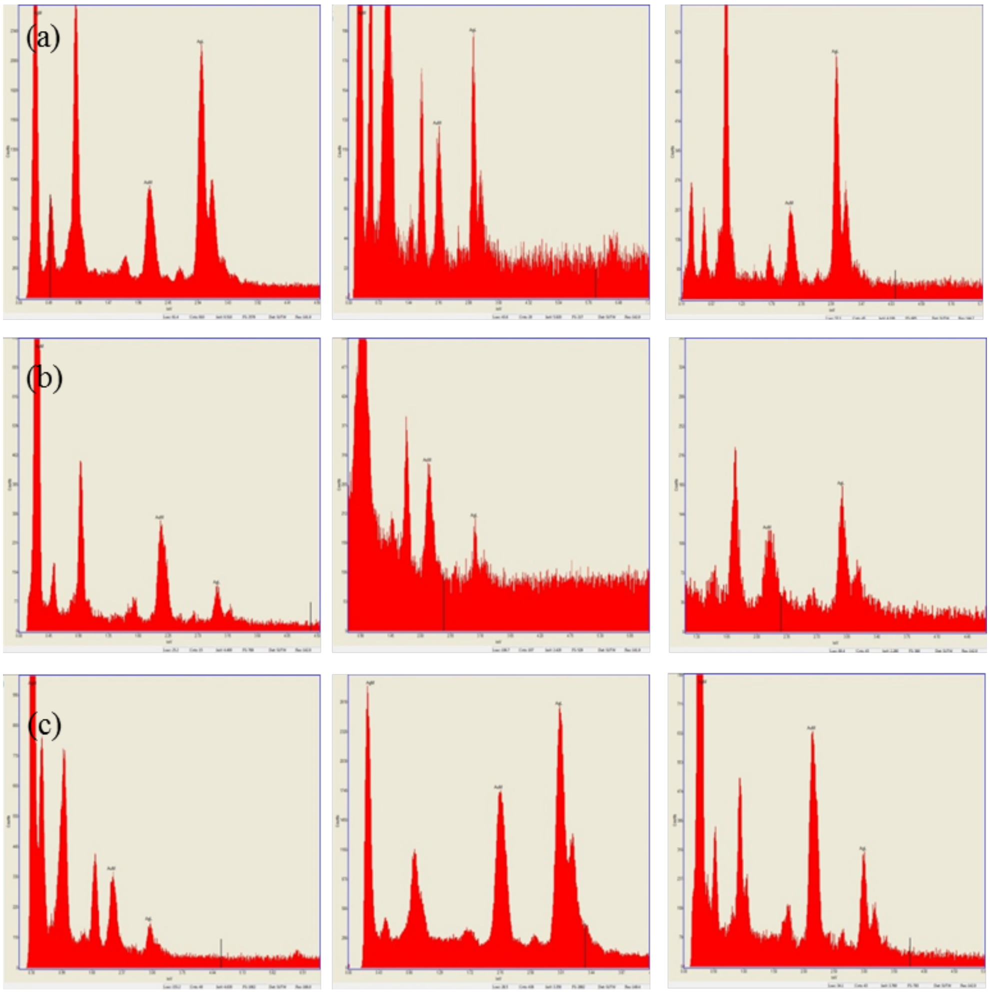

Figure A.7: EDAX spectra collected for nanohollows, prepared by starting from SNPs synthesised in the presence of PVP, with different concentration of gold cations, as reported in Table 4.6

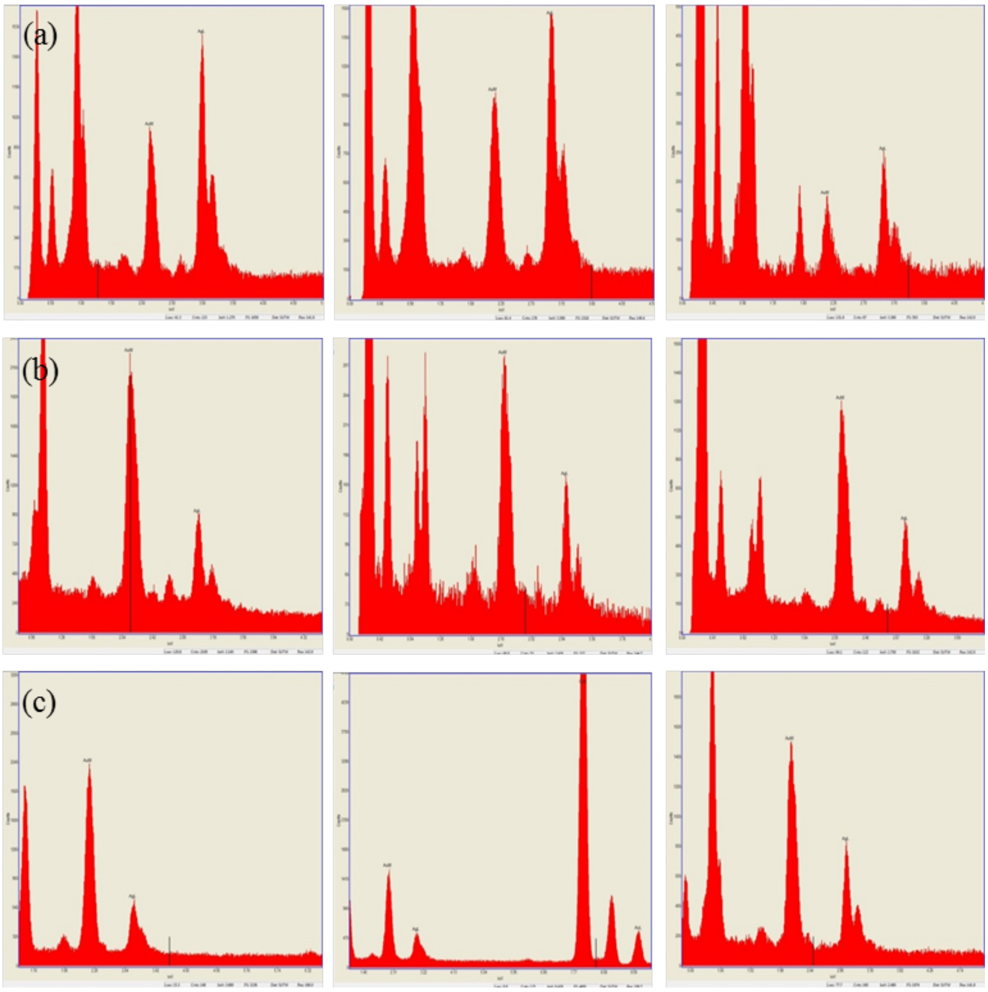

Figure A.8: EDAX spectra collected for nanohollows, prepared starting from SNPs synthesised in the absence of PVP, with different concentration of gold cations, as reported in Table 4.6

Appendix B

B.1 RD vs ET plotted for Silver Nanoprisms Synthesised at Different Flow Rates

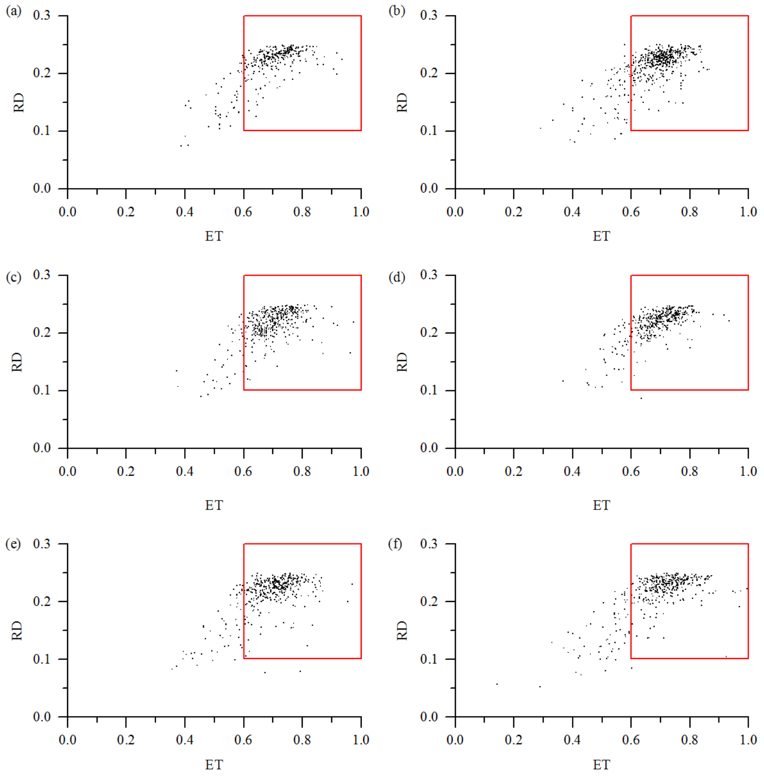

Figure B.1: RD vs ET plotted for silver nanoprisms synthesised at different flow rates (a) 3.41 mL/h, (b) 3.21 mL/h, (c) 3.01 mL/h, (d) 2.81 mL/h, (e) 2.61 mL/h, (d) 2.41 mL/h.

B.2 Light Source Spectrum

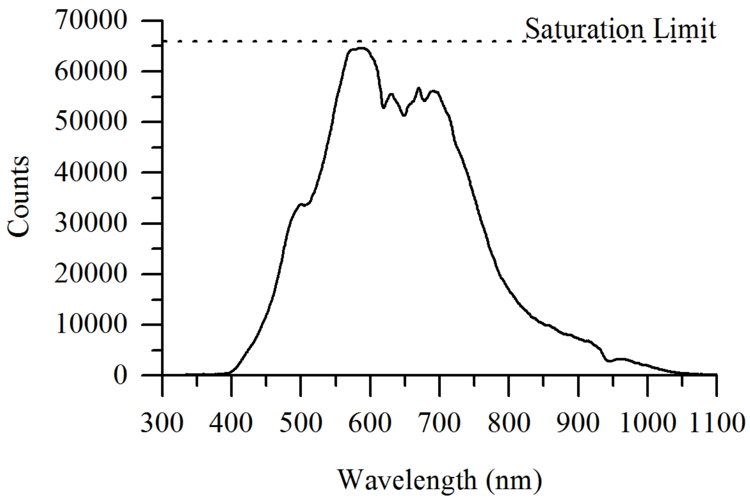

Figure B.2: Spectrum of the light source collected as water was flowing through the microreactor channel.

Appendix C

C.1 Series of Silver Core Shape and Size Distribution

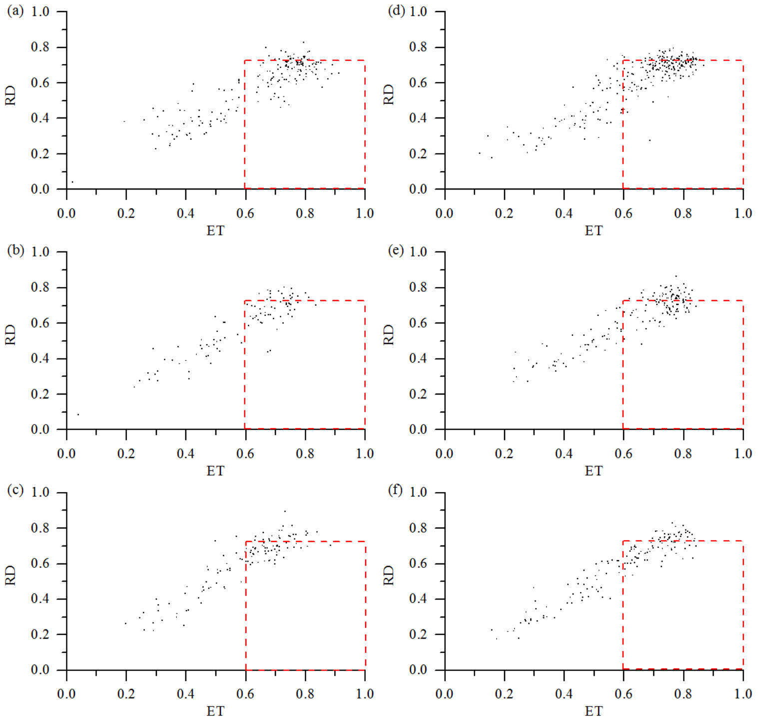

Figure C.1: Different silver core shape distribution. Figure C.1a-Figure C.1c refer to particles prepared without PVP, while Figure C.1d-Figure C.1f refer to particles prepared in presence of PVP.

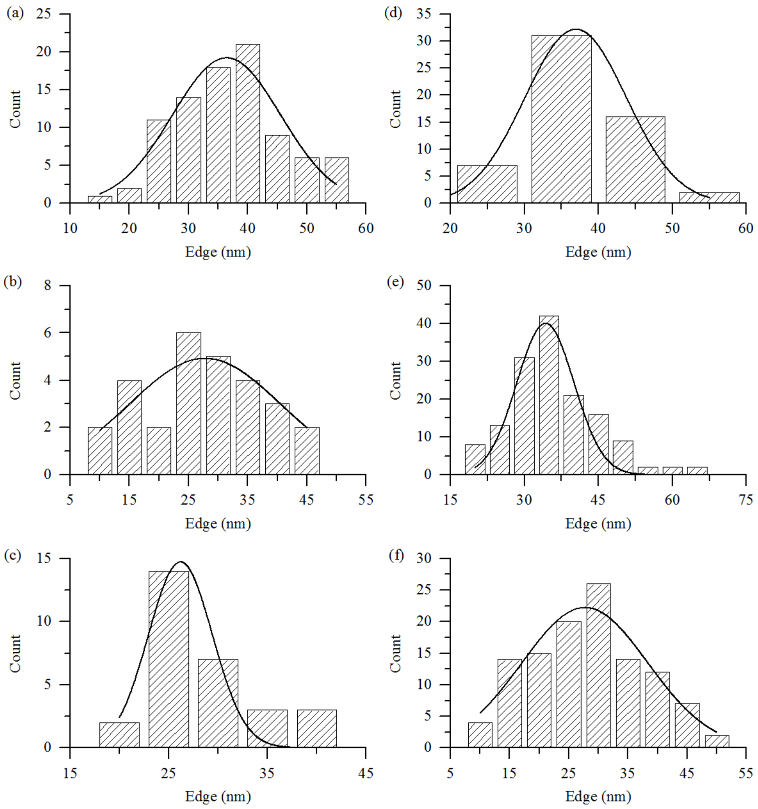

Figure C.2: Different silver core size distribution. Figure C.2a-Figure C.2c refer to particles prepared without PVP, while Figure C.2d-Figure C.2f refer to particles prepared in presence of PVP.

C.2 EDAX Spectra of Samples Prepared with Different Ratio TEOS/ATES

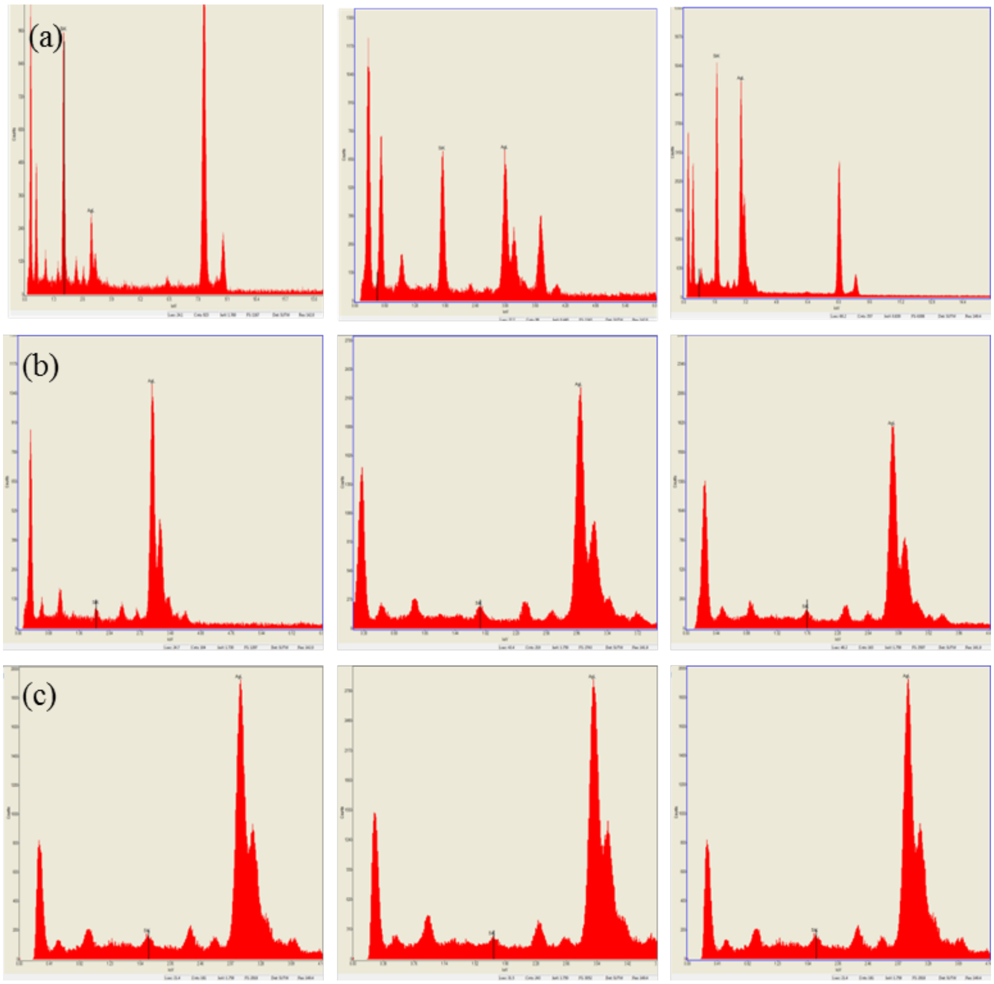

Figure C.3: EDAX data used for the calculation of data in Figure 6.16. The ratio TEOS/ATES are (a) 100/0, (b) 80/20 and (c) 60/40.

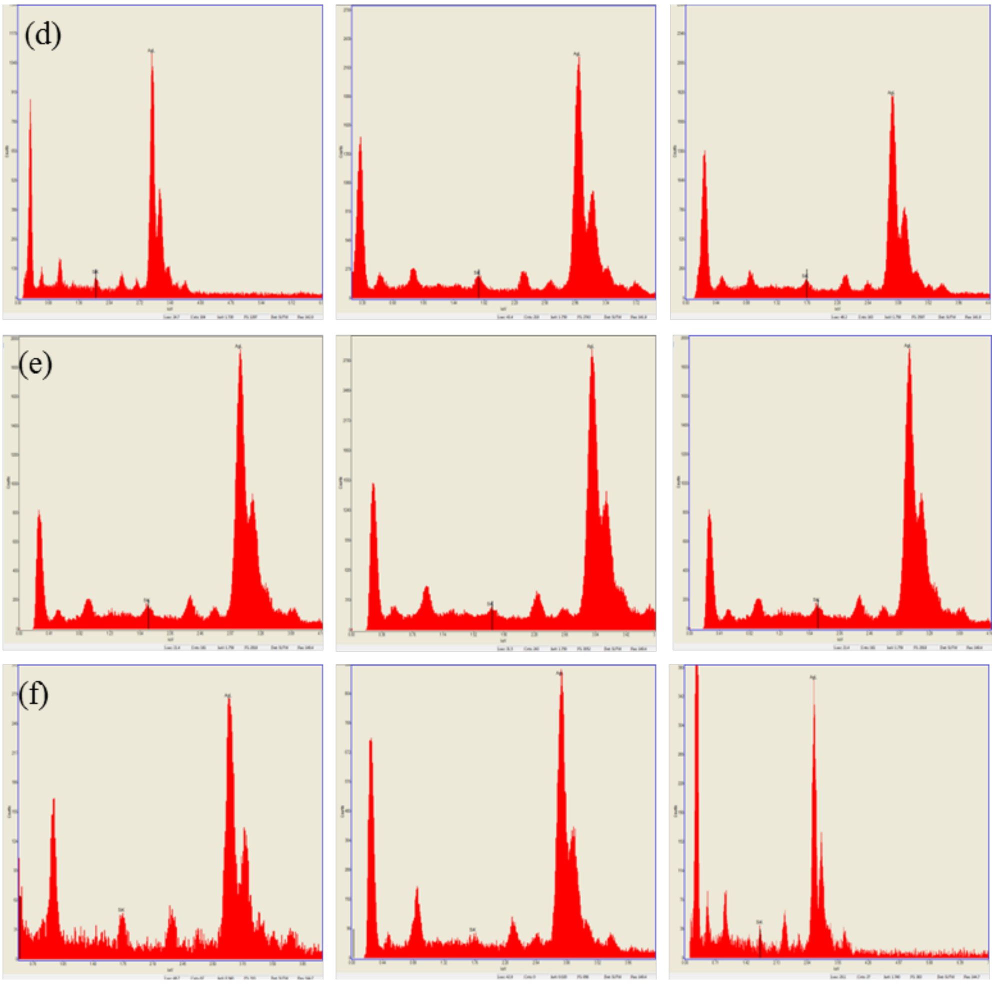

Figure C.4: Continues from Figure C.4. EDAX data used for the calculation of data in Figure 6.16. The ratio TEOS/ATES are (d) 40/60, (e) 20/80 and (f) 0/100.

Appendix D

D.1 NMR Spectra of Different Polymer Fraction Solutions

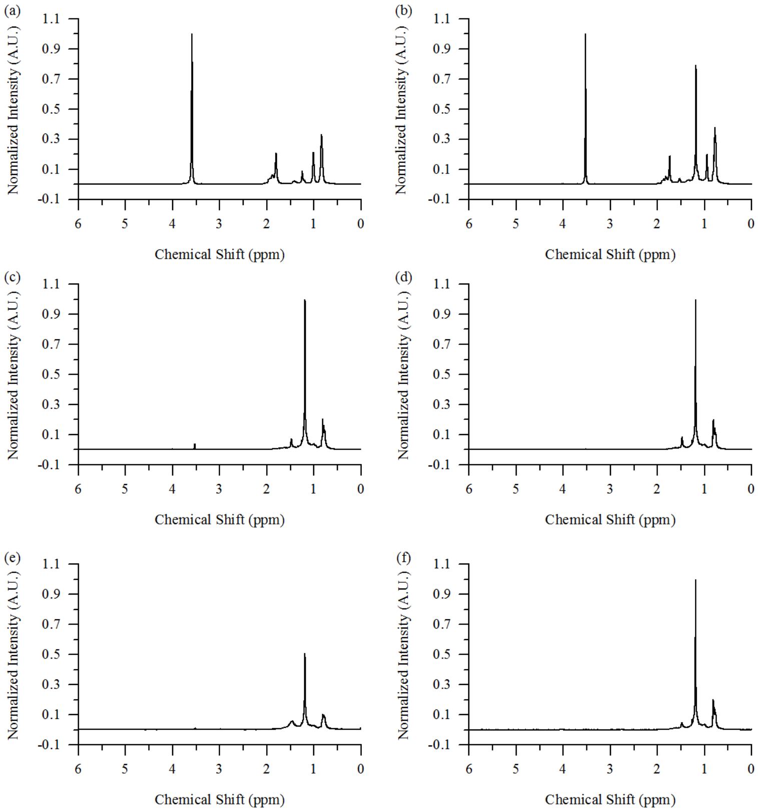

Figure D.1: NMR spectra for surfactant collected from (a) Fraction 1 to (f) Fraction 6 in Table 7.2

D.2 TEM Images of Polymer Attached on SNPs@SiO$_2$

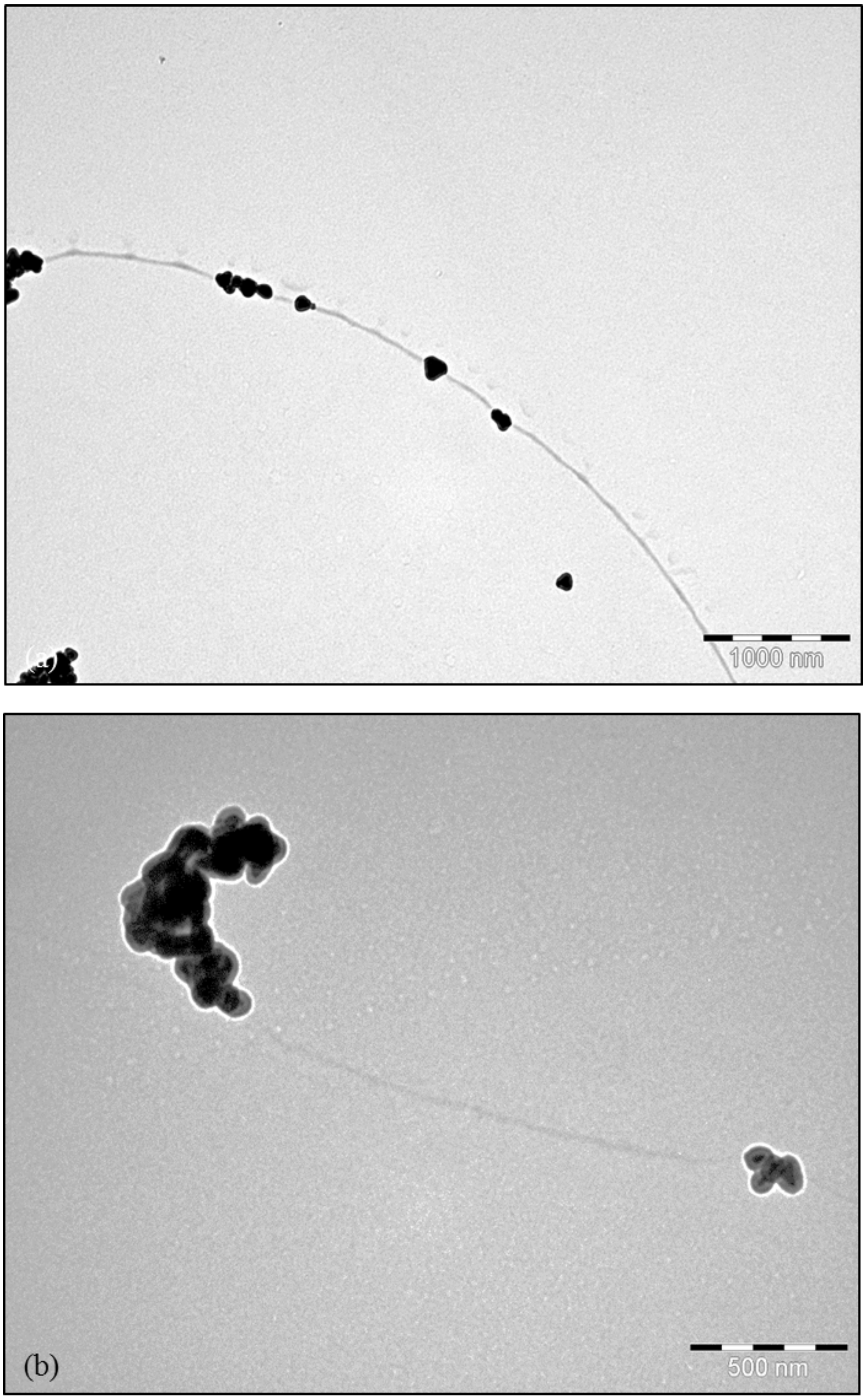

Figure D.2: Double-sized pictures of Figure 7.11

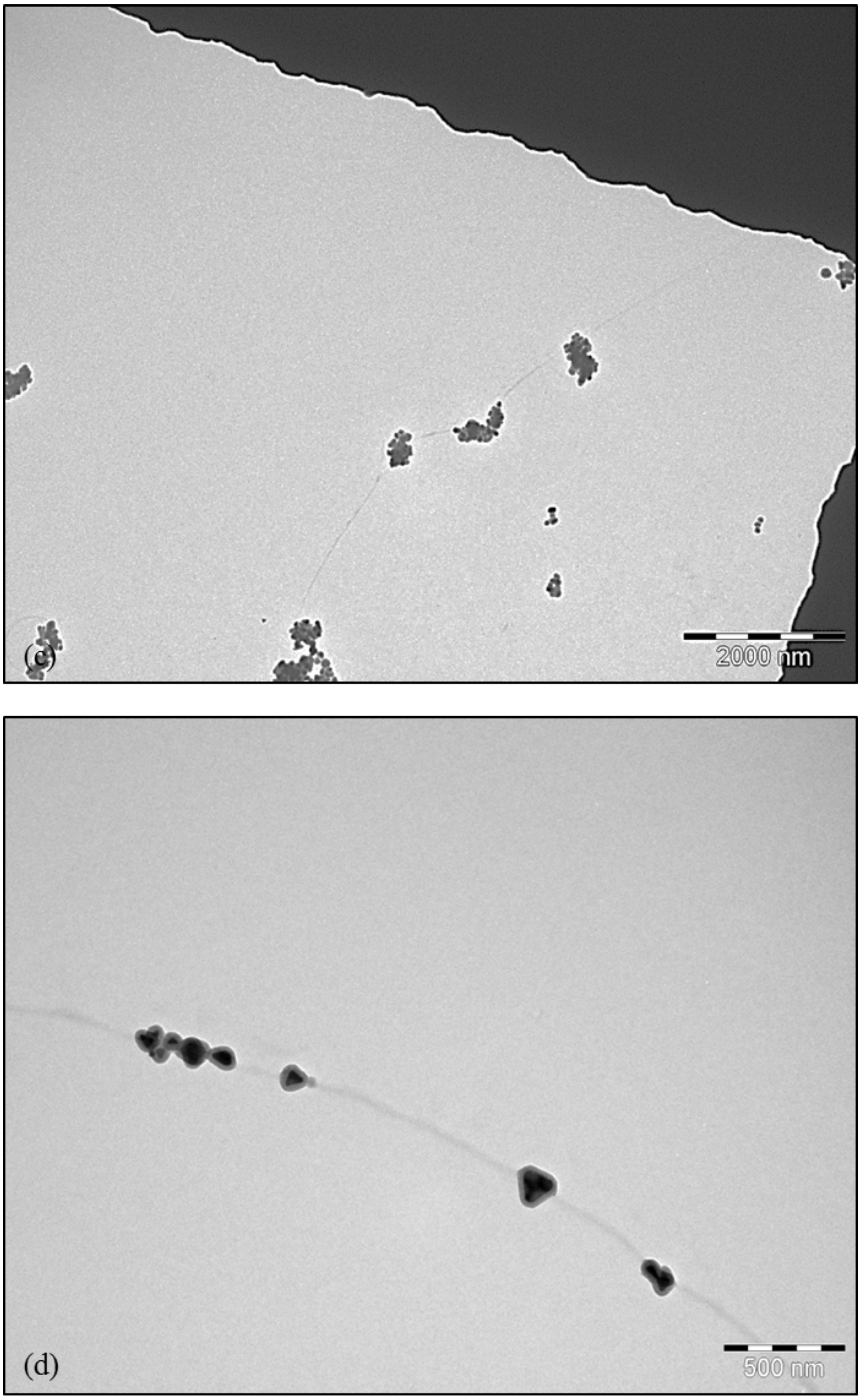

Figure D.3: Continues from Figure D.2.Double-sized pictures of Figure 7.11

Appendix E

E.1 List of Publications

- M. Carboni, L. Capretto, D. Carugo, E. Stulz, and X. Zhang. Microfluidics-based continuous flow formation of triangular silver nanoprisms with tuneable surface plasmon resonance. Journal of Materials Chemistry C, 1(45):7540–7546, 2013.
- R. Zmijan, M. Carboni, L. Capretto, E. Stulz, and X. Zhang. *In-situ* micro-spectroscopic monitoring within a micro-reactor. RSC Advances, 4(28):14569–14572, 2014
- M. Carboni, E. Stulz, and X. Zhang. Silver nanoprisms embedded in a polymeric matrix for energy saving glazing. In preparation.
- D. Carugo, T. Octon, W. Messaoudi, A. Fisher, M. Carboni, N. R. Harris, M. Hill, and P. Glynne-Jones. A thin-reflector microfluidic resonator for continuous-flow concentration of microorganisms: a new approach to water quality analysis using acoustofludics. Lab On a Chip, Complete-Under revision.
- D. Carugo, L. Capretto, B. Roy, M. Carboni, M. Caine, A. L. Lewis, M. Hill, S. Chakraborty, and X. Zhang. Spatio-temporal dynamics of doxorubicin elution from embolic beads within a biomimetic microvascular network. Journal of Controlled Release, Complete - To be submitted.

E.2 Conferences Abstract

- Interreg Conference, Poster Presentation, 08-12-10
- MPA Conference, Poster Presentation, 27-6-11
- Interreg Meeting, Oral Presentation, 19-7-11
- School of Engineering Sciences, 17th PG Conference, Oral Talk, 01-10-11
- IMRET Conference, Poster Presentation, 01-2-12
- FEE 1st PG conference, Poster Presentation, 01-11-12

- Set for Britain, Poster Presentation, 17-3-14

References

Agura, H., Suzuki, A., Matsushita, T., Aoki, T. and Okuda, M. *Thin Solid Films*, 2003;445(2):pp. 263–267.

Aherne, D., Ledwith, D. M., Gara, M. and Kelly, J. M. *Advanced Functional Materials*, 2008;18(14):pp. 2005–2016.

Aiken III, J. D. and Finke, R. G. *Journal of Molecular Catalysis A*, 1999;145(1):pp. 1–44.

Al-Dahoudi, N. and Aegerter, M. A. *Thin Solid Films*, 2006;502(1):pp. 193–197.

Al-Kattan, A., Wichser, A., Vonbank, R., Brunner, S., Ulrich, A., Zuin, S. and Nowack, B. *Environmental Science: Processes & Impacts*, 2013;15(12):pp. 2186–2193.

Alschinger, M., Maniak, M., Stietz, F., Vartanyan, T. and Träger, F. *Applied Physics B*, 2003;76(7):pp. 771–774.

An, J., Tang, B., Zheng, X., Zhou, J., Dong, F., Xu, S., Wang, Y., Zhao, B. and Xu, W. *The Journal of Physical Chemistry C*, 2008;112(39):pp. 15176–15182.

ASHRAE. *Handbook of American Society of Heating, Refrigerating and Air Conditioning Engineers*, 2001;.

Avendaño, E., Azens, A., Niklasson, G. and Granqvist, C. *Solar Energy Materials and Solar Cells*, 2004;84(1):pp. 337–350.

Aymonier, C., Bortzmeyer, D., Thomann, R. and Mülhaupt, R. *Chemistry of Materials*, 2003;15(25):pp. 4874–4878.

Babulanam, S., Eriksson, T., Niklasson, G. and Granqvist, C. In *30th Annual Technical Symposium*. International Society for Optics and Photonics, 1987; pp. 8–18.

Baetens, R., Jelle, B. P. and Gustavsen, A. *Solar Energy Materials and Solar Cells*, 2010;94(2):pp. 87–105.

Bange, K. *Solar Energy Materials and Solar Cells*, 1999;58(1):pp. 1–131.

Bao, S., Tajima, K., Yamada, Y., Okada, M. and Yoshimura, K. *Applied Physics A*, 2007;87(4):pp. 621–624.

Bárta, J., Pospíšil, M. and Čuba, V. *Journal of radioanalytical and nuclear chemistry*, 2010;286(3):pp. 611–618.

Betz, U., Kharrazi Olsson, M., Marthy, J., Atamny, F. et al. *Surface and Coatings Technology*, 2006;200(20):pp. 5751–5759.

Bigelow, D. J. and Inesi, G. *Biochemistry*, 1991;30(8):pp. 2113–2125.

Bollero, A., Grossberg, M., Asenjo, B. and Gutiérrez, M. *Surface and Coatings Technology*, 2009;204(5):pp. 593–600.

Boltzmann, L. *Annalen der Physik*, 1884;258(6):pp. 291–294.

Bönnemann, H. and Richards, R. M. *European Journal of Inorganic Chemistry*, 2001; 2001(10):pp. 2455–2480.

Bovey, F. and Tiers, G. *Journal of Polymer Science Part A: Polymer Chemistry*, 1996; 34(5):pp. 711–720.

Bruggeman, V. D. *Annalen der Physik*, 1935;416(7):pp. 636–664.

Callegari, A., Tonti, D. and Chergui, M. *Nano Letters*, 2003;3(11):pp. 1565–1568.

Capretto, L., Carugo, D., Cheng, W., Hill, M. and Zhang, X. *Journal of Colloid and Interface Science*, 2011;357(1):pp. 243–251.

Carbon Trust. *UK*, 2000;.

Cárdenas, M. Á., Basurto, F. C., García-López, D., Merino, J. C. and Pastor, J. M. *Polymer Bulletin*, 2013;70(8):pp. 2169–2179.

Carotenuto, G., Pepe, G. and Nicolais, L. *The European Physical Journal B-Condensed Matter and Complex Systems*, 2000;16(1):pp. 11–17.

Cathcart, N., Frank, A. J. and Kitaev, V. *Chemical Communication*, 2009;(46):pp. 7170–7172.

Chan, E. M., Mathies, R. A. and Alivisatos, A. P. *Nano Letters*, 2003;3(2):pp. 199–201.

Chatenet, M., Molina-Concha, M. B., El-Kissi, N., Parrour, G. and Diard, J.-P. *Electrochimica Acta*, 2009;54(18):pp. 4426–4435.

Chen, J., Wiley, B., McLellan, J., Xiong, Y., Li, Z.-Y. and Xia, Y. *Nano letters*, 2005; 5(10):pp. 2058–2062.

Chen, S., Wang, Z. L., Ballato, J., Foulger, S. H. and Carroll, D. L. *Journal of the American Chemical Society*, 2003;125(52):pp. 16186–16187.

Chopra, K. L. *Thin Film Phenomena*, vol. 137. McGraw-Hill New York, 1969.

Claesson, M. E. and Philipse, A. P. *Colloids and Surfaces A: Physicochemical and Engineering Aspects*, 2007;297(1):pp. 46–54.

Correa, G. and Almanza, R. *Solar Energy*, 2004;76(1):pp. 111–115.

Crooks, R. M., Zhao, M., Sun, L., Chechik, V. and Yeung, L. K. *Accounts of Chemical Research*, 2001;34(3):pp. 181–190.

Cui, B., Clime, L., Li, K. and Veres, T. *Nanotechnology*, 2008;19(14):pp. 145302–145307.

Cui, H., Feng, Y., Ren, W., Zeng, T., Lv, H. and Pan, Y. *Recent Patents on Nanotechnology*, 2009;3(1):pp. 32–41.

Cui, Y., Zheng, X.-S., Ren, B., Wang, R., Zhang, J., Xia, N.-S. and Tian, Z.-Q. *Chemical Science*, 2011;2(8):pp. 1463–1469.

Dai, H., Wong, E. W., Lu, Y. Z., Fan, S. and Lieber, C. M. *Nature*, 1995;375(6534):pp. 769–772.

Dai, L., Cao, C., Gao, Y. and Luo, H. *Solar Energy Materials and Solar Cells*, 2011; 95(2):pp. 712–715.

DeLongchamp, D. M., Kastantin, M. and Hammond, P. T. *Chemistry of Materials*, 2003;15(8):pp. 1575–1586.

Dolgaev, S., Simakin, A., Voronov, V., Shafeev, G. and Bozon-Verduraz, F. *Applied Surface Science*, 2002;186(1):pp. 546–551.

Dong, S.-A. and Zhou, S.-P. *Materials Science and Engineering: B*, 2007;140(3):pp. 153–159.

Drude, P. *Annalen der Physik*, 1900;306(3):pp. 566–613.

Duval Malinsky, M., Kelly, K. L., Schatz, G. C. and Van Duyne, R. P. *The Journal of Physical Chemistry B*, 2001;105(12):pp. 2343–2350.

Ebisawa, J. and Ando, E. *Current Opinion in Solid State and Materials Science*, 1998; 3(4):pp. 386–390.

Ederth, J., Heszler, P., Hultåker, A., Niklasson, G. and Granqvist, C. *Thin Solid Films*, 2003;445(2):pp. 199–206.

Edmonds, I. R. *Applied Optics*, 1995;34(28):pp. 6522–6526.

Energy Information Administration. *United States*, 2006;.

Energy Information Administration. *United States*, 2011;.

Energy Information Administration. *United States*, 2012;.

Estrada, W., Andersson, A. M. and Granqvist, C. G. *Journal of Applied Physics*, 1988; 64(7):pp. 3678–3683.

Fan, J. C. and Bachner, F. J. *Applied Optics*, 1976;15(4):pp. 1012–1017.

Faraday, M. *Philosophical Transactions of the Royal Society of London*, 1857;147:pp. 145–181.

Fedlheim, D. L., Colby Jr, A. et al. *Metal nanoparticles: synthesis, characterization, and applications.* CRC Press, 2002.

Ferriol, M., Gentilhomme, A., Cochez, M., Oget, N. and Mieloszynski, J. *Polymer Degradation and Stability*, 2003;79(2):pp. 271–281.

Fischer, F., Waitz, T., Vollath, D. and Simha, N. *Progress in Materials Science*, 2008; 53(3):pp. 481–527.

Frenz, L., El Harrak, A., Pauly, M., Bégin-Colin, S., Griffiths, A. D. and Baret, J.-C. *Angewandte Chemie International Edition*, 2008;47(36):pp. 6817–6820.

Fukano, T., Motohiro, T. and Hashizume, H. *Japanese Journal of Applied Physics*, 2005; 44:pp. 8747–8752.

Gao, Z., Liu, J., Chang, J., Wu, D., He, J., Wang, K., Xu, F. and Jiang, K. *Crystal Engineering Communications*, 2012;14(20):pp. 6639–6646.

Giesche, H. *Journal of the European Ceramic Society*, 1994;14(3):pp. 205–214.

Gourari, A., Bendaoud, M., Lacabanne, C. and Boyer, R. F. *Journal of Polymer Science: Polymer Physics Edition*, 1985;23(5):pp. 889–916.

Graf, C., Vossen, D. L., Imhof, A. and van Blaaderen, A. *Langmuir*, 2003;19(17):pp. 6693–6700.

Granqvist, C. G. *Handbook of inorganic electrochromic materials.* Access Online via Elsevier, 1995.

Granqvist, C. G. *Solar Energy Materials and Solar Cells*, 2000;60(3):pp. 201–262.

Granqvist, C. G. *Solar Energy Materials and Solar Cells*, 2007;91(17):pp. 1529–1598.

Granqvist, C.-G., Lansåker, P., Mlyuka, N., Niklasson, G. and Avendano, E. *Solar Energy Materials and Solar Cells*, 2009;93(12):pp. 2032–2039.

Grodzicki, A., Łakomska, I., Piszczek, P., Szymańska, I. and Szłyk, E. *Coordination Chemistry Reviews*, 2005;249(21):pp. 2232–2258.

Ha, T. H., Koo, H.-J. and Chung, B. H. *The Journal of Physical Chemistry C*, 2007; 111(3):pp. 1123–1130.

Haacke, G. *Annual Review of Materials Science*, 1977;7(1):pp. 73–93.

Hao, E., Schatz, G. and Hupp, J. *Journal of Fluorescence*, 2004;14(4):pp. 331–341.

Harned, H. S. *Proceedings of the National Academy of Sciences of the United States of America*, 1954;40(7):pp. 551–556.

Harris, L., Goff, J., Carmichael, A., Riffle, J., Harburn, J., St. Pierre, T. and Saunders, M. *Chemistry of Materials*, 2003;15(6):pp. 1367–1377.

Heinilehto, S. T., Lappalainen, J. H., Jantunen, H. M. and Lantto, V. *Journal of Electroceramics*, 2011;27(1):pp. 7–12.

Hirai, H., Yakura, N., Seta, Y. and Hodoshima, S. *Reactive and Functional Polymers*, 1998;37(1):pp. 121–131.

Huang, H., Ni, X., Loy, G., Chew, C., Tan, K., Loh, F., Deng, J. and Xu, G. *Langmuir*, 1996;12(4):pp. 909–912.

Igathinathane, C., Pordesimo, L., Columbus, E., Batchelor, W. and Methuku, S. *Computers and Electronics in agriculture*, 2008;63(2):pp. 168–182.

Inasawa, S., Sugiyama, M. and Koda, S. *Japanese Journal of Applied Physics*, 2003; 42(10):pp. 6705–6712.

Itoyama, K. *Journal of The Electrochemical Society*, 1979;126(4):pp. 691–694.

Jain, R., Bhargava, M. and Sharma, N. *Industrial & engineering chemistry research*, 2003;42(2):pp. 243–247.

Jana, N. R. *Small*, 2005;1(8-9):pp. 875–882.

Jana, N. R., Gearheart, L. and Murphy, C. J. *Advanced Materials*, 2001a;13(18):pp. 1389–1393.

Jana, N. R., Gearheart, L. and Murphy, C. J. *The Journal of Physical Chemistry B*, 2001b;105(19):pp. 4065–4067.

Jensen, K. F. *Chemical Engineering Science*, 2001;56(2):pp. 293–303.

Jepsen, P. U., Fischer, B. M., Thoman, A., Helm, H., Suh, J., Lopez, R. and Haglund Jr, R. *Physical Review B*, 2006;74(20):p. 205103.

Jiang, P., Li, S.-Y., Xie, S.-S., Gao, Y. and Song, L. *Chemistry-A European Journal*, 2004;10(19):pp. 4817–4821.

Jin, P., Xu, G., Tazawa, M. and Yoshimura, K. *Applied Physics A*, 2003a;77(3-4):pp. 455–459.

Jin, R., Cao, Y., Mirkin, C. A., Kelly, K., Schatz, G. C. and Zheng, J. *Science*, 2001; 294(5548):pp. 1901–1903.

Jin, R., Cao, Y. C., Hao, E., Métraux, G. S., Schatz, G. C. and Mirkin, C. A. *Nature*, 2003b;425(6957):pp. 487–490.

John, G., Clements-Croome, D. and Jeronimidis, G. *Building and Environment*, 2005; 40(3):pp. 319–328.

Jorgenson, G. and Lee, J. *Solar Energy Materials*, 1986;14(3):pp. 205–214.

Kabashin, A., Evans, P., Pastkovsky, S., Hendren, W., Wurtz, G., Atkinson, R., Pollard, R., Podolskiy, V. and Zayats, A. *Nature Materials*, 2009;8(11):pp. 867–871.

Karlsson, B., Shimshock, R., Seraphin, B. and Haygarth, J. *Solar Energy Materials*, 1983;7(4):pp. 401–411.

Kashiwagi, T., Inaba, A., Brown, J. E., Hatada, K., Kitayama, T. and Masuda, E. *Macromolecules*, 1986;19(8):pp. 2160–2168.

Kelly, K. L., Coronado, E., Zhao, L. L. and Schatz, G. C. *The Journal of Physical Chemistry B*, 2003;107(3):pp. 668–677.

Khan, K. and Granqvist, C. *Applied Physics Letters*, 1989;55(1):pp. 4–6.

Kim, B.-C., Lee, J.-H., Kim, J.-J. and Ikegami, T. *Materials letters*, 2002a;52(1):pp. 114–119.

Kim, F., Song, J. H. and Yang, P. *Journal of the American Chemical Society*, 2002b; 124(48):pp. 14316–14317.

Kim, S.-M., Seo, K.-H., Lee, J.-H., Kim, J.-J., Lee, H. Y. and Lee, J.-S. *Journal of the European Ceramic Society*, 2006;26(1):pp. 73–80.

Kirchhoff, G. *Annalen der Physik*, 1860;185(2):pp. 275–301.

Kirchmeyer, S. and Reuter, K. *Journal of Material Chemistry*, 2005;15(21):pp. 2077–2088.

Kitayama, T., Horii, H., Hatada, K. and Kashiwagi, T. *Polymer Bulletin*, 1989;21(4):pp. 433–437.

Knauer, A., Csaki, A., Moller, F., Huhn, C., Fritzsche, W. and Kohler, J. M. *The Journal of Physical Chemistry C*, 2012;116(16):pp. 9251–9258.

Knauer, A. and Khler, J. *Chemie Ingenieur Technik*, 2013;85(4):pp. 467–475.

Kobayashi, Y., Katakami, H., Mine, E., Nagao, D., Konno, M. and Liz-Marzán, L. M. *Journal of Colloid and Interface Science*, 2005;283(2):pp. 392–396.

Kobayashi, Y., Misawa, K., Takeda, M., Kobayashi, M., Satake, M., Kawazoe, Y., Ohuchi, N., Kasuya, A. and Konno, M. *Colloids and Surfaces A*, 2004;251(1):pp. 197–201.

Kulkarni, A. P., Noone, K. M., Munechika, K., Guyer, S. R. and Ginger, D. S. *Nano Letters*, 2010;10(4):pp. 1501–1505.

Kumar, A., Welsh, D. M., Morvant, M. C., Piroux, F., Abboud, K. A. and Reynolds, J. R. *Chemistry of Materials*, 1998;10(3):pp. 896–902.

Kunz, M., Niklasson, G. and Granqvist, C. *Journal of Applied Physics*, 1988;64(7):pp. 3740–3742.

Kwong, C., Choy, W., Djurišić, A., Chui, P., Cheng, K. and Chan, W. *Nanotechnology*, 2004;15(9):pp. 1156–1161.

La Mer, V. K. and Dinegar, R. H. *Journal of the American Chemical Society*, 1950; 72(11):pp. 4847–4854.

Lacroix, J., Kanazawa, K. and Diaz, A. *Journal of the Electrochemical Society*, 1989; 136(5):pp. 1308–1313.

Lai, J., Shek, C. and Lin, G. *Scripta Materialia*, 2003;49(5):pp. 441–446.

Lampert, C. *Circuits and Devices Magazine, IEEE*, 1992;8(2):pp. 19–26.

Lampert, C. M. *Solar Energy Materials*, 1981;6(1):pp. 1–41.

Lampert, C. M. *Solar Energy Materials and Solar Cells*, 2003;76(4):pp. 489–499.

Le Bellac, D., Niklasson, G. and Granqvist, C. *Journal of Applied Physics*, 1995a; 78(4):pp. 2894–2896.

Le Bellac, D., Niklasson, G. and Granqvist, C. *Thin Solid Films*, 1995b;266(2):pp. 94–95.

Lee, M.-H. and Cho, J.-S. *Thin Solid Films*, 2000;365(1):pp. 5–6.

Leftheriotis, G. and Yianoulis, P. *Solar Energy Materials and Solar Cells*, 1999;58(2):pp. 185–197.

Leisner, T., Rosche, C., Wolf, S., Granzer, F. and Wöste, L. *Surface Review and Letters*, 1996;3(01):pp. 1105–1108.

Li, B. and Yao, R. *Renewable Energy*, 2009;34(9):pp. 1994–1998.

Li, S.-Y., Niklasson, G. A. and Granqvist, C. G. *Journal of Applied Physics*, 2010a; 108(6):p. 063525.

Li, W., Guo, Y. and Zhang, P. *The Journal of Physical Chemistry C*, 2010b;114(14):pp. 6413–6417.

Lin, X. Z., Terepka, A. D. and Yang, H. *Nano letters*, 2004;4(11):pp. 2227–2232.

Linder, V., Gates, B. D., Ryan, D., Parviz, B. A. and Whitesides, G. M. *Small*, 2005; 1(7):pp. 730–736.

Liu, D., Xiang, Y., Zhang, Z., Wang, J., Gao, Y., Song, L., Liu, L., Dou, X., Zhao, X., Luo, S. et al. *Nanotechnology*, 2005;16(11):pp. 2665–2669.

Liz-Marzán, L. M., Giersig, M. and Mulvaney, P. *Langmuir*, 1996;12(18):pp. 4329–4335.

Lu, Y., McLellan, J. and Xia, Y. *Langmuir*, 2004;20(8):pp. 3464–3470.

Lu, Y., Yin, Y., Li, Z.-Y. and Xia, Y. *Nano Letters*, 2002;2(7):pp. 785–788.

Maeda, K., Ishizuka, S., Tsujino, T., Yamamoto, H. and Takigawa, A. In *San Diego,'91, San Diego, CA*. International Society for Optics and Photonics, 1991; pp. 138–148.

Manring, L. E. *Macromolecules*, 1991;24(11):pp. 3304–3309.

Manz, H. *Energy and Buildings*, 2004;36(2):pp. 127–136.

Martin-Gallego, M., Bernal, M., Hernandez, M., Verdejo, R. and Lopez-Manchado, M. *European Polymer Journal*, 2013;49(6):pp. 1347–1353.

Maxwell, J. C. *Philosophical Transactions of the Royal Society of London*, 1865;pp. 459–512.

Mbise, G., Smith, G., Niklasson, G. and Granqvist, C. *Applied Physics Letters*, 1989; 54(11):pp. 987–989.

Mdluli, P. S., Sosibo, N. M., Mashazi, P. N., Nyokong, T., Tshikhudo, R. T., Skepu, A. and van der Lingen, E. *Journal of Molecular Structure*, 2011;1004(1):pp. 131–137.

Métraux, G. S. and Mirkin, C. A. *Advanced Materials*, 2005;17(4):pp. 412–415.

Microchem. 2014. www.microchem.com.

Mie, G. *Annalen der Physik*, 1908;330(3):pp. 377–445.

Millstone, J. E., Métraux, G. S. and Mirkin, C. A. *Advanced Functional Materials*, 2006; 16(9):pp. 1209–1214.

Millstone, J. E., Wei, W., Jones, M. R., Yoo, H. and Mirkin, C. A. *Nano letters*, 2008; 8(8):pp. 2526–2529.

Mlyuka, N., Niklasson, G. and Granqvist, C.-G. *Applied Physics Letters*, 2009;95:pp. 171909–171909–3.

Mohelníková, J. *Solid State Phenomena*, 2009;144:pp. 226–231.

Molzen, W. W. *Journal of Vacuum Science and Technology*, 1975;12(1):pp. 99–102.

Moores, A., Goettmann, F., Sanchez, C. and Le Floch, P. *Chemical Communications*, 2004;pp. 2842–2843.

Mori, S. and Mikami, Y. Suspended particle device, light control device using the same, and method for driving the same. 2012. EP Patent 2,469,332.

Morin, F. *Physical Review Letters*, 1959;3(1):pp. 34–36.

Mortimer, R. J. *Chemical Society Reviews*, 1997;26(3):pp. 147–156.

Mulvihill, M. J., Ling, X. Y., Henzie, J. and Yang, P. *Journal of the American Chemical Society*, 2010;132(1):pp. 268–274.

Munechika, K., Chen, Y., Tillack, A. F., Kulkarni, A. P., Plante, I. J.-L., Munro, A. M. and Ginger, D. S. *Nano letters*, 2010;10(7):pp. 2598–2603.

Munechika, K., Smith, J. M., Chen, Y. and Ginger, D. S. *The Journal of Physical Chemistry C*, 2007;111(51):pp. 18906–18911.

Muraoka, Y., Ueda, Y. and Hiroi, Z. *Journal of Physics and Chemistry of Solids*, 2002; 63(6):pp. 965–967.

Nagai, J., McMeeking, G. D. and Saitoh, Y. *Solar Energy Materials and Solar Cells*, 1999;56(3):pp. 309–319.

Naghavi, K., Saion, E., Rezaee, K. and Yunus, W. M. M. *Radiation Physics and Chemistry*, 2010;79(12):pp. 1203–1208.

Nair, M. and Nair, P. *Journal of Physics D*, 1991;24(3):pp. 450–453.

Nehl, C. L., Liao, H. and Hafner, J. H. *Nano Letters*, 2006;6(4):pp. 683–688.

Niklasson, G. A. and Granqvist, C. G. *Journal of Materials Chemistry*, 2007;17(2):pp. 127–156.

Nikoobakht, B. and El-Sayed, M. A. *Chemistry of Materials*, 2003;15(10):pp. 1957–1962.

O'Brien, N. A., Gordon, J., Mathew, H. and Hichwa, B. P. *Thin Solid Films*, 1999; 345(2):pp. 312 – 318.

Ogilvie, I., Sieben, V., Floquet, C., Zmijan, R., Mowlem, M. and Morgan, H. *Journal of Micromechanics and Microengineering*, 2010;20(6):p. 065016.

Okitsu, K., Ashokkumar, M. and Grieser, F. *The Journal of Physical Chemistry B*, 2005;109(44):pp. 20673–20675.

Ould-Ely, T., Luger, M., Kaplan-Reinig, L., Niesz, K., Doherty, M. and Morse, D. E. *Nature Protocols*, 2011;6(1):pp. 97–104.

Park, J.-E., Atobe, M. and Fuchigami, T. *Ultrasonics Sonochemistry*, 2006;13(3):pp. 237–241.

Park, S. and Hong, J. W. *Thin Solid Films*, 2009;517(10):pp. 3183–3186.

Pastoriza-Santos, I. and Liz-Marzán, L. M. *Nano Letters*, 2002;2(8):pp. 903–905.

Peng, Z., Kisielowski, C. and Bell, A. T. *Chemical Communications*, 2012;48(13):pp. 1854–1856.

Perez-Lombard, L., Ortiz, J. and Pout, C. *Energy and Buildings*, 2008;40(3):pp. 394–398.

Pérez-Tijerina, E., Pinilla, M. G., Mejia-Rosales, S., Ortiz-Méndez, U., Torres, A. and José-Yacamán, M. *Faraday Discussions*, 2008;138:pp. 353–362.

Reppel, J. and Edmonds, I. *Solar Energy*, 1998;62(3):pp. 245–253.

Rivollier, S., Debayle, J. and Pinoli, J. In *Image Processing Theory Tools and Applications (IPTA), 2010 2nd International Conference on.* IEEE, 2010; pp. 411–416.

Roncali, J. *Chemical Reviews*, 1997;97(1):pp. 173–206.

Rushworth, C. M., Davies, J., Cabral, J. T., Dolan, P. R., Smith, J. M. and Vallance, C. *Chemical Physics Letters*, 2012;554:pp. 1–14.

Saeli, M., Piccirillo, C., Parkin, I. P., Binions, R. and Ridley, I. *Energy and Buildings*, 2010;42(10):pp. 1666–1673.

Sakai, T. and Alexandridis, P. *The Journal of Physical Chemistry B*, 2005;109(16):pp. 7766–7777.

Salkar, R., Jeevanandam, P., Aruna, S., Koltypin, Y. and Gedanken, A. *Journal of Material Chemistry*, 1999;9(6):pp. 1333–1335.

Salvati, R., Longo, A., Carotenuto, G., De Nicola, S., Pepe, G., Nicolais, L. and Barone, A. *Applied Surface Science*, 2005;248(1):pp. 28–31.

Sanedrin, R. G., Georganopoulou, D. G., Park, S. and Mirkin, C. A. *Advanced Materials*, 2005;17(8):pp. 1027–1031.

Sanghi, R. and Verma, P. *Bioresource Technology*, 2009;100(1):pp. 501–504.

Schaefer, C., Bräuer, G. and Szczyrbowski, J. *Surface and Coatings Technology*, 1997; 93(1):pp. 37–45.

Schelm, S., Smith, G., Garrett, P. and Fisher, W. *Journal of Applied Physics*, 2005; 97(12):pp. 124314–124314–8.

Schelm, S. and Smith, G. B. *Applied Physics Letters*, 2003;82(24):pp. 4346–4348.

Schlotter, P., Baur, G., Schmidt, R. and Weinberg, U. *Optical Materials Technology for Energy Efficiency and Solar Energy Conversion XIII*, 1994;2255:pp. 351–362.

Schwarzer, H.-C. and Peukert, W. *Chemical Engineering Communications*, 2004; 191(4):pp. 580–606.

Shabbeer, H. S., Khan, A. M., Shah, A., Rehman, Z.-U., Shah, S. M., Khan, A. Y., Shah, S. S. et al. *Walailak Journal of Science and Technology (WJST)*, 2012;9(3):pp. 229–237.

Shalom, D., Wootton, R. C., Winkle, R. F., Cottam, B. F., Vilar, R., demello, A. J. and Wilde, C. P. *Materials Letters*, 2007;61(4):pp. 1146–1150.

Sherry, L. J., Chang, S.-H., Schatz, G. C., Van Duyne, R. P., Wiley, B. J. and Xia, Y. *Nano letters*, 2005;5(10):pp. 2034–2038.

Sherry, L. J., Jin, R., Mirkin, C. A., Schatz, G. C. and Van Duyne, R. P. *Nano letters*, 2006;6(9):pp. 2060–2065.

Shestopalov, I., Tice, J. D. and Ismagilov, R. F. *Lab Chip*, 2004;4(4):pp. 316–321.

Shih, N.-J. and Huang, Y.-S. *Building Research & Information*, 2001;29(1):pp. 30–39.

Shiraishi, Y. and Toshima, N. *Journal of Molecular Catalysis A*, 1999;141(1):pp. 187–192.

Shirakata, S., Sakemi, T., Awai, K. and Yamamoto, T. *Superlattices and Microstructures*, 2006;39(1):pp. 218–228.

Shuford, K. L., Ratner, M. A. and Schatz, G. C. *The Journal of Chemical Physics*, 2005; 123:p. 114713.

Silvestrini, S., Carofiglio, T. and Maggini, M. *Chemical Communications*, 2013;49(1):pp. 84–86.

Smith, G., Dligatch, S., Sullivan, R. and Hutchins, M. *Solar Energy*, 1998;62(3):pp. 229–244.

Smith, G., McPhedran, R. and Derrick, G. *Applied Physics A*, 1985;36(4):pp. 193–204.

Smith, G., Niklasson, G., Svensson, J. and Granqvist, C. *Journal of Applied Physics*, 1986;59(2):pp. 571–581.

Smith, T. and Guild, J. *Transactions of the Optical Society*, 1931;33(3):p. 73.

Song, Y., Kumar, C. S. and Hormes, J. *Journal of Nanoscience and Nanotechnology*, 2004;4(7):pp. 788–793.

Sottile, G. *Materials Science and Engineering: B*, 2005;119(3):pp. 240–245.

Sounart, T., Safier, P., Voigt, J., Hoyt, J., Tallant, D., Matzke, C. and Michalske, T. *Lab on a Chip*, 2007;7(7):pp. 908–915.

Srivastava, M., Srivastava, S., Nirala, N. and Prakash, R. *Analytical Methods*, 2014; 6(3):pp. 817–824.

Stockman, A. and Sharpe, L. T. *Vision Research*, 2000;40(13):pp. 1711–1737.

Stokes, N. L., Edgar, J. A., McDonagh, A. M. and Cortie, M. B. *Journal of Nanoparticle Research*, 2010;12(8):pp. 2821–2830.

Su, K.-H., Wei, Q.-H., Zhang, X., Mock, J., Smith, D. R. and Schultz, S. *Nano Letters*, 2003;3(8):pp. 1087–1090.

Sun, Y., Mayers, B. and Xia, Y. *Nano Letters*, 2003;3(5):pp. 675–679.

Sun, Y. and Xia, Y. *Advanced Materials*, 2003;15(9):pp. 695–699.

Suslick, K. S. and Price, G. J. *Annual Review of Materials Science*, 1999;29(1):pp. 295–326.

Svensson, J. and Granqvist, C. *28th Annual Technical Symposium*, 1984;pp. 30–37.

Svensson, J. and Granqvist, C. *Applied Physics Letters*, 1986;49(23):pp. 1566–1568.

Swihart, M. T. *Current Opinion in Colloid & Interface Science*, 2003;8(1):pp. 127–133.

Tang, B., Xu, S., An, J., Zhao, B., Xu, W. and Lombardi, J. R. *Physical Chemistry Chemical Physics*, 2009;11(44):pp. 10286–10292.

Tang, W. and Cameron, D. *Thin Solid Films*, 1994;238(1):pp. 83–87.

Teng, X., Wang, Q., Liu, P., Han, W., Frenkel, A. I., Wen, W., Marinkovic, N., Hanson, J. C. and Rodriguez, J. A. *Journal of the American Chemical Society*, 2008;130(3):pp. 1093–1101.

Torres, V., Popa, M., Crespo, D. and Calderón Moreno, J. M. *Microelectronic Engineering*, 2007;84(5):pp. 1665–1668.

Toshima, N. and Yonezawa, T. *New Journal of Chemistry*, 1998;22(11):pp. 1179–1201.

Tung, K.-L. and Lu, K.-T. *Journal of Membrane Science*, 2006;272(1):pp. 37–49.

Turkevich, J., Stevenson, P. C. and Hillier, J. *Discussions of the Faraday Society*, 1951; 11:pp. 55–75.

Ung, T., Giersig, M., Dunstan, D. and Mulvaney, P. *Langmuir*, 1997;13(6):pp. 1773–1782.

Ung, T., Liz-Marzán, L. M. and Mulvaney, P. *Langmuir*, 1998;14(14):pp. 3740–3748.

Ung, T., Liz-Marzan, L. M. and Mulvaney, P. *The Journal of Physical Chemistry B*, 1999;103(32):pp. 6770–6773.

Valkonen, E., Karlsson, B. and Ribbing, C. *Solar Energy*, 1984;32(2):pp. 211–222.

Valkonen, E. and Ribbing, C. *Materials Letters*, 1984;3(1):pp. 29–32.

Verbeeck, G. and Hens, H. *Energy and Buildings*, 2005;37(7):pp. 747–754.

Vodnik, V. V., Vuković, J. V. and Nedeljković, J. M. *Colloid and Polymer Science*, 2009;287(7):pp. 847–851.

Waechter, H., Bescherer, K., Durr, C. J., Oleschuk, R. D. and Loock, H.-P. *Analytical Chemistry*, 2009;81(21):pp. 9048–9054.

Waechter, H., Munzke, D., Jang, A. and Loock, H.-P. *Analytical Chemistry*, 2011; 83(7):pp. 2719–2725.

Wagner, J. and Köhler, J. *Nano letters*, 2005;5(4):pp. 685–691.

Wang, W., Banerjee, S., Jia, S., Steigerwald, M. L. and Herman, I. P. *Chemistry of Materials*, 2007;19(10):pp. 2573–2580.

Weng, C.-H., Huang, C.-C., Yeh, C.-S., Lei, H.-Y. and Lee, G.-B. *Journal of Micromechanics and Microengineering*, 2008;18(3):p. 035019.

Whittaker, L., Jaye, C., Fu, Z., Fischer, D. A. and Banerjee, S. *Journal of the American Chemical Society*, 2009;131(25):pp. 8884–8894.

Wiley, B., Herricks, T., Sun, Y. and Xia, Y. *Nano Letters*, 2004;4(9):pp. 1733–1739.

Xu, G., Jin, P., Tazawa, M. and Yoshimura, K. *Solar Energy Materials and Solar Cells*, 2004;83(1):pp. 29–37.

Xu, G., Jin, P., Tazawa, M. and Yoshimura, K. *Applied Surface Science*, 2005;244(1):pp. 449–452.

Xu, X., Gibbons, T. and Cortie, M. *Gold Bulletin*, 2006;39(4):pp. 156–165.

Xue, C., Chen, X., Hurst, S. J. and Mirkin, C. A. *Advanced materials*, 2007;19(22):pp. 4071–4074.

Xue, C., Li, Z. and Mirkin, C. A. *Small*, 2005;1(5):pp. 513–516.

Yamamura, H., Takahashi, Y. and Kakinuma, K. *Nippon Seramikkusu Kyokai Gakujutsu Ronbunshi*, 2001;109(12):pp. 1000–1003.

Yang, L., Wang, Y., Luo, G. and Dai, Y. *Microporous and Mesoporous Materials*, 2005; 84(1):pp. 275–282.

Yang, P., Portales, H. and Pileni, M.-P. *The Journal of Physical Chemistry C*, 2009; 113(27):pp. 11597–11604.

Yin, Y., Lu, Y., Sun, Y. and Xia, Y. *Nano Letters*, 2002;2(4):pp. 427–430.

Yu, Chang, S.-S., Lee, C.-L. and Wang, C. R. C. *The Journal of Physical Chemistry B*, 1997;101(34):pp. 6661–6664.

Yue, J., Schouten, J. C. and Nijhuis, T. A. *Industrial & Engineering Chemistry Research*, 2012;51(45):pp. 14583–14609.

Yuste, M., Galindo, R. E., Carvalho, S., Albella, J. and Sánchez, O. *Applied Surface Science*, 2011;258(5):pp. 1784–1788.

Zhang, Q., Li, W., Moran, C., Zeng, J., Chen, J., Wen, L.-P. and Xia, Y. *Journal of the American Chemical Society*, 2010;132(32):pp. 11372–11378.

Zhao, L., Jiang, D., Cai, Y., Ji, X., Xie, R. and Yang, W. *Nanoscale*, 2012;4(16):pp. 5071–5076.

Zhu, J., Liao, X. and Chen, H.-Y. *Materials Research Bulletin*, 2001;36(9):pp. 1687–1692.

Zinoveva, S., De Silva, R., D Louis, R., Datta, P., SSR Kumar, C., Goettert, J. and Hormes, J. *Nuclear Instruments and Methods in Physics Research Section A*, 2007; 582(1):pp. 239–241.